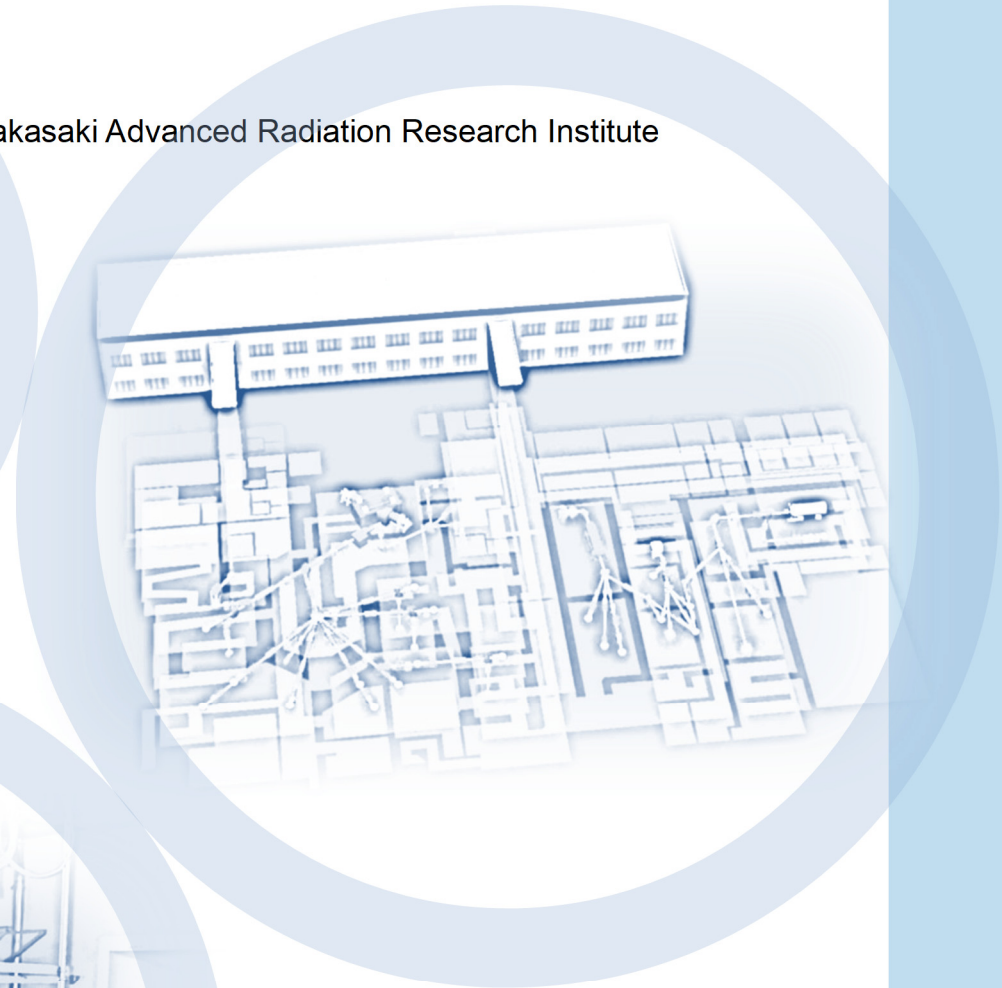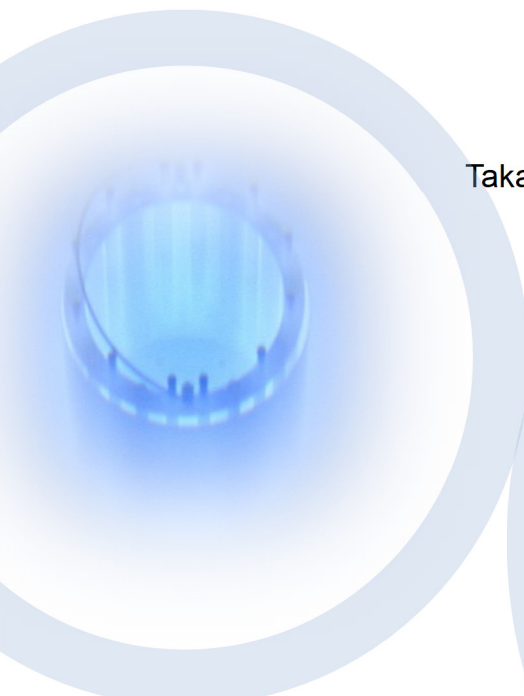# QST Takasaki Annual Report 2018

Takasaki Advanced Radiation Research Institute

National Institutes for Quantum and

Radiological Science and Technology

Preface

Hisayoshi Itoh

Director General
Takasaki Advanced Radiation Research Institute
Quantum Beam Science Research Directorate
National Institutes for Quantum and Radiological Science and
Technology

National Institutes for Quantum and Radiological Science and Technology (QST) was established in April 2016 by integrating the National Institute of Radiological Sciences (NIRS) and some institutes promoting quantum beam science research and nuclear fusion research in the Japan Atomic Energy Agency (JAEA). The QST has now three R&D directorates, *i.e.*, "Quantum Beam Science Research Directorate (QuBS)", "Quantum Medical Science Directorate" and "Fusion Energy Directorate", and one institute, *i.e.*, "Institute for Quantum Life Science". The QuBS is constituted by three research institutes, "Takasaki Advanced Radiation Research Institute (TARRI)", "Kansai Photon Science Institute (KPSI)" and "Institute for Advanced Synchrotron Light Source (IASLS)". We are intensively performing fundamental and applied researches in a wide range of fields like materials science, life science and quantum beam technology, using advanced beam facilities. Both TARRI and KPSI have two research sites, *i.e.*, Takasaki and Tokai sites of TARRI, and Kizu and Harima sites of KPSI. Typical beam facilities we used are Takasaki Ion Accelerators for Advanced Radiation Application (TIARA) at Takasaki site, Japan Proton Accelerator Research Complex (J-PARC) at Tokai site, Japan-Kansai Advanced Relativistic Engineering Laser System (J-KAREN) at Kizu site, and highly sophisticated beamlines of Super Photon Ring-8 GeV (SPring-8) at Harima site.　In IASLS, we are constructing a new Advanced Synchrotron Light Source for soft X-rays with ultra-high intensity and coherence.

In the TARRI, we have 17 Research Projects conducting quantum beam science R&Ds with TIARA, 2 MeV electron accelerator, ^{60}Co gamma-ray irradiation facilities, etc., for contributing to the progress of science and technology as well as the promotion of industry. Especially for strongly promoting alliance with industries, the Advanced Functional Polymer Materials Research Group has been launched in 2017 under QST innovation hub program to develop next generation graft-polymer materials with combined use of quantum beam processing and analysis techniques as well as materials informatics. The Quantum Sensing and Information Materials Research Group has been launched in August 2018 to conduct fundamental and applied researches for realizing quantum devices, *e.g.*, quantum sensors, quantum bits, spin transistors, etc., based on wide-bandgap semiconductors like diamonds as well as two-dimensional materials like graphene. We are also performing R&D of advanced ion beam technology at the Beam Engineering Section of the Department of Advanced Radiation Technology. In addition, our beam facilities are opened to industry,

academia, and governmental research institutes, and the beam time is allocated for users based on the evaluation of their R&D programs.

This Annual Report covers the research activities at the TARRI primarily for the fiscal year 2018 (FY 2018). This report consists of two parts, Part I and Part II. In Part I, the recent activities of all Research Projects, the Advanced Functional Polymer Materials Research Group and the Beam Engineering Section are described. Part II presents the recent R&D results obtained by using quantum beam facilities of the TARRI. This part is composed of 88 research papers in the fields of materials science, life science, and advanced quantum beam technology, and 8 status reports on operation / maintenance of the quantum beam facilities. It should be noted as a typical topic in the field of materials science that irradiation of a hydrophobic polydimethylsiloxane (PDMS) film with a low-energy electron beam (55 kV) in air generated hydrophilic microwells with ~40μm-thick silica-like layer, on which microbials and cells in nano- / pico-litter droplets could be easily trapped. The present method can be utilized to stable and reliable lab-on-chips and other biological applications. In the life science field, comprehensive RNA-seq revealed contrasting cellular responses to γ-ray and α-particle therapy, leading to the identification of four potential candidate genes that may serve as molecular imaging and *meta*-^{211}At-astato-benzylguanidine (^{211}At-MABG) therapy targets. These results suggest possible mechanism of the anti-tumor effect of ^{211}At-MABG in pheochromocytoma. As for the advanced quantum beam technology, local distribution of remaining elements inside extraction chromatography adsorbents have been observed by particle induced X-ray emission-computed tomography (PIXE-CT) with 3 MeV proton microbeam. For details of all R&Ds performed at the TARRI, please refer to the main text of this Annual Report.

Concerning the status of quantum beam facilities, three electrostatic accelerators in TIARA have been operated steadily and safely as well as MeV-electron and ^{60}Co gamma-ray irradiation facilities. The main coils of the AVF cyclotron, in which a serious layer short was found in December 2016, was replaced with new ones. Therefore, the operation of the cyclotron was stopped during the replacement (from July 2018 to March 2019). The RI security system of the ^{60}Co gamma-ray irradiation facilities has been upgraded to be adapted to the new regulations which will come into force on September 2019.

Finally, we extend gratitude to both our domestic and foreign colleagues for their cooperation, support, and encouragement for our quantum beam science R&Ds as well as technological advance in the facilities of TARRI.

Facilities

Charged particle beams and RI facilities

Takasaki Ion Accelerators for Advanced Radiation Application (TIARA) consisting of four ion accelerators, an electron accelerator, and gamma irradiation facilities are available to researchers in QST and other organizations for R&D activities on new functional and environmentally friendly materials, biotechnology, radiation effects of materials, and quantum beam analysis. We are developing microbeams, single ion hits and uniform wide-area irradiation technique at the cyclotron. In addition, technical developments of three dimensional in-air PIXE analysis and production/acceleration of cluster ion beam such as C_{60} fullerene at the electrostatic accelerators are in progress.

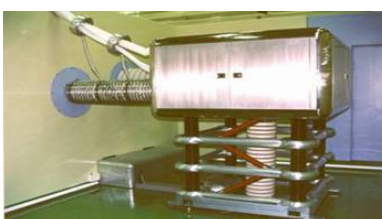## Takasaki Ion Accelerators for Advanced Radiation Application: TIARA
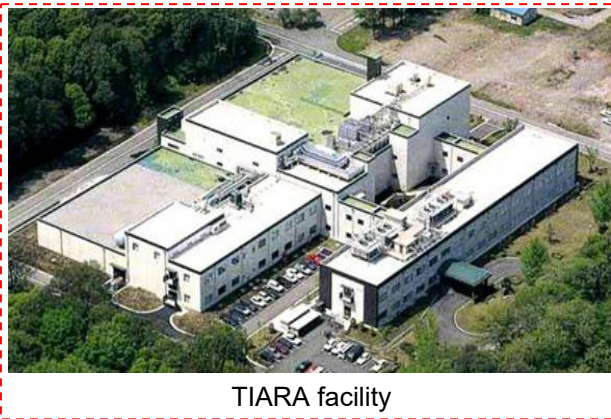
TIARA facility

Cyclotron
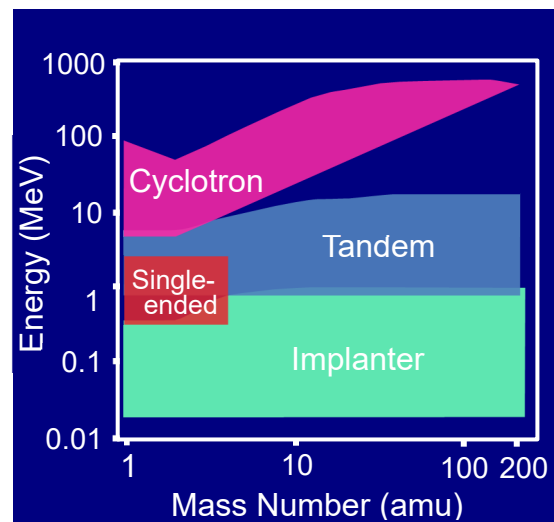

Tandem accelerator

Single-ended accelerator

Ion implanter

Typical available ions

Accelerator	Ion	Energy (MeV)
AVF Cyclotron (K=110MeV)	H	10～90
	He	20～107
	C	75～320
	Ne	75～350
	Ar	150～520
	Fe	200～400
	Kr	210～520
	Xe	324～560
	Os	490
Tandem Accelerator (3 MV)	H	0.8～6.0
	C	0.8～18.0
	Ni	0.8～18.0
	Au	0.8～18.0
	C_{60}	0.8～6.0
Single-ended Accelerator (3 MV)	H	0.4～3.0
	D	0.4～3.0
	He	0.4～3.0
	e^-	0.4～3.0
Ion Implanter (400 kV)	H	0.02～0.38
	Ar	0.02～0.38
	Bi	0.02～0.37
	C_{60}	0.02～0.36

Energy-element range covered by the four accelerators

Cobalt-60 gamma-ray and electron beam irradiation facilities

Gamma-ray irradiation facility building

Gamma-ray irradiation room

Electron accelerator
（0.5〜2.0 MeV　0.1〜30 mA）

Electron irradiation room with conveyor system

Specification

Apr. 2019

Name of facility	Cobalt-60 activity(PBq)	Number of rooms	Principal utilization
Co No.1 bld.	8.4	3	Radiation-resistance test Radiation effects on polymers
Co No.2 bld.	7.2	3	R & D on functional organic materials, dosimetry
Food Irrad.	2.4	2	Radiation effects on biological substance and semiconductors

Dose-rate range

Unit：kGy/h

Name of room	10^{-4}	10^{-3}	10^{-2}	10^{-1}	10^{-0}	10^{1}	10^{2}	10^{3}	10^{4}	10^{5}
Co No.2					▬	▬				
Co No.7				▬	▬					
Food No.1		▬	▬	▬						
EB accel.								▬	▬	

Contents

Part Ⅱ

Part I

Part Ⅰ

1. Materials Science

P1-1 Project "Functional Polymer"

Leader : Yasunari Maekawa

Project "Functional Polymer" has been developing functional polymer materials for high performance fuel cells and hydrogen collection systems using quantum beams such as electron beams, γ-rays and ion beams. We have synthesized proton- and anion-conducting electrolyte membranes (PEM and AEM) and hydrogen permselective membranes. We report herein two recent developments: poly(ethylene-co-tetrafluoroethylene) (ETFE)-based AEMs for alkaline fuel cells applied in automobiles and poly(ether ether keton) (PEEK)-based PEMs for fuel cells and electrolytic enrichment of tritium. {1-16~17 in Part II}

Preparation of Aniline-Containing Anion-Conducting Polymer Electrolyte Membranes by Radiation-Induced Graft Polymerization [1]

Recently, we prepared poly(vinylbenzyl trimethylammonium hydroxide)-grafted ETFE membranes (BA-AEM/OH) by using a radiation graft technique [2]. The BA-AEM/OH with a high ion exchange capacity maintained a high conductivity in 1 M KOH at 80 ºC. However, the membranes degraded to exhibit low mechanical stability in alkaline solution. In order to overcome alkaline durability, in this study, we newly synthesized N,N-dimethylaminostyrene (DMASt) having lower basicity anion-exchange group without benzyl structure to improve the alkaline stability of the AEM.

Poly(trimethylaminostyrene hydroxide)-grafted ETFE membranes (An-AEM/OH) were prepared by the radiation-induced graft polymerization of DMASt on ETFE membranes, followed by N-alkylation and anion-exchange reactions. The alkaline durability of the AEMs was evaluated by change in the conductivity in 1 M KOH at 80 ºC. The conductivity of An-AEM/OH with ion exchange capacity (IEC) = 1.59 mmol/g decreased to 46% of the initial value after a week, while the AEM maintained the shape even after immersion for 3 weeks, as shown in Fig. 1. Thus An-AEM/OH exhibited higher chemical stability than BA-AEM/OH with similar IEC. The degradation mechanism was confirmed as the same nucleophilic attack of hydroxide ion on the three methyl groups from the results of ATR-IR. The decrease in the conductivity of An-AEM/OH corroborated the decrease of the basicity of the ionic group, which consequently prevented the decomposition of ETFE.

Graft-type PEEK-based polymer electrolyte membranes for electrochemical devices such as fuel cells and electrolytic tritium enrichment [3]

Polymer electrolyte membranes have been applied to various electrochemical equipment. Nafion® as a representative perfluorosulfonic acid (PFSA) membrane have been used for fuel cells due to the chemical stability. However, an operating temperature of the fuel cell is limited to below 80 ºC. The operation under high temperature (>100 ºC) and low humidity have been required for the fuel cells from the viewpoint of simplification of cooling system. On the other hand, in an electrolytic enrichment using water electrolysis, PFSA membranes have been used. Few investigations have been made into other type of materials. In this study, the PEEK-based PEMs with high thermal stability and low water uptake were investigated for the applications to the fuel cell and the electrolytic enrichment of tritium.

PEEK-based PEMs with/without additives were prepared by using the radiation-induced polymerization method, as previously reported [4]. For a fuel cell test, catalytic coated membranes were prepared using additive-free PEM with IEC = 2.4 mmol/g. As a result of a durability test for the PEM with 0.15 S/cm of a conductivity under the condition of 110 ºC and 50% relative humidity, the PEM exhibited 1500 h of a lifetime at 0.3 A/cm². The cell voltage maintained 97% of the initial voltage at 1300 h. In the case of Nafion®, the cell voltage decreased to zero at about 150 h. For the electrolytic enrichment of tritium, the PEEK-based PEMs with talc were prepared. Solid polymer electrolysis device composed of the PEEK-based PEMs with IEC = 0.9 mmol/g exhibited 1.35 of a tritium enrichment ratio as a tritium enrichment index at 30 ºC, which is 20% higher than that of Nafion, as shown in Fig. 2. The higher tritium enrichment ratios in PEEK-based PEMs were explained by the smaller amount of transported water.

References

[1] T. Hamada *et al.*, J. Appl. Polym. Sci., **135**, 46886 (2018).
[2] H. Koshikawa *et al.*, Macromol. Chem. Phys., **214**, 1756 (2013).
[3] A. Fukaya *et al.*, Int. J. Hydrogen Energy, **43**, 8927 (2018).
[4] S. Hasegawa *et al.*, Polymer, **52**, 98 (2011).
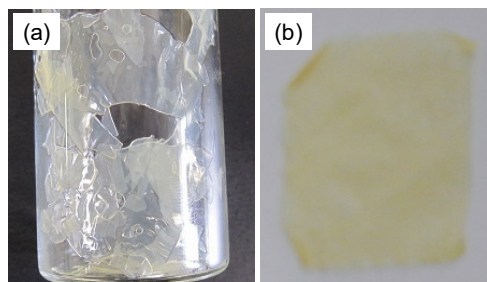
Fig. 1. Photographs of (a) BA-AEM/OH with IEC = 1.62 mmol/g and (b) An-AEM/OH with IEC = 1.59 mmol/g after immersion in 1 M KOH at 80 ºC for 72 h and 504 h, respectively.
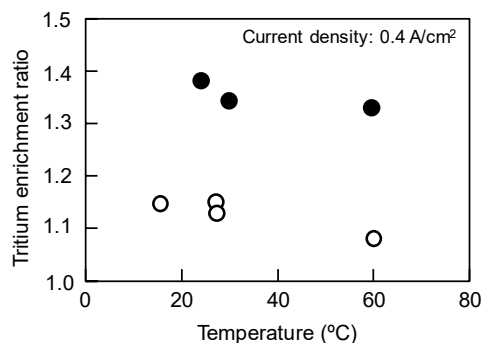
Fig. 2. Temperature dependence of the tritium enrichment ratio; (●) PEEK-based PEM with talc and (○) Nafion1110.

P1-2 Project "Advanced Catalyst"

Leader : Yasunari Maekawa

Our main research target is to develop catalytic materials for next-generation energy devices for future hydrogen society by effective use of ion and electron beams. The advantage of our overarching research strategy is that these quantum beams can lead to lattice defects in solids, active-site formation via non-equilibrium chemical reactions, and structural fabrication of micro-to nano-meter scale, which have a great potential to facilitate the development of novel functional materials through innovative interdisciplinary methodologies. This report deals with applications of the quantum beams to R&D for component materials in proton exchange membrane fuel cells. {1-12~15 in Part II}

Fabrication of a nitrogen-doped carbon catalyst from a precursor polymer using the electron beam irradiation technique [1] {1-14}

Recently, nitrogen (N)-doped carbon catalysts have been extensively studied because they exhibit catalytic activity for an oxygen reduction reaction (ORR), $O_2 + 4H^+ + 4e^- \rightarrow 2H_2O$, which is comparable to the platinum catalysts. It has been reported that the requirements for the catalytic activity of the N-doped carbon catalysts are formation of graphitic nanostructure and incorporation of N as a pyridinic structure. Therefore, it is important to develop a method to fabricate such N-doped graphitic nanostructure in high efficiency. In the temperature range of 800 - 1000 °C, the graphitic nanostructure is formed, while the doped nitrogen is thermally evaporated from the graphite. Owing to the mismatch of these temperature ranges, it is difficult to control both of the formation of the graphitic nanostructure and the N-doping. This is caused by that the conventional process is a thermally equilibrium process. Thus, we propose a novel fabrication process of the N-doped carbon catalyst utilizing high energy-electron beam (EB) irradiation on a precursor polymer under ammonia (NH_3) gas atmosphere in this work. A blend of phenolic resin and cobalt chloride was irradiated by 2 MeV EB under NH_3 gas flow by heat treatment up to 800 °C.

It was found that the EB irradiation produces the carbon material with high content of graphite phase (Fig.1 (a)) and enhances the amount of N-doping, especially pyridinic-N, comparing with the common heat treatment in an electric furnace (Fig.1 (b)). The obtained carbon material exhibited catalytic activity for the ORR with the ORR potential of 0.7 V vs. RHE in 0.5 M H_2SO_4. It was demonstrated that high-energy EB irradiation enables the formation of a graphitic nanostructure and N-doping simultaneously and thus it is effective for fabricating a carbon material with catalytic activity for the ORR.

X-ray absorption study of platinum nanoparticles on an ion-irradiated carbon support [2, 3] {1-12}

In order to reduce the Pt loading in the fuel cells, the catalytic activity and durability of the Pt nanoparticles have to be improved. One of the promising approaches for this purpose is to use the interfacial effect of support materials on the Pt nanoparticles. In our previous study, lattice vacancies were introduced in a glassy carbon (GC) substrate by irradiation with 380 keV argon ions and contributed to the interaction with the Pt nanoparticles.

The enhancement of the Pt–C interfacial interaction due to the ion-induced vacancies was revealed by the broadening of the Pt $4f_{7/2}$ and C 1s peaks observed in X-ray photoelectron spectroscopy measurements [4]. The understanding of the role of this unique interfacial interaction in the ORR catalysis can be obtained by taking account of the chemical state and the local structure of the Pt nanoparticles.

In this study, the chemical state and local structure of 2.6-nm-sized Pt nanoparticles on an ion-irradiated GC substrate were investigated by X-ray absorption fine structure (XAFS) measurements at beamline BL14B1 of SPring-8. The partial oxidation of the Pt nanoparticles was confirmed by the peak intensity in the near-edge region of the absorption spectrum. The analysis of the extended region revealed a higher coordination number and shorter bond length of Pt–Pt compared to those of the Pt nanoparticles on the non-ion-irradiated GC. Therefore, the ion-irradiated carbon support was found to provide the Pt nanoparticles with a rigid Pt–Pt metallic coordination against oxidation.

References

[1] A. Idesaki *et al.*, Jpn. J. Appl. Phys., **58**, SDDF03 (2019).
[2] K. Kakitani *et al.*, Radiat. Phys. Chem., **153**, 152 (2018).
[3] K. Kakitani *et al.*, Surf. Coat. Technol., **355**, 259 (2018).
[4] T. Kimata *et al.*, Surf. Coat. Technol., **306**, 123 (2016).
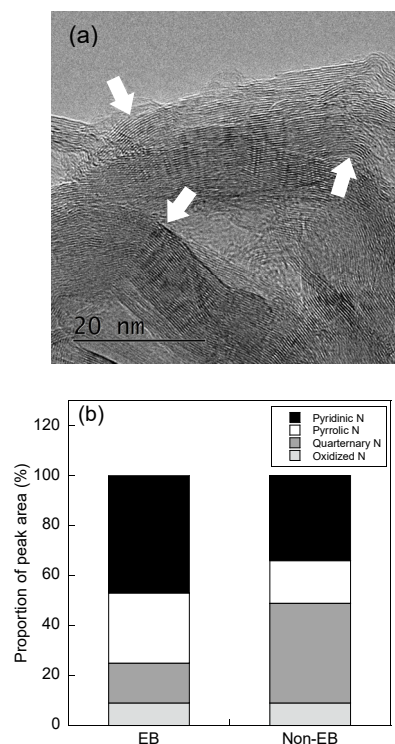
Fig. 1. The N-doped carbon material fabricated by EB irradiation technique: (a) TEM image and (b) proportion of peak area of N 1s XPS spectrum.

P1-3 Project "Positron Nanoscience"

Leader : Atsuo Kawasuso

The aim of the project "Positron Nanoscience" is to develop new and potential positron beam technologies for the advanced solid state physics. So far, we have been developing (i) the spin-polarized surface positronium spectroscopy that is substantially useful for detecting spin-polarization of electrons at the first surface layer, (ii) the spin-polarized positron annihilation spectroscopy in strong magnetic field for detecting vacancy-induced magnetism and (iii) the low-energy positron diffraction for the structural analysis of surfaces containing heavy atoms. In this report, we pick up the achievements of theme (i) and (iii) in the last fiscal year (2018).

Development of Spin-polarized Positronium Time-of-Flight System [1]

Using spin-polarized positronium (Ps) annihilation spectroscopy, the electron spin polarization of top-surface layer can be determined because Ps is formed only at the vacuum side of the surface. If the energy-resolved and spin-polarized Ps annihilation spectroscopy is available, spin-polarized electron density of states (DOS) associated with the top-surface layer is expected to be obtained. In connection with the spin-Hall effect, Rashba effect and topological insulators, the spin polarization at the Fermi level is very important for evaluating the spin transportation in devices. The spin-polarized Ps time-of-flight method (SP-PsTOF) will respond to such offers. We have been developing SP-PsTOF apparatus.

Spin-polarized positrons from a ^{22}Na source (440 MBq) and a solid Kr moderator are injected into the sample. The time-of-flight of emitted Ps can be determined by the detection times of secondary electrons from the sample when positrons impact it and ortho-Ps annihilation gamma rays. The sample is magnetized by an external magnetic field. When the surface electron is spin-polarized, by alternating the magnetic field direction, the intensity of ortho-Ps changes. It is expected that difference intensity appears on the SP-PsTOF spectrum. For a Ni (ferromagnetic) and Pt (nonmagnetic) film sample, SP-PsTOF measurements were carried out. In the case of Pt film, no significant differences were found. Contrarily, for a Ni film sample, the negative polarization near the Fermi level was detected. This means that the spin-polarized surface electrons are successfully detected. Although similar results are reported in other spin measurement techniques, such as spin- and angle-resolved photoelectron spectrometry (SARPES), our SP-PsTOF method has an advantage for surface sensitivity because positrons can pick up only the outermost electrons.

Development of Low Energy Positron Diffraction [2]

Low-energy positron diffraction (LEPD), which is the positron counterpart of low-energy electron diffraction (LEED), has been proposed by a LEED theorist as an ideal surface structure analysis method; LEPD is more surface sensitive, suffers less multiple scattering, and shows much simpler smooth scattering factors than LEED. In 1979, the first LEPD was observed by the Brandeis University group

with a channel electron multiplier using a slow-positron beam from a radioisotope (RI) source emitting positrons, which is transported by electrostatic lenses. Subsequently, they developed a system for observing an LEPD pattern with multiple spots and demonstrated that LEPD experimental results are more closely reproduced by a dynamical diffraction theory than in LEED. However, LEPD experimental research has been discontinued for about the last two decades because of the difficulty in obtaining a low-energy positron beam with sufficient intensity and adequate quality.

We have developed an experimental system for the study of LEPD with a slow-positron beam generated by a linear-electron-accelerator (linac). Diffraction patterns of a Ge(001)-2×1 surface structure have been observed (Fig. 1). This is the first LEPD observation with a linac-based high-intensity pulsed slow-positron beam.

A linac-based slow-positron beam has a pulsed time-structure reflecting that of the linac beam, which could cause a multi-hit problem in the detection system with a position-sensitive detector. To solve this problem, a pulse stretcher with a Penning-Malmberg trap, approximately 6 m long, has been developed.

Linac-based systems transport the beam from a remote positron production unit along with a magnetic field and it is difficult to shield the diffraction observation system from the magnetic field. A new transmission-type brightness-enhancement system with electrostatic lenses has been developed to produce low-energy positron beams, interacting with a sample in a non-magnetic field region, with sufficient intensity and adequate quality.

LEPD is expected to be particularly useful for structural analysis of the surfaces containing heavy atoms, which are difficult to be analyzed by LEED. LEPD is also applicable to less flat surfaces and also expected to be developed into a method for the analysis of local surface structure, as a complementary method to total-reflection high-energy positron diffraction (TRHEPD).

References

[1] M. Maekawa *et al.*, J. Phys. Conf. Ser., **791**, 021009 (2017).
[2] K. Wada *et al.*, e-J. Surf. Sci. Nanotech., **16**, 313 (2018)
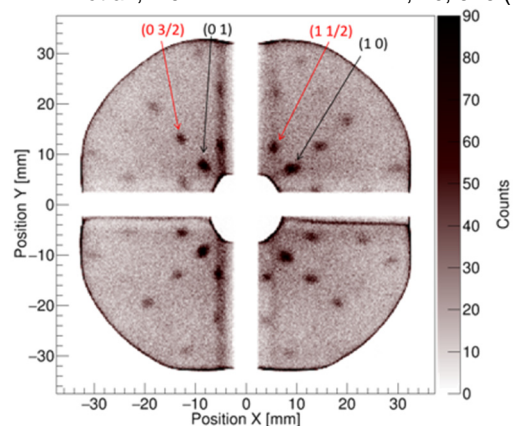
Fig. 1. Diffraction pattern from a Ge(001)-2x1 structure observed with a 144.5 eV positron beam generated by a linac [2].

P1-4 Project "Spintronics in Two-dimensional Materials"

Leader : Seiji Sakai

Our project aims at developing novel quantum electronics and spintronics techniques for future information technology by taking advantages of the low dimensionality and quantum electronic properties of two-dimensional materials and related heterostructures. The advanced quantum beam techniques of QST and of our research groups (Two-dimensional Materials Spintronics Project and QST Advanced Study Laboratory for Quantum Materials Science) could allow us to explore and design the local atomic and electronic structures in low-dimensional materials, heterostructures and even at their interfaces above the technological limits in nanomaterials science so far.

Growth of graphene on SiO₂ with hexagonal boron nitride buffer layer [1]

Graphene has been attracted wide and intensive attention as one of the most promising materials for nanoelectronics and spintronics in recent years. One of the key technologies which enable significant improvements in the performance of graphene devices is the weakening of the interface interaction between graphene and insulator substrate by employing an inert buffer layer. In this study, we successfully fabricated a heterostructure of graphene/hexagonal boron nitride(*h*-BN)/SiO₂, in which single atomic layer *h*-BN is inserted between graphene and SiO₂ as an insulating buffer layer, by chemical vapor deposition (CVD). It was found that *h*-BN dramatically promotes the growth of graphene on SiO₂, whereas the graphene growth without *h*-BN is extremely difficult (Fig.1(a)). The analysis of the electronic states by Raman spectroscopy, X-ray photoemission spectroscopy (XPS) and X-ray absorption spectroscopy revealed that there is no chemical interaction both at the graphene/*h*-BN interface and *h*-BN/SiO₂ interface (Figure 1(a)), and also the charge density distribution in graphene by unintentional doping from the SiO₂ substrate is greatly suppressed by single atomic layer *h*-BN (Figure 1(b)). The present study shows that the *h*-BN layer grown with CVD can be a superior buffer layer for graphene devices, which enables a direct graphene growth on it and to decrease the interface interactions with insulator substrates.
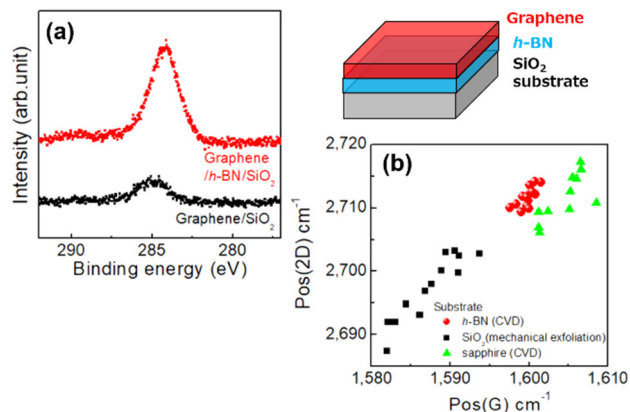
Fig. 1. (a) C 1s XPS spectra of graphene/*h*-BN/SiO₂ (red dots) and graphene/SiO₂ (black dots). The growth rate of graphene on *h*-BN was estimated to be at least 75 times faster than that on SiO₂ from

the peak intensities. (b) Distributions of the peak positions of the G and 2D bands (Pos(G) and Pos(2D)) in graphene/*h*-BN/SiO₂ taken from the randomly selected areas on the sample surface by micro-Raman spectroscopy (red circles). For comparison, the date for graphene/SiO₂ obtained by micromechanical exfoliation (black squares) and graphene/sapphire grown by CVD (green triangles) [2] are also shown in the figure. The small peak-position distributions of Pos(G) and Pos(2D) in graphene/*h*-BN indicate that the *h*-BN buffer layer contributes to promote the growth of graphene with high uniformity in electronic state and crystallinity.

Novel 2D CuO supported in bilayer graphene pore [3]

A wide family of 2D materials with various atomic structures and electronic properties has been studied intensively in these days. Notably, the findings of 2D materials without bulk counterparts suggest expandability and multifunctionality of the 2D materials family in quantum materials science and device applications. We found that a nanometer-scale pore generated in bilayer graphene by electron beam irradiation serves as a template for the growth of novel 2D CuO with atomic thickness and an unusual rectangular lattice different from bulk copper oxides [2]. Our comprehensive investigation by experimental and theoretical approaches revealed that the growth of the 2D CuO sheet within the bilayer graphene pore is initiated by the co-presence of a small number of Cu and O atoms migrating around the pore edges and is finally completed by the formation of the pore-filling 2D CuO sheet with a Cu-terminated interface between the surrounding bilayer graphene (Figure 2). Theoretical calculations showed that the formation of the 2D CuO-bilayer graphene heterostructure gives rise to noticeable spin-polarization in bilayer graphene. Our findings testified that the bilayer graphene pore can be used as a promising template for the synthesis of new 2D materials and for designing the electronic and spintronic properties of 2D materials and their heterostructures.
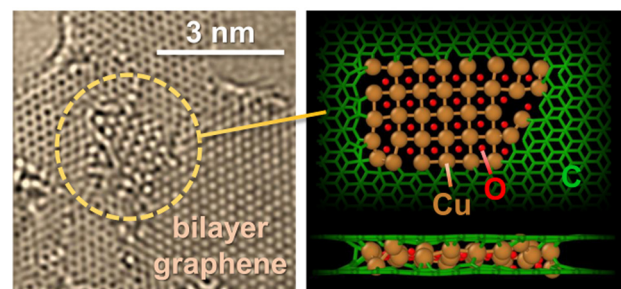
Fig. 2. Transmission electron microscope image (left-side panel) and theoretically derived atomic structure (right-side panel) of bilayer graphene-2D CuO heterostructure in which a 2D CuO sheet fills the pore (2 nm in diameter) in bilayer graphene. The heterostructure was fabricated at ambient temperature under 80 keV electron beam irradiation.

References

[1] S. Entani *et al.*, Appl. Surf. Sci., **475**, 6-11 (2019).
[2] S. Entani *et al.*, Nano Res., **8**, 1535-1545 (2015).
[3] D. G. Kvashnin *et al.*, J. Phys. Chem., C **123**, 17459-17465 (2019).

P1-5 Project "Semiconductor Radiation Effects"

Leader : Takeshi Ohshima

Technologies based on quantum effects, such as quantum computation, quantum cryptography information and quantum sensing, are quite hot topics since the quantum technologies can change our life to be more comfortable, safer and more secure. Color centers of which optical and spin properties can be manipulated with high fidelity are expected to be quantum bits (qubits) and quantum sensors. We create color centers in wide bandgap semiconductors such as diamond and silicon carbide (SiC) using ion and electron beams, and investigate their optical and spin properties. On the other hand, when semiconductor devices are subjected to radiations such as ions, electrons and gamma-rays, their characteristics degrades and as a result, the malfunctions occur. We study radiation response of semiconductor devices, in order to establish radiation resistant technologies for development of long lifetime and highly reliable semiconductor devices that can be used in high radiation environments such as space, nuclear and accelerator facilities. {1-01, 02, 03 in Part II}

Creation of silicon vacancy (V_{Si}) in SiC pn diodes by Proton Beam Writing (PBW) [1]

Silicon vacancy (V_{Si}) in SiC is known as a color center with luminescence wavelengths around 900 nm. Since the luminescence from V_{Si} is observed and electron spin (S=3/2) for V_{Si} can be manipulate at room temperature, V_{Si} is expected to be applied to a quantum sensor and a qubit working at room temperature [2]. To develop V_{Si} based quantum applications, it is important to introduce V_{Si} in certain locations and operate its luminescence/spin properties using device operation. In this study, V_{Si}s are introduced into planar pn diodes on SiC by PBW.

Figure 1 shows fluorescence (electroluminescence, EL) mapping for a planar SiC diode irradiated with protons at 0.5 MeV using PBW. The current at 500 μA is injected to the diode by applying forward biases and mapping was obtained at room temperature. The bright spots are clearly observed from proton irradiated points, in which 1×10^7 protons/point were irradiated. We also observed photoluminescence (PL) from those points. In addition, both EL and PL spectra with a peak at wavelengths around 900 nm were confirmed. The results indicate that V_{Si}s are created in a SiC pn diode, and the luminescence properties of V_{Si} can be operated by device operation (applying forward bias).

Enhancement of creation yield of nitrogen-vacancy (NV) center in diamond by elevated temperature electron irradiation [3]

Creation of high concentration of nitrogen-vacancy (NV) centers in diamond is important for quantum sensing since the sensitivity increases with increasing number of NVs. Electron irradiation is thought to be a powerful tool to create NVs in diamonds because uniform damage (vacancies) regions can be created in diamond substrates of which thickness are typically in 1 mm or less. In order to create high concentration of NVs, it is necessary to conduct electron irradiation with high fluence. However, the quality of diamond crystal is degraded by electron irradiation, and as a result, the recovery of crystal is not

possible even by subsequent annealing. This indicates that optical/spin properties of NVs in such diamonds are also degraded due to crystal damage. To avoid this degradation, we have developed an electron irradiation technique under elevated temperature. Figure 2 shows N to NV conversion yield for diamonds either irradiated at elevated temperature (2 MeV-electrons, 1×10^{18}/cm^2, 740 °C) or irradiated at room temperature and subsequently annealed at 740 °C. Thus, the annealing time are the same as the duration of elevated temperature irradiation (21 hours). As shown in the figure, NV conversion yield for diamonds irradiated at elevated temperature is always higher than that for diamonds irradiated at room temperature although annealing temperature and the duration are the same as elevated irradiation. This result strongly suggests that elevated temperature irradiation is a useful method to improve NV conversion yield.

References

[1] Y. Yamazaki *et al.*, J. Mater. Res., **33**, 3355 (2018).
[2] T. Ohshima *et al.*, J. Phys., D **51**, 333002 (2018).
[3] M. Capelli *et al.*, Carbon, **143**, 714 (2019).
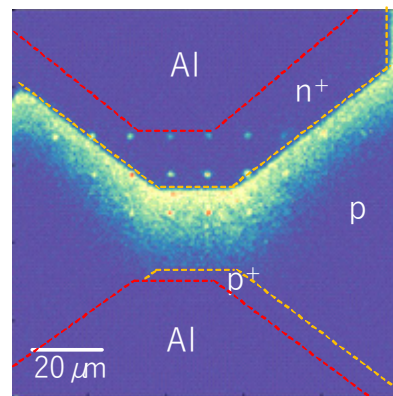
Fig. 1. EL map for a SiC pn diode. Current at 500 μA are injected into the diode. A 808 nm long pass filter were used. The dotted and broken lines indicate boundary of n$^+$ or p$^+$ region/Al electrode and n$^+$ or p$^+$ regions/p-type layer, respectively.
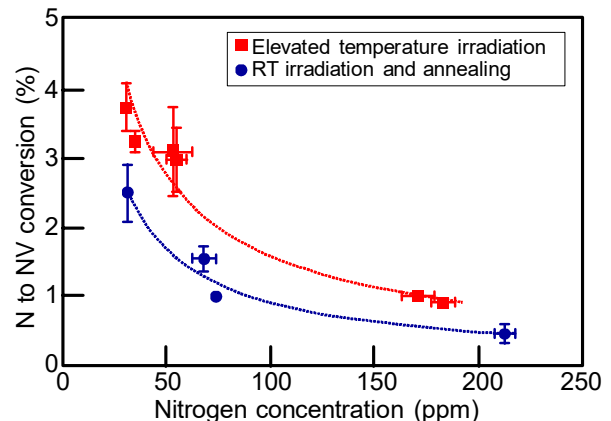
Fig. 2. N to NV conversion yield as a function of N concentration in diamonds irradiated at elevated temperature (squares) and room temperature (circles). The dotted lines are guide of the eye.

P1-6 Project "Biocompatible Materials"

Leader : Mitsumasa Taguchi

Project "Biocompatible Materials" has been developing the functional biocompatible materials based on the radiation-induced crosslinking technique. The obtained materials can be utilized for the bio-devices in diagnostic, treatment and regenerative medicine {1-18 in Part II}.

Single-step fabrication of polydimethylsiloxane microwell arrays with long-lasting hydrophilic inner surfaces [1]

Polydimethylsiloxane (PDMS) is widely used in lab-on-a-chip technologies because of its biocompatibility, optical transparency, low autofluorescence, flexibility, and ease of handling. However, a significant drawback is its hydrophobicity, as illustrated by a water contact angle (WCA) of ~100°, owing to its repeating dimethylsiloxane [$-OSi(CH_3)_2-$] units. PDMS surfaces are commonly hydrophilized by plasma irradiation. Although this technique is simple and effective, it must be applied immediately prior to chip use owing to rapid hydrophobic recovery. A method that provides long-lasting hydrophilization of PDMS surface is required to obtain stable and reliable lab-on-a-chips.

PDMS films were prepared by pouring a mixture of the precursor SIM-260 and curing agent CAT-260 on a Si mold and heating at 150 °C for 30 min. The film was then peeled from the mold. Low-energy electron beam (LE-EB) at the energy of 55–90 kV generated from a table-top accelerator (IWASAKI) deposit their energies by penetrating the PDMS from the surface to a depth range of ~40–110 μm, these interaction ranges are much deeper than that provided by plasma (less than a few hundred nanometers). LE-EB irradiation (55 kV) in air at a dose rate of 330 kGy/s (Gy = J/kg) alters the PDMS hydrophilicity within 1 min; the WCA decreases corresponding to the irradiation dose, changing from ~103° to ~60° for an absorbed dose of 10 MGy (evaluated using calorimetry), and subsequently remaining between 40° and 50° for doses above 15 MGy as shown in Fig. 1a. For samples partially irradiated with LE-EB through patterned masks, concave pattern formation can be visually confirmed (Fig. 1b). From micrographs of sample cross-sections (Fig. 1b), we determined the depth of the concave features as dozens of micrometers. For example, the depth is ~40 μm when irradiated with a 55 kV LE-EB for a dose of 15 MGy through a circular mesh pattern (φ330 μm). Hydrophilic microwells are generated on the hydrophobic non-irradiated PDMS surface, and a nanoliter droplet array can be successfully formed by wetting the surface and removing the excess water (Fig. 1c).

The FTIR and XPS measurements indicate that the chemical strucuture changes of PDMS induced by LE-EB are similar to those by plasma. Both methods decompose $-CH_3$ groups, evaporating H_2 and CH_4 from the matrix while absorbing O_2 from the ambient air. The main oxygenated group produced by either irradiation is likely Si–OH (silanol). The major difference between the two irradiation techniques is the depth over which hydrophilization is induced. Another major difference is the durability of the hydrophilicity. The PDMS specimen irradiated with LE-EB exhibits excellent hydrophilic stability compared to the low-pressure air-plasma-irradiated PDMS under various storage conditions. Remarkably, the LE-EB-irradiated PDMS remains hydrophilic (WCA <75°) for more than 10 months storage in deionized water at room temperature (RT, ~22 °C) .

One of the most promising applications of locally functionalaized PDMS is in cell culture. Both the durable hydrophilicity and dozens-μm-deep concave features play important roles in cell trapping and adhesion. A ~35 μm square microwell array chip with a depth of 30 μm was fabricated by 20 MGy irradiation of 55 kV LE-EB using a 400-mesh grid as the mask. The 3T3-Swiss albino mouse embryo fibroblast cells (10 μL) stained with calcein-AM were seeded on the chip at a density of 2×10^5 cells/mL. After 2 h incubation, the chip was washed several times with cell-culture medium to remove the non-adherent cells. The cells favorably adhered to the hydrophilic bottoms of the microwells, and single-cell-level trapping was successfully achieved as shown in Fig. 2.

Reference
[1] T. G. Oyama *et al.*, Appl. Phys. Lett., **112**, 213704 (2018).
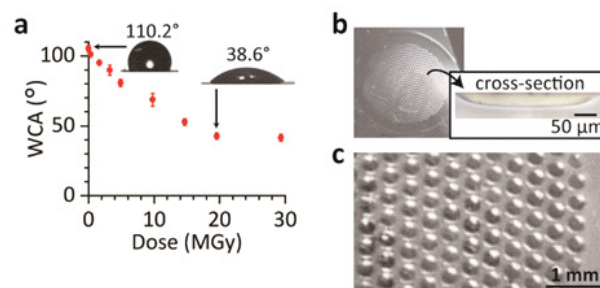
Fig. 1. (a) WCAs of PDMS samples as a function of the 55 kV LE-EB irradiation dose. Error bars showing the mean ± standard error of the mean (s.e.m.) of n = 6 independent experiments. The inset images are typical droplets corresponding to the data points indicated by the arrows. (b) Photograph of a typical PDMS film after LE-EB irradiation through a patterned mask, and a micrograph of a cross-section of the concave well. (c) Photograph of the droplet array obtained after wetting the sample surface with water (dose: 15 MGy, irradiated pattern: φ330 μm).
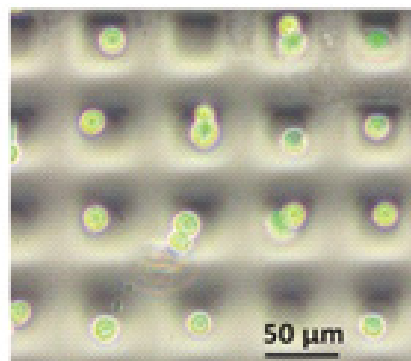
Fig. 2. A fluorescence images of calcein-stained 3T3 cells trapped by the fabricated square microwell array chip.

P1-7 Project "Environmental Polymer"

Leader : Noriaki Seko

Project "Environmental Polymer" has been developing the functional polymer fabrics for metal adsorbents by radiation induced graft polymerization technique using such as electron beams and γ-rays. The developed adsorbents can be expected for applications in removing and recovering trace metal ions from water. To development lost cost, environmental-friendly and high performance adsorbents, we started this research from both basic and applied science.

Establishment of determination method for molecular weight analysis of graft chains [1]

To establish an efficient method for the molecular weight determent of the graft chains, the graft bonds of styrene-grafted poly(vinylidene difluoride) films (PVDF-g-St) were cleaved by boiling xylene extraction. It was confiremed by FTIR and NMR spectra that the polystyrene graft chains could be completely separated from the grafted films and dissolved in the solution, while the pristine PVDF films were remained in the boiling xylene. Furthermore, the molecualr weights of the PVDF-g-St film were largely increased after the grafting, inciating that the polystyrene was convalently bonded on the PVDF films.
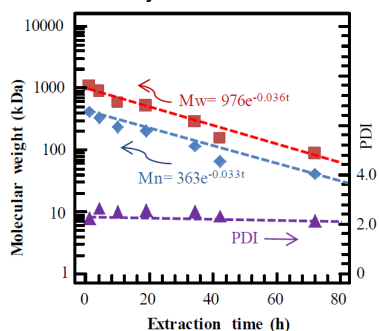
Fig. 1. Relative molecular weight (Mw and Mn) and polydispersity index (PDI) of the extracted polystyrene graft chains determined by GPC instrument.

As analysized by NMR instruments, the extracted material from the grafted PVDF film was polystyrene. Figure 1 displays the molecular weight (Mn and Mw) and PDI (Mw/Mn) of the polystyrene as a function of extraction time. As can be seen, the molecular weight of polystyrene decreased with increasing extraction time, whereas the PDI remained virtually unchanged. Such an exponential decrease tendency can be attributed to the thermal degradation of the polystyrene in the xylene solution at high temperature. From Figure 1, we can obtain the molecular weight of the graft chains without deterioration by extending the trend straight line to the extraction time of 0 h. Thus, the Mn and Mw of the non-degraded graft chains were determined to be 363 and 976 kDa, respectively.

From the comparison with the Mn and Mw of the graft chains at 19 h extraction time (201 and 515 kDa, respectively), it can be concluded that about one C–C bond for each polystyrene chain was cleaved within 19 h of extraction time. Furthermore, within 4 h of extraction time, the Mw decreased about 8.9% (from 976 to 889 kDa) while the degree of separation of the graft

chains reached more than 46%. Therefore, the weight loss of the residual film during the boiling xylene extraction was mainly due to the cleavage of the graft bonds. That is, the cleavage of graft bonds was significantly faster than the degradation of the graft chains. Thus, most of the graft chains were integrally cleaved from the graft sites without degradation during the initial extraction period, thereby allowing the determination of the molecular weight of the graft chains.

New functionalized biomass materials developed by radiation-induced grafting [2]

In our previous studies, the synthetic monomers and resins were used for the preparation of grafted materials by radiation-induced grafting. In this study, both monomer and trunk materials were obtained from biomass and the new functional biomass materials were developed.

Figure 2 showed the process for the grafting. A bio-derived monomer of methacrylated vanillin (MV) was synthesized using the production of lignin for the grafting. After grafting, the Kabachnik-Fields three-component reaction was carried out to introduce amine and phosphites groups on the grafted cellulose, resulting in a multifunctional grafted biomass material.
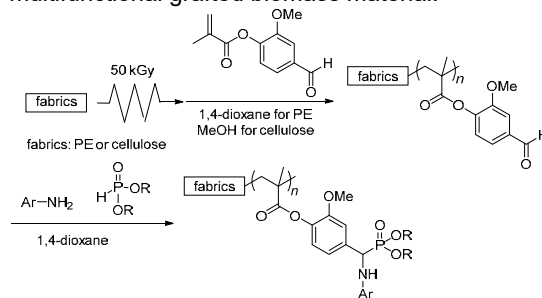
Fig. 2. Process for the development of the new functional grafted biomass materials by radiation grafting and subsequent Kabachnik-Fields reaction.

The graft polymerization was performed by preirradiation of the cellulose fabrics with Co60 gamma rays (20 kGy) and subsequent immersion in a MV/methanol solution at 60 °C for 5 h, yielding poly(methacrylated vanillin)-grafted cellulose with degree of grafting of 57%. The grafted cellulose was then reacted with p-anisidine and diisopropyl phosphite by the Kabachnik-Fields reaction to introduce the amine and phosphite groups on it. The yield of the targeted material reached 72% and the cellulose fabric was still intact without any detectable damage during these reactions. The results expand the preparation of functional fabric materials sourced from wood biomass compounds and the utilization of the radiation grafting method.

References
[1] J. Chen, N. Seko, Polymers, **11**, 1098 (2019).
[2] T. Hamada, S. Yamashita, M. Omichi, K. Yoshimura, Y. Ueki, N. Seko, R. Kakuchi, ACS Sustainable Chem. Eng., **7**, 7795-7803 (2019).

P1-8 Project "Element Separation and Analysis"

Leader : Hironori Ohba

Quantum beams are versatile sources for materials processing. Our project explores basic process of the laser-matter interaction to separate elements from industrial waste liquid, and performs synthesis of novel nanomaterials by ion or electron irradiation. In the former research, we applied the separation using laser-induced particle formation technique for recovery of precious metals from mixed solution. In the latter research, newly structured carbon nanomaterials inside silicon carbide nanotubes have been found. The recent results of our project are introduced as follows. {1-14 in Part II}

In situ time-resolved XAFS studies on laser-induced particle formation of palladium metal in an aqueous/EtOH solution [1]

The reaction kinetics of laser-induced particle formation in an aqueous/EtOH solution of $PdCl_4^{2-}$ without a photo-activator was investigated by transmission electron microscopy (TEM) and dispersive X-ray absorption fine structure (DXAFS) measurements. Pd particles were generated by the irradiation of a nanosecond pulsed 266 nm laser with a fluence of 19.9-59.7 mJ/cm^2. The TEM observation showed the dependence of the particle size on the laser fluence and the promotion of particle growth by the irradiation of a high-fluence laser. The DXAFS data were analyzed by three methods: (i) deconvolution of the X-ray absorption near-edge structure (XANES) spectrum by a linear combination fitting, (ii) model fitting of the extended XAFS (EXAFS) oscillation of the $PdCl_4^{2-}$ ion, and (iii) fitting of the spectrum edge of XANES using an error function. These methods give the ratio of Pd^{2+}, the coordination number of Pd-Cl bond, and the edge width of XANES, which are related to the Pd^{2+} concentration. Temporal changes of the Pd^{2+} concentration obtained by these three methods were analyzed on the basis of the Finke-Watzky two-step mechanism. The analysis elucidates that, in laser-induced particle formation in the absence of a photo-activator, the photons contribute to reduction of the $PdCl_4^{2-}$ ion by the one-photon process and to the autocatalytic growth of Pd particles by the multiphoton process as shown in Fig.1.

Ion irradiation-induced novel microstructural change of carbon layer in C-SiC coaxial nanotube [2] {1-14}

A novel hybrid carbon nanomaterial was synthesized by ion irradiation of a C-SiC coaxial nanotube. The hybrid consisted of one-dimensionally stacked graphene nanodisks with diameters less than 50 nm and cylindrical multiwalled carbon nanotubes inside an amorphous SiC tubular layer. A sudden emergence of new continuous graphitic layers in the microstructure were observed by in situ transmission electron microscopy following ion irradiation, where these layers were perpendicular to the nanotube's length direction. The SiC crystals in the C-SiC coaxial nanotube became amorphous, also due to the ion irradiation, although the critical amorphization dose was higher than that for bulk SiC. Most remarkably, the carbon layer remained crystalline, even after an irradiation dose higher than 20 dpa (displacement per atom). Such results show that these carbon layers possess better resistance against amorphization when subjected to ion irradiation

than the SiC layers in the C-SiC coaxial nanotube. Figure 2 shows the relationship between the ion fluence and the lattice plane spacing of graphitic shells estimated in C-SiC coaxial nanotubes. The lattice plane spacing of graphitic shells in the carbon layer increased up to the point of irradiation damage demonstrated by the complete amorphization of SiC crystals. The disorder in the carbon layer increased with increasing ion fluence because the induced defects had accumulated. Therefore, the lattice plane spacing of the graphitic shell in the nanotube increased with increasing the ion fluence. Surprisingly, afterward it started to decrease. This demonstrates that the carbon layer experiences high compression stress during ion irradiation. The lattice plane spacing of graphitic shells perpendicular to length is almost the same value as graphite. Thus, the ion irradiation of C-SiC coaxial nanotubes gives rise to a novel development of the microstructure and can be considered as one of the new synthetic processes for making novel carbon nanomaterials.

References

[1] M. Saeki *et al.*, J. Phys. Chem., C, **123**, 817-824 (2019).
[2] T. Taguchi *et al.*, Acta Materialia, **173**, 153-162 (2019).
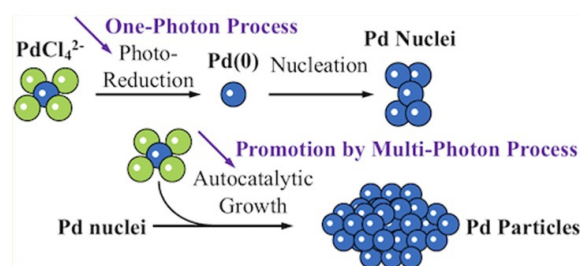
Fig. 1. Schematic drawing of the reaction kinetics in the irradiation of the pulsed UV laser. The photons contribute not only to reduction of $PdCl_4^{2-}$, but also to the autocatalytic growth of Pd particles at high fluence.
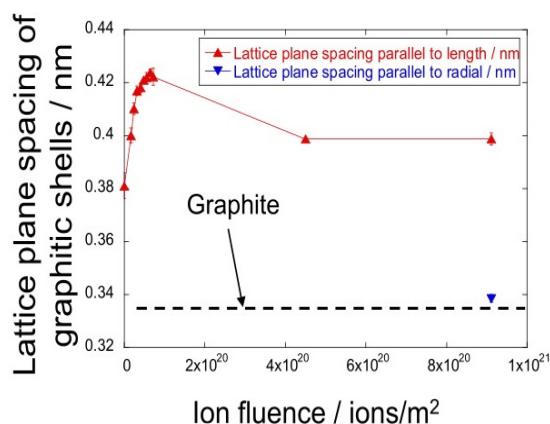
Fig. 2. Relationships between the ion fluence and the lattice plane spacing of graphitic shells estimated in C-SiC coaxial nanotubes.

P1-9 Advanced Functional Polymer Materials Group

Leader : Yasunari Maekawa

The research of "Advanced Functional Polymer Materials Group" has been focused on efficient development technique for advanced functional polymer materials, which are widely used in advanced devices and construction materials. The technique includes materials informatics such as machine learning and neural network in addition to the established radiation techniques regarding to the radiation-induced graft polymerization and the X-ray/neutron structural analysis. This group has been conducting mainly the R&D for "Advanced functional polymer materials alliance" under QST innovation hub program in collaboration with participant companies.

Research results of "Advanced functional polymer materials alliance"

On the alliance project of the 2nd year, main achievements in four research subjects are as follows.

(1) Graft-polymerizability prediction: The functional polymer samples were prepared by the radiation-induced graft polymerization of 60 kinds of monomers on polyethylene non-woven fabric to establish database for reactivity (polymerizability) prediction. The polymerizability prediction model, in which the grafting degree is the objective variable, was derived by the multiple linear regression analysis with the data-set composed of explanatory variables such as chemical structure and electronic state of the monomers.

(2) Structural data accumulation: We analyzed the hierarchical structures of the polymer materials using quantum beam facilities such as small angle X-ray/neutron scattering (SAXS/SANS). Proton-conducting polymer electrolyte membranes (PEMs) were visualized and digitalized by the multi-scale simulation based on molecular dynamics. The result of the simulation was consistent with SAXS profile of the PEMs. We confirmed that the simulation method is useful to expand the structural data.

(3) Property prediction: We evaluated the ion conductivity of the PEMs using statistical analysis such as least-square method and multivariate analysis, and machine learning. Fifteen explanatory variables were selected from the property and structural data of the polymers after the certification of multicollinearity. The ion conductivity of the PEMs could be estimated using the prediction model based on the artificial neural network method. The prediction accuracy was about 0.9.

(4) Database preparation: To improve the database for materials informatics of graft-polymers, a collection of the papers concerning the grafted polymer materials were continuously performed. Furthermore, the data were extracted from scientific articles with a data extractor developed by alliance members.

Reverse relationships of water uptake and alkaline durability with hydrophilicity of imidazolium-based AEMs [1]

We have previously reported the relationship between the morphology and properties of anion-conducting polymer electrolyte membranes (AEMs) with graft copolymer that composed of anion-conducting 2-methyl-*N*-vinylimidazolium (Im) and hydrophobic styrene (St) units

[2]. In this study, we characterized two new structural models in the imidazolium-based AEMs, governing electrolyte properties and alkaline stability, using SANS measurement with a contact variation method.

Three AEMs with different monomer compositions (Im/St ratio = 6/4, 4/6, 3/7) were prepared by the radiation-induced graft polymerization on ETFE membranes, denoted as ImSt64, ImSt46 and ImSt37, respectively. The AEMs had a similar IEC of ~ 1.0 mmol/g and exhibited a conductivity of ~ 60 mS/cm. The water uptake and the alkaline stability of the AEMs increased and decreased with the increase of hydrophobic St content, respectively. This is completely opposite tendency to that of the traditional AEMs. We confirmed that the distribution of graft polymers in the AEMs was well elucidated by a newly proposed "conducting/non-conducting two-phase system" model. Volume fraction of graft polymers in conducting phase was quantitatively evaluated by the conducting/non-conducting two-phase system model. It was suggested that the volume fraction is an important parameter for functional prediction. Furthermore, based on the hard-sphere model, it was found that ImSt46 and ImSt37 possessed nanophase-separated water puddles with diameters of 3-4 nm, whereas ImSt64 with best alkaline stability did not show any nanophase separation. (Fig. 1). The imidazolium groups located at the boundary between graft polymers and water puddles were susceptible to hydrolysis, resulting in lower alkaline stability.

References

[1] K. Yoshimura *et al.*, Soft Matter, **14**, 9118 (2018).
[2] Y. Zhao *et al.*, Soft Matter, **12**, 1567 (2016).
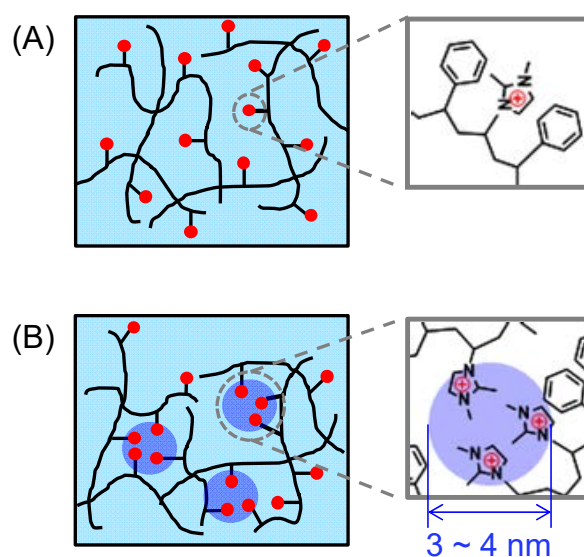
Fig. 1. Illustrations of the morphology of the hydrophilic ion channels in the AEMs; (A) "dispersed ions" model for ImSt64 and (B) "water-puddle" model for ImSt46 and ImSt37.

Part Ⅰ

2. Life Science

P2-1 Project "Ion Beam Mutagenesis"

Leader : Yutaka Oono

The ultimate goal of our project is to develop applications of quantum beam technology in applied biological fields such as sustainable agriculture and environmental conservation. Ion beams are recognized as useful mutagens for plant and microbe breeding because they are thought to cause mutations by distinct mechanism from chemical mutagens or gamma rays. To develop more efficient ion-beam mutagenesis techniques, we have tried to understand the characteristics of the ion-beam-induced mutations by using specific gene markers or genome-wide sequencing {2-10, 12, 21, and 22 in Part II}. In addition, under collaborations with academic or industrial research organizations, we are aiming to isolate valuable mutants in various organisms such as parasitic plants, plant growth-promoting rhizobacteria, oil-producing algae, sake yeasts, and other bacteria by ion-beam irradiation {2-11, 14, 16~19, and 25}. Revealing molecular biology basis of radioresistant organisms is another major business of our project {2-15, 20, and 26}.

Genome sequence of a radioresistant bacterium in the sky above Japan [1]

Bacteria classified in the genus *Deinococcus* are well known as radioresistant bacteria (Fig. 1). They live almost everwhere in the world. Approximately 70 *Deinococcus* species have been isolated from various enviroments such as soil, hot springs, foods, faeces, air-borne dust, alpine environments, activated sludge, freshwater, and rhizosphere. How they protect and repair DNA from highly harmful ionizing radiation is a very attractive issue to be clarified. Recently, comparative genome approach is getting powerful to elucidate the special features of *Deinococcus* bacteria in genomic level. Satoh et al. reported draft genome sequence of *Deinococcus aerius* strain TR0125, which was initially isolated as an orange-pigmented, non-motile, desiccation-tolerant, UV- and gamma-resistant, and coccoid bacterium in the dust sample collected from the upper troposphere in Japan.

The genome sequence suggested that the strain TR0125 lacks several genes involved in metabolisms of nitrogen, arginine, ornithine and carbohydrate. It is consistent with the biochemical feature of this bacterium. The strain TR0125 exhibited much slower growth than *D. radiodurans*. This feature might be related to the fact that the strain TR0125 genome possesses only one rRNA operon, contrasting many other *Deinococcus* bacteria, which have multiple rRNA operons (Table 1). Whereas, genes related to radiation/desiccation resistance such as *pprI*, *pprA*, *recA*, *ddrA*, and *ddrO*, which are characteristic of *Deinococcus* bacterial spicies, are also conserved in the strain TR0125. Accumulating genome sequence data of *Deinococcus* bacteria will facilitate better understanding of molecular mechanisms relating their highly efficient DNA repair ability.

Discovery of another organism hyper resistant to DNA double-strand breaks [2]

Every living organism has DNA, which holds information in its chemical structure for building and maintaining an organism, in their cells. Therefore, protecting DNA from various types of damage is highly critical for all living organisms. Among various types of DNA damage, double-strand breaks (DSBs) are most serious and difficult to repair exactly. *Deinococcus* bacteria demonstrated above have superior ability in repairing DSBs effectively, but there are several other organisms that also show strong resistance to DSBs. According to the recent report by Yokota et al., the moss *Physcomitrella patens* seems to be eligible to join the group of organisms that are hyper resistant to DSBs (Fig.2). The γ-irradiation experiments revealed that *P. patens* single cells (protoplasts) were 200-times more radioresistant than human single cells. Subsequently, DSB yield measurement by a pulsed-field gel electrophoresis assay indicated that the DSB yield in *P. patens* was half to one-third of those in mammals and yeasts. Furthermore, the DSB yield per cell per 50% lethal dose in *P. patens* was three- to six-times higher than those in mammals and yeasts. The series of findings suggested that DSB induction is inhibited in *P. patens* cells and that they can survive even when a large number of DSBs are induced. Revealing molecular mechanisms of the DSB resistance in *P. patens* is a challenge of the future.

References

[1] K. Satoh *et al.*, Genome Announc., **6**, e00080-18 (2018).
[2] Y. Yokota *et al.*, Genes, **9**, 76 (2018).
[3] Y. Yang *et al.*, Int. J. Syst. Evol. Microbiol., **59**, 1862 (2009).
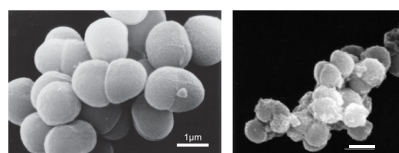
Fig. 1. Scanning electron micrographs of *D. radiodurans* (left) and *D. aerius* (right). Bars indicate 1 μm. The photograph for *D. aerius* is from [3] with modification to highlight the size bar.

Table 1
Comparison of *Deinococcus* genome sequences.

	D. radiodurans	*D. grandis*	*D. aerius*
No. of nucleotides determined	4,092,497	3,344,765	4,524,446
% GC	66.3	66.5	68.0
No. of genes	3,079	4,043	4,446
No. of tRNAs	50	51	52
No. of rRNAs (5S/16S/23S)	3/3/3	4/4/4	1/1/1
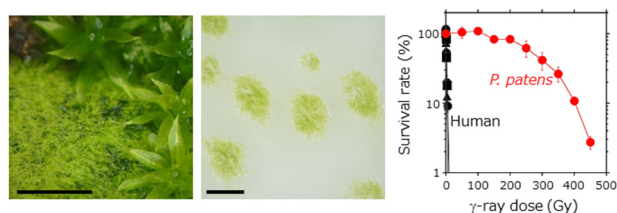
Fig. 2. Clonogenic ability of *P. patens* (left) was measured by a colony formation assay (centre). Bars indicate 2 mm. *P. patens* cells were 200-times more radioresistant than human cells (right).

P2-2 Project "Microbeam Radiation Biology"

Leader : Tomoo Funayama
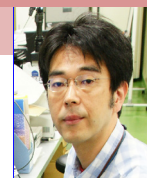
Project "Microbeam Radiation Biology" has developed methods for irradiating biological material with heavy-ion microbeam, and analyzed local irradiation effect of wide range of biological targets [1]. Using mammalian cultured cells, we have investigated the effect of heavy-ion hit and radiation induced bystander effects {2-1, 2-2 in Part II}. In addition, we have employed animal individuals, such as silkworm, medaka fish, and nematode *Caenorhabditis elegans*, as a target of microbeam irradiation, and analyzed local irradiation effect on whole animal response {2-4~6 in Part II}.

Development of polydimethylsiloxane (PDMS) based microfluidic chips for enclosing biological samples [2]

The nematode *Caenorhabditis elegans* is a well-established model organism for studying processes in neurobiology. We previously investigated radiation effects in this organism, and found that motility decreased following whole-body irradiation in a time- and dose-dependent manner [3-4]. To investigate a responsible region of this phenomenon, we planned to carry out the targeted irradiation of central nervous system (CNS) of *C. elegans* with our collimating heavy-ion microbeam.

For this region-specific microbeam irradiation, we introduced the use of on-chip immobilization, instead of the conventional method using anesthesia. The on-chip immobilization is a method to inhibit free motion of *C. elegans* by enclosing an individual animal in a straight channel on a PDMS microfluidic chip with a buffer solution. Based on this method with a conventional hydrophobic PDMS chip, we conducted region-specific irradiation to animals, and we demonstrated that the reduction in motility following whole-body irradiation was not caused by the radiation response on the CNS [5].

However, the conventional hydrophobic PDMS chip had a limitation to prevent improvement of experimental throughput that more than 30 min of on-chip immobilization in the microfluidic channels will result in the animals drying out as the buffer solution gradually evaporates.

Therefore, we designed and developed a new PDMS microfluidic chip with water retention for worm immobilization and microbeam irradiation. In addition, we established optimized enclosure buffer composition for prolonging worm enclosure duration for efficient irradiation procedure using microbeam.

A chip used in previous experiment was too thick (approximate 2.5 mm) for irradiated heavy-ions to penetrate, so that we could not count ion penetrated the sample with ion detector installed at the opposite side of the beam exit. This means that we could not control exact number of ions irradiated on targeted region. Thus, we designed new chip with a thickness less than ion projectile used for irradiation experiments (~300 µm).

We fabricated two types of chips with wettable and unwettable (hydrophobic) PDMS base materials. These chips have ultra-thin thickness of 300 µm, and 25 straight microfluidic channels with depth of 70 µm and width of 60 µm are engraved on the surface (Fig.1).

Animals were kept on each device for 1 h to evaluate the effects of drying following enclosure in the devices on motility. We also examined the locomotion of animals following on-chip immobilization in different buffers. Locomotion was decreased in certain buffers on hydrophobic chips as a result of dehydration due to evaporation, but not on chips with water retention. However, locomotion was unaffected on either chip in the presence of a gelatin-based wash buffer.

These results indicated that our ultra-thin microfluidic chip with water retention will facilitate studies of the effects of region-specific irradiation on behaviors in *C. elegans*.

Actually, we have already carried out the targeted irradiation with exact number of heavy ions to the CNS of *C. elegans* and demonstrated that dose-dependent effects of targeted irradiation to the CNS on motility {2-6 in Part II}.

Furthermore, this ultra-thin PDMS microfluidic chip and on-chip immobilization technology of biological material have been applied for patent, and commercialized as "Worm Sheet" by the co-inventor company (Biocosm Inc., Hyogo). The sales channels are expanded at home and abroad.

In addition, the thickness and transparency of the Worm Sheet means that it will have applications not only in microbeam irradiation, but also in neurobiological assays, including optical imaging (Fig. 2). In the future, we will expand this enclosure technology to wide range of animals other than nematodes.

References
[1] T. Funayama *et al.*, IEEE Plasma Sci., **36**, 1432 (2008).
[2] M. Suzuki *et al.*, J. Neurosci. Methods., **306**, 32 (2018).
[3] T. Sakashita *et al.*, J. Radiat. Res., **49**, 285 (2008).
[4] M. Suzuki *et al.*, J. Radiat. Res., **50**, 119 (2009).
[5] M. Suzuki *et al.*, J. Radiat. Res., **58**, 881 (2017).
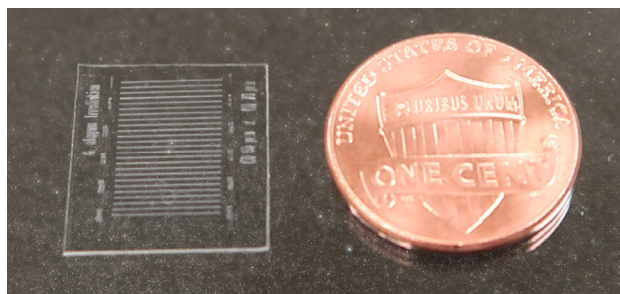
Fig. 1. Newly designed and fabricated PDMS microfluidic chip for microbeam irradiation (left) and one cent coin.

100 µm
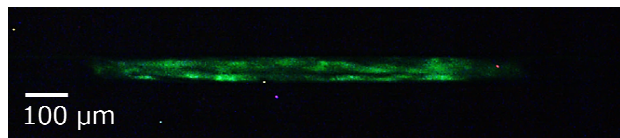
Fig. 2. An example of fluorescence imaging of *C. elegans* enclosed in a channel of a PDMS microfluidic chip.

P2-3 Project "Medical Radioisotope Application"

Leader : Noriko S. Ishioka

The research objective of our project is to develop the radiopharmaceuticals labelled with useful radioisotopes for cancer diagnosis and therapy. Our project focuses on research of the radioisotope drug delivery system (RI-DDS) using bioactive compounds such as antibodies and peptides in order to make the most of the ability of radioisotopes. We also search for novel molecular targets that enable effective diagnosis or therapy with radiopharmaceuticals.

Anti-tumor effects and potential therapeutic response biomarkers in α-emitting *meta*-^{211}At-astato-benzylguanidine therapy for malignant pheochromocytoma explored by RNA-sequencing [1]

Targeted α-particle therapy is a promising option for patients with malignant pheochromocytoma. Recent observations of *meta*-^{211}At-astato-benzylguanidine (^{211}At-MABG) in a pheochromocytoma mouse model showed a strong anti-tumor effect, but its molecular mechanism remains elusive [2]. Here, we showed the first comprehensive RNA-sequencing (RNA-seq) data of pheochromocytoma cells from in vitro ^{211}At-MABG administration experiments, and screened key genes and pathways in the tumor α-particle radiation response, in order to obtain novel molecular imaging and therapeutic targets.

We evaluated genome-wide transcriptional alterations of rat pheochromocytoma cell line (PC12) at 3, 6, 12 h after ^{211}At-MABG treatment. In order to highlight ^{211}At-MABG specific gene expression, we carried out the control experiment of ^{60}Co γ-rays irradiation. Ten-percent and eighty-percent iso-survival dose (0.8 and 0.1 kBq/ml for ^{211}At-MABG, 10 and 1 Gy for ^{60}Co γ-rays) were used for the comparison of both treatments.

Enrichment analysis of the differentially expressed genes (DEGs) and analysis of the gene expression profiles of the cell cycle checkpoints showed similar modes of cell death via p53-p21 signalling pathway following ^{211}At-MABG treatment and γ-ray irradiation (Fig. 1). Ten-persent iso-survival dose of γ-ray irradiation and ^{211}At-MABG showed cell cycle arrest at G2/M phase. Representative DEGs of ^{211}At-MABG-treated cells between 80% and 10% survival showed the expression of key genes not only on the decrease in the survival, but also on the anti-therapeutic effects such as DNA repair, invasion, and metastasis. Furthermore, representative DEGs between γ-ray irradiation and ^{211}At-MABG demonstrated that the expression of four potential genes including Otub1 (Ovarian tumor domain-containing ubiquitin aldehyde-binding protein 1) related to ubiquitin mediated proteolysis was remarkably elevated only after treatment with ^{211}At-MABG. Western blot analysis indicated the increase of translocator protein 18 kDa (TSPO) expression in ^{211}At-MABG treated cells, suggesting the potential PET imaging probe.

Comprehensive RNA-seq revealed contrasting cellular responses to γ-ray irradiation and targeted α-particle therapy leading to the identification of four novel potential genes (Mien1, Otub1, Vdac1 and Vegfa) for molecular imaging and therapeutic targets of ^{211}At-MABG therapy

(Fig. 2). Here, Mien1 is migration and invasion enhancer 1, Vdac1 is 32-kDa voltage-dependent anion channel 1 and Vegfa is vascular endothelial growth factor A. Moreover, our results suggest possible mechanism of the anti-tumor effect of ^{211}At-MABG in pheochromocytoma.

References
[1] Y. Ohshima *et al.*, Theranostics, **9**, 1538 (2019).
[2] Y. Ohshima *et al.*, Eur. J. Nucl. Med. Imaging., **45**, 999 (2018).
[3] Y. Moriya *et al.*, Nucleic. Acids Res., **35**, W182 (2007).
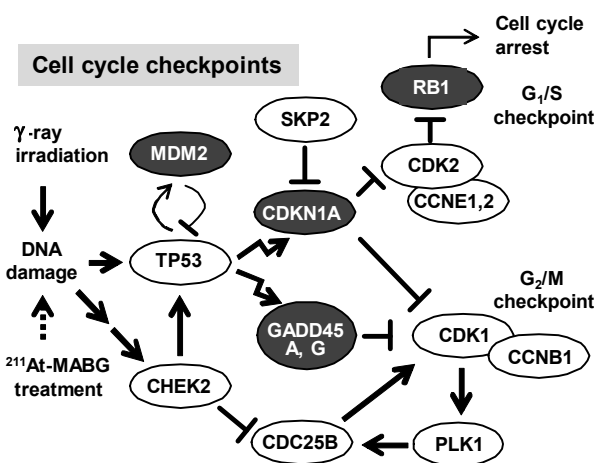
Fig. 1. Cell cycle checkpoints and the p53-p21 pathway. The gene regulatory network for cell cycle checkpoints was configured with reference to the KEGG pathway map [3]. Gray and white ellipses represent the increase or decrease in gene expression (vs. control) after both ^{60}Co γ-ray irradiation and ^{211}At-MABG treatment, respectively. Both treatments showed similar gene expression profiles.
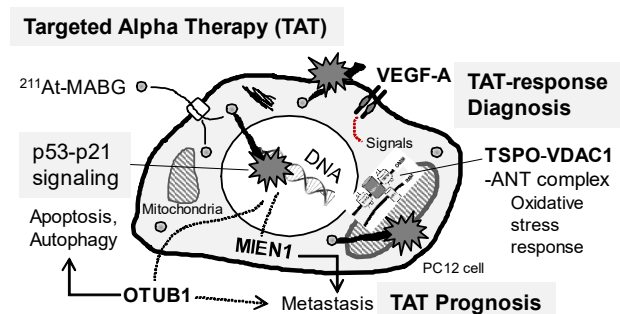
Fig. 2. Potential biomarkers of ^{211}At-MABG-therapy. The present RNA-seq analysis suggests that ^{211}At-MABG therapeutic effects are associated with p53-p21 signalling and inhibition of ubiquitination by OTUB1. Furthermore, our analysis demonstrated novel targets for ^{211}At-MABG-therapy. OTUB1 and MIEN1 may be of importance for therapy and VDAC1 (TSPO) and VEGF-A for imaging. ANT is inner membrane adenine nucleotide transporter.

P2-4 Project "Generation of Radioisotopes with Accelerator Neutrons"

Leader : Kazuyuki Hashimoto

In our project, we have developed the production of medical radioisotopes (RI) for cancer diagnosis and therapy such as ^{99}Mo/^{99m}Tc, ^{90}Y, ^{64}Cu, and ^{67}Cu using fast neutrons from a cyclotron accelerator. The neutrons were obtained by irradiating 40-50 MeV deuterons to beryllium or carbon. A separation and purification method of aimed radioisotope from the target materials and radioactive impurities has also been developed. We also investigate the production of medical RI such as ^{211}At and ^{95m}Tc by the tandem accelerator in Tokai (Japan Atomic Energy Agency). Our final goal is to build a domestic production system of medical radioisotopes using accelerator driven neutrons.

^{99}Mo Yield Using Large Sample Mass of MoO$_3$ for Sustainable Production of ^{99}Mo [1]

In Japan, approximately 0.7–0.9 million diagnostic procedures per year are carried out using ^{99m}Tc with a half- life ($T_{1/2}$) of 6 h. This medically important radioisotope is obtained from the decay of ^{99}Mo ($T_{1/2}$ = 66 h), all of which Japan imports. A reliable and constant supply of ^{99}Mo is key to ensuring the routine application of ^{99m}Tc. Most ^{99}Mo is produced by the fission reaction of highly enriched or low- enriched ^{235}U. Approximately 80% of the world's ^{99}Mo supply is provided by the research reactors which have been operating for more than 40 years. This vulnerable situation is the impetus for the study of alternative methods for producing ^{99}Mo and/or ^{99m}Tc without ^{235}U in reactors or accelerators worldwide. As one of the promising approaches, a new route for the production of ^{99}Mo with the ^{100}Mo($n,2n$)^{99}Mo reaction using an accelerator neutron source was proposed by Nagai and Hatsukawa [2]. A neutron source from the C(d,n) reaction with an incident deuteron energy of 40 MeV provides a most probable neutron energy at 14 MeV and a forward peak with respect to the deuteron beams, which are valuable for producing a variety of medical radioisotopes such as ^{99}Mo with a minimum level of radioactive waste.

We have precisely measured the yield of ^{99}Mo produced by the ^{100}Mo($n,2n$)^{99}Mo reaction using a ^{nat}MoO$_3$ sample of 100 g mass to solve the discrepancy of the neutron flux between existing data. This measurement was performed by using accelerator neutrons provided by the C(d,n) reaction using a 0.1 μA beam current of 40 MeV deuterons at the AVF cyclotron at Cyclotron and Radioisotope Center (CYRIC), Tohoku University. The experimental setup at the ^{nat}MoO$_3$ sample position is shown in Fig. 1. The sample was irradiated with the neutrons for 40 min. We used four pellet ^{nat}MoO$_3$ samples of 25.869, 25.868, 25.483, and 25.220 g mass (in total 102.440 g mass) with dimensions of 30 mmϕ x 11.6 mm (total length 46.4 mm). It should be mentioned that such a large mass sample of ^{100}MoO$_3$ would be used for domestic production of ^{99}Mo. The activities of radionuclides at the EOI were determined by the γ-ray spectrometry with the HPGe detector. The ^{99}Mo yield agrees well with that estimated by using the latest data on the neutron flux, which provides important evidence to calculate the maximum yield of ^{99}Mo as well as other radioisotopes

under a given condition. This result establishes an important finding for the domestic production of ^{99}Mo: approximately 50% of the demand for ^{99}Mo in Japan could be met using a 100 g ^{100}MoO$_3$ sample mass with a single accelerator of 40 MeV, 2 mA deuteron beams.
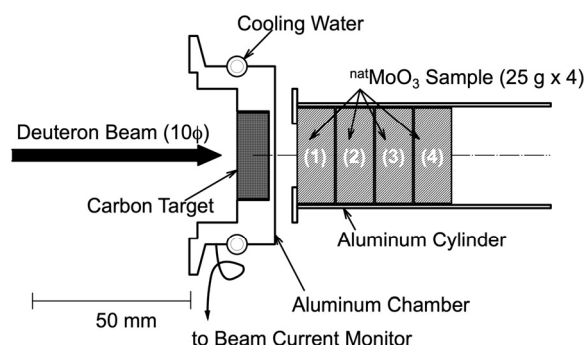
Fig. 1. Schematic view of the experimental setup at the ^{nat}MoO$_3$ sample position.

Electron-tracking Compton Camera Imaging of Technetium-95m [3]

Technetium-99m is the most widely adopted radioisotope for medical diagnostic scans such as single-photon emission computed tomography (SPECT). There are over 31 commonly used radiopharmaceuticals based on ^{99m}Tc for diagnostic imaging and functional studies of the human body. Various ^{99m}Tc-labeled compounds are injected into the patient's body as radioactive tracers, and subsequently, γ-rays emitted from the accumulated ^{99m}Tc are measured using position-sensitive γ-ray detectors.

If a Tc isotope that emits high-energy γ-rays is used as an alternative to ^{99m}Tc, all radiopharmaceuticals developed for ^{99m}Tc can be, in principle, used because the Tc chemistry is the same. Therefore, ^{95g}Tc, ^{95m}Tc, and ^{96}Tc are potential candidates for high-energy γ-ray emitters. Hayakawa et al. have quantitatively estimated the relative γ-ray intensities and production rates using a compact medical cyclotron for various Tc isotopes [4]. Although the relative γ-ray intensity of ^{95m}Tc is lower than that of ^{99m}Tc, its relatively long half-life of 61 d enables its use to study the behavior of Tc isotopes in the human body.

Over the last decades, the Compton camera, which was originally developed to observe stellar gamma-ray bursts, was applied to medical uses such as medical diagnostic scanning or the monitoring of radiation therapy. Even if the γ-ray energy is in the MeV region, one can measure γ-ray images using the Compton camera. The Compton camera provides an additional advantage in that the size and weight of the detection device system can be reduced due to the large viewing angle of the camera and absence of a collimator. To determine the direction of an incident γ-ray, both the angles of the scattered γ-ray and scattered electron should be measured. However, conventional Compton cameras can only measure the

angle of the scattered γ-ray. Recently, the electron-tracking Compton camera (ETCC) was developed for astronomical observations, the measurement of radioactivity in fields, and medical scans.

In the present study, we produced ^{95m}Tc using the ^{95}Mo$(p,n)^{95m}$Tc reaction on a ^{95}Mo-enriched target to measure images of ^{95m}Tc using an ETCC. After chemical separation, 500 kBq of ^{95m}Tc was obtained. The ETCC images were obtained for γ-rays with three different energies, 204 keV, 582 keV, and 835 keV, emitted from ^{95m}Tc (Fig. 2). The spatial resolution increased as the γ-ray energy increased, indicating that the ETCC system can measure images even in the presence of γ-rays with various energies and is useful for the medical imaging of deep tissue and organs in the human body.
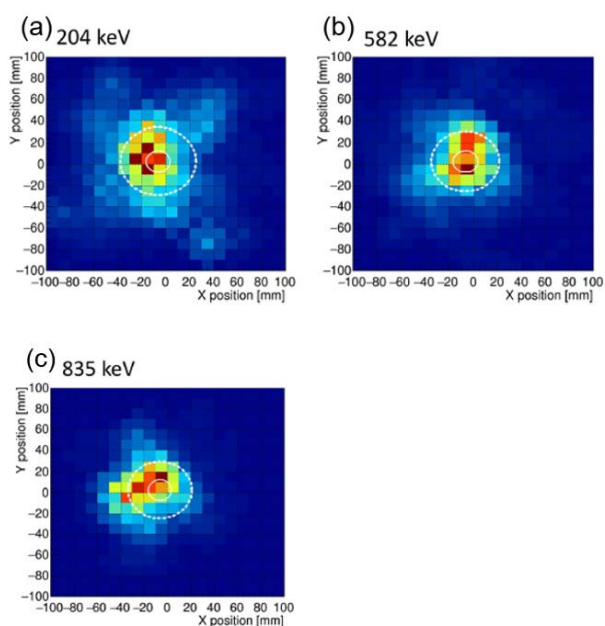
Fig. 2. Compton camera images obtained from ^{95m}Tc contained in a 10-mm-diameter vial. Energy windows are set at (a) 204 keV, (b) 582 keV, and (c) 835 keV. These images were reconstructed using an interactive reconstruction technique. The solid line shows a vial size of 10 mm in diameter. Fifty percent of all events exist inside of the dashed line circle.

References
[1] K. Tsukada *et al.*, J. Phys. Soc. Jpn. **87**, 043201 (2018).
[2] Y. Nagai and Y. Hatsukawa, J. Phys. Soc. Jpn. **78**, 033201 (2009).
[3] Y. Hatsukawa *et al.*, PLoS ONE **13**(12): e0208909 (2018).
[4] T. Hayakawa *et al.*, Heliyon **4**(1), e00497 (2018).

P2-5 Project "Radiotracer Imaging"

Leader : Naoki Kawachi

The aim Radiotracer imaging research project is to measure, visualize the radiation sources, and characterize the biological processes of organs, using radioisotopes (RI) and imaging apparatus. We will establish systematized the most advanced techniques for live-imaging using radiotracers, nuclear imaging apparatus, and kinetic analytical methods for understanding the transport function related to agriculture and medicine within living systems. {2-27~29, 2-31, 2-33 in Part II}.

Development of Compton camera for astatine-211 Imaging for targeted α-particle radiotherapy

Astatine-211 is a promising radionuclide for targeted α-particle radiotherapy of cancers. It is required to image the distribution of targeted radiotherapeutic agents in a patient's body before or during treatment for optimization of treatment strategies and determination of the suitability of a given agent for a particular patient. Astatine-211 and its daughter radionuclide ^{211}Po emit high-energy gamma rays with the energies of 570 keV, 687 keV, and 898 keV at the total intensity of 0.9%. Since these gamma rays are not substantially attenuated in the body, Compton cameras are suitable for visualizing ^{211}At distribution noninvasively.

We developed a cost-effective Compton camera using high-sensitive inorganic scintillators and a commercially available data acquisition system for a positron emission tomography camera[1]. We implemented maximum-likelihood expectation-maximization algorithm to the experimental data to improve the image. We performed imaging experiments of ^{211}At source using the developed Compton camera, and the source was successfully imaged. We have demonstrated the capability of imaging ^{211}At with the high-energy gamma rays using the Compton camera. This technique can be applied to targeted alpha therapy imaging[2].

Development of methods for carbon dynamics images of photosynthetic products

Radionuclide imaging technologies have opened up experimental opportunities for biological research. However, the conventional measurement tools used in plant science are invasive and require calibration by statistical analysis over a large number of test plants. RI imaging is one of the most powerful tools for conducting research on the distribution and translocation nutrition of water, nitrogen, mineral nutrients, etc., and environmental pollutants in plants, noninvasively.

For analysis of carbon kinetics in a plant body, it is possible with the positron-emitting radioisotope C-11, which has a short half-life, and positron imaging systems of the positron emitting tracer imaging system (PETIS) and positron emission tomography (PET)[3]. The carbon kinetics makes it a strong potential candidate for application to the analysis of physiologies involved in photosynthesis and photoassimilate translocation. The ^{11}C imaging approach has been used for real-time and quantitative video imaging of tracer dynamics during carbon fixation, photosynthesis, and photoassimilate translocation. Recently, we have developed leading technologies to image the dynamics of ^{11}C compounds in the plant body using RI imaging method and discussed its applicability to investigations of the kinetics of carbon nutrients during photosynthesis and photoassimilate translocation and unloading. Elucidation of the carbon kinetics in a plant body clearly leads to agricultural study on the growth and development of grains and fruits[4].

References

[1] Y. Nagao *et al.*, NIM-A, in press (2018).
[2] Y. Nagao *et al.*, Appl. Radiat. Isot., **139**, 238 (2018).
[3] K. Kurita *et al.*, NIM-A, in press (2018).
[4] K. Hidaka *et al.*, Front. Plant Sci., **9**, 1946 (2019).
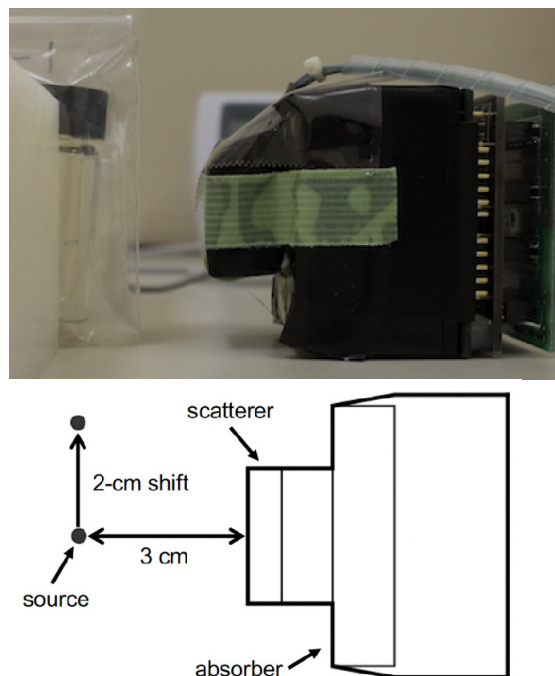
Fig. 1. Photograph of the experimental setup of ^{211}At source and the Compton camera head from a side view and schematic diagram of the setup.
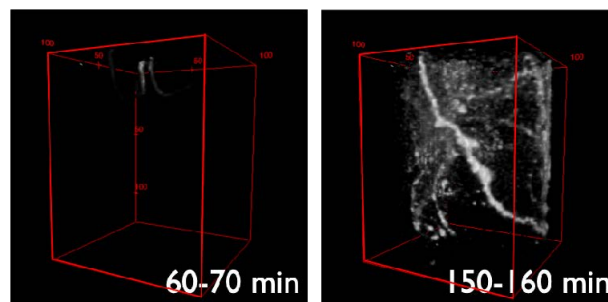
Fig. 2. Volume-rendered 3D dynamic images of ^{11}C-labeled photoassimilate translocation to a root of a soybean underground using a positron emission tomography (PET) and ^{11}C-labeled carbon dioxide infusion.

P2-6 Project "Radiation and Biomolecular Science"

Leader : Akinari Yokoya

The objective of our project is to elucidate the radiation effect of living systems from molecular to cellular level using various radiation sources. Particularly, DNA damage and its repair have been the most important targets of our projects. A live cell imaging of the human cells transfected with fluorescent protein expressing plasmid DNA was applied to evaluate to repairability of X-ray induced DNA damage. Furthermore, using high brilliant synchrotron soft X-rays below 1 keV, carbon, nitrogen and oxygen atoms were targeted as inner-shell excitation/ionization in DNA-related small molecules. Spectroscopic approaches of X-ray absorption near edge structure (XANES) as well as electron paramagnetic resonance (EPR) were used to reveal unstable unpaired electron processes involved in the DNA damage induction.

Live cell imaging of the cells transfected with X-ray irradiated plasmid DNA

Enhanced green fluorescent protein (EGFP)-expressing plasmid DNA solution was exposed to X-rays (150 kpV) of various doses from 0 to 1.5 kGy, and then transfected into non-irradiated human brest cancer cells (MGF7) using lipofectamine. The repair kinetics of the plasmids in the cells were visualized under microscopy as the EGFP fluorescence emitted by transfected cells. Using an agarose gel electrophoresis method, the yields of single- and double-strand breaks of the plasmids were also quantified. As positive control experiments, plasmid DNA with single- or double-strand breaks induced by a nicking or restriction enzyme were also transfected into the cells. The DNA repair rates were obtained by scoring the number of EGFP expressing cells plotted against incubation time (Fig. 1). For the X-ray-irradiated plasmids the repair ratewere significantly lower than those of the enzymatically digested positive control samples, and the repair rates decreased with increasing dose. These results indicate that X-rays could induce less repairable damage than that induced by enzymes [1].

Electron paramagnetic pyrimidine bases exposed to soft X-rays around N and O K-edge energies

The physicochemical processes underlying radiation damage to DNA initiated by K-shell photoabsorption have not clarified yet. To evaluate these processes, we have developed an X-band EPR spectrometer installed in a synchrotron soft X-ray beamline, BL23SU in SPring-8 (Hyogo, Japan) to detect unstable intermediate species induced by K-shell excitation/ionizaton of nitrogen or oxygen, and subsequent Auger relaxation. By altering the substituents of the pyrimidine ring of nucleobases, we found a substituent effect on the yield of unpaired electrons induced by photoabsorption (Fig. 2) [2]. For uracil, which containing amino groups, the yield significantly increased by the donation of electrons. On the other hand, for halogenated nucleobases, such as 5-bromouracil, known to be a typical radiation sensitizer for cell killing, the yields decreased by the withdrawal of electrons. These specific processes for each base might modify the base lesions through electron/hall propergation along the DNA molocule depending on the base sequence around the K-photoabsorption site, and determin the chemical structure of DNA damage.
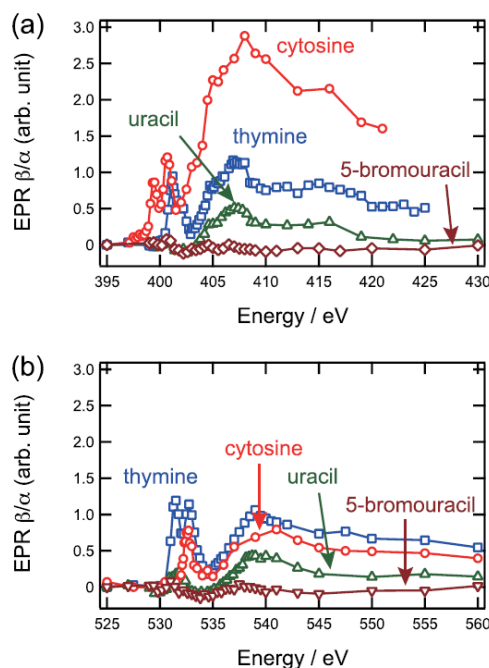
Fig. 2. Soft X-ray energy dependence of relative EPR intensity for uracil, 5-bromouracil, cytosine, and thymine around the nitrogen K-edge (a) and the oxygen K-edge (b). β/α in the vertical axes shows a relative photon-energy dependence of the EPR intensity (see the original article [2]).

Fig. 1. Left photographs: Fluorescent images of the EGFP-expressing cells transfected with non-irradiated (upper) and X-ray irradiated (1.2 kGy) pEGFP-C1 plasmid DNA (lower panel) after 48 h incubation. The images were taken under 4× magnification. Right panel: Dependence of the number of EGFP-expressing cells on incubation time. Because there were no EGFP-expressing cells observed before 5 h after lipofection, the data for this period were omitted from the graph.

References
[1] H. Nakaue, A. Yokoya, *et al.*, Radiat. Protect. Dosim. **183**, 79 (2019).
[2] T. Oka, A. Yokoya, *et al.*, Appl. Phys. Lett. **113**, 243701 (2018).

P2-7 Project "Biomolecular Function"

Leader : Motoyasu Adachi

Protein molecules play fundamental roles in biological system and exhibit unique functions on molecular recognitions, chemical reactions and energy transfer. Our research project had been focused on developments of the molecular design based on protein functional analysis using neutron, X-ray diffractions, and ultra-short pulse laser. Here, we show three studies contributing to molecular engineering and application for industry and human health.

Elucidation of the extended structure of PprA from *Deinococcus radiodurans* [1]

Pleiotropic protein promoting DNA repair A (PprA) is a unique and key protein facilitating the extreme radiation resistance of *Deinococcus radiodurans*. PprA exists as an oligomer ranging from a tetramer to an ~100-mer depending on protein concentrations according to our previous results. In this study, the X-ray crystal structure of PprA was determined to clarify how PprA contributes radiation resistance. The tertiary structure of dimeric PprA was elucidated by using two mutants of W183R and A139R (Fig. 1(a)). Based on the two mutant strcutres, the linear and oligomerized PprA model could be constructed as a left-handed face-to-face periodic screw structure as shown in Figs. 1(b) and (c), since the mutant A139R and W183R proteins have dimeric assemblies exhibiting two different interfaces of AA- and BB-faces. In addition, the linear structure in solution was confirmed by small-angle scattering experiments, and the site-directed mutational analysis identified key amino acid residues for DNA binding. These analytical data support the hypothesis that a complex assembly of PprA molecules surrounds and stretches the DNA strand, possibly acting as a novel guide to colocalize the DNA strands for efficient DNA repairs.
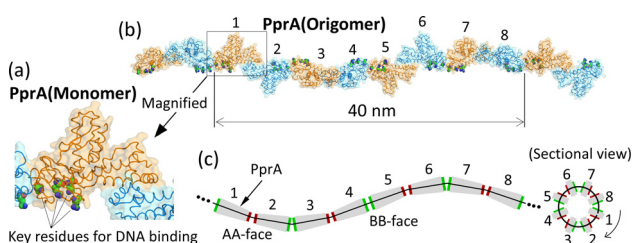
Fig. 1. Structural information of PprA analyzed by X-ray beam. (a) PprA monomer corresponding to each half of A139R and W183R dimers. (b) Model structure of the oligomerized PprA. (c) Schematic drawing of (b).

Neutron crystal structure analysis of the human protein kinase CK2 [2]

Casein kinase 2 (CK2) has broad phosphorylation activity against various regulatory proteins, which are important factors responsible for cancer. In order to clarify the hydration structure and catalytic mechanism of CK2, we determined the crystal structure of the alpha subunit of human CK2 that includes hydrogen and deuterium atoms by joint crystallographic analysis using 1.9 Å resolution neutron data and 1.1 Å resolution X-ray data (Fig. 2(a)). The analysis revealed the structure of a long and potential hydrogen bonding network originating from the catalytic Asp156 acting as nucleophilicity of the substrate OH

group to the γ-phospho group of ATP by elimination of the proton. His148 and Asp214 conserved in the protein kinase family are located in the middle of the network connecting to a characteristic pentagonal water network as shown in Figs. 2(b) and (c). Our findings shed new light on the catalytic mechanism of this protein kinase, in which the hydrogen bond network through the C-terminal domain may assist the general base catalyst to extract a proton with link to the bulk solvent via intermediates of a pair of residues.
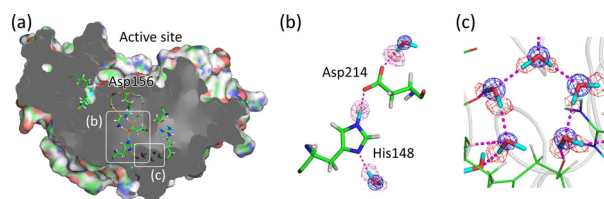
Fig. 2. CK2 structure obtained by neutron crystallography. (a) Sectional view representing key residues in CK2. (b) A part of the long hydrogen bond network connecting to a characteristic pentagonal water network of (c).

Polypentagonal ice-like water networks observed in an activity-improved variant of ice-binding protein [3]

The ice-binding protein (IBP) is one of the interesting proteins, which can bind on ice crystals and inhibit ice growth in bio-organism cells. To investigate their functions of the IBP, we determined X-ray crystal structures of a fish (*Zoarcidae*)-derived IBP including wild-type of defective isoform, and its five single mutants of A20L, A20G, A20T, A20V, and A20I. The order of ice-binding strength was confirmed to be A20L < A20G < wild-type < A20T < A20V < A20I. The crystal structure analysis of A20I mutant showed the polypentagonal water network composed of about 50 semiclathrate waters as shown in Fig. 3(a). The water network appeared to include a tetrahedral water cluster exhibiting a perfect position match to the first prism plane corresponding to a single ice crystal (Fig. 3(b)). These results suggest that a fine-tuning on the surface of this IBP is assisted by a side-chain group of protein (e.g., mutation site in this study), and that the holding property of its polypentagonal water network should regulate the function to lead the IBP to specific ice planes.
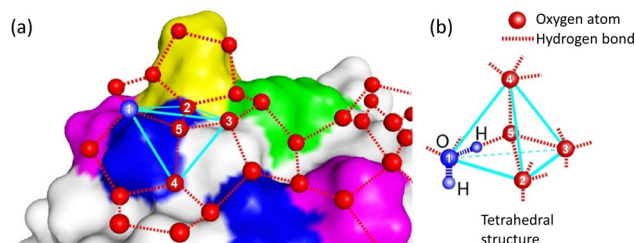
Fig. 3. (a) A part of 50 semiclathrate waters on IBP from *Zoarcidae*. (b) The tetrahedral water cluster extracted from (a).

References
[1] M. Adachi *et al.*, FASEB J., **3**, 3647 (2018).
[2] C. Shibazaki *et al.*, J. Mol. Biol., **430**, 5094 (2018).
[3] S Mahatabuddin *et al.*, Proc. Natl. Acad. Sci. USA., **115**, 5456 (2018).

P2-8 Project "Biomolecular Structure and Dynamics"

Leader : Taro Tamada

The relationship between protein structure and dynamics is important for ultimate understanding of protein functions. Project "Biomolecular Structure and Dynamics" aims to contribute to a wide range of biological and life sciences by performing research and development of molecular imaging methods using neutrons, along with other quantum beams like X-rays and computer simulations. In this report, we describe our latest activities for protein structure and dynamics.

Development of technologies for neutron protein crystallography [1, 2]

Structural information of hydrogen atoms and hydration water molecules obtained by neutron protein crystallography is expected to contribute to the elucidation and improvement of protein function. However, many proteins, especially membrane proteins and protein complexes, have large molecular weights, and the unit cells of their crystals have large volumes, which are out of the range of unit-cell volumes measurable by conventional diffractometers. A large unit-cell volume causes difficulty in separating Bragg peaks close to each other in the spatial and time dimension in diffraction images. In addition, the average intensity of Bragg peaks decreases as the number of peaks increases with large unit cells.

We plan to design a high-resolution biomacromolecule neutron time-of-flight diffractometer, which allows us to collect diffraction data from crystals with a large unit cell volume at MLF in J-PARC (Fig. 1). A decoupled hydrogen moderator (DM), which has a narrow pulse width with short tail, is selected as the neutron source because such characteristic feature of DM is crucial for the separation of Bragg peaks from crystals with large unit cells. The proposed diffractometer adopts a large camera distance (L_2 = 800 mm) and more than 40 novel large-area detectors (larger than 320 mm × 320 mm). This diffractometer is estimated to be able to measure crystals with a lattice length of 250 Å along each axis at d_{min} = 2.0 Å. Ellipsoidal and curved shapes were introduced in the vertical and the horizontal guide design, respectively, which provide an estimated neutron flux of 6×10^5 n s^{-1} mm^{-2} in the wavelength range of 1.5 – 5.5 Å. The resultant neutron dose levels were found to show sufficient radiation shielding protection and to fully satisfy the safety regulations at MLF in J-PARC, as shown in Fig. 1.

The implementation of a sample chamber, which is operated under vacuum or helium gas to decrease background signals, is useful for the exact integration of weak Bragg peaks from crystals with large unit cells. In addition, this neutron diffractometer will be combined with an X-ray diffractometer for consecutive data collection with two different quantum beams at a measuring station.

Structural changes of cardiac muscle proteins caused by a disease-causing mutation [3]

Cardiac muscle contraction is regulated by protein complexes called thin filaments in a Ca^{2+}-dependent manner. Thin filaments consist of the filamentous actin (F-actin), tropomyosin (Tm), and troponin (Tn), which consists of TnC, TnI, and TnT. When Ca^{2+} binds to TnC, this signal is transmitted from Tn to Tm, and then Tm

moves around F-actin so that myosin-binding sites on actin are exposed. This allows myosin binding to actin, leading to force generation. There are, however, many mutations in Tn that causes familial cardiomyopathy. Among these, the E244D mutation of TnT is known to increase the maximum force, causing hypertrophic cardiomyopathy. Although functional studies have extensively been carried out, the molecular mechanism of the functional aberration has not been understood.

Here, we used small-angle X-ray scattering (SAXS) to investigate the effect of the E244D mutation of TnT on the structure of the thin filaments. The SAXS measurements were carried out on thin filaments containing the wild-type Tn (WTF) and those containing the E244D mutant of Tn (DTF) in both the absence and presence of Ca^{2+} using BL45XU at SPring-8. Analysis based on a model calculation has shown that in the WTF, upon Ca^{2+}-binding, Tm moved around F-actin by 10° to expose myosin-binding sites on actin, and Tn also moved around F-actin in the same direction (Fig. 2 (a)). In the DTF, in the absence of Ca^{2+}, the Tm position was the same as that of the WTF, suggesting that myosin binding is inhibited. However, upon Ca^{2+}-binding, Tn moved in the opposite direction to that in the WTF, and Tm moved around F-actin by 20° (Fig. 2 (b)), leading to more exposure of myosin-binding sites on actin than the WTF. These structural changes would promote more myosin binding, resulting in the increase in the maximum force as observed for this mutation.

References

[1] K. Kurihara *et al.*, J. Appl. Cryst., **51**, 596 (2018).
[2] K. Tomoyori *et al.*, J. Phys. Conf. Proc., **22**, 011026 (2018).
[3] T. Matsuo *et al.*, J. Struct. Biol., **205**, 196 (2019).
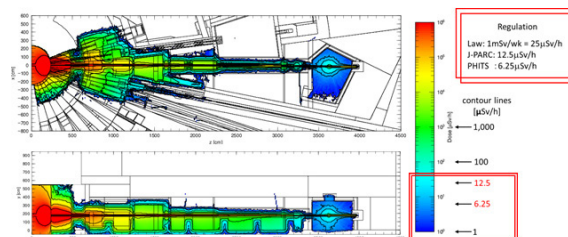
Fig. 1. Simulated distribution of radiation dose rate from neutrons and photons with sample.
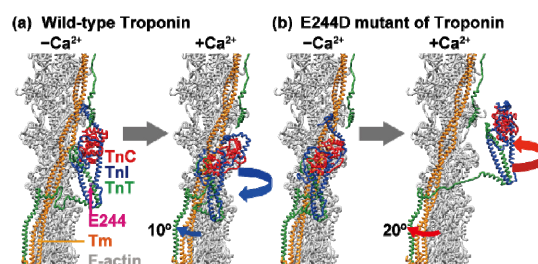
Fig. 2. Obtained models of thin filaments containing the wild-type Tn (a) and those containing the E244D mutant of Tn (b). −Ca^{2+} and +Ca^{2+} denote the absence and presence of Ca^{2+}, respectively.

Part Ⅰ

3. Advanced Quantum-Beam Technology

P3-1 Project "LCS Gamma-ray"

Leader : Ryoichi Hajima

The research objective of LCS Gamma-ray Research Project is developing the technologies of high-brilliance γ-ray generation and exploring its scientific and industrial applications such as nuclear physics, nuclear astrophysics and non-destructive measurement of nuclear material. The γ-ray source is based on laser Compton scattering (LCS), which enables one to generate energy-tunable mono-energetic γ-rays. In the research project, we are developing critical components for electron accelerators to achieve small-emittance and high-average current beams, γ-ray optics and a Monte Carlo simulation code.

^{95g}Tc and ^{96g}Tc as alternatives to medical radioisotope ^{99m}Tc [1]

Various radioisotopes, such as ^{99m}Tc (half-life 6.02 h), ^{201}Tl (half-life 3.04 d), and ^{133}Xe (half-life 5.27 d), are used for single-photon emission computed tomography (SPECT) in medical diagnostic scans. In particular, ^{99m}Tc has become the most important medical radioisotope at present. The ^{99m}Tc radioisotopes are supplied by ^{99}Mo/^{99m}Tc generators, which continuously generate ^{99m}Tc through the β-decay of the parent nucleus ^{99}Mo accumulated inside the generators. At present, the parent nucleus ^{99}Mo is produced in nuclear reactors by the neutron-induced fission of ^{235}U in highly enriched uranium (HEU) targets, in which the fraction of ^{235}U is approximately 90%. As world-wide concern about nuclear security is growing, maintaining HEU reactors is becoming difficult. Therefore, the development of an alternative method to supply Tc radioisotopes without HEU is expected.

We studied ^{95g}Tc and ^{96g}Tc as alternatives to the medical radioisotope ^{99m}Tc. ^{96g}Tc (^{95g}Tc) can be produced by (p, n) reactions on an enriched ^{96}Mo (^{95}Mo) target with a proton beam provided by a compact accelerator such as a medical cyclotron that generate radioisotopes for positron emission tomography (PET). Figure 1 shows the relative reaction rates calculated with PHITS. In the energy region of E<14 MeV, ^{95g}Tc and ^{95m}Tc are the dominant products of the p+ ^{95}Mo reaction. Above 14 MeV, the production yields of ^{94g}Tc and ^{94m}Tc, which are produced by (p, 2n) reactions, suddenly increase. In this reaction, the production rates of the niobium isotopes are lower than that of the dominant product by at least two orders of magnitude in the energy region of E≤13 MeV. We concluded that energies of 11–12 MeV are suitable for ^{95g}Tc production. We have similar results for ^{96g}Tc as well.
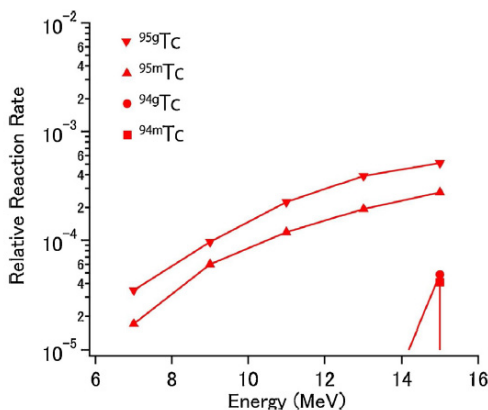
The γ-rays are measured with an electron-tracking Compton camera (ETCC). We calculated the relative intensities of the γ-rays from ^{95g}Tc and ^{96g}Tc. The calculated γ-ray intensity of a ^{96g}Tc (^{95g}Tc) nucleus is as high as 63% (70%) of that of a ^{99m}Tc nucleus. We also calculated the patient radiation doses of ^{95g}Tc and ^{96g}Tc, which were larger than that of ^{99m}Tc by a factor of 2–3 based on the applied assumptions. A medical PET cyclotron which can provide proton beams with energies of 11–12 MeV and a current of 100 μA can produce 12 GBq (39 GBq) of ^{96g}Tc (^{95g}Tc) for operation time of 8 h, which can be used for 240 (200) diagnostic scans.

Properties of the RF transmission line of a C-shaped waveguide [2]

Waveguides are used to transmit radio frequency (RF) power. There are many types of waveguides, which can be classified based on their structure, e.g., rectangular, circular, coaxial, elliptical, radial, or conical. In certain waveguides, such as the rectangular waveguide (RWG) and the circular waveguide (CWG), only an outside conductor is present. Other waveguides, such as the coaxial waveguide, have both outer and inner conductors. Because the RWG and the CWG have a cut-off frequency, they can be used as higher-order mode (HOM) couplers of superconducting cavities to extract HOM from the cavities.

Here, we have proposed a new type of waveguide. This waveguide is named the C-shaped waveguide (CSWG) because the shape of the cross-section view is similar to that of the letter C. Even though the structure of this waveguide is similar to the coaxial line, it features a cut-off frequency, easy cooling, and easy connection to the coaxial waveguide. Figure 2 depicts the transformation from a coaxial-waveguide converter to a C-shaped waveguide. The CSWG has unique characteristics, such as a cut-off frequency and easy cooling of the inner conductor, that are absent in the coaxial line. The results of calculations using a 3-dimensional simulation software and a measurement with a CSWG model are in good agreement with the analytical solution. The CSWG can be applied to a pickup port with a high-pass filter that can attenuate the higher-order modes over the cut-off frequency without attenuating the accelerating mode.

Fig. 1. Calculated relative reaction rates of the p + ^{95}Mo reaction. The thickness of the ^{95}MoO$_3$ target is 1 mg/cm^2.

Fig. 2. Transformation from a coaxial-waveguide converter (top left) to a C-shaped waveguide (bottom left).

Short-Lived Radioisotope ⁹⁸Tc Synthesized by the Supernova Neutrino Process [3]

Neutrinos are a key component of the physics of core-collapse supernovae (SNe) and their associated nucleosyntheses. The nucleosyntheses by neutrino-induced reactions in SNe (the ν-process) have been proposed as the mechanism for the origin of several rare isotopes of light-to-heavy elements. A large number of energetic neutrinos are emitted from the protoneutron star formed during the early post-collapse phase of a core-collapse SN. When these neutrinos pass through the outer layers of the progenitor star they can induce nuclear reactions on atomic nuclei.

The isotope ⁹⁸Tc decays to ⁹⁸Ru with a half-life of 4.2×10^6 y and could have been present in the early Solar System. We have reported on the first calculations of the production of ⁹⁸Tc by neutrino-induced reactions in core-collapse SNe. Figure 3 shows a partial nuclear chart around ⁹⁸Tc and associated nucleosynthesis flows. Our predicted ⁹⁸Tc abundance at the time of the solar system formation is not much lower than the current measured upper limit raising the possibility for its detection in the not too distant future. When the initial abundance is precisely measured, the ⁹⁸Tc nuclear cosmochronometer could be used to evaluate a much more precise value of the duration time from the last core-collapse SN to the formation of the solar system. Moreover, a unique and novel feature of the ⁹⁸Tc ν-process nucleosynthesis is the large contribution (~20%) from charged current reactions with electron antineutrinos. This means that ⁹⁸Tc becomes a unique new ν-process probe of the temperature of the electron antineutrinos.
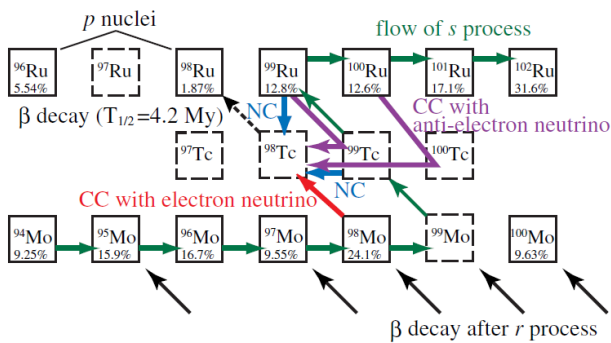
Fig. 3. Partial nuclear chart around 98Tc and associated nucleosynthesis flows.

Dipole strength distribution in ²⁰⁶Pb for the evaluation of the neutron capture cross section of ²⁰⁵Pb [4]

Photon strength functions (PSFs) have attracted growing interest in the context of nuclear astrophysics and nuclear technologies. They give information on average electromagnetic decay properties of a nucleus and are dominated by the electric giant dipole resonance (GDR). Furthermore, the dipole strength distribution close to the neutron separation energy has a large impact on the neutron-capture cross sections. The PSFs are essential ingredients of statistical nuclear reaction calculations to estimate cross sections of nuclear reactions, for example, neutron capture.

From the viewpoint of nuclear engineering, cross-section data of capture reactions induced by fast neutrons are crucial for the development of the transmutation technique through accelerator driven systems (ADS).

Neutron-capture cross sections of ²⁰⁵Pb have been measured using thermal neutrons from the Oak Ridge High Flux Isotope Reactor. However, no experimental data of capture cross sections at the fast-neutron energy region are available. To evaluate the neutron-capture cross sections of ²⁰⁵Pb, nuclear photon-scattering or nuclear resonance fluorescence (NRF) data combined with the photoneutron (γ, n) data can be used.

We investigated the dipole strength distribution of ²⁰⁶Pb via a nuclear resonance fluorescence experiment using bremsstrahlung radiations produced with an electron beam at a kinetic energy of 10.5 MeV at the Electron Linac for beams with high Brilliance and low Emittance (ELBE). We identified 88 states resonantly excited at energies from 3.7 to 8.2 MeV. The analysis of the measured γ-ray spectra includes the quasicontinuum of levels at high energy. Monte Carlo simulation of γ-ray cascades were performed to obtain the intensities of inelastic transitions and branching ratios of the ground-state transitions. The extracted photoabsorption cross section shows enhanced dipole strength at the excitation energies around 5.5 and 7 MeV, which may relate to a pygmy dipole resonance. The present (γ, γ) data combined with (γ, n) data from the previous literature were used for confining input parameters of the statistical calculation code CCONE to derive the neutron-capture cross section of the unstable ²⁰⁵Pb nucleus. Figure 4 shows the resulting uncertainty of the neutron-capture cross section of ²⁰⁵Pb obtained from experimental data and following analysis.
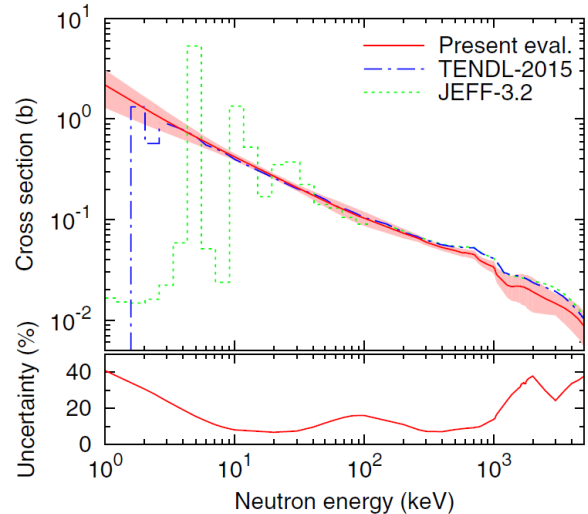
Fig. 4. Neutron-capture cross section of ²⁰⁵Pb calculated by using the PSF deduced from the photonuclear data in the top panel. The deduced uncertainty is overlaid as a band around the cross section and presented in the bottom panel. The evaluated cross sections of TENDL-2015 (dot-dashed line) and JEFF-3.2 (dotted line) are also shown for comparison.

References

[1] T. Hayakawa *et al.*, Heliyon, **4**, e00497 (2018).
[2] M. Sawamura *et al.*, Nucl. Instr. Meth. A, **882**, 30 (2018).
[3] T. Hayakawa *et al.*, Phys. Rev. Lett., **121**, 102701 (2018).
[4] T. Shizuma *et al.*, Phys. Rev. C, **98**, 064317 (2018).

P3-2 Beam Engineering Section

Section Manager : Yasuyuki Ishii

The research objectives in our section are development of various accelerator-related-techniques including ion-beam-irradiation-techniques and ion-beam-analyses. Each member has been engaging in individual researches more than one. Recent remarkable studies are shown as follows; the first article is hollow beam formation in the energy range of several tens MeV using octupole magnets, and the second one is local distribution measurements of remaining elements in extraction chromatography adsorbents. {3-01,09, 2-31~38 in Part II}

Hollow ion beam formation using multipole magnets [1]

The use of multipole magnets enables us to form unique beam profiles that can never be obtained by common linear focusing using quadrupole magnets. As an example of such beam profile manipulations, we have experimentally investigated the formation of an ion beam with a hollow transverse profile using multipole magnets, such as sextuple magnet and octupole magnet.

The beam formation experiment was conducted at a beam line of the TIARA cyclotron where two octupole and two sextupole magnets were installed together with several quadrupole magnets. The transverse intensity distribution of the beam was adjusted using phosphor screens and measured using radiochromic films on the target. When the beam was focused using two octupole magnets with proper polarities and strengths, the tail of the original beam was folded inward and thus the intensity distribution was made highly hollow. As shown in Fig. 1, the cross-section of the hollow beam could be easily changed between ellipse, rounded rectangle and rhombus shapes by controlling intensity of the octupole magnets. We have found that the hollow beams have a steep and narrow peak at the peripheral edge.

As a conventional method of generating high-energy hollow ion beams, a plasma lens that can be activated by a pulsed discharge is known. The present method is applicable to various beams including a coasting beam.

A study of research and development is ongoing in collaboration with Osaka Univ. for the application of hollow beams at the cyclotron.
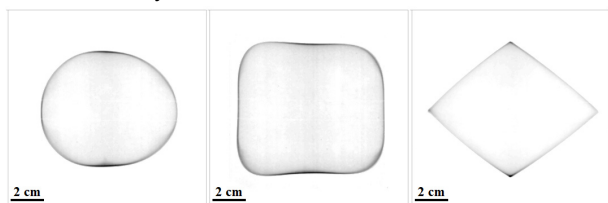
Fig. 1. Various profiles of the hollow beams (10 MeV proton) formed by focusing with two octupole magnets of different strengths.

Local distribution of remaining elements inside extraction chromatography adsorbents [2]

Extraction chromatography is a promising technology for the recovery of minor actinoids (MA(III): Am(III) and Cm(III)) from high level liquid waste (HLLW). In this technology, an extractant is impregnated into styrene-divinyl benzene copolymer coating around porous silica particle and the particles are utilized as an adsorbent. We propose application of an adsorbent with mixture of octyl(phenyl)-N,N-diisobutylcarbonoylmethylphosphine oxide (CMPO) and bis(2-ethylhexyl)hydrogen phosphate (HDEHP) extractants. In this study, the distribution of non-radioactive Eu(III), which is instead of Am(III) and Cm(II) for the similar chemical feature, in the adsorbents was measured by μ-PIXE-CT after adsorption/elution processes.

A reconstructed 3-dimensional image of Eu and cross sections of the 3-dimensional image for a particle of absorbent were obtained by PIXE-CT after the elution of CH_3COONH_4 as shown in Fig. 2. In PIXE-CT, the 3-dimensional image was numerically synthesized from the 2-dimensional images of Eu distribution. These images were obtained by measuring X-ray spectra generated by PIXE with 3 MeV proton microbeam. The left figure corresponds to the reconstructed 3-dimensional image. The right 3 images show the cross sections at the dashed lines in the 3-dimensional image. A boundary like shadow could be found between the core and surface regions in the cross section at middle of the particle. Concentration of Eu at outside of the boundary seems to be smaller than that at the core. Distributions of Eu before and after the elution process with DTPA solution were uniform throughout the particle for both [HDEHP]/[CMPO] compositions. These results suggest that Eu adsorbed in the core region of the adsorbent is more difficult than those at the surface region to be discharged by the elution process.

The distribution of the remaining elements after the process could be evaluated owing to μ-PIXE-CT analyses, and improvements the structure of the adsorbent as well as the eluent for lanthanides were revealed to be essential.
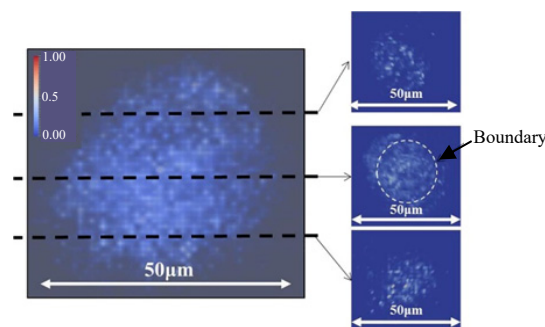
Fig. 2. The reconstructed 3-dimensional image and cross-sectional distributions of Eu for the particle with [HDEHP]/[CMPO] = 0.5 after elution by CH_3COONH_4 solution.

References
[1] Y. Yuri *et al.*, Prog. Theor. Exp. Phys. **2019**, 053G01 (2019).
[2] S. Watanabe *et al.*, Nucl. Instr. Meth. **B404**, 202-206(2017).

Part Ⅱ

Part Ⅱ

1. Materials Science

1 - 01   Near Infrared Photoluminescence from Nitrogen-Vacancy Centers in 4H-SiCs Irradiated with Ion Beams

S.-I. Sato [a], T. Narahara [a, b], Y. Yamazaki [a], Y. Hijikata [b], B. C. Gibson [c],
A. D. Greentree [c] and T. Ohshima [a]

[a] Department of Advanced Functional Materials Research, TARRI, QST,
[b] Graduate School of Science and Engineering, Saitama University,
[c] ARC Centre of Excellence for Nanoscale BioPhotonics, RMIT University

Optically active point defects in wide-gap semiconductors of which spin states are controllable have attracted strong attention because of their potential of quantum technology applications such as quantum information processing, quantum sensing, and quantum metrology. Silicon Carbide (SiC) semiconductor is one of the most attractive host materials for these applications [1,2], since the crystal growth and device fabrication technology are well developed and thus SiC-based electrically driven quantum devices are feasible. Recently, $N_C V_{Si}^-$ centers in SiC, *i.e.* negatively-charged pairs of Si vacancy (V_{Si}) and nitrogen (N) atom at carbon sub-lattice site (SiC-NV centers), have been proposed as an optically active defect with zero phonon lines (ZPLs) at wavelengths around 1200 nm. This optical property is advantageous for *in vivo* imaging and sensing (temperature, magnetic field, etc.) since the near-infrared (NIR) light can penetrate biological tissues more efficiently than visible light [3]. However, the optical spin-state manipulation (*e.g.* optically detected magnetic resonance, ODMR) of NV centers has not been demonstrated to date. One of the reasons is that SiC-NV centers have not been observed in any as grown SiC materials and the formation mechanism is less well understood.

Here we show investigation of NIR photoluminescence (PL) properties of 4H-SiCs irradiated with energetic charged particles for the purpose of clarifying the formation mechanism of SiC-NV centers and of controlling their formation. Samples used in this study were high purity semi-insulating (HPSI) 4H-SiC substrates with the N impurity concentration of 3.3×10^{15} cm^{-3}. The samples were irradiated with 2 MeV-nitrogen (N) ions, 4 MeV-silicon (Si) ions, 7 MeV-iodine (I) ions at room temperature (RT), and subsequently thermally annealed at 1000 °C for 30 min under Ar atmosphere. Those energies were chosen so that the peak defect concentration appeared at 1.5 μm from the surface. NIR-PL spectra at irradiated region in the samples were investigated using micro-PL measurement system at RT. The excitation laser wavelength was 1064 nm.

Figure 1 (a) shows typical PL spectra at RT of HPSI 4H-SiC samples before and after ion irradiation. Sharp peaks appeared were assigned to be Raman scatterings of 4H-SiCs. Strong NIR PL luminescence ranging from 1100 nm to 1500 nm is observed for sample irradiated with 2 MeV-N ions. Since four sharp peaks originated from ZPLs with SiC-NV centers were observed from low temperature (80 K) PL spectra (not shown in this report),

the broad peak at RT is concluded to be PL for SiC-NV centers with their phonon side bands.

Figure 1 (b) shows variation of the PL integrated intensity ranging from 1150 nm to 1450 nm with irradiated fluences. In all cases, the PL integrated intensity increases with increasing fluence and no saturation trend is observed in this fluence range. However, the PL integrated intensity for the 2 MeV-N ion irradiated HPSI 4H-SiC is obviously higher than those for samples irradiated with other two ion species. This fact strongly indicates that implanted N atoms formed SiC-NV centers after thermal annealing. It can be also mentioned that SiC-NV centers are formed from small amounts of impurity N atoms in HPSI 4H-SiC in the case of 4 MeV-Si and 7 MeV-I irradiations and there is still a surplus of N atoms even after the highest fluence irradiation.
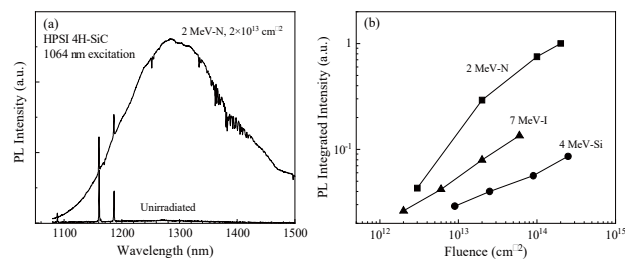
Fig. 1. (a) PL spectrum at RT of HPSI-4H-SiC irradiated with 2 MeV-N at the fluence of 2×10^{13} cm^{-2}. The PL spectrum of unirradiated sample is also shown. (b) The PL integrated intensity (1150 nm to 1450 nm) of irradiated HPSI 4H-SiCs as a function of fluence. The ordinate is normalized by the value of 2 MeV-N at the fluence of 2×10^{14} cm^{-2}.

References
[1] H. Kraus, *et al.*, Nano Lett. **17**, 2865 (2017).
[2] Y. Yamazaki, *et al.*, J. Mater. Res. **33**, 3355 (2018).
[3] A. M. Smith, *et al.*, Nat. Nanotechnol. **4**, 710 (2009).

1 - 02

Study on Radiation Resistance of New Generation Triple-junction Solar Cells

Y. Shibata [a)], T. Sumita [a)], T. Nakamura [a)], A. Ogura [a)], M. Imaizumi [a)],
S.-I. Sato [b)] and T. Ohshima [b)]

[a)] Research and Development Directorate, JAXA,
[b)] Department of Advanced Functional Materials Research, TARRI, QST

InGaP/GaAs/Ge lattice-matched (LM) triple-junction (3J) solar cells are still widely applied to spacecraft, and they are being updated on higher performance. Radiation resistance is one of the important properties for space solar cells, therefore, we should well understand radiation response of electrical characteristics of solar cells to understand and improve radiation tolerance of solar cells. Such knowledge is necessary to accurately predict solar cell performance in orbit. In this study, we performed irradiation tests on a new generation LM3J and a newly developed inverted metamorphic (IMM) 3J solar cell, and the results were compared with those of a current LM3J cell.

In this study, we prepared three types of solar cells (LM3J-A, LM3J-B and IMM3J). LM3J-A is a currently used LM3J cell with the initial conversion efficiency (η_{ini}) of 28.7%. LM3J-B is a new generation LM3J cell with η_{ini} of 30.7%. IMM3J is an InGaP/GaAs/InGaAs inverted metamorphic 3J cells with η_{ini} of 31.0%. No shielding material such as a coverglass or a film was applied to the front surface of the cells. The cells were irradiated with 1 MeV electrons. The short-circuit current density (J_{sc}), open-circuit voltage (V_{oc}), maximum power (P_{max}) and fill factor (FF) were obtained from current-voltage (I-V) characteristics under Air Mass Zero illumination before and after irradiation. In addition, we measured subcell photocurrents by LED biased light I-V measurement method [1] before and after irradiation to identify a current-limiting subcell.

Figure 1 shows the degradation characteristics of P_{max}, J_{sc}, and V_{oc} for the two LM3J and IMM 3J cells irradiated with 1 MeV electrons. The values of P_{max} and J_{sc} for LM3J-B are superior to that of LM3J-A in the entire fluence region. In lower fluence region, P_{max} of LM3J-B are inferior to that of the IMM3J. However, in higher fluence region, P_{max} of LM3J-B approaches that of IMM3J. This means that the radiation resistance of LM3J-B is the highest among the three cells.

Figure 2 depicts the change in the subcell photocurrents (I_{ph}) for LM3J-A and LM3J-B cells by 1-MeV electron irradiation. I_{ph} of middle subcell for LM3J-A is significantly degraded by the irradiation. The current-limiting subcell switches from the top subcell to the middle one at fluence of 1×10^5 cm^{-2}. On the other hand, I_{ph} of middle subcell for LM3J-B does not degrade so much. The radiation resistance of the middle subcell in LM3J-B is remarkably improved compared to that in LM3J-A.

In conclusion, radiation resistance of the new generation LM3J solar cell is considerably improved to comparable level with the IMM3J, and it is due to the improvement of

radiation tolerance of its middle subcell.
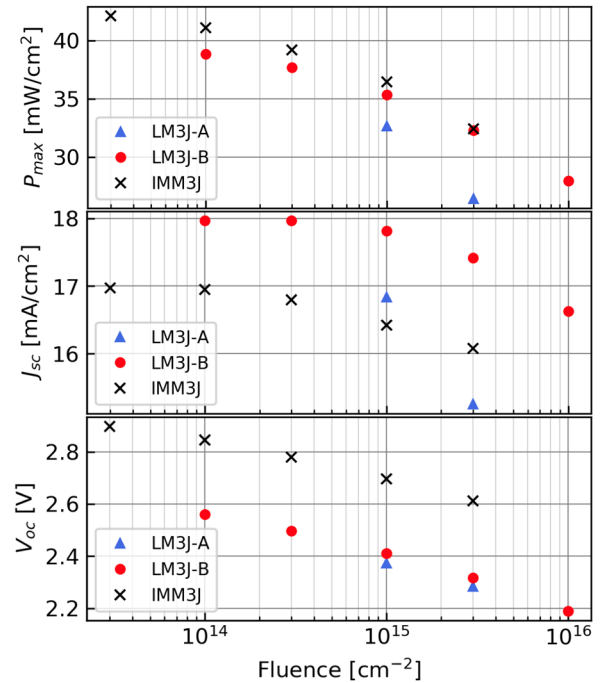
Fig. 1. Degradation characteristics of P_{max}, J_{sc}, and V_{oc} due to 1-MeV electron irradiation.
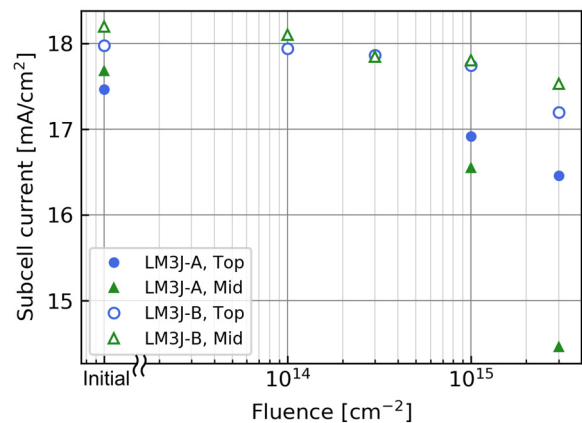
Fig. 2. Change in subcell photocurrent induced by 1-MeV electron irradiation.

Reference

[1] M. A. Steiner *et al.*, IEEE J. Photovoltaics **3**, 2, 2156-3381 (2013).

1 - 03 Single Event Effects Induced on Atom Switch Based Field Programmable Gate Array

K. Takeuchi [a], T. Sakamoto [b], M. Tada [b], A. Takeyama [c]
T. Ohshima [c], S. Kuboyama [a] and H. Shindo [a]

[a] Research and Development Directorate, JAXA,
[b] System Platform Research Laboratories, NEC Corp.,
[c] Department of Advanced Functional Materials Research, TARRI, QST

Field programmable gate arrays (FPGAs) are becoming widely used in space applications along with the growing demand for high-throughput satellites. The unique programmable feature of FPGAs enables not only various functional capabilities but also a short development turnaround-time (TAT) and low cost, as compared with manufacturing application-specific integrated circuits. There are currently three types of FPGAs available in the space industry market: antifuse-based, static random-access memory (SRAM)-based and Flash-based FPGAs. While the antifuse-based FPGA is physically programmed once with the desired circuits on it, both SRAM-based and Flash-based FPGAs have re-programmable capability. However, these SRAM- and Flash-based FPGAs suffer from leakage power loss with the latest semiconductor manufacturing processes and are also vulnerable to single event effects (SEEs) [1].

The atom switch FPGA (AS-FPGA) is another type of FPGAs based on atom switch technology. Atom switches (ASs) are programmable conductive bridges electrically formed between two metals grown by electrochemical phenomenon. ASs have a Ru-Polymer solid electrolyte (PSE)-Cu sandwich structure. As the formation or annihilation of a Cu ion bridge causes a low or high resistance states corresponding to each digital state, it is classified as resistive random-access memory (RRAM).

In this work, we evaluate AS-FPGAs in terms of single event upsets (SEUs) and single event transients (SETs). Heavy ion and pulsed laser irradiation were conducted to investigate these single event effects.

The radiation tolerance of AS-FPGAs was evaluated by using the Takasaki Ion Accelerators for Advanced Radiation Application (TIARA) at QST. A cocktail heavy ion beam of Xe and Kr was used for the evaluation. All irradiations were performed at normal incidence. PULSCAN [2] is the test system for pulsed laser irradiation and was utilized for the experiment. The wavelength and pulse duration are 1064 nm and 30 ps, respectively. Thus, single photon laser absorption was used for evaluation to trigger SEUs and SETs in the CMOS layer.

Figure 1 (b) shows the distributions of SET pulse width. The SET pulse width in AS-FPGA w/o DFF was randomly distributed from nanoseconds to a few tens of nanoseconds regardless of operating frequency. The locations where SETs were captured are consistent with the configured module in the logic tile (Fig. 2). The cross-sections of SETs in pulsed laser testing (distributed
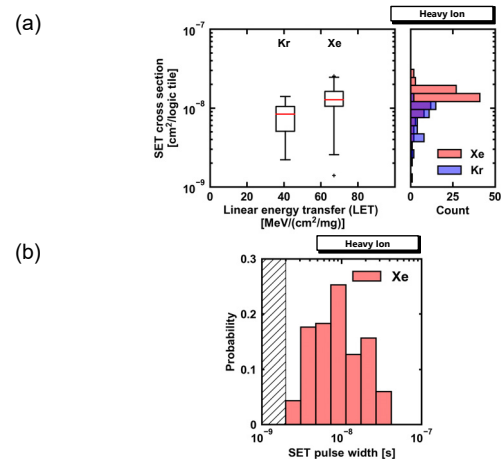
Fig. 1. (a) Box-and-whisker plot and histogram of SET cross-section in AS-FPGA w/o D-FF; (b) Histogram of SET pulse width distributions acquired in Xe irradiation with AS-FPGA w/o D-FF. The shaded area represents an unreliable region due to less sampling resolution.
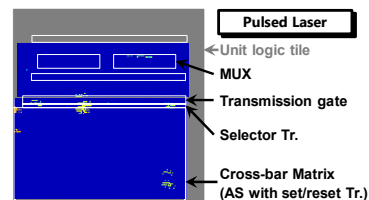
Fig. 2. Example result of pulsed laser irradiation test at 9000 pJ. Blue areas are scanned by laser and yellow colored dots represent the points where SET occurred. The gray square is the area of the unit logic tile, and white-lined squares are functional modules in the logic tile.

about 10^{-8} to 10^{-6} cm^2/logic tile) were varied with laser energy and were roughly consistent with the heavy ion test. All SETs that occurred in pulsed laser irradiation should come from the CMOS layer, because the laser could not reach the ASs located between metal layer.

According to the further discussion on [3], the set/reset transistors with ASs were responsible for the unexpectedly prolonged SETs.

References

[1] H. Quinn et al., Reconfigurable logic: architecture, tools, and applications., P.-E. Gaillardon, Ed. FL, USA: CRC Press, 2015, pp. 31–69.
[2] S. Jonathas, RADLAS 2017 Workshop, 2017.
[3] K. Takeuchi et al., IEEE Trans. Nucl. Sci., 2019 (To be printed).

1 - 04   Impact of Combinational Logic Delay for Single Event Upset on Flip Flops in a 65 nm FDSOI Process

Y. Tsukita, J. Furuta and K. Kobayashi

Graduate School of Science & Technology, Kyoto Institute of Technology

Radiation-induced single event effects (SEEs) are significant issues for space applications, aircrafts and high performance computers. SEEs are affected by circuit configuration and running application. Single event transients (SETs) are vanished by logical and timing-window masking effects during propagation through combinational logic circuits [1]. These effects also prevent single event upsets (SEUs) in flip-flops (FFs) propagating to next FF. We measured SEUs by heavy-ion irradiation tests at TIARA (Takasaki ion accelerators for advanced radiation application, Japan).

We fabricated a test chip in a 65 nm FDSOI process to measure SEU rates. Figure 1 shows the implemented SEU-measurement circuit. 11-stage buffer chains are inserted between FFs as a combinational logic, which propagation delay time is 1.1 ns. SEU on the slave latch at CLK = 0 cannot reach next FF in the implemented shift register over the clock frequency of 480 MHz since it is less than 1.1 ns from the rising edge of the clock signal as shown in Fig. 2. Three types of target FFs are implemented in the fabricated chip: the standard FF, the stacked FF and ACFF (Adaptive Coupling FF) [2]. All implemented FFs have no SEU mitigation in the slave latches but the stacked FF and ACFF have SEU mitigation in the master latches.

The test chip was irradiated in a vacuum chamber to prevent decay of ion energy by the air. Irradiated ions are $^{40}Ar^{8+}$ and $^{84}Kr^{17+}$ whose linear energy transfer are 17.5 and 40.0 MeV-cm^2/mg, respectively. Total Ar fluence is 1.17×10^8 ion/cm^2 and Kr fluence is 8.08×10^7 ion/cm^2. During irradiation, 500 kHz or 480 MHz clock signals were applied to shift registers given from the external LSI tester or an implemented ring oscillator, respectively.

Figure 3 shows measurement results of SEU cross sections at clock frequencies of 500 kHz and 480 MHz. The SEU cross section of the standard FF does not depend on clock frequency. In contrast, SEU cross sections at 480MHz of the stacked FF and ACFF are reduced to 25% – 55% of 500 kHz. It is because SEU on the slave latch that holds a stored value when clock becomes 0 cannot propagate through the combinational logic connected to the slave latch. Radiation hardness of a slave latch is not mandatory when FFs connected to combinational logics with larger delay than a half clock cycle. We assume SEU in the stacked FF and AC FF at clock frequency of 480 MHz are induced by SET pulses. For better radiation hardness, SET-pulse mitigation on slave latches is more significant than SEU mitigation on slave latches.
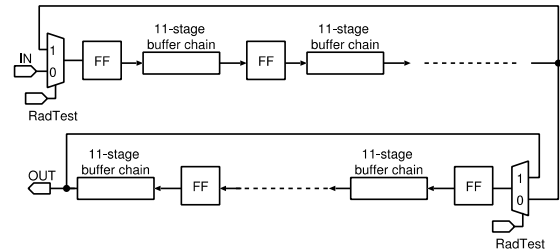
Fig. 1. Schematic diagrams of the SEU measurement circuit.
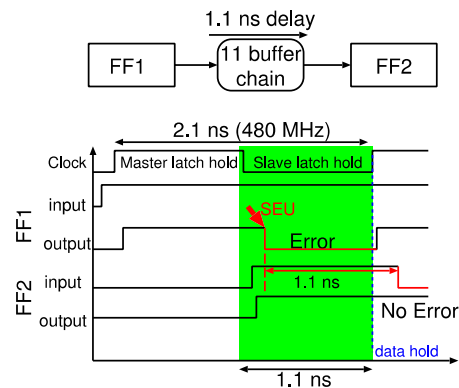
Fig. 2. Masking effect for SEU on slave latch by the propagation delay of the buffer chain.
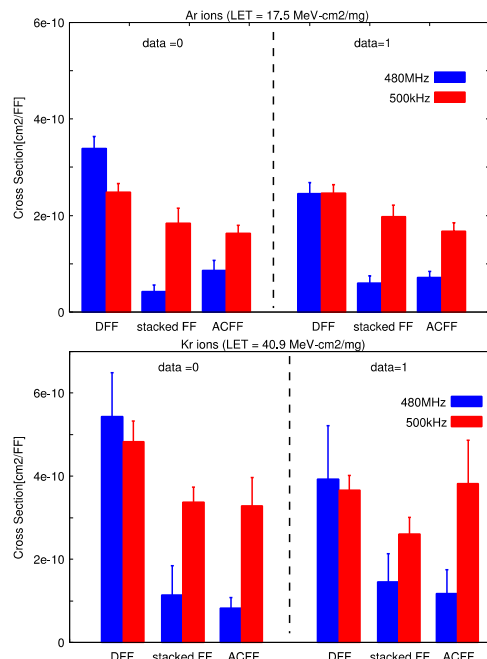
Fig. 3. Measurement results of SEU cross sections at clock frequencies of 500 kHz and 480 MHz.

References

[1] N. N. Mahatme *et al.*, IRPS, pp. 1031-1035 (2010).
[2] C. K. Teh *et al.*, ISSCC, pp. 338-340 (2011).

1 - 05   Radiation Damage Test of Solid State Amplifier 2

C. Ohmori [a)], K. Ishii [a)], Y. Hashimoto [a)] and M. Paoluzzi [b)]

[a)] Accelerator Laboratory, High Energy Accelerator Research Organization (KEK),
[b)] The European Organization for Nuclear Research (CERN)

The LHC Injectors Upgrade (LIU) project aims at increasing the intensity and brightness in the LHC injectors for high luminosity LHC, HL-LHC. It includes the replacement of the present PS booster RF systems by new wideband systems. The installation works will end in the October. The similar system was also installed CERN Proton Synchrotron, PS. These wideband RF systems consist of nano-crystalline material, Finemet®, loaded cavity and solid-state amplifier. The expected Total Ionizing Dose (TID) during the operation is about 1 kGy/year in the PS. Therefore, solid-state amplifiers have not been used. However, the recent progress on the rad-hard type solid-state amplifier for the PS booster shows the potential to use the solid-state amplifiers in the PS tunnel. This paper summarizes that the irradiation test using gamma-rays on the amplifier up to 8.8 kGy.

Figure 1 shows the circuit diagram of the rad-hard solid-state amplifier. A reference MOSFET is employed to compensate TID effect on the MOSFETs. A constant current circuit adjust the gate bias voltage of MOSFETs to regulate the rest current of 1 A. The same gate voltage was supplied for both reference and amplifier MOSFETs. During the power test, auto-level control, ALC, circuit is used to keep the RF output power constant. The RF power of 100 W was consumed at the dummy load near the amplifier. The experimental setup is shown in Fig. 2.
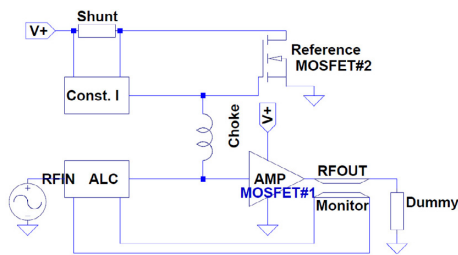
Fig. 1. A mitigation circuit for the irradiation tests at the CHARM and QST Takasaki [1, 2].

Figure 3 shows the results obtained at the QST-Takasaki. Two sets of amplifiers using different type of MOSFET were irradiated. One amplifier uses VDMOS-type, VRF151G, and the other uses LDMOS-type BLF574. The LDMOS shows an excellent result although it showed single event effects under the mixed field irradiation condition [1]. The test results at the QST-Takasaki were submitted to IEEE TNS with the other test results [2].

In parallel, the test of OSL dosimetry system was performed [3].

Fig. 2. Irradiation test of VRF151G and BLF575 solid-state amplifiers at QST-Takasaki [2].
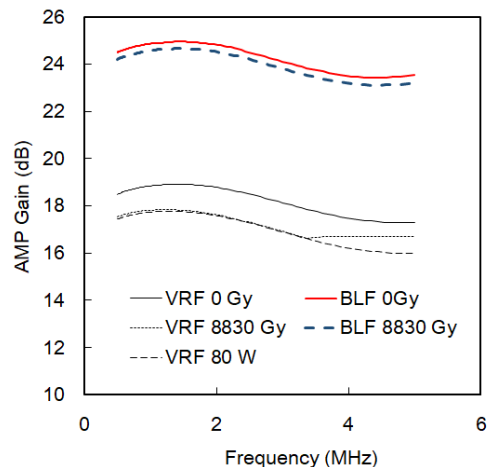
Fig. 3. Variation of amplifier gain by the gamma-ray irradiation at QST Takasaki [2]. Total ionization dose of 8.8 kGy was irradiated.

References

[1] C. Ohmori and M. Paoluzzi, "RF Amplifier using VRF151G and BLF574 Power RF Mosfets," CHARM Radiation Test Report, 2017.

[2] C. Ohmori and M. Paoluzzi, submitted to IEEE TNS on Mar. 13, 2019.

[3] T. Okazaki *et al.*, "Preliminary study of the portable Optically Stimulated Luminescence dosimetry system for measuring radiation doses more than 100 Gy, THP137, in Proceedings of the 15th Annual Meeting of PASJ, Nagaoka, Japan, Aug. 2018, p.1256-1259.

1 - 06　　Research of the Radiation Tolerance in Space Environment of General Electronic Devices

K. Tomita [a], K. Nakano [a], K. Uzuki [a], K. Akashi [a], K. Kurokawa [a],
T. Ohshima [b], S. Onoda [b] and T. Makino [b]

[a] Advanced Engineering Services Co., Ltd. (AES),
[b] Department of Advanced Functional Materials Research, TARRI, QST

In small satellite development, COTS (commercial off-the-shelf) devices are needed to use due to some severe restrictions of resource for installed components. For this reason, it is important to keep reliability for using COTS devices in small satellite development. Therefore, in order to ensure reliability for small satellite, our company has evaluated COTS devices mainly for tolerance of single event at Takasaki Advanced Radiation Research Institute (TARRI) from fiscal year 2008.

近年、小型人工衛星の開発が盛んになり、衛星搭載機器の低コスト化、小型化及び高機能化が要求されている。これらの要求を満たすため、民生電子部品の使用が望まれている。しかしながら、一般的に民生電子部品は宇宙環境下での使用を考慮して設計されておらず、耐放射線性は不明である。そこで民生電子部品の宇宙環境における動作状況、劣化状況を放射線試験により確認し、宇宙への適合性を把握することが必要となる。

放射線の電子部品への影響は、トータルドーズ(TID: Total Ionization Dose)とシングルイベント効果(SEE: Single Event Effect)の大きく2パターンに分けられる。TID は β 線、γ線、陽子線により発生する電子部品の性能劣化である。SEE は重粒子の入射により引き起こされる機能障害である。本研究において、民生電子部品の使用を想定している小型人工衛星は、低軌道かつ運用期間が 1 年と短いため、TID による影響は少ないと考える。一方、SEE は一度の発生で電子部品そのものや周辺回路を破壊する可能性がある。本研究は、様々な民生電子部品の試験を行い、SEE の発生を観測することで宇宙環境における耐放射線性の評価を行うことを目的としている。

本研究では量子科学技術研究開発機構施設共用制度を利用し、高崎量子応用研究所 TIARA 第 4 重イオン室の散乱ビーム照射試験装置を用い、AVF サイクロトロンからのカクテルビーム(N、Ne、Ar の 3 線種)で試験した。SEE 発生頻度は、試験により得られた反転断面積、LET(Linear Energy Transfer)閾値と CREME96 [Cosmic Ray Effects on Micro-Electronics(1996 Revision)] を用いて計算した軌道上放射線分布より算出した。

本研究で民生電子部品の使用を想定している小型人工衛星の軌道条件は、高度 700 km、軌道傾斜角 98 度、衛星構体は 2 mm 厚アルミニウム、運用期間 1 年である。算出した SEE 発生頻度と想定運用期間を比較し、民生電子部品の耐放射線性を評価した。

2018 年度は、民生の温度測定 IC を試料とした。この IC は、温度センサを取付けた箇所の温度を測定し、常に温度をモニタすることで衛星の動作状態を確認する目的で使用する。

2018 年度に試験を実施した試料、評価項目、試験結果及び想定軌道条件における SEE 発生頻度の算出結果を Table 1 に示す。

本試験では以下を評価項目とした。
・　SEL (Single Event Latch-up)
・　SEU (Single Event Up-set)
・　SEFI (温度測定異常)
・　SEFI (応答異常)
　　(SEFI: Single Event Functional Interrupt)

SEL に関しては、試料の消費電流が SEL 判定閾値(通常動作時消費電流の 2 倍)以上に増加した場合に、SEL と判断し発生回数をカウントすることとした。また、同時に試料の電源リセットにより正常復帰の確認を行うこととした。SEU に関しては、温度測定値の一時的な飛びが発生した場合に発生回数をカウントすることとした。SEFI に関しては、試料の誤動作を検知した場合に発生回数をカウントすることとした。

試験の結果、SEL は Ne 及び Ar 照射時に発生したが、電源リセットを行い、正常に復帰することを確認した。また、SEU 及び SEFI (応答異常)は、全線種で発生しなかったが、SEFI (温度測定異常)は全線種照射時に発生した。SEFI (温度測定異常) は発生後、次のデータ測定時に正常復帰することを確認した。各線種照射後に温度測定データを取得し、問題なく動作することを確認した。

Table 1 より、SEL 及び SEFI（温度測定異常）の発生頻度は想定している 1 年という運用期間に対して高い。特に SEFI（温度測定異常）については、およそ 6 分に 1 回の頻度で温度測定異常が発生する。そのため、1 日に数分の利用といった限定的な使い方であっても、宇宙での使用は難しいと考えられる。

最後に、試料である民生電子部品は、宇宙環境での使用を想定して製造されたものではないため、本試験の結果が部品自体の性能・機能の優劣を示すものではないということを付記しておく。

Table 1　Single event probability.

Device under test	Evaluation Item	LET Threshold (MeV-cm^2/mg)	Cross-sectional area (cm^2)	Single Event Probability (event/year)
Temperature measurement IC	SEL	3.987	5.17E-03	3.43E+00
	SEFI (Temperature measurement error)	0.001	4.82E-05	9.00E+04

1 - 07　Characterization of Composition Control in $Ti_{1-x}Al_xN$ Thin Films on Monocrystalline AlN by Reactive CVD

Y. Kasukabe [a, b)], H. Shimoda [b)], S. Yamamoto [c)] and M. Yoshikawa [c)]

a) Global Learning Center, Tohoku University,
b) Department of Metallurgy, Tohoku University,
c) Department of Advanced Functional Materials Research, TARRI, QST

Films of $Ti_{1-x}Al_xN$ have been known as the material which exhibits superior mechanical and thermal properties, and those are widely used as coatings for industrial applications such as cutting tools. Irrespective of those attracting performance, little is studied on the growth mechanism as well as the chemical process. In this work, $Ti_{1-x}Al_xN$ thin films have been prepared by reactive Chemical Vapor Deposition (CVD) and analyzed by Field Emission Gun Scanning Electron Microscopy (FEG-SEM), Transmitting Electron Microscope (TEM) [1], and X-ray Diffraction (XRD).

Recently, it has been reported that $Ti_{1-x}Al_xN$ films have been grown by use of the titanium tetra chloride, $TiCl_4$, and c-plane (0001) monocrystalline hexagonal aluminium nitride, AlN, precursors [2]. The AlN has been prepared at 1500 °C with the gas mixture of NH_3 and $AlCl_3$ on c-plane (0001) monocrystalline hexagonal sapphire. During the $Ti_{1-x}Al_xN$ growth, hydrogen gas is supplied in order to promote the reactivity. The growth has been performed at various temperatures between 800 °C and 1200 °C on the 100-nm-thick monocrystalline AlN on sapphire.

Figure 1 shows the surface morphologies of $Ti_{1-x}Al_xN$ layers deposited at (a) 800 °C, (b) 900 °C, (c) 1000 °C and (d) 1200 °C on monocrystalline AlN substrates. At temperatures lower than 1000 °C, surface morphologies appears to be smooth. As the temperature is raised, the grain size appears to become larger, but there is almost no substantial change between 800 °C and 1000 °C. However, the surface morphology deposited at 1200 °C is quite different form the others. The grains are much smaller than those fabricated at less than 1000 °C, and some of them
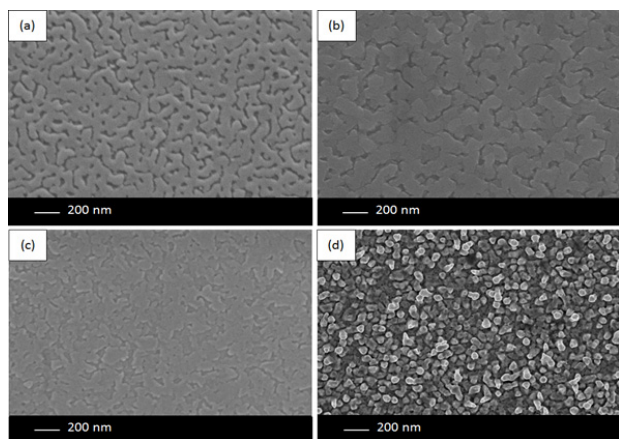
seem to grow in a columnar shape. It can be considered that this difference results from the reactivity between $TiCl_4$ and condensed AlN. Generally, as temperature is raised, reaction rate increases. If the reaction rate increases in this system, it can be expected that $TiCl_4$ and AlN react as soon as $TiCl_4$ reaches the AlN surface, leading to grow in a columnar shape. At temperature lower than 1000 °C, reaction rate is not as high compared to the system at 1200 °C, therefore, sufficient time to diffuse on the surface exists, leading to an increase of surface flatness.

Figure 2 shows TEM image taken from the cross section of the layer deposited at 1200 °C for 15 minutes. This image indicates at the first stage of deposition, the layer grows parallel to the substrate AlN. However, after the layer sufficiently grew, island-like grains are made. In order to analyze the chemical composition of the layer, the
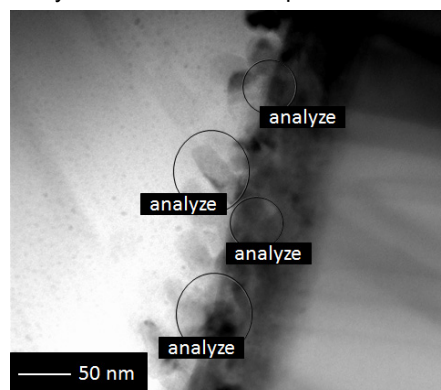
Fig. 2. The cross section TEM image taken from the layer fabricated at 1200 °C on monocrystalline AlN.

analysis of EDX equipped with TEM were performed. The analysis of these regions shown in Fig. 2 clarified the average of 25-30% Al was contained, even at the top of the surface, which agree with Vegard's law. It indicates that 15 minutes of deposition time is enough for Al atoms to diffuse in the deposited layer and to compose $Ti_{1-x}Al_xN$ layers. As well as this sample, the composition analyses of other samples were performed on the layers fabricated at 900 °C and 1000 °C. The analysis clarified the average of 35-40% Al was contained in the layer fabricated at 1000 °C and 75-80% was contained at 900 °C, which agree with Vegard's law. This indicates that Al content in the fabricated layer can be controlled by changing substrate temperature.

Fig. 1. Surface morphologies of the layers fabricated on monocrystalline AlN at (a) 800 °C, (b) 900 °C, (c) 1000 °C and (d) 1200 °C observed by FEG-SEM.

References
[1] H. Abe *et al.*, JAERI-Research 96-047 (1996) 1.
[2] R. Boichot *et al.*, Surf. Coat. Technol. 205 (2010) 1294.

1 - 08   Annealing Behavior of Nitrogen-point Defect Complexes in Silicon Crystal Introduced by the Electron Irradiation

N. Inoue [a, b)], S. Okuda [b)] and S. Kawamata [b)]

a) Graduate School of Engineering, Tokyo University of Agriculture and Technology,
b) Radiation Research Center, Osaka Prefecture University

Almost all people in the world use advanced silicon devices in the mobile phone. Defect – free silicon crystal is grown by nitrogen doping which suppresses point defect induced defects. Nitrogen – point defect (N-PD) behavior, however, is not understood yet, due to low concentration. We are studying it by electron irradiation, forming N-PD, and infrared absorption spectroscopy (IR) [1].

The electron irradiation was done to 2 mm thick nitrogen doped (NFZ) samples (about 5×10^{15} atoms/cm^3) at 1 MeV for 1×10^{17}/cm^2 from both sides at room temperature. IR measurement was done at RT for 2 cm^{-1} wavenumber resolution. Differential absorption spectra were obtained with the non-irradiated reference sample.

Nitrogen forms N_iN_i (interstitial) pair (planar N-Si-N-Si ring) mainly in silicon. We found the decrease of NN pairs by irradiation, suggesting the N-PD formation [1]. Then, we found new absorptions at 728 and 778 cm^{-1} beside the NN absorption line at 766 cm^{-1} by deleting the latter arithmetically [2]. The close location to NN line suggests that their origin has similar structure. We attributed them to VN_2 ($V:N_i$-N_i, planar), first observed and identified N-PD [2]. The absorption at 780 and 790 cm^{-1} was related to VN_2 whose calculated wavenumber was 774 cm^{-1} [3]. The present result is close to that. In O containing CZ silicon, neither decrease of NN nor new absorption were observed, due that V reacted with O and the broken NN recovered.

This year we examined the annealing behavior in detail [4] based on the previous analysis as follows. In 200 °C annealing, no new big peaks appeared, but a decrease of VN_2 absorption was observed [5]. In 400 °C annealing, a new big peak appeared at 689 cm^{-1} in accordance with more decrease of VN_2 and increase of NN loss, being V_2N_2 a candidate of origin [5]. Annealing temperature dependence of these dominant lines was quantitatively examined [5]. Now, it is considered that V from complete VO decomposition at 400 °C reacted with VN_2 and NN to form V_2N_2 (VN:VN, $(VN_s)_2$, nonplanar). 689 cm^{-1} is nearly equal to the observed 691 cm^{-1} which was attributed to VN_s [3]. This is the second and most important N-PD. Theoretically predicted V_2N_2, most stable in V-rich condition [6], has essentially different structure so that its absorption was expected to be far from the NN line [3].

At 600 °C, small peaks appeared, under the NN lines at 762 and 951 and 961 cm^{-1}. Similar absorptions have been observed in the annealed NCZ silicon (containing NN and NO ring groups) recently [7]. We cannot assign them yet, but the close location suggests the NN or planar related configuration. Some structures including NN with more V were proposed theoretically [3]. At 800 °C, absorption lines described above did not appear but another line was distinctly observed at 714 cm^{-1}. In fact it was observed

after annealing at all temperatures, with the line at 733 cm^{-1}. It is possible that VN and VN_2 groups react within each group like C_iO_i and IC_iO_i [8] and NN and NO group[7].

It is to be noted that the NN line was stronger after annealing at 800 °C than before irradiation [4]. This suggests that unknown N formed NN after irradiation and annealing at 800 °C. One possible source was the N monomer. In N-implanted Si, weak absorption was observed at 551, 653 and 687 cm^{-1} and related to ^{14}C, assigned to N_s and unassigned, respectively in 1980's [9, 10]. Later, calculation gave 550 for N_i, 637 for N_s (653 proposed) and 663 for VN_s (690 proposed) [3]. In the present study, weak absorption at 551 [4] and 688 cm^{-1} was observed in the as-grown samples and assigned to N_i and VN_s, respectively. Loss of absorption at 551 cm^{-1} by irradiation and recovery by annealing were observed. In addition to those described above, weak absorptions were observed at 773 and 780 cm^{-1} after irradiation, at 667 cm^{-1} between 200 and 800 °C, and at 683 cm^{-1} at 600 °C.

In summary, about 10 absorption lines were observed in electron irradiated and annealed NFZ silicon. Some were identified to be **VN_2, V_2N_2, N_i and VN_s** originated. This shows that the electron irradiation is the powerful tool to clarify the nitrogen – point defect reaction which plays the important role in realizing the defect – free silicon crystal.
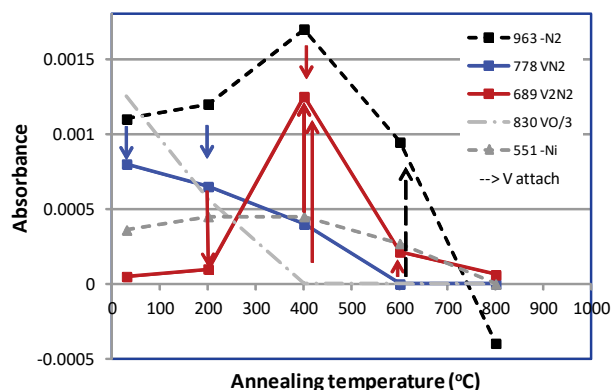
Fig. 1. Annealing temperature dependence of new absorption lines in electron irradiated NFZ silicon. Arrows show V attach.

References
[1] N.Inoue *et al.*, Proc.Forum Sci.Tech. Silicon Mater.**12** (2007).
[2] N. Inoue *et al.*, AIP Conf. Proc. **1583**, 19 (2014).
[3] J. P. Goss *et al.*, Phys. Rev. B, **67**, 045206 (2003).
[4] N. Inoue and Y. Kawamura, J. Appl. Phys. **123**,185701 (2018).
[5] N. Inoue *et al.*, Phys. Status Solidi (c), **13**,833 (2016).
[6] H. Sawada and K. Kawakami, Phys. Rev. B **62**, 1851 (2000).
[7] N. Inoue, S. Okuda, S. Kawamata, ECS Trans. **86-10**, 87 (2018).
[8] N. Inoue *et al.*, Solid State Phenom., **228**, 205-206 (2013).
[9] H. J. Stein, Appl. Phys. Lett., **47**, 1339 (1985).
[10] K. Murakami, H. Ito *et al.*, Appl. Phys. Lett. **45**,176 (1984).

1 - 09   The Change of Electronic Structure at the Interface Between Pt Nanoparticles and the Carbon Support by the Ion Irradiation

H. Okazaki [a], A. Idesaki [a], H. Koshikawa [a], D. Matsumura [b], S. Yamamoto [a], Y. Maekawa [a] and T. Yamaki [a]

[a] Department of Advanced Functional Materials Research, TARRI, QST
[b] Materials Sciences Research Center, JAEA

Pt nanoparticles on the Ar⁺-irradiated glassy carbon (GC) substrate were found to show a higher oxygen reduction reaction (ORR) activity than those on the non-irradiated one [1,2]. This activity enhancement suggests that Pt would be electronically affected by the irradiation lattice defects in GC. From our extended X-ray absorption fine structure (EXAFS) analysis, we found that the Pt nanoparticles on the irradiated carbon support are distorted [3]. Our theoretical research reported that vacancies at the graphite surface would lower d-band center energy of the supported Pt nanoparticles; this is probably the reason for higher activity [4]. In this research, we investigated the electronic structure of carbon support near the interface between Pt nanoparticles and the carbon by X-ray absorption spectroscopy measurements [5] of carbon supports in order to elucidate how the irradiated carbon support affects the strain of Pt nanoparticles and the lowering of d-band center energy.

The HOPG supports were irradiated with 380 keV Ar⁺ at a fluence of 1.0×10^{14} ions/cm² in a 400-kV ion implanter. Since we can distinguish the C-C σ^* and C-C π^* components in the XANES spectra by using HOPG and selecting the E-vector direction of proving light, we used the HOPG as the carbon supports. The Pt nanoparticles were then deposited on the irradiated HOPG supports by RF magnetron sputtering. The Pt deposition was done on the non-irradiated HOPG supports for comparison. The X-ray absorption near-edge structure (XANES) spectra of the C K-edge of the samples were measured at BL-8, SR Center at Ritsumeikan University. We used the linear polarized light with E-vector normal to incident direction and exposed at 90º and 30º from vertical direction of the sample plane.

Figure 1 shows the C-K XANES spectra for an incident angle of 30° for the irradiated HOPG, Pt/HOPG, and Pt/irradiated HOPG. The C-C π^* peak (285.3 eV), C-C σ^* peak (293 eV), and the peak due to surface carbon with adsorbate (288 eV) for the irradiated HOPG were identified by the comparison with the spectrum for 90°. For the Pt/non-irradiated HOPG and Pt/irradiated HOPG, we observed C-C π^* peak shifts toward lower energy (284.9 eV), indicating the valence band shift of graphite by electron transfer from the Pt nanoparticles to graphite. Additionally, the shoulder structure specified by an arrow in the figure is observed at around 284 eV in the XANES spectra. This indicates that the formation of electronic structure due to the Pt-C bond at the interface. We
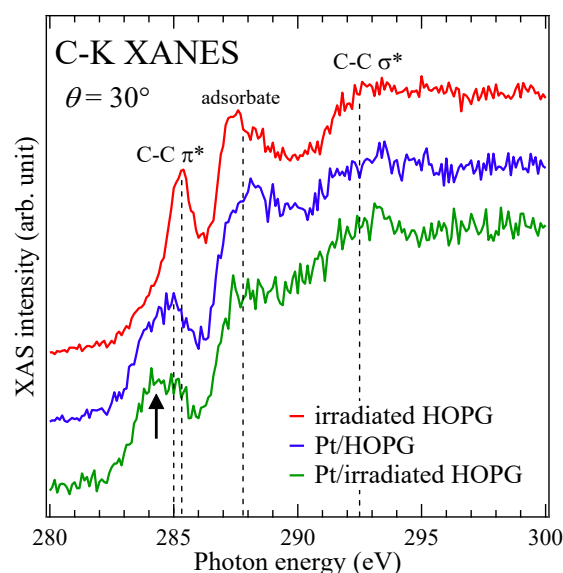
Fig. 1. XANES spectra of C K-edge for the incident angle with 30°.

estimated the intensity change of the shoulder structure by curve fitting. The intensity increases by vacancy introduction due to the ion irradiation to carbon support. This means that the electronic structure of carbon support at interface changes due to the change of Pt-C bond near the vacancies in carbon support introduced by the ion irradiation. Therefore, the change in the electronic structure at interface between Pt nanoparticles and carbon support due to vacancy introduction results in the strain in Pt nanoparticles, and then lowering d-band center energy, which introduces the improvement of ORR activity.

References
[1] T. Kimata *et al.*, Surf. Coat. Technol. **306**, 123 (2016).
[2] T. Kimata *et al.*, Nucl. Inst. Methods Phys. Res. B **444**, 6 (2019).
[3] K. Kakitani *et al.*, Radiat. Phys. Chem. **153**, 152 (2018).
[4] K. Kakitani *et al.*, Surf. Coat. Technol. **355**, 259 (2018).
[5] H. Okazaki *et al.*, Phys. Rev. B **80**, 035420 (2009).

1 - 10 Electron Beam Induced Formation of Pt Nanoparticles on Oxide Films

S. Yamamoto, T. Taguchi, A. Idesaki, H. Okazaki, H. Koshikawa and T. Yamaki

Department of Advanced Functional Materials Research, TARRI, QST

Cerium oxide (CeO$_2$) and tin oxide (SnO$_2$) have been used as promoters in catalysts combined with noble metals such as platinum. Platinum modified with oxides such as cerium oxide (CeO$_2$) and tin oxide (SnO$_2$) is considered as promising cathode materials for the use in polymer membrane electrolyte fuel cells. A key process to make this active is formation of highly dispersed Pt nanoparticles on the oxide surface. Platinum nanoparticles in a solution have been prepared so far by a precipitation method using ionizing radiations such as electro-beam and γ-rays [1]. On the other hand, high energy (≥0.2 MeV) electron-beam radiation has a potential to introduce oxygen defects in CeO$_2$ crystals [2]. Therefore, there is a strong motivation for us to use this method for the formation of highly dispersed Pt nanoparticles and the modification of Pt-CeO$_x$ and Pt-SnO$_x$ interface structure.

We deposited CeO$_2$ and SnO$_2$ films on mirror-polished glassy carbon (GC) substrates by r.f. magnetron sputtering using a sintered CeO$_2$ and SnO$_2$ target in an Ar-O$_2$ gas mixture. The films with thickness of 10 nm were deposited at temperature of 500 °C. The oxide films in an aqueous solution containing 0.1 mmol/L H$_2$PtCl$_6$ and 0.5 vol% C$_2$H$_5$OH were irradiated with 2 MeV electron beam (~600 kGy at dose rate of 1.5 kGy/s) from a 2 MV electron accelerator. The oxide films with Pt particles were characterized by scanning electron microscope (SEM) and transmission electron microscope (TEM) and Rutherford backscattering spectroscopy (RBS) using a 2.0 MeV ^{4}He$^+$ beam from a 3 MV single-stage-accelerator. The oxygen reduction reaction (ORR) activity of the Pt nanoparticles on CeO$_2$ and SnO$_2$ films were examined by electrochemical testing.

Figure 1 shows TEM images of Pt nanoparticles formed by electron beam radiation technique on (a) CeO$_2$ and (b) SnO$_2$ films. The films in the aqueous solution were exposed to 500 kGy dose of electron beam. TEM samples were prepared by scratching off the films. Formation of spherical Pt nanoparticles with a size of less than 3 nm was observed on both CeO$_2$ and SnO$_2$ grains. The results suggested that this technique has a potential to prepare highly dispersed Pt nanoparticles on oxide.

Figure 2 shows the areal atomic density of Pt on CeO$_2$ and SnO$_2$ films as a function of electron beam irradiation dose. The areal atomic density of Pt on the films was measured by RBS. The RBS measurements showed that the areal atomic density of Pt on the oxide films slightly increases with increasing the dose and saturates approximately 5 × 10^{15} atoms/cm^2. The electrochemical measurements indicated that ORR activity and stability of the Pt nanoparticles on CeO$_2$ and SnO$_2$ films are influenced by the electron irradiation dose. Therefore, it is expected that ORR activity of Pt nanoparticles on oxides will be improved by the optimization of electron beam irradiation conditions in the present method.

Acknowledgement

References

[1] J. Belloni, Catal. Today, **113**, 141-156 (2006).
[2] K. Yasuda *et al.*, Microscopy, **46**, 3, 165-169 (2011).
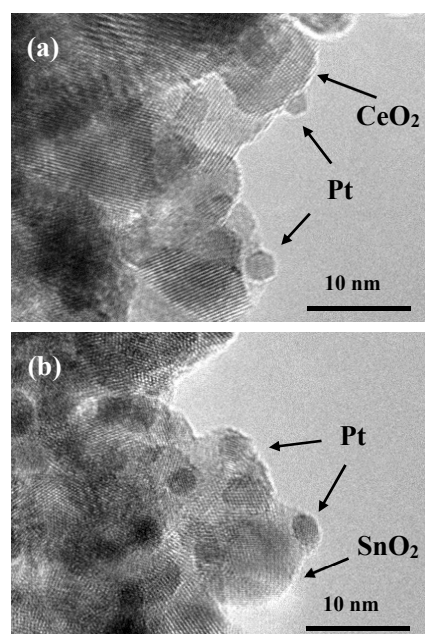
Fig. 1. TEM images of Pt nanoparticles on (a) CeO$_2$ and (b) SnO$_2$ films.
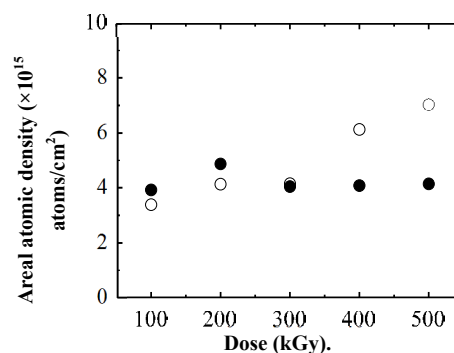
Fig. 2. Areal atomic density of Pt on CeO$_2$ (hollow circles) and SnO$_2$ (solid circles) films as a function of dose.

1 - 11   Effect of High Temperature-Electron Beam-Irradiation on Fabrication of Nitrogen-doped Carbon Catalyst

A. Idesaki, S. Yamamoto, M. Sugimoto, Y. Maekawa and T. Yamaki

Department of Advanced Functional Materials Research, TARRI, QST

Nitrogen-doped (N-doped) carbon materials which exhibit the catalytic activity for an oxygen reduction reaction (ORR), $O_2 + 4H^+ + 4e^- \rightarrow 2H_2O$, have been considered as platinum-alternative catalyst in the cathode of proton exchange membrane fuel cells. It has been reported that the requirements for catalytic activity of N-doped carbon are the formation of a graphite and the incorporation of N into graphite as a pyridinic-nitrogen structure [1], therefore, it is important to develop a method to fabricate N-doped graphite in high efficiency. In many cases, the N-doped carbon have been fabricated by pyrolysis of blends of precursor polymers and/or metal-compounds. In order to obtain the graphite in the relatively low temperature range of 800-1000 °C, transition metal compounds of Fe, Co, Ni, and so on are generally added to the starting materials. The graphite is catalytically formed in the presence of transition metals. However, nitrogen is eliminated in the temperature range of 800-1000 °C where the graphite is formed. Due to the mismatch of these temperature ranges, it is difficult to control both the formation of the graphite and N-doping. Thus, we have examined fabrication of the N-doped carbon material utilizing high-energy electron beam (EB) irradiation on a precursor polymer in an ammonia (NH_3) gas atmosphere at 800 °C. So far, we have reported that the amount of pyridinic-nitrogen which contributes to the ORR activity is enhanced by the EB irradiation and that the obtained carbon material exhibits the ORR potential of 0.7 V vs RHE in 0.5 M H_2SO_4 [2]. In this work, the effect of EB irradiation on the formation of graphite structure was investigated.

The precursor was prepared by mixing of a novolac-type phenolic resin and cobalt chloride ($CoCl_2$) with 5 wt%. The precursor was irradiated by 2 MeV EB under NH_3 gas flow at 800 °C in an irradiation vessel equipped with an auxiliary heater. The precursor was merely heat-treated at 800 °C under NH_3 gas flow in an electric furnace as a reference. The powder X-ray diffraction (XRD) pattern was obtained and the XRD pattern around 15°-35° was divided into two peaks from the graphite (002) component and the amorphous carbon component (Fig. 1). The fraction of graphite, referred as F_g, was evaluated by ratio of the peak area according to following equation [3]:

$$F_g = Area_{graphite} / (Area_{graphite} + Area_{amorphous})$$

The value of F_g for the EB irradiated sample was 0.40, which is higher than the value of 0.31 for the non-EB irradiated sample. This result indicates that the EB irradiation produces a high content of graphite component. On the other hand, the carbon yield was 14.6% and 40.0%
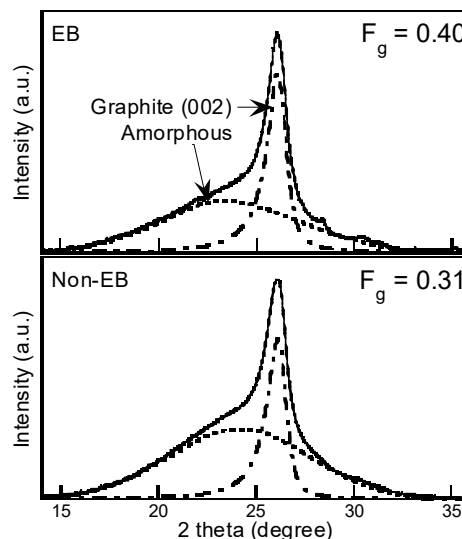
Fig. 1. XRD patterns of obtained carbon material with and without EB irradiation.

in weight for samples with and without EB irradiation, respectively. Such difference is considered to be caused by gasification of carbon by NH_3 as shown by the following reaction [4, 5]:

$$C_{solid} + NH_{3\,gas} \rightarrow HCN_{gas} + H_{2\,gas}$$
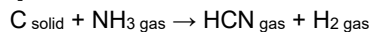
It has been reported that the gasification reaction occurs above 700 °C. In the EB irradiation, $\bullet NH_2$ and $\bullet NH$ radicals are also generated, and this would promote the gasification reaction. According to the high value of F_g of the EB irradiated sample, it is clear that the gasification reaction mainly occurs in the amorphous carbon phase which is not attributed to the ORR activity.

As a conclusion, it was found that the EB irradiation enables the doping of nitrogen as the pyridinic-nitrogen and enhances content of graphite component eliminating the amorphous carbon phase.

Acknowledgement

References
[1] N. Kannnari *et al.*, Carbon, **50**, 2941-2952 (2012).
[2] Y. Kanuma *et al.*, QST Takasaki Annu. Rep. 2017, **QST-M-16**, 44 (2019).
[3] J. Ozaki *et al.*, Electrochim. Acta, **55**, 1864-1871 (2010).
[4] U. I. Kramm *et al.*, J. Phys. Chem. C, **115**, 23417-23427 (2011).
[5] F. Jaouen *et al.*, J. Phys. Chem. C, **111**, 5963-5970 (2007).

1 - 12　Hydrogen Trapping of Defects Introduced by Irradiation in Intermetallics

F. Hori [a], Y. Sumikura [a], K. Sugita [a], A. Takano [a], A. Iwase [a], M. Maekawa [b],
A. Kawasuso [b], Q. Xu [c] and K. Ohsawa [d]

[a] Graduate school of Engineering, Osaka Prefecture University,
[b] Department of Advanced Functional Materials Research, TARRI, QST,
[c] Research Reactor Institute, Kyoto University,
[d] Research Institute of Applied Mechanics, Kyushu University

Intermetallic compound is expected for various type of new functional material because of their good properties such as specific strength to weight ratio, oxidation resistance and strength in elevated temperature. On the other hand, hydrogen embrittlement has reported for some ordered alloys. Considering of this hydrogen and defects interaction, we suggest that intermetallic alloys can be proposed as the hydrogen storage material by control of defects. However, the nature of basic defects in this alloy is not necessarily cleared yet. For instance, A-B type compound alloys possibly have more than two types of vacancies, A-vacancy and B-vacancy basically. Then it is very important to understand the interaction between hydrogen atom and each type of defect. In this study, local structure change of B2 ordered Fe based alloys with irradiation and hydrogen trapping behavior was examined.

Fe-48%Al alloy samples were prepared by arc melting method. Sliced specimens with the thickness of 0.5 mm were annealed at 1073 K for 3 h followed by quenched into water. These specimens were irradiated with 2 MeV electron by CW type accelerator at QST-Takasaki and 8 MeV electron by LINAC at KURRI, Kyoto University to the fluence of 5×10^{17} and 1×10^{18} /cm^2. In both cases, irradiations were carried out at room temperature. Proton irradiation was also carried out for same alloys at TIARA in QST, Takasaki. Cathodic charged hydrogen implantation have performed for before and after electron irradiated samples. All samples were examined by X-ray diffraction (XRD), positron annihilation coincidence Doppler broadening (CDB) measurements. Also thermal desorption spectroscopy (TDS) measurement have done for hydrogen implanted alloy samples with annealing up to 870 K.

Before irradiation, it was confirmed that the bulk structure of all samples was B2. Figure 1 shows positron annihilation CDB ratio spectrum of Fe-48%Al alloys with 2 or 8 MeV electron irradiation ratio to that of before irradiation. In this figure, we can see the slight difference between 2 and 8 MeV electron irradiation. In general, threshold energy of atom displacement from lattice site for each kind of atom in a compound is different. Taking into account for this fact, this difference may be caused by the production of Al vacancy mainly by 2 MeV electron irradiation and Fe and Al vacancy by 8 MeV electron irradiation. Figure 2 shows the hydrogen emission behavior of hydrogen charged Fe-48%Al alloys with 2 and 8 MeV electron irradiation. In this figure, the different temperature
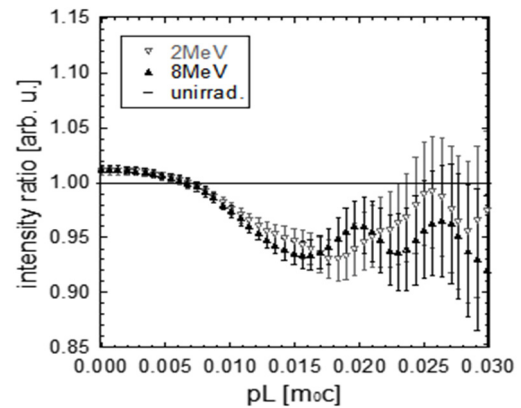
Fig. 1. CDB ratio curves for 2 and 8 MeV electron irradiated Fe48%Al alloys.
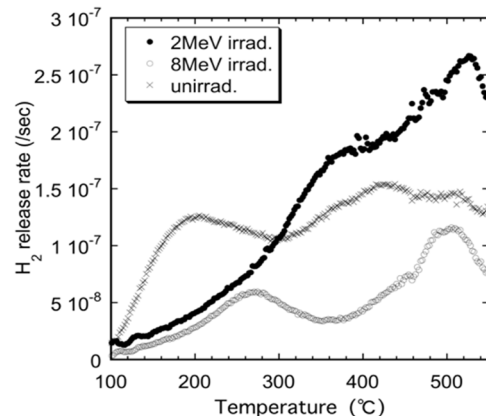
Fig. 2. TDS spectra for hydrogen charged Fe48%Al alloys before and after 2 and 8 MeV electron irradiation.

of hydrogen emission is seen clearly. This result shows that hydrogen trapping occurs at different type of vacancy for 2 and 8 MeV electron irradiation. We found that large amount of hydrogen can be trapped at defect introduced by 2 MeV irradiation that is Al vacancy. This result well agrees with our first principle calculation. That is the hydrogen potential for Al vacancy is higher than that for Fe vacancy. Also TDS for proton irradiated sample shows different behavior of hydrogen emission. It is considered that hydrogen trapping is very sensitive for defect type and structure.

1 - 13

Fabrication of Bi Doped Si
for Quantum Information Applications

K. Miki [a)], M. Maekawa [b)], N. Happo [c)], K. Kimura [d)], J. Tang [a)], N. Miyamoto [a)],
R. Shimazu [a)], H. Maeda [a)], A. Kitafuji [a)], K. Nawata [a)], S. Kitamura [a)], H. Tajiri [e)],
S. Hayashi [d)] and A. Kawasuso [b)],

[a)] Department of Electrical Material and Engineering, University of Hyogo,
[b)] Department of Advanced Functional Materials Research, TARRI, QST,
[c)] Department of Computer and Network Engineering, Hiroshima Citi Univ.,
[d)] Department of Physical Science and Engineering, Nagoya Institute of Technology,
[e)] SPring-8, Japan Synchrotron Radiation Research Institute.

Recently, it has been proposed and demonstrated that heavy elements are potentially suitable for new computing schemes using bound electrons for high temperature operation, e.g. quantum information processing [1]. However, in practice doping heavy elements into the Si crystal is difficult for a variety of reasons. These include, their low diffusion coefficient and solid solubility for thermal diffusion methods [2], their strong tendency towards surface segregation during molecular beam epitaxy (MBE) [3,4]. To overcome those problems, we used one solution to realize Bi doping in Si crystal with a use of ion implantation. In this work, we made Bi doped Si sample with Bi density of 10^{21} cm^{-3} over 100 nm thickness, at TIARA facility, QST, then we succeeded in obtaining the first Bi hologram from the made sample, at the beamline BL39XU, Spring-8.

We fabricated the Bi doped Si sample with the dopant density of around 1.3×10^{21} cm^{-3} over 100 nm thickness by a multiple ion implantation: 370 keV, 5.2×10^{15} cm^{-2}; 225 keV, 3.5×10^{15} cm^{-2}; 110 keV, 2.8×10^{15} cm^{-2}; 50 keV, 1.8×10^{15} cm^{-2}. Design of the sample profile is shown in Fig. 1. Subsequent annealing (600 ºC, 30 min) was applied after chemical cleaning. Decrease of point defects was characterized by the S parameter analysis of positron annihilation measurement, at QST.

In order to look local structures of Bi directly, we applied fluorescence X-ray holography technique to Bi: Si with donor carrier density of 1.34×10^{21} cm^{-3}. We measured the fluorescence X-ray hologram of Bi, with detection of Bi La (10.8 keV) signal, under the X-ray irradiation of 13.5 - 18.0 keV, from the Bi: Si sample. The local structure around the Bi atom, deduced from the Bi hologram, is shown in Fig. 2, where Bi locates at (0,0) position. ○ indicates predicted neighbor atom positions in case Bi locates atomic substitution position. The bright spots corresponds to ○ positions, therefore we conclude that atomic substitution sites could be a major Bi dopant position. For making Bi dopant minor positions clear, we will optimize the anneal process in the next step.

Acknowledgments
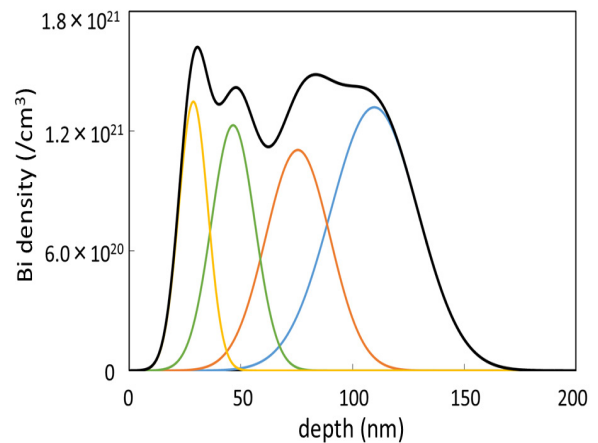
Fig. 1. Bi dopant profile in Si crystal, fabricated with the 400 keV ion implanter at TIARA, QST.
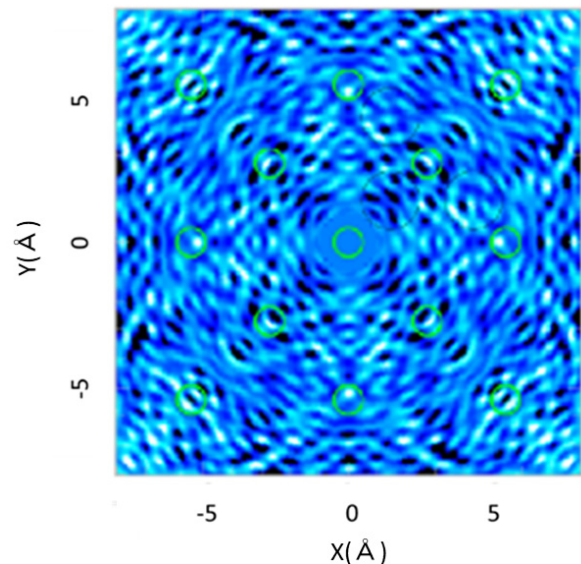
Fig. 2. Bi Hologram from Bi: Si (001), taken at BL39XU, SPring-8.

References

[1] A.M. Stoneham, *et al.*, J. Phys. Condens. Matter **15,** L447 (2003).
[2] F.A. Trumbore, Bell Syst. Tech. J. **39,** 205 (1960).
[3] K. Sakamoto *et al.*, Jpn. J. Appl. Phys. **32,** L204 (1993).
[4] K. Murata *et al.*, Appl. Phys. Lett. **111**, 152104 (2017).

1 - 14 Ion Irradiation-Induced Novel Microstructural Change of Carbon Layer in C-SiC Coaxial Nanotube

T. Taguchi [a)], S. Yamamoto [b)] and H. Ohba [a)]

[a)] Tokai Quantum Beam Science Center, TARRI, QST,
[b)] Department of Advanced Functional Materials Research, TARRI, QST

Silicon carbide (SiC) is well known as not only wide-band-gap semiconducting material for high temperature and high power use but also high temperature structural materials. On the other hand, it is reported that one-dimensional nanomaterials, such as nanowires, nanorods and nanotubes possess new properties different from those of bulk materials. Hitherto, we have succeeded in synthesizing polycrystalline single-phase SiC nanotubes and C-SiC coaxial nanotubes, in which multi-walled carbon nanotubes (MWCNTs) were coated with a SiC layer [1, 2]. We have also reported that in-situ transmission electron microscopy (TEM) was used to observe the microstructural change of SiC nanotubes under ion irradiation, and the results are significantly different from those of bulk SiC [3]. Therefore, the novel microstructural change of C-SiC coaxial nanotubes by ion irradiation is expected. In this study, we investigated the microstructural change of C-SiC coaxial nanotubes during the ion irradiation by using in-situ TEM observation technique.

Carbon nanotubes (GSI Creos Corporation, Tokyo, Japan) were used as the template. The C-SiC coaxial nanotubes were synthesized by heating MWCNTs with Si powder (The Nilaco Corporation, Tokyo, Japan) at 1,200 °C for 100 h in a vacuum. The samples heated at the above conditions included many unreacted MWCNTs besides the C-SiC coaxial nanotubes. Therefore, the samples were then heated at 700 °C for 2 h in air in order to eliminate unreacted MWCNTs. The molybdenum grid holder, which deposited the C-SiC coaxial nanotubes, were irradiated with 200 keV Si^+ ions from 400 kV ion implanter at room temperature in TEM (Model JEM-4000FX, JEOL Ltd., Japan). In-situ TEM observation of C-SiC coaxial nanotube under Si^+ ions irradiation was carried out. The ion fluence was up to 9.1×10^{20} ions/m^2, and the corresponding irradiation damages for the SiC and carbon layer in C-SiC coaxial nanotubes were calculated by SRIM 2008 to be 23.8 and 22.3 dpa respectively.

In the results of the ion irradiation of C-SiC coaxial nanotubes, the SiC layer in the nanotube was transformed into an amorphous structure. The critical amorphization doses for SiC crystals were larger than those found from previous studies on bulk SiC. The reason is considered to be that the induced point defects, elicited by the irradiation, may diffuse and be readily released from the surface and grain boundaries in the C-SiC coaxial nanotubes because of their larger specific surface area compared to the bulk counterpart. Despite the complete amorphization of SiC crystals, the carbon layer in the C-SiC coaxial nanotube was confirmed to have remained crystalline, even after the irradiation dose exceeded 20 dpa. In addition, new graphitic shells perpendicular to the nanotube length direction suddenly emerged after ion irradiation in the C-SiC coaxial nanotube. Therefore, the carbon layer possessed better resistance against amorphization after ion irradiation, compared with the SiC layer in the C-SiC coaxial nanotube. Figure 1 shows the relationship between the ion fluence and the lattice plane spacing of graphitic shells estimated in C-SiC coaxial nanotubes. The lattice plane spacing of graphitic shells in the carbon layer increased up to the point of irradiation damage demonstrated by the complete amorphization of SiC crystals. The disorder in the carbon layer increased with increasing ion fluence because the induced defects had accumulated. Therefore, the lattice plane spacing of the graphitic shell in the nanotube increased with increasing the ion fluence. Surprisingly, afterward it started to decrease. In general, the lattice plane spacing of MWCNT increases monotonically and is saturated by irradiation. These results indicate that the compression stress on the carbon layer is generated because of the SiC layer undergoing configuration change during irradiation. The compression stress was calculated to be approximately 2 GPa. The lattice plane spacing of the newly produced graphitic shells perpendicular to the nanotube length direction was smaller than that parallel to the nanotube length direction before ion irradiation; having almost the same value as graphite. Therefore, the newly produced graphitic shells had a favorable crystallinity.

References

[1] T. Taguchi *et al.*, J. Am. Ceram. Soc. **88**, 459 (2005).
[2] T. Taguchi *et al.*, Physica E **28**, 431 (2005).
[3] T. Taguchi *et a*l., Acta Materialia **154**, 90 (2018).
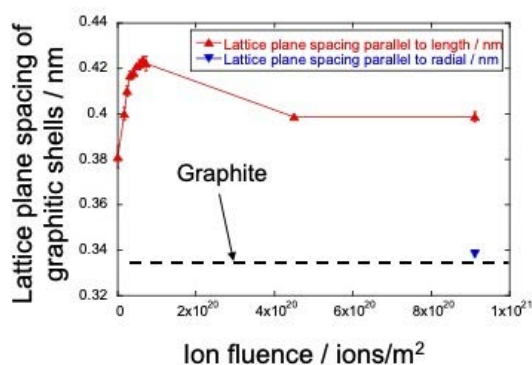
Fig. 1. Relationship between the ion fluence and the lattice plane spacing of graphitic shells estimated in C-SiC coaxial nanotubes.

1 - 15   Gamma Ray Irradiation Effects to the Laser Properties of Nd:YAG/Cr:YAG Composite

K. Tamura [a], H. Ohba [a], M. Saeki [a], T. Taguchi [a], H. Lim [b], T. Taira [b, c] and I. Wakaida [d]

[a] Tokai Quantum Beam Science Center, TARRI, QST,
[b] National Institutes of Natural Sciences (NINS),
[c] Riken Spring-8 center,
[d] Collaborative Laboratories for Advanced Decommissioning Science, JAEA

Decommissioning of TEPCO Fukushima Daiichi nuclear power plant (F1-NPP) is a challenging mission, and information inside the reactor core is needed, where molten fuel debris (mixture of melted fuel core, fuel cladding and construction materials) might be submerged in water. Due to the limited space for inspection by composites such as pipes and electric supply, remote sensing technique in narrow space is required.

To remotely inspect the site and the properties of the fuel debris for their recovery at the reactor, a fiber-optic probe laser-induced breakdown spectroscopy (LIBS) is considered one of the promising methods [1]. Giant-pulse microchip laser (MCL) is compact with high peak power of MW level [2]. Since the feature is suitable for LIBS application, it was applied to remote LIBS system, where MCL is set close to the target and bright plasma is generated by direct laser irradiation with the reduced risk of the fiber damage. Based on this innovative system, effective remote inspection system is expected. However, radiation effects to optical properties and laser operation needs to be investigated considering their influences in the radiation environment. For the application of the MCL in radiation environments, influences of the laser medium by the radiation need to be studied.

In this study, properties of the laser system using a monolithic Nd:YAG/Cr:YAG ceramics composite were measured, and the influences of high dose irradiation were investigated with gamma ray up to 10^4 Gy/h for the application in severe radiation environment.

Radiation effects were measured for a monolithic Nd:YAG/Cr:YAG composite ceramics (Konoshima Chemical Inc.), where Nd:YAG is a gain medium (Nd dopant 1.1%) and Cr:YAG is a saturable absorber (initial transmittance 30%) with a dimension of 3.0 × 3.0 × 10.0 (L) mm (Nd:YAG 8.2 mm, Cr:YAG 1.8 mm). The YAG composite was set in a holder in an irradiation area at the ^{60}Co gamma irradiation facility number-1 at QST Takasaki. The composite was irradiated with gamma ray (1.173 MeV, 1.333 MeV) using ^{60}Co source in atmosphere at room temperature. In this experiment, dose rate was increased step by step from 0 to 10^4 Gy/h by approaching the composite to the radiation source and changing the distance.

Figure 1 shows minimum Laser diode (LD) current required to start to oscillate the MCL at the LD duration of 500 μs. The threshold was estimated by apparent increase of laser output power measured with the power meter. By the increase of radiation dose rate up to 10000 Gy/h, the threshold current increased for about 5.6 A (corresponding to LD power of about 4.6 mJ), showing that MCL required more LD current for oscillation by radiation effect. The laser output power and slope efficiency also decreased by the increase of radiation dose rate.

The results suggest that optical loss in the cavity increased by radiation. On the other hand, the influences of the radiation to laser operation were fully recovered after exposure within 2 days at longest within this cumulative dose range. Therefore, it is expected that the quick and complete recovery will facilitate the repeated usage of the composite in severe radiation environment. We plan to evaluate the relation between the laser oscillation and the absorbed dose in the next experiment.

Acknowledgement

References

[1] M. Saeki et al., J. Nucl. Sci. Technol., **51**, 930-938 (2014).
[2] H. Sakai et al., Opt. Express **16**, 19891–19899 (2008).
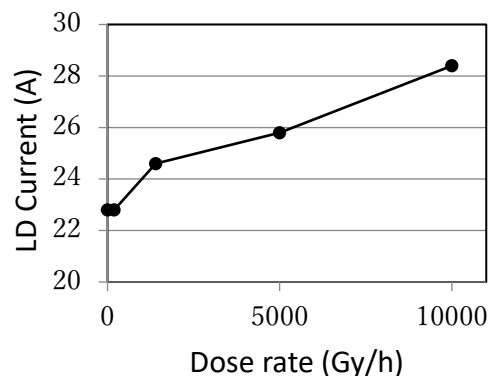
Fig. 1. LD pump current required to oscillate Nd:YAG/Cr:YAG microchip composite at LD pump duration of 500 μs by gamma-ray irradiation for the dose rate from 0.19 to 10 kGy/h.

1 - 16   Solvent-induced Morphological Control of a Poly(ether ether ketone) Film for Acceleration of Radiation-induced Graft Polymerization

S. Hasegawa [a)], A. Hiroki [a)], Y. Zhao [a)], K. Yoshimura [a)], K. Ohwada [b)], A. Machida [b)], T. Watanuki [b)] and Y. Maekawa [a)]

[a)] Department of Advanced Functional Material Research, TARRI, QST,
[b)] Synchrotron Radiation Research Center, KPSI, QST

Radiation-induced graft polymerization is a useful technique for introducing new functional polymers into polymer substrates, and advantageously work the development of fuel cell membrane [1]. From the viewpoint of industrial use, quickly reaching the target grafting degree is a very important matter in the graft polymerization.

We previously reported that the graft polymerization in poly(ether ether ketone) (PEEK) beforehand immersed in a divinyl benzene (DVB) / 1,4-dioxane (DOX) 50/50 vol.% solution at 50 °C for 18 hours was accelerated to exhibit high grafting degrees [2]. The graft polymerization on the PEEK film, however, is almost blocked by the 14 nm lamellar structure that occurs in the film with a crystallinity of 25% or more formed by thermal annealing as same as PEEK with the crystallinity of 32% (h-PEEK) [3]. So far, it has been considered that the acceleration of this reaction is owing to the remained double bond of DVB. However, the same acceleration was newly found on PEEK membrane immersed into DOX without vinyl group to reach high grafting degrees. Therefore, we investigated the change in a morphology of PEEK by solvent immersion to understand the acceleration factor of graft polymerization.

l-PEEK films of 16 μm thickness with the crystallinity of 11% (Victrex Inc.) were immersed in DVB and DOX solution at 50 ºC for 24 hours and then vacuum at room temperature for 24 hours. The obtained films were irradiated with γ-rays at 150 kGy, and then immersed into the DOX solution of 50 wt% ethyl styrene sulfonate (ETSS) at 80 °C to obtain ETSS-grafted PEEK films (Fig. 1).

Grafting degrees (*GDs*) of ETSS in the PEEK films were plotted in Fig. 2. GDs in pretreated PEEK films reached about 100% for 24 hours regardless of immersion solvents, which were higher than that in untreated films. The

acceleration of the graft polymerization was considered due to a morphological change of PEEK by the immersion, because even DOX without vinyl group showed the same accelerated reaction. Then, the morphological change of PEEK after solvent immersion was observed by small-angle X-ray scattering (SAXS) at BL22 of SPring-8. Q-IQ curves of SAXS measurements for the pretreated PEEK films are shown in Fig. 3. The untreated l-PEEK film has no lamellar structure. The PEEK films treated in DOX and DVB have 8-9 nm lamellar structure. Consequently, it was found that the 8-9 nm lamellar structure formed only by the solvent immersion treatment enhances the graft polymerization of ETSS.
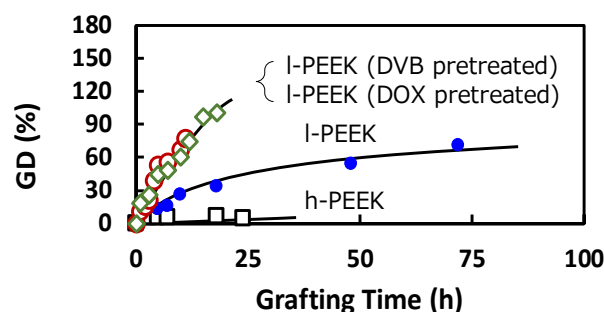
Fig. 2. Plots of *GD*s of ETSS-grafted PEEK films as a function of reaction time: (●) l-PEEK, (□) h-PEEK, (○) l-PEEK (DVB pretreated), (◇) l-PEEK (DOX pretreated), respectively.
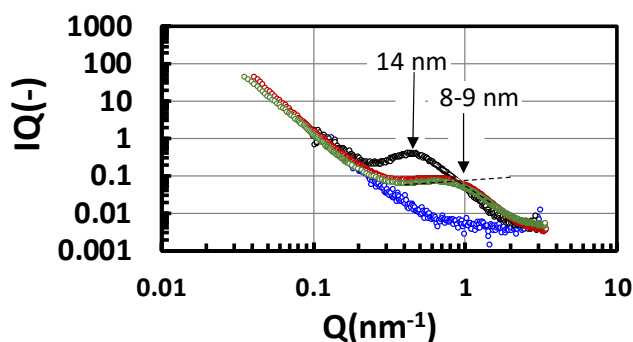
Fig. 3. SAXS profiles of PEEK films with pretreatment: h-PEEK (black), l-PEEK (blue), DVB immersion (green), and DOX immersion (red).

Fig. 1. Synthetic scheme of ETSS-grafted PEEK films by radiation-induced graft polymerizations.

References
[1] T. Hamada *et al.*, J. Mater. Chem. A, **3**, 20983(2015).
[2] J. Chen *et al.*, J. Membr. Sci. **344**, 266(2009).
[3] S. Hasegawa *et al.*, Polymer, **54**, 2895(2013).

1 - 17   Interplay Between Morphology and Anion Transport Behavior in Imidazolium-Based Radiation Grafted Anion Conducting Polymer Electrolyte Membranes

Y. Zhao [a)], K. Yoshimura [a)], A. Hiroki [a)], H. Shishitani [b)],
S. Yamaguchi [b)] and Y. Maekawa [a)]

[a)] Department of Advanced Functional Materials Research, TARRI, QST,
[b)] Daihatsu Motor Co., Ltd.

Anion-conducting polymer electrolyte membranes (AEMs) represent a new disruptive technology for low-temperature fuel cells that could potentially eliminate the main cost barriers of conventional proton exchange membrane (PEM) fuel cells. However, the performance of AEM fuel cells is not as good as that of PEM ones, especially due to their low chemical stability in alkaline conditions; to date, the knowledge about AEM materials, including molecular design, hierarchical structures of the membranes, and morphology/properties relationship, is still limited. Recently, we developed new series of AEMs composed of 2-methyl-N-vinylimidazole (Im) and styrene (St). The AEMs with various Im/St ratios (6/4, 4/6, and 3/7) grafted onto poly(ethylene-co-tetrafluoroethylene) films (named AEM64, AEM46, and AEM37) werer prepared by a radiation induced grafting method with a dose of 80 kGy from a ^{60}Co γ-ray source at room temperature [1]. These AEMs exhibit well-balanced properties of high ion conductivity (> 100 mS/cm in OH$^-$ form) and good alkaline stability. In our previous work, we reported the detailed hierarchical structures of these AEMs using small angle scattering method [1]. Here, in this work, we correlate anion transport properties with their microscopic structures.

The anion transport properties were evaluated based on the transport efficiency defined as a ratio of anion diffusion coefficients in AEMs to dilution solutions (D/D_0) as shown in Fig. 1. We found that D/D_0 of AEM64 normalized by hydration numbers (n_w) was independent on a grafting degree (GD) and anion species because of the similar structures in the homogeneous conducting phase [1]. However, D/D_0 values for AEM46 and AEM37, showed two tendencies depending on hydration conditions. At low hydration levels, the values located onto the same master curve of AEM64, indicating similar anion transports behaviors. At high hydration levels, they were lower than those of AEM64. This deviation at high hydration levels can be explained by the morphological transition from a homogeneous conducting phase to a heterogeneous phase as shown in Fig. 2 [1]. The anion transport through the heterogeneous phase is suppressed [2].

The ion transport mechanisms through polymer membranes in fuel cells is of great scientific interest. This work reveals mechanistic details about the ion transport during the micro-phase transition. In particular, the ion transport at high and low hydration levels is of significance and relevant in order to establish improved design rules for fuel cell membranes. A guideline to improve the design is practically provided in Fig. 2. In the case of homogeneous conducting phase, a simple increase in the connectivity of the ion channels by increasing the hydration level is a good way to enhance the ion transport ability; however, if the morphology changes from a homogeneous to a heterogeneous phase, the ion transport ability will be suppressed at high hydration conditions.
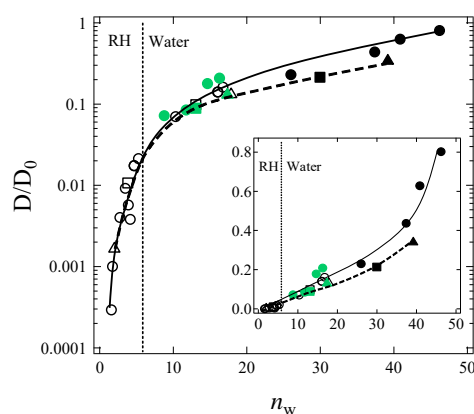
Fig. 1. D/D_0 as a function of n_w for AEM64 (circles), AEM46 (squares), and AEM37 (triangles). Counter anions are Cl$^-$ (opened), HCO$_3^-$ (shaded), and OH$^-$ (filled). The inset is the corresponding linear plot.
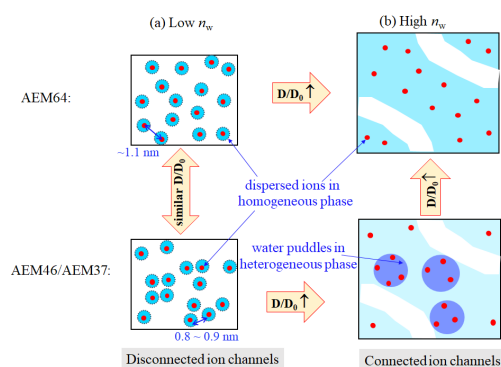
Fig. 2. Schematic illustration of the structures in AEMs.

References

[1] K. Yoshimura *et al.*, Soft Matter, **12**, 1567 (2018).
[2] Y. Zhao *et al.*, J. Electrochem. Soc., **166(8)**, F472 (2019).

1 - 18　　Synthesis of Polysaccharide Hybrid Gel in Ionic Liquids via Radiation-induced Crosslinking

A. Kimura, N. Nagasawa and M. Taguchi

Department of Advanced Functional Materials Research, TARRI, QST

Natural polysaccharides have been recognized to be the most promising materials because of outstanding properties such as high biocompatibility and biodegradability, and procurability from animals and plants on the Earth. Some polysaccharides are, however, radiation degradation type polymers and have poor solubility in water and organic solvents as well as low chemical reactivity. These limitations could be circumvented by use of specific solvents such as room temperature ionic liquids (RTILs). Carboxylate-based RTILs, in particular, have high proton-accepting ability and can cleave the hydrogen bonds of polysaccharide main chains to form solution in the concentration range of 0.1-20 wt.%. Recently, we reported the first synthesis of polysaccharide chemical gels, conducted in the absence of any crosslinking reagents, using ionizing radiation in carboxylate-based RTILs [1]. However, the maximum formation yields, which are expressed as gel fractions, of the cellulose and chitosan gels produced using this methodology were less than 15% as shown by broken lines in Fig. 1. Furthermore, their mechanical properties were too low to measure and insufficient for practical use as soft gel electrodes. In an attempt to improve their production yields and mechanical properties, the production of polysaccharide hybrid gels was investigated in RTILs by using ionizing radiation.

Cellulose and chitosan powders were dissolved in 1-ethyl-3-methylimidazolium (EMI)-acetate using a hybrid mixer. The water content in the solution was controlled by changing the humidity level in the surrounding air. The solutions were irradiated using a ^{60}Co γ-ray source in the dose range of 5–100 kGy (Gy = J kg^{-1}). The formation yields of the hybrid gels were evaluated after washing with acetic acid, lithium chloride in *N, N*-dimethylacetamide, and then EMI-acetate as shown by solid line in Fig. 1 [2]. The obtained hybrid gel was a chemical gel and the mechanical properties were improved compared to each individual polysaccharide gel. The swelling ratio and elasticity of the hybrid gel reached maximum values of 16 g g^{-1} and 25 kPa, respectively. The biodegradability of the hybrid gel was slightly lower than that of chitosan, yet higher than that of cellulose. The hybrid gel was stable for 180 min at 393 K, which is the upper limit temperature of heat resistance of soft gel actuators. The electronic conductivity of the hybrid gel, swollen in EMI-acetate at 298 K, was found to be 3.3 mS cm^{-1}. This value is higher than that (0.1 mS cm^{-1}) of typical organic solid electrolytes. Thus, the hybrid gel is practically suitable as a bioelectrode. The displacement of the hybrid gel increased to 30 μm with an electronic voltage of up to 2 V. The curvature of the

hybrid gel was 0.09 m^{-1} V^{-1} and was stable for 30 min (Fig. 2). The obtained cellulose/chitosan hybrid gel displayed favorable properties such as high degree of solvent swelling, sufficient elasticity, biodegradability, thermal stability, and high electronic conductivity, and is expected to be of use in bio-devices and soft actuators in the near future.
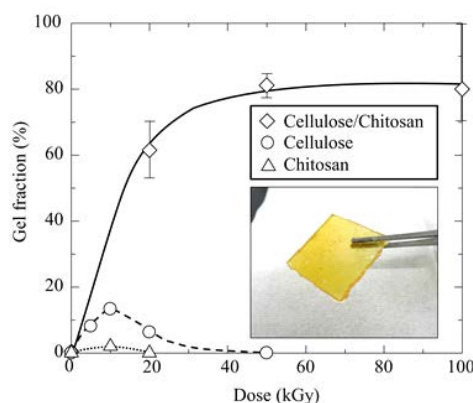
Fig. 1. Gel fraction of 1-ethyl-3-methylimidazolium (EMI)-acetate solution of 5 wt.% cellulose with 5 wt.% chitosan (diamond) mixture, 20 wt.% cellulose (circle), and 20 wt.% chitosan (triangle) as a function of absorbed dose. Inset: Photograph of cellulose/chitosan hybrid gel swollen with EMI-acetate at 100 kGy.
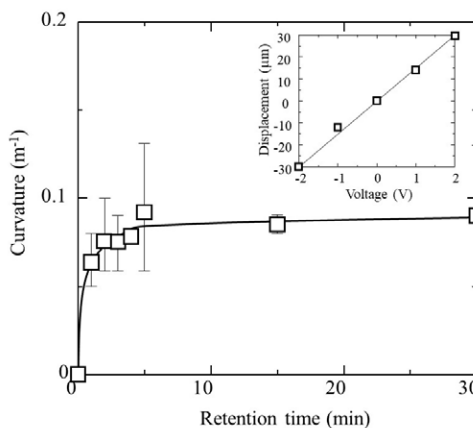
Fig. 2. Curvature of hybrid gel mixture of 5 wt.% cellulose and 5 wt.% chitosan in 1-ethyl-3-methylimidazolium-acetate as a function of retention time at an electronic voltage of 1 V. Inset: Displacement of cellulose/chitosan hybrid gel by response of electronic voltage of up to 2 V.

References
[1] A. Kimura *et al.*, Radiat. Phys. Chem., **124**, 130–134 (2016).
[2] A. Kimura *et al.*, Polym. Degrad. Stab., **159**, 133-138 (2019).

1 - 19　　Synthesis of Fibrous Grafted Metal Adsorbent Having Piperazinyl-Dithiocarbamate Group

Y. Ueki and N. Seko

Department of Advanced Functional Materials Research, TARRI, QST

Radiation-induced grafting, one of the surface modification techniques of polymers, can impart desired functional groups into trunk polymers without deteriorating their physical and chemical properties. This technique was applied to the synthesis of a novel high-performance adsorbent. Especially, when a glycidyl methacrylate (GMA) is used as a grafting monomer, various functional groups could be easily introduced onto the trunk polymers through the epoxy ring opening reaction of GMA-grafted chains. In our previous study, a fibrous grafted metal adsorbent having piperazinyl-dithiocarbamate (PZ-DTC) group was synthesized by radiation-induced emulsion grafting followed by two-step chemical modification with piperazine (PZ) and carbon disulfide (CS_2) [1]. However, the fibrous grafted metal adsorbent synthesized by the above synthesis method had a low PZ-DTC group density and did not have practically sufficient performance as a metal adsorbent. The reason for the low PZ-DTC group density was that the majority of PZ introduced onto the GMA-grafted chains were self-crosslinked. The objectives of this study were to completely prevent the self-crosslinking of PZ and to synthesize a fibrous grafted metal adsorbent having a practically sufficient amount of PZ-DTC groups.

As shown in Fig. 1, the fibrous grafted metal adsorbent having PZ-DTC group was synthesized by radiation-induced emulsion grafting with GMA followed by three-step chemical modification such as amination with N-Boc-piperazine (NBPZ), deprotection of Boc with HCl and dithiocarbamation with CS_2. Polyethylene nonwoven (PENW) fabric, of which the fiber diameter was 13 μm, was used as a trunk polymer. Firstly, the PENW fabric was irradiated with an electron beam (20 kGy) using a low energy electron accelerator. Then, the irradiated PENW fabric grafted with a deaerated GMA emulsion (5 wt% GMA / 0.5 wt% Tween20 / 94.5 wt% H_2O) for 1 h at 40 °C. After grafting, the GMA-grafted fabric was aminated with 0.25 M NBPZ aqueous solution for 4 h at 80 °C, and then treated with 1 M HCl aqueous solution for 2 h at 80 °C, to deprotect the Boc group functioning as a protecting group of NBPZ. Finally, the Boc-deprotected sample was further treated with CS_2 solution (20 wt% CS_2 / 35 wt% 10 M NaOH aqueous solution / 45 wt% methanol) for 24 h at 40 °C, to introduce DTC group at the terminal nitrogen on PZ group. The DTC group containing two sulfur atoms acts as a bidentate chelating ligand through sulfur atoms.

By using NBPZ as an amination reagent, the self-crosslinking of PZ could be completely prevented, because the NBPZ had only one NH group which could contribute to the amination. The effect of amination time on the degree of amination was investigated, and it was found that the amination of using NBPZ proceeded smoothly and quickly, and it was completely finished within only 1 h. The Boc groups of NBPZ never cleaved even after 24 h, since this amination process was carried out under a basic condition at pH 10.5, and, consequently, the self-crosslinking reaction via PZ did not occur at all.

To introduce DTC group onto the NBPZ group, the Boc group of NBPZ must be deprotected. So, the effect of deprotection temperature and time on the degree of deprotection were investigated. As expected, higher deprotection temperatures led to faster deprotection of the Boc group. At 80 °C, the required time to complete deprotection was only 1 h, which is less than one sixth of the time required at 50 °C. In addition, in this Boc-deprotection process, the self-crosslinking reaction of PZ did not occur after deprotection, because there was no epoxy group capable of reacting with the terminal NH groups of Boc-deprotected NBPZ.

After CS_2 treatment, the PZ-DTC density of fibrous grafted metal adsorbent synthesized via NBPZ reached 2.122 mmol-PZ-DTC/g-ad. This value became about 21 times higher than that of the metal adsorbent synthesized via PZ. The Pb adsorption capacity of fibrous grafted metal adsorbent synthesized via NBPZ was 1.06 mmol-Pb/g-ad., and this value was a sufficient capacity for the practical use as the metal adsorbent.
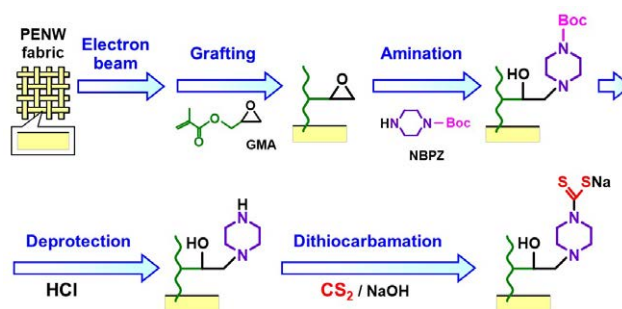
Fig. 1. Synthesis schemes of the fibrous grafted metal adsorbent.

Reference

[1] Y. Ueki *et al.*, QST Takasaki Annu. Rep. 2017, **QST-M-16**, 56 (2019).

1 - 20   A Simplified Radiation-Induced Emulsion Graft Polymerization Method

M. Omichi, Y. Ueki, N. Seko and Y. Maekawa

Department of Advanced Functional Materials Research, TARRI, QST

An emulsion graft polymerization method is remarkable in that it required a lower radiation dose, a decreased monomer concentration, and a shorter reaction period than the normal graft polymerization process, which uses organic solvents. The monomer solution is emulsified by the surfactant in an aqueous system instead of in an organic solvent. Although the densely grafted product cannot be fabricated by the normal method at low-dose pre-irradiation, the emulsion graft polymerization method can achieve a sufficient degree of grafting even when a low total dose of 10 kGy irradiation is used. However, the method has the disadvantage of foaming because the monomer solution contains a surfactant. Especially, at low dose irradiation, dissolved oxygen in the monomer solution had much effect on the graft reaction.

To solve the problem concerning the dissolved oxygen, we developed the simplified radiation-induced emulsion graft polymerization (SREG) method without using a gas/vacuum manifold as follows (Fig. 1). (1) The pre-irradiated Polypropylene/Polyethylene (PP/PE) fabric was set in the commercially available sealed glass jar, made up of the glass lid, the rubber packing, and the jar itself. At ambient atmosphere, the de-aerated monomer emulsion was poured into the glass jar with nitrogen bubbling and then sealed. (2) After the lid was closed, a weight was placed on top of the sealed gas jar, and degassing of the monomer solution was carried out in a vacuum desiccator. (3) On releasing the desiccator's vacuum, the loaded weight causes a pressure difference between the internal and external pressures. This pressure difference prevents atmospheric oxygen from re-entering the monomer solution. (4) The sealed glass jar was then held at a constant temperature in a water bath, and the graft reaction proceeded without oxygen. A loaded weight on the lid of the jar was used to control the jar's internal pressure as degassing of the monomer solution took place using a vacuum pump. This method of degassing was highly reproducible, and bumping of the monomer solution did not occur.

Graft polymerizations of glycidyl methacrylate (GMA) monomers to PP/PE fabrics, irradiated at a dose range of 5 - 20 kGy were carried out using the SREG method. The monomer emulsion of 5 wt% GMA was prepared by adding GMA to a 0.5 wt% Tween 20 aqueous solution that was then stirred at room temperature for 5 min. After bubbling with nitrogen to displace dissolved oxygen in the GMA emulsion, 120 mL of the de-aerated GMA emulsion was poured into a sealed glass jar (WE-975, Weck, Germany) that contained the irradiated PP/PE fabric. The lid was closed, and a weight of 400 g was placed on the sealed

jar's lid. The 400 g weight (the total weight, including the lid, was 445 g, area 28.3 cm^2), corresponding to 1540 Pa, was chosen. When the pressure in the desiccator reached 2700 Pa, degassing in the monomer solution visibly started. Vigorous degassing was observed at 2000 Pa, and the pressure in the sealed glass jar was estimated to be around 3540 Pa, which is the sum of the pressure of the loaded weight (1540 Pa) and the pressure in the desiccator (2000 Pa). This value is reasonable considering that degassing effectively occurs at just above the vapor pressure of water. After the initial vigorous degassing, the speed slowed down, and discernible degassing was no longer observed; however, the process was allowed to continue for a further 15 min to ensure that as much dissolved oxygen as possible was removed. The degassing process was highly reproducible, and bumping of the monomer solution containing the surfactant (Tween 20) did not occur, even though the pressure of the vacuum pump was not regulated. After vacuum degassing, the grafting reaction was carried out by keeping the sealed glass jar in a 40 °C water bath for 1-3 hour.

As a result, even at a dose as low as 5 kGy, the graft reaction proceeded and the degree of grafting obtained had very high reproducibility. The initial velocity was 4.2, 2.0, and 1.1 %/min at 20, 10, and 5 kGy, and proportional to the dose of pre-irradiation. This result indicated that oxygen was eliminated sufficiently from the monomer solution so that still remaining those had little effect on the graft reaction at 5 kGy. The SREG method is expected to be applicable to a wide variety of applications because high-dose-rate gamma-ray radiation and expensive experimental equipment such as gas/vacuum manifold are not necessary.
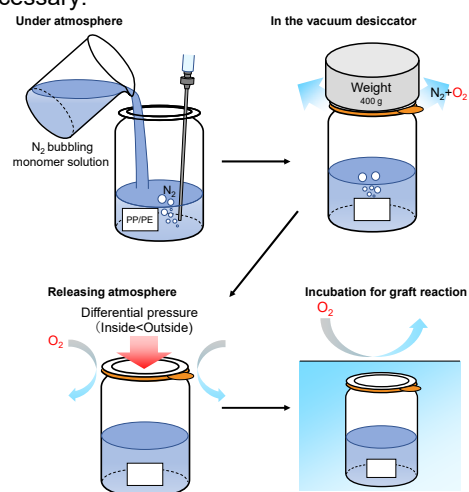
Fig. 1. Schematic image of a simplified radiation-induced emulsion graft polymerization (SREG).

1 - 21   Cleavage and Characterization of Graft Chains of the PVDF-g-St Films Prepared by Radiation Grafting

J. Chen, N. Kasai, Y. Ueki, H. Hoshina, M. Omichi and N. Seko

Department of Advanced Functional Materials Research, TARRI, QST

Radiation-induced graft polymerization can introduce the graft chains not only on the surface but also in the interior of solid materials, since the radiation can penetrate throughout the materials, thereby allowing a more uniform of radicals. Although the molecular weight of the graft chains is an important parameter that affects the properties of the grafted materials, it has rarely been studied. This is due to the difficult cleavage of the covalent graft bonds. In our previous study [1], chloromethylstyrene-grafted poly(ethylene-co- tetrafluoroethylene) (ETFE-g-CMS) films were immersed in xylene at 120 °C for more than 44 h and considerable amount of poly(CMS) were separated. However, it was difficult to confirm whether the obtained poly(CMS) stemmed from the graft chains having chemical bonds with the ETFE backbones or from homopolymer interpenetrated into the ETFE backbones.

In this study, we aimed to investigate the cleavage of the graft chains from grafted films using poly(vinylidene difluoride) (PVDF) as the backbones and polystyrene as the graft chains, from which styrene-grafted PVDF (PVDF-g-St) films were prepared via a pre-irradiation grafting method. Unlike the ETFE films, the PVDF films are soluble in polar aprotic solvents such as dimethylformamide (DMF) for molecular weight analysis. Herein, we describe the successful separation of the polystyrene chains from the PVDF-g-St films by boiling xylene extraction.

As shown in Fig. 1, the NMR spectrum of the starting PVDF-g-St film shows peaks around 6.5-7.5 and 1.3-2.6 ppm, which can be attributed to the aromatic protons and the protons of the CH_2CH aliphatic groups of polystyrene, respectively. In addition, peaks at 3.10 and 2.43 ppm can be assigned to the head-to-tail and head-to-head configurations of PVDF. For the extracted material obtained from the extraction solution, only the peaks assigned to polystyrene and to the impurities are observed. Therefore, it can be concluded that polystyrene was extracted from the grafted film, whereas the PVDF remained in the film during the extraction. In contrast, for the spectrum of the 72 h-extracted residual film, the peaks for the polystyrene almost disappear, whereas those for PVDF are present. These results prove that the polystyrene graft chains were cleaved from the grafted film during the extraction and dissolved into the solvent. Furthermore, most of the polystyrene, with or without graft bonds, was removed from grafted film under the xylene extraction, indicating that the polystyrene and PVDF could be well separated.

After confirming that the extracted materials were composed of polystyrene graft chains by NMR spectroscopy, the molecular weights of the graft chains, the pristine PVDF film, the starting PVDF-g-St film, and the polystyrene homopolymer were analyzed by GPC instrument and the results were presented in Table 1. The M_n and M_w of the pristine PVDF film were 284 and 460 kDa, respectively. After graft polymerization, the M_n and M_w of PVDF-g-St significantly increased to 996 and 1,979 kDa, respectively. On the other hand, the M_n and M_w of the polystyrene graft chains were 363 and 976 kDa, respectively. Therefore, the molecular weight of the polystyrene graft chains is of the same order of magnitude as that of the PVDF backbones, and each PVDF-g-St chain can be envisioned as one or two polystyrene graft chains hanging from the PVDF backbone, forming a T- or TT-type structure.
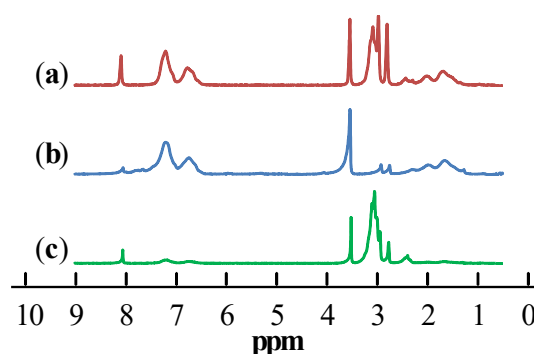
Fig. 1. 1H NMR of (a) starting PVDF-g-St film, (b) extracted material, and (c) 72 h-extracted residual film.

Table 1
Molecular weights of the pristine PVDF, starting PVDF-g-St, polystyrene graft chains, and the homopolymer.

Materials	M_n (kDa)	M_w (kDa)	PDI (Mw/Mn)
PVDF	284	460	1.62
PVDF-g-St	996	1,979	1.99
Graft chain	363	976	2.69
Homopolymer	250	487	1.95

Reference
[1] J. Chen *et al.*, Polymers, **9**, 307 (2017).

1 - 22　Properties of Surface Crosslinked Silicone Rubber Synthesized by Electron Beam Irradiation

T. Makabe [a)], M. Oshida [a)], H. Sando [a)], Y. Ueki [b)] and N. Seko [b)]

[a)] Mitsuba Corporation,
[b)] Advanced Functional Materials Research Division, TARRI, QST

Surface crosslinked silicone rubber was synthesized by radiation-induced crosslinking technique using an electron beam. With increasing irradiation dose, the swelling rate of the surface crosslinked silicone rubber decreased, but its surface hardness increased. This is due to the influence of the crosslinked structure newly formed in the rubber surface layer by the electron beam. As a particularly excellent property, the surface crosslinked layer had an effect of suppressing surface bleeding with respect to low molecular weight compounds present inside the rubber. As a result, the glass surface-water contact angle of the surface crosslinked silicone rubber having the bleed suppression effect was lower than that of un-crosslinked one.

　我々はこれまでに、放射線グラフト重合法を活用したゴム表面改質に関する研究に取り組み、低摩擦係数を示す表面親水化エチレン-プロピレン-ジエンゴム（EPDMゴム）の開発に成功してきた[1]。シリコーンゴムはゴムの中でも耐熱性、耐候性など優れた多くの特性をもつことから、航空宇宙産業から家庭用品に至るまで幅広い分野で利用されている。しかし、従来のシリコーンゴムでは、ゴム内部の低分子成分がゴム表面に滲み出やすく、その滲出成分が他部材を汚染することが問題となっている。本研究では、シリコーンゴムからの滲出成分制御を目的とし、電子線架橋技術により形成した表面架橋層の効果について検証した。

　本研究では、予め熱架橋処理を施したシリコーンゴムシートに対し、電子線を照射することにより、ゴム表面層に新たに電子線由来の架橋構造（表面架橋層）を有する表面架橋型シリコーンゴムを作製した。

　表面架橋型シリコーンゴムの膨潤率は n-ヘキサン浸漬試験により評価し、また、ゴム表面硬度はデュロメーターA 硬度計により評価した。Figure 1 に電子線照射線量が及ぼすシリコーンゴムの膨潤率、及び、ゴム表面硬度への影響を示す。照射線量の増加に伴い、膨潤率は低下し、その一方で、表面硬度は向上した。これは、ゴム表面層に形成された表面架橋層の効果によるもので

あり、照射線量が増加するにつれて表面架橋層の架橋密度が向上したためである。また、電子線の加速電圧を変化させることにより、表面架橋層の厚みを自在に制御可能であった。特に、電子線の浸透深さが 100 µm 程度となる加速電圧 90 keV の電子線を用いた場合では、ゴム内部が柔らかく、表面が硬い新規シリコーンゴムを創製することに成功した。

　表面架橋層による滲出成分抑制効果は、シリコーンゴムをガラス面に圧着させた後、ガラス面-水の接触角を測定することにより評価した。未照射シリコーンゴムでは、滲出成分抑制効果が乏しいため接触角は 72°と大きな値を示した。一方、表面架橋型シリコーンゴムでは 55°となり、接触角を大幅に低減することに成功した（Fig. 2）。これは、高架橋密度の表面架橋層が防漏フィルターとして機能したためであり、表面架橋層には滲出成分抑制効果があることが実証された。しかしながら、滲出成分抑制効果には照射線量依存性があるものの、照射線量 500 kGy 以上においては、その効果は殆ど向上しないことがわかった。

Reference
[1] N. Mizote *et al.*, J. Appl. Polym. Sci., **123**, 2172-2176 (2012).
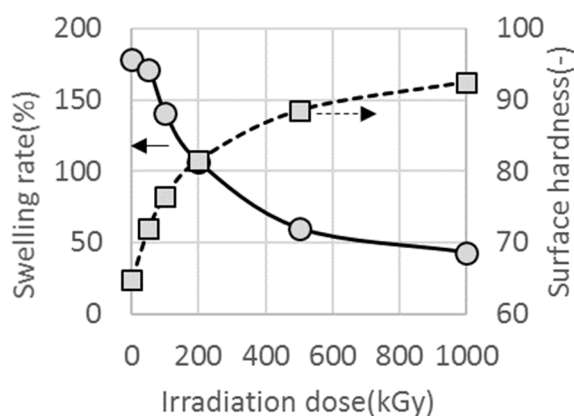
Fig. 1. Effect of irradiation dose on swelling rate and surface hardness of surface crosslinked silicone rubber.
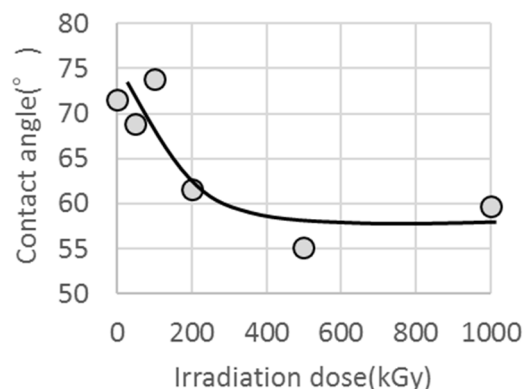
Fig. 2. Effect of irradiation dose on the glass surface-water contact angle of surface crosslinked silicone rubber.

1 - 23   Evaluation of New HBC Stripper Foil in J-PARC RCS

M. Yoshimoto [a)], T. Nakanoya [a)], Y. Yamazaki [a)], P.K. Saha [a)], M. Kinsho [a)],
S. Yamamoto [b)], H. Okazaki [b)], T. Taguchi [c)], N. Yamada [d)] and R. Yamagata [d)]

[a)] Accelerator Division, J-PARC center, JAEA,
[b)] Department of Advanced Functional Materials Research, TARRI, QST,
[c)] Tokai Quantum Beam Science Center, TARRI, QST,
[d)] Department of Advanced Radiation Technology, TARRI, QST

In the high intensity proton accelerator, the multi-turn charge-exchange H- beam injection scheme with stripper foils was adopted. The performance of the stripper foils is one key issue for stable operation of the accelerator. In the J-PARC RCS, Hybrid type Boron-doped Carbon (HBC) stripper foil, which was developed in KEK to improve the lifetime [1], has been mainly used since early beam commissioning in 2007 [2]. Recently, the deposition apparatus for the HBC foils from the KEK Tsukuba-site was relocated to the JAEA Tokai-site, and we started fabrication of new HBC foil in 2017. The new one fabricated in JAEA we call J-HBC foil. The performance of the original HBC foil had been evaluated previously using the ion beams in TIARA [3]. J-HBC foil was also evaluated to compare with the original one before using in the RCS.

HBC foils were analysed by the major elemental composition obtained from RBS method employing proton beam of 3 MV in the TIARA 3-MVsingle-ended accelerator. Figure 1 shows the RBS spectra compared between the original-HBC and the J-HBC foil and ratio of the atomic composition in the foils. The boron to carbon ratio is almost same, but the oxygen dosage was significantly decreased in the J-HBC foil.

Impurities in the foil, especially high-Z material, become the source of the large angle beam scattering and generate the radionuclide in the foil. Figure 2 shows the micro-PIXE spectra of the original-HBC and the J-HBC foil and typical impurities in the foil. Same elements were identified in both foils. But, in the J-HBC foil, the trace impurities can be reduced drastically as compared with the original-HBC foil.

To investigate the endurance against the beam irradiation, argon ion beam irradiation tests were carried out in the TIARA 400-kV ion implanter. In this test, Ar^+ beam of 300 kV were irradiated on the foil. After the J-HBC foil was irradiated for 30 minutes, in which the beam size is 4 mm in diameter and the beam current is 50 nA, the surface structure was changed but the foil was not broken. Figure 3 shows the foil surface after the beam irradiation observed by the digital microscope. The irradiation spot was flattened. The surrounds were shrinking and waving but surface structures didn't affect. This transition of the surface structure was the same as the original HBC foils.

The series of evaluation tests of the J-HBC foils in the TIARA confirmed the performance as the original HBC foil. After that, the J-HBC foil was successfully demonstrated to use for the RCS user operation.
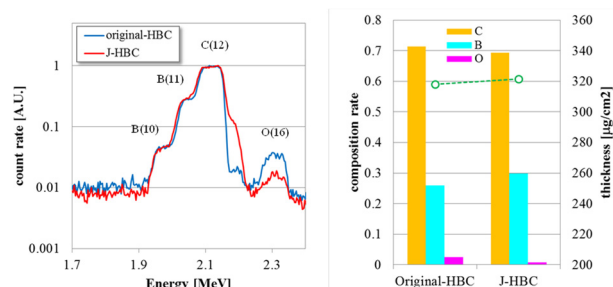
Fig. 1. RBS spectra of original-HBC and J-HBC foil (left) and atomic composition ratio in the foil (right).
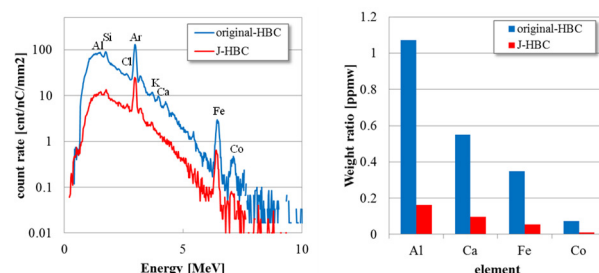
Fig. 2. PIXE spectra of original-HBC and J-HBC foil (left) and typical impurities in the foil (right).
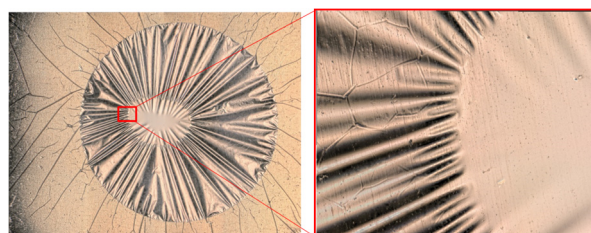
Fig. 3. Surface structure of the J-HBC foil after Ar^+ beam irradiation as observed by a digital microscope.

References
[1] I. Sugai *et al.*, NIM A**561**, pp.16-23 (2006).
[2] M. Yoshimoto *et al.*, J. Phys.: Conf. Ser. **417**, 012073 (2013).
[3] Y. Yamazaki *et al.*, JRNC, **3**, 305, pp.859-864 (2015).

1 - 24 Study of Corrosion Mechanism in Consideration of Surface Excitation Effect Under Gamma-ray Irradiation

H. Ogawa and I. Ioka

Fuels and Materials Engineering Division, NSEC, JAEA

Radiation field makes corrosion of the materials (Zr, SUS, etc.) accelerate. The amount of ions generated by a radiolysis of the water or the steam becomes important as controlling factor of corrosion acceleration. In previous model, the amount of ions formed by gamma-ray radiation, H^+, OH^-, O^- etc., are evaluated conventionally by a G value. In the radiation field, corrosion of the materials is promoted by these ions. However, the increase in corrosion rate at a radiation field can't be explained sufficiently by the evaluation from the G value. So, new corrosion model by the excitation effect of the material's surface was proposed as shown in Fig.1[1]. When gamma-ray was applied to the material surface, a large amount of electrons are formed by the photoelectric effect, Compton effect, pair production. The electrons released from the material surface ionizes the water or steam of the metal surface neighborhood. The water or the steam in the vicinity of material surface is irradiated by direct gamma-ray and the electrons emitted from the metal surface. Therefore, more ions (H^+, OH^-, O^- etc.) are produced at the surface in comparison with a distant place. These ions make the corrosion in the material surface promote. The objective of our research is to clarify corrosion mechanism of materials under the gamma-ray radiation field.

The irradiation was performed at the gamma-ray irradiation facility of Takasaki Advanced Radiation Research Institute of QST. The ^{60}Co gamma-ray absorbed dose rate is 10 kGy/h. An irradiation time was set to 30 or 90 min. Commercial purified water was used in the experiment. The difference in dissociation ratio of the water by the radiolysis was checked using the pH method, the electric conductivity method, the oxidation-reduction potential method. In order to clearly evaluate the influence of a radiolysis of the water, the glass beads were scattered in water to increase reaction surface area.

Figure 2 shows changes in pH, the electric conductivity and the redox potential of the water which scattered glass beads by the gamma-ray irradiation. During the gamma-ray irradiation, pH and the redox potential decreases, and the electric conductivity showed a tendency to increase. After the gamma-ray irradiation, pH and the electric conductivity have not returned to the value before irradiation. It is considered that the hydrogen peroxide and the ozone generated by the radiolysis of the water is one of these causes. However, there was hardly the difference in pH, electric conductivity and redox potential between the purified water and the purified water including glass beads. It was not confirmed that the radiolysis of the water definitely increased by the surface excitation under this test condition. It seems that the reason is not to be able to mix the water sufficiently in the case of glass beads because the radiolysis of the water occurs at the extreme surface of glass beads.

We are planning to improve the experimental method to detect the radiolysis of the purified water correctly.

Reference
[1] H. Ogawa *et al.*, Nucl. Sci. Eng., **152**, 204 (2006).
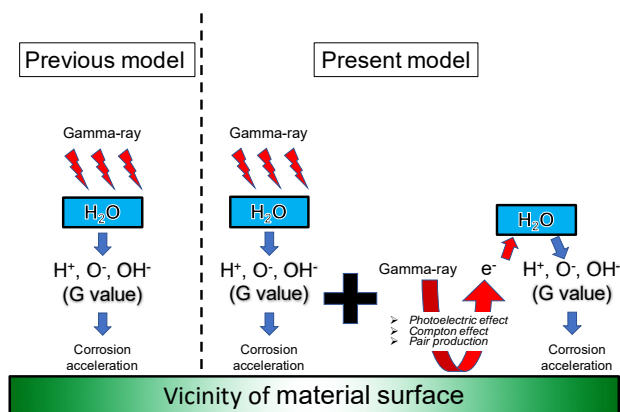
Fig. 1. Proposed new corrosion model by the excitation effect of the material's surface.
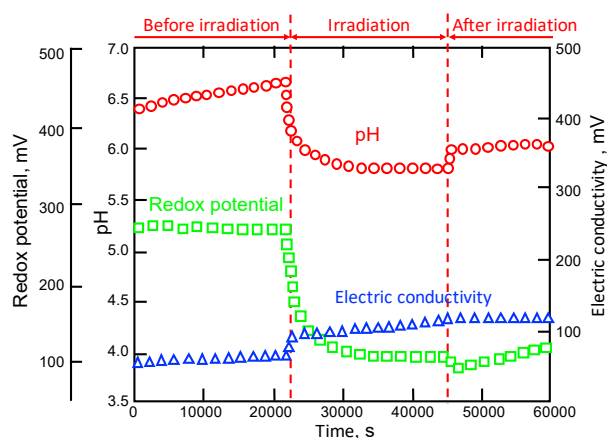
Fig. 2. Changes in pH, the electric conductivity and the redox potential of the water which scattered glass beads by the gamma-ray irradiation.

1 - 25   Study on Fusion Neutron Irradiation Effects Using Multiple Ion-Beam Irradiation

D. Hamaguchi, M. Ando and H. Tanigawa

Department of Fusion Reactor Materials Research, RFI, QST

Reduced activation ferritic/martensitic steels (RAFMs) such as F82H and Eurofer97 are candidates for the blanket structural material for DEMO fusion reactors. Extensive work has shown the neutron irradiation effects in RAFMs but there still remains a lot of uncertainty on details of fusion neutron effects. One of the irradiation features for the blanket structure material is the high-dose and high-energy neutron irradiation that leads to an accumulation of displacement damage along with high levels of He and H production. One of the difficulties in predicting details of the development of this damage under fusion conditions is the lack of neutron irradiation facilities that produce irradiation conditions similar to the fusion reactor environment. Therefore, our approach is to develop information on particular events that are a specific part of the response under fusion neutron irradiation. We do this using existing irradiation facilities. Recently, we have conducted a series of ion irradiation experiments of RAFMs in the temperature ranged 300 to 500 °C for doses ranged from 20 to 80 dpa. These irradiations were mainly conducted at TIARA complex ion-beam irradiation facility using Fe ions with or without He and H co-implantations. We have started post-irradiation examination (PIE) to collect information on dose and temperature dependence of microstructure changes along with irradiation hardening in this temperature and dose range.

The material used in this study was F82H and Eurofer97. F82H includes IEA standard version and three other modified versions (Mod3, BA07, BA12) aimed to improve fracture toughness property under irradiation. The basic chemical composition for IEA is Fe-8Cr-2W-0.2V-0.04Ta-0.1C. For the heat treatment, IEA was normalized at 1040 °C for 0.63 h followed by a tempering at 750 °C for 1 h. The other modified versions have slightly different Ta content and heat treatment conditions. The irradiations were carried out with 10.5 MeV Fe^{3+} ions plus 0.38 MeV H^+ and/or 1.05 MeV He^+ ions. In following explanations, triple-beam refers to Fe plus He and H and dual-beam refers to Fe plus He multiple ion-beam irradiation. In multiple ion-beam irradiation, He and H implantation rate were fixed to be 10 and 40 appm/dpa, respectively.

Figure 1 shows the irradiation matrix achieved so far during the series of irradiation campaign using TIARA facility. Extensive irradiation experiments have been conducted in the temperature ranged from 400 to 500 °C, where cavity growth should become eminent. The irradiation matrix is mostly fulfilled for triple beam irradiation with the temperature in 20 °C incremental steps and the doses in 20 dpa incremental steps up to 80 dpa. On the other hand, the matrix has not been filled for complimentary dual and single beam irradiations. Furthermore, the data points within these matrixes will be achieved only by single irradiation test and therefore the irradiation tests will be continued to acquire another set of data to increase data accuracy as well as to acquire missing data points for dual and single beam irradiations. The PIE campaign has been started and part of the irradiation hardness information has been obtained. Figure 2 shows the hardness changes of F82H-IEA obtained by nano-indentation hardness tests in temperature range from 400 to 500 °C. Here, clear hardenings by Fe-ion irradiation were seen only below 430 °C and tend to show softening above 450 °C along with irradiation doses. In addition, even at 430 °C, irradiation hardening saturates at around 20 dpa and tends to decrease with doses. On the other hand, although clear effect of He co-implantation was not seen at above 450 °C, there shows higher hardening below 430 °C and did not saturate with doses. Clear explanation of the effect of He on this hardening tendency has not been yet made but this may be due to a formation of tiny He bubbles since the bubbles start to become larger above 450 °C, which was confirmed by microstructure observations.
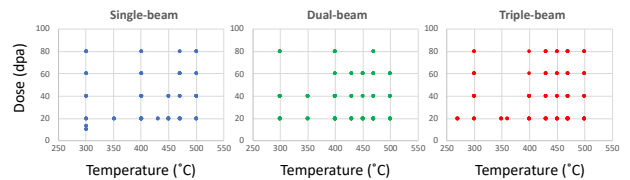
Fig. 1. Irradiation matrix achieved so far using TIARA facility.
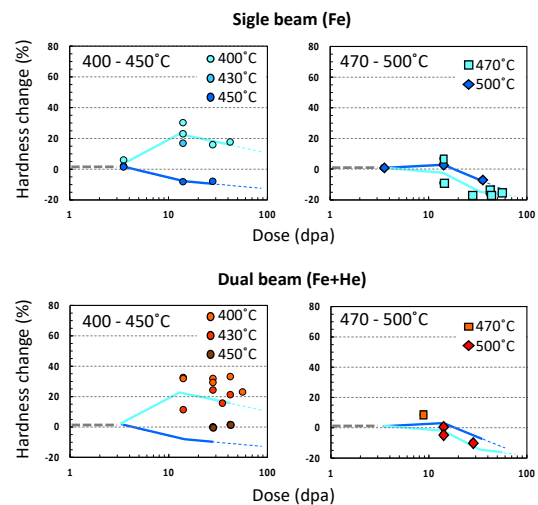
Fig. 2. Hardness changes of F82H-IEA obtained by nano-indentation hardness tests in temperature range from 400 to 500 °C. Blue colored lines indicate the irradiation hardening trends for Fe single-beam irradiation.

1 - 26   Effects of Displacement Damage, Helium and Hydrogen on Electrical Properties of Silicon Carbide

T. Nozawa [a)], M. Ando [a)], D. Hamaguchi [a)], T. Taguchi [b)] and H. Tanigawa [a)]

[a)] Department of Fusion Reactor Materials Research, RFI, QST,
[b)] Tokai Quantum Beam Science Center, TARRI, QST

Silicon carbide (SiC) is a promising candidate material of liquid metal breeding blanket for a fusion DEMO reactor, e.g., functional structure of flow channel inserts for the dual cool blanket system [1], due to superior therm-mechanical properties, chemical inertness, irradiation stability, etc. To realize the liquid metal system, electrical insuration is a key function of SiC. It has been more emphasized that one notable irradiation behavior of SiC was radiation-induced electrical degradation (RIED)-like behavior [2-5]. It was in particular noted that morphological change of the irradiated surface of SiC might affect the RIED-like behavior. However, knowledge about the synergetic effect of displacement damage at higher dose and transmutation He/H effect on RIED was insufficient. This study therefore aims to evaluate the effects of displacement damage with He/H co-irradiation on surface electrical resistivity by single/dual/triple ion beam simulated irradiation.

Chemical vapor deposited (CVD) SiC disk (ϕ3 mm × 50 μm) was irradiated by single (6.0 MeV Si^{2+}, 1.0×10^{-3} dpa/s), dual (single + 1.0 MeV He^+, 130 appm/dpa) and triple (dual + 340 keV H^+, 40 appm/dpa) ion beams to evaluate the effect of transmutation He/H atoms to simulate fusion irradiation environment. The maximum dose was 31 dpa, which was the representative value calculated at the depth of 1.3 μm from the irradiation surface by the SRIM code, and irradiation temperature was ranged in approximately 600–1000 °C. Surface electrical resistivity was compared before and after irradiation at room temperature by the two-probe guard ring AC impedance method. Details of the specimen configuration and the electric circuit for the measurement were described in [6].

Figure 1(a) summarizes the effect of irradiation temperature on surface resistivity of SiC. By irradiation with doses of 10–15 dpa, slight decrease of surface resistivity was obvious but the reduction ratio was almost the same over the wide irradiation temperature range of 600–1000 °C. By contrast, for the high-dose irradiation case (25–31 dpa), considerable reduction of the surface resistivity was marked by irradiation at comparably higher irradiation temperatures (>750 °C). Figure 1(b) shows the dose dependence of the surface resistivity. It tended to decrease with increasing dose and it is worth noting that this trend was more emphasized for higher temperature irradiation cases. For both cases, by considering data scatter for non-irradiated specimen case, it is speculated that the impact of He/H co-irradiation was minor.

In addition to further irradiation experiments, surface morphological change will be evaluated in detail by microstructural observation and other techniques, e.g., X-ray photoelectron spectroscopy (XPS), to identify the key mechanism.
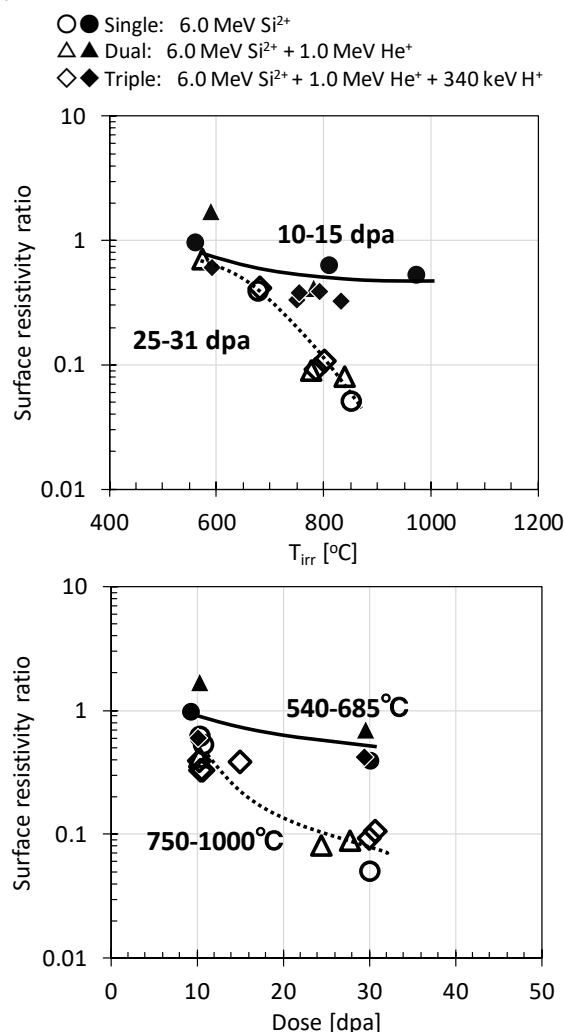
Fig. 1. Surface resistivity ratio (irrad./non-irrad.) of CVD SiC: (a) irradiation temperature dependence and (b) displacement damage dependence. Note that the irradiation temperature was measured by thermography assuming a constant emissivity of 0.8.

References
[1] P. Norajitra *et al.*, Fusion Eng. Des., **69**, 669-673 (2003).
[2] T. Tanaka *et al.*, J. Plasma Fus. Res., **9**, 282-287 (2010).
[3] B. Tsuchiya *et al.*, Fusion Eng. Des., **86**, 2487-2490 (2011).
[4] B. Tsuchiya *et al.*, J. Nucl. Mater., **455**, 645-648 (2014).
[5] B. Tsuchiya *et al.*, J. Plasma Fus. Res., **90**, 47-51 (2014).
[6] N. Okubo *et al.*, Nucl. Inst. Methods B, **314**, 208-210 (2013).

1 - 27 Irradiation Tests of Radiation Hard Components and Materials for ITER Blanket Remote Handling System

M. Saito, Y. Noguchi, M. Kazawa, K. Nakata, H. Kozaka and N. Takeda

Department of ITER Project, NFI, QST

Introduction

The ITER blanket remote handling system (BRHS) will replace the first wall panels in a radation environment having a dose rate of 500 Gy/h. The ITER requirement for radiation hardness is 1 MGy for all BRHS components, however, 5 MGy was set as the target value to increase the availability of the system. In this study, cables that use improved sheath materials from a past study [1] and electroless Ni plating were investigated.

Results

Cable samples (Φ26 mm, 2000 mm) were manufactured by using an EPDM rubber compound developed in [1]. These cables were irradiated at 1.7 kGy/h to 1.9 kGy/h up to 1 MGy (at 1.9 kGy/h), 2 MGy (at 1.7 kGy/h), 3 MGy (at 1.9 kGy/h), and 5 MGy (at 1.8 kGy/h). Three cable samples were used for each dose. After irradiation, the cables were bent 5000 times in bend tests to confirm their bend resistance. After 1 MGy of irradiation, all cables passed bend testing, however, after 2 MGy, two of three cables had cracks. All cables had cracks after 3 MGy and 5 MGy of irradiation. Dumbbell test pieces were taken from the bent sections of each cable and underwent tensile testing. Figure 1 shows the elongation rate of rubber samples after irradiation. Cables that passed the bend tests had an elongation rate of 50% or more. In [1], which used rubber sheets, elongation rates were consistently above 50% even if irradiated up to 5 MGy, however, in this test, after 2 MGy of irradiation, elongation rates of test pieces taken from the cables were under 50%. This difference in elongation rate is most likely due to the different fabrication processes for cables and sheets.

The electroless Ni plating samples were irradiated at 1.1 kGy/h in an environment using the saturated salt method where relative humidity was kept at 20% at 30 °C using CH_3CO_2K. The appearance of electroless Ni plating samples after irradiation testing is shown in Table 1. No surface degradation was observable on test pieces irradiated up to 1 MGy at 20% humidity, however, degradation was observed after 2 MGy. Corrosion progressed as the irradiation dose increased. The corroded areas of the samples were analyzed, the corrosion products of which were oxides, hydroxides, or nitrates of Ni or Fe. GD-OES results indicated that the corrosion of Ni plating was only on the outermost surface; the interior did not corrode. Irradiation tests up to 5 MGy at 20% humidity confirmed that (1) The physical appearance of samples irradiated up to 1 MGy did not change and no degradation of physical properties were observed, (2) Partial corrosion was observed on the surface of samples irradiated up to 2 MGy. An increased amount of O was detected at the corroded areas, but the material properties did not degrade, and (3) The entire surface of the samples irradiated up to 5 MGy corroded and their physical properties deteriorated.

Conclusion

Our improved cables had 1 MGy of radiation hardness verified by bend tests. The cables that passed bend tests had an elongation rate of 50% or more. These results are different to those of our past study [1], which used samples from rubber sheets. In future tests we will research how the different fabrication processes affect radiation hardness. Electroless Ni plating was irradiated in an environment having 20% humidity to evaluate its corrosion resistance. We verified that electroless Ni plating has good resistance to radiation in dry environments, however, this resistance decreased with increasing relative humidity.

Acknowledgments
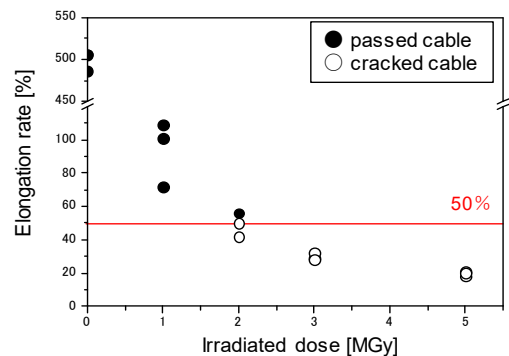
Fig. 1. Elongation rate of rubber samples after irradiation.

Table 1 Surface of electroless Ni plating samples after irradiation.

Reference

[1] M. Saito *et al.*, QST Takasaki Annu. Rep. 2017, **QST-M16**, 66 (2019).

1 - 28   Gamma Ray Irradiation Experiment for ITER Diagnostic Systems in JADA

S. Kitazawa, T. Hatae, M. Ishikawa, T. Oikawa, R. Imazawa, E. Yatsuka, H. Ogawa,
T. Maruyama, T. Ushiki, S. Tanaka, T. Sugie, H. Murakami and T. Yokozuka

Department of ITER Project, NFI, QST

JADA (ITER Japan Domestic Agency) are developing to procure five diagnostic systems, microfission chamber (MFC), poloidal polarimeter (PoPola), Edge Thomson Scattering (ETS), divertor impurity monitor (DIM) and divertor infrared thermography (IRTh) [1].

The reliability in the ITER radiation conditions of relevant equipment to be installed in the vacuum vessel, in the interspaces (IS) between the vacuum boundary and the biological shield and in the port cells (PC) outside the biological shields should be evaluated. In this study, we have launched gamma-ray irradiation experiments in QST Takasaki Advanced Radiation Research Institute from 2018.

In the preliminary experiments, optical components on DIM, IRTh and ETS were irradiated up to 10 MGy for IS items or up to 200 kGy for PC items in 6th Cell at Co-60 2nd Building or 1st cell at Food irradiation Building and observed their optical properties. For DIM items, lens materials (SiO_2, CaF_2 and $LiCaAlF_6$) that are candidate materials for the actual equipment, Polka dot half mirror, dot-like Al mirror coated on the surface of SiO_2 substrate with MgF_2 protective coating, and low high and high OH concentration optical fibres were irradiated and measured their optical transmittance. For IRTh items, change of transmittance by gamma-ray irradiation for optical elements (sapphire substrates, band pass filters and beam splitters) and transmission fibre (InF_3, ZrF_4) which are planned to be used in PC were tested. For ETS items, irradiations up to 150 kGy for two kinds of SiO_2 vacuum windows were performed. One has reflection reducing coating for 1064 nm light and its damage threshold is 20 J/cm^2 for high power laser incidence, and the other has reflection reducing coating for 500 - 1100 nm light for Thomson scattering observation.

Several interesting results were obtained in the preliminary experiments. For DIM system, the designed observing optical range is in the range between 200 and 1000 nm. In the range, the irradiation effects on optical transmittance are striking in the UV region of 200 - 400 nm. The SiO_2, CaF_2 and Polka dot half mirror showed a few percent increase on optical absorbance even with 200 kGy irradiation, and it was found that the light attenuation was within an acceptable range. For $LiCaAlF_6$, the change of optical density by the gamma-ray irradiation is shown in Fig. 1 [2]. The increase in optical density was large in the wavelength region below 300 nm, and it was found that using this glass material is impractical because large-scale shielding is required when used in high radiation field. An interesting property was observed in the irradiation to

$LiCaAlF_6$ above 100 kGy produced a larger absorption near 245 nm (P2) than F center of 262 nm (P1). The irradiation of several hundred kGy to the candidate optical fibres induced large decrease in transmittance in the spectral region below 300 nm, and it is necessary to study further the design of the fibre materials and system.
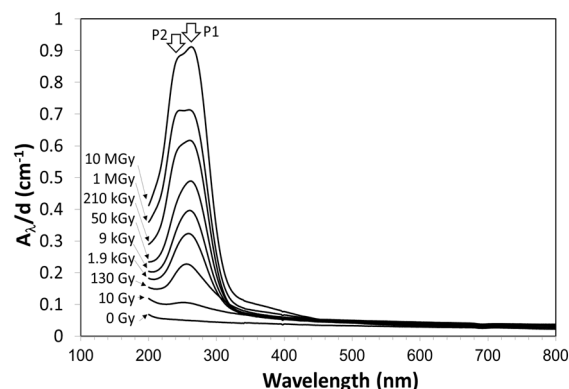
Fig. 1. Optical absorption features of $LiCaAlF_6$ gamma-irradiated up to 10 MGy.

In IRTh system, no significant change in transmittance was observed with gamma-ray irradiation of about 0.5 kGy-4.5 kGy to the optical components. In addition, although no significant change was observed in the transmittance for InF_3 at 1 kGy irradiation to the transmission fibres, decreases in transmittance in the wavelength region below 2 μm were confirmed for ZrF_4. In the next irradiation experiments, we will continue to confirm the reliability of optical components used in PC.

In ETS system, it was confirmed that each sample can maintain the same spectral transmittance as that before irradiation. In the next step, we plan to conduct a laser resistance test of the anti-reflection coat.

References
[1] K. Itami *et al.*, J. Plasma Fusion Res., **92**, 433 (2016).
[2] S. Kitazawa *et al.*, J. Plasma Fusion Res., **14,** 3405089 (2019).

1 - 29   Evaluation of Irradiation Hardening of Tungsten Materials by Nanoindentation Techniques

T. Miyazawa [a], S. Oizumi [a], J. Yu [b], A. Hasegawa [a], S. Nogami [a], M. Ando [b] and H. Tanigawa [b]

[a] Graduate School of Engineering, Tohoku University,
[b] Department of Fusion Reactor Materials Research, RFI, QST

Tungsten (W) is the primary candidate materials as a diverter or a plasma facing material (PFM) in fusion devices, primarily due to its high melting temperature, good thermal conductivity, and low sputtering rate, but its irradiation-induced hardening behavior has been identified as the life-defining issues, since W is going to be used in a wide range of temperature, from 350 to 1100 °C. In this study, nanoindentation tests on pure W irradiated with self-ion and proton was conducted to investigate the irradiation hardening due to displacement damage.

The self-ion irradiation experiment was carried out at the nominal irradiation temperature of 500 and 800 °C with 18 MeV W^{6+} ions by a tandem accelerator at the Takasaki Advanced Radiation Research Institute of QST. The nominal displacement damages stand for the values at around 0.5 µm depth from the irradiated surface was 1.0 dpa. The nominal damage rate was 1.2×10^{-4} dpa/s. Damage profile was calculated by SRIM code using the threshold displacement energy of 90 eV.

Materials used in this study was a powder metallurgical processed pure W followed by hot rolling, stress-relieve heat treatment. Four different types of specimens with different production conditions were prepared: a plate made by the same fabrication conditions which are used to procure the ITER divertor tungsten (ID: ITER); a plate made by the same condition as ITER, but cross rolled (ID: CLW); a plate made by the same condition as CLW but with higher rolling reduction ratio (ID: CHW), and pure W additionally heat treated (1500 °C x 1 hour) for the recrystallization.

Nano-indentation results on 500 and 800 °C irradiated ITER, CLW, and CHW W irradiated up to 0.3, 1.0 and 2.4 dpa were shown in fig.1. It was indicated that slightly larger irradiation hardening was observed in CLW-W, and generally larger hardening at 800 °C at 1 dpa.

The proton irradiation experiment was carried out in parallel on recrystallized pure W at the irradiation temperature of 800 °C with 1 MeV H^+ ions by the Dynamitron Accelerator at Tohoku University. The nominal displacement damages stand for the values at around 2.76 µm depth from the irradiated surface was 1.0 dpa. The nominal damage rate was 7.6×10^{-5} dpa/s.

As a result of the nanoindentation test on recrystallized pure W irradiated by self-ion and proton at 800 °C up to 1 dpa, bulk equivalent hardness H_0 was evaluated from the intercept of the linear fitting with the Nix-Gao plot as shown in Fig. 2, in order to minimize indentation size effect (ISE). The average value of 5.4 GPa was obtained as the bulk equivalent hardness of unirradiated specimen. The bulk equivalent hardness of the proton-irradiated specimen was obtained by extrapolating up to 0.8 µm as the damaged region and the bulk equivalent hardness of the self-ion irradiated specimen was obtained by extrapolating up to 0.5 µm as the damaged region. The average value of 7.6 GPa was obtained as the bulk equivalent hardness of proton irradiated specimen and the average value of 8.5 GPa was obtained as the bulk equivalent hardness of self-ion irradiated specimen. From these results, the value of irradiation hardening by proton irradiation was smaller than that by self-ion irradiation. The larger irradiation hardening was, the larger the calculated value of Young's modulus. Pile-up that overestimates Young's modulus and hardness might have occurred. Regarding the proton-irradiated specimen, the value of irradiation hardening of bulk equivalent hardness was larger than irradiation hardening calculated from the microstructure. From these results as well, it is considered that the hardness is overestimated due to the effect of pile-up.
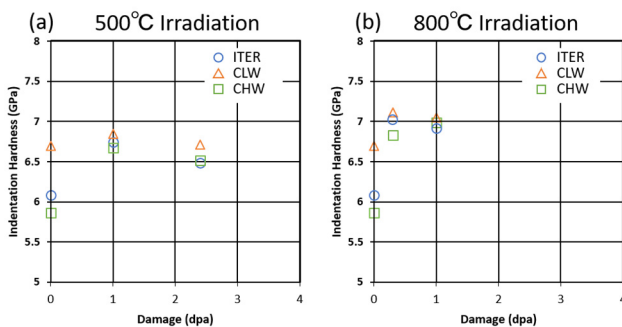
Fig. 1. Nano indentation results on 500 and 800 °C irradiated ITER, CLW and CHW-W up to 2.4 dpa.
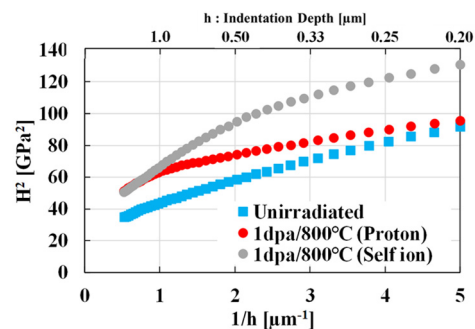
Fig. 2. Nix-Gao plots of nanoindentation hardness on proton and self-ion irradiated recrystallized pure W.

1 - 30 Study on Corrosion of FeCrAl-ODS Steels in Nitric Acid Solutions Under γ-ray

H. Ambai [a], K. Koizumi [a], M. Watanabe [a], A. Sakamoto [a], Y. Takahatake [a],
M. Takeuchi [a], Y. Sano [a], S. Yamashita [b] and K. Sakamoto [c]

[a] Department of Reprocessing Technology Development, NBTC, JAEA,
[b] Nuclear Science and Engineering Center, JAEA,
[c] Nippon Nuclear Fuel Development, Co., Ltd.

A FeCrAl-ODS steel has been developed for the accident tolerant fuel cladding of light water reactors in Japanese projects. In this study, corrosion behavior of FeCrAl-ODS steels in nitric acid solutions under γ-ray was evaluated to estimate the influence of those on a reprocessing process.

The experimental apparatus was set in Takasaki Advanced Radiation Research Institute and the corrosion tests under γ-ray of ^{60}Co were conducted. FeCrAl-ODS steels consist mainly of Fe and its strength under high temperature is enhanced by the addition of Cr, Al, Zr and Y_2O_3. Nitric acid solutions containing V(substitute for Pu) and Ru were used for corrosion tests, and their composition were based on dissolver solution in a reprocessing process [1][2].

The corrosion rates of FeCrAl-ODS steels were 0.7 ~ 0.9 mm/y from the immersion tests. The surface of test coupon didn't change at 3 hours immersion and its good corrosion resistance was revealed. The corrosion rate under non γ-ray was smaller than under γ-ray, but the difference between them wasn't so large. In addition, the electrochemical tests were conducted to consider the corrosion mechanism (Fig. 1). The cathode current and corrosion potential were increased by V and Ru addition. This could be caused by the reduction reactions of high valent V (V) and Ru (more than IV). In an actual process, Pu is contained in nitric solution instead of V. Pu would have an effect similar to V on the corrosion reaction considering its redox potential. The polarization curve didn't change by γ-ray as well as the results of immersion tests. The following reactions proceed under γ-ray, and radiolysis products such as nitrous acid generate and change the property of a solution [3].

$$NO_3^- \rightarrow NO_2^- + O\cdot$$
$$NO_3^- \rightarrow NO_2 + O\cdot + e^-$$
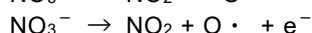
In this study, the irradiation time was considerably short (2 ~ 3 hours). Therefore, it is expected that the γ-ray irradiation made little influence on the corrosion reaction.

In order to evaluate the effect on a reprocessing process, the chemical composition dissolved from FeCrAl-ODS steels was calculated from the results of the corrosion tests, and compared with existing substances which are consist of spent fuel and corrosion products from equipment in a reprocessing process. The amount of dissolved substances from FeCrAl-ODS steels is considered to be small enough that this new fuel cladding is acceptable for a reprocessing process as shown in Table 1.

Acknowledgments

References

[1] F. Wada, Zairyo-to-Kankyo, **48**, 12, 771-775 (1999).
[2] Handbook,2, JAEA-Review, 2008-037 (2008).
[3] Kazanjian, A. R. *et al.*, Trans. Farad. Soc., **66**, 2192-2198 (1970).
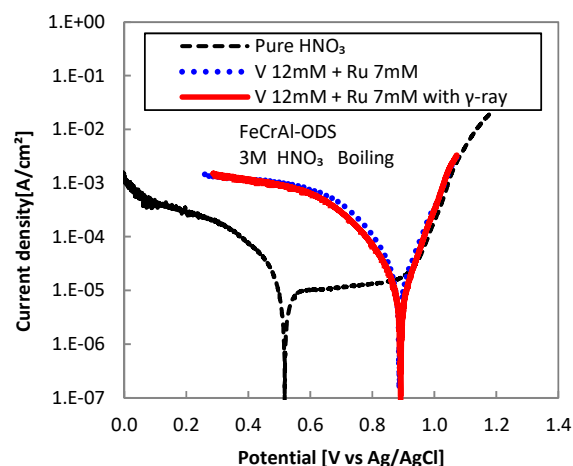
Fig. 1. Effects of metal ions and γ-ray on polarization curve of FeCrAl-ODS in HNO₃.

Table 1
Chemical composition in high level vitrified waste [wt%].

Composition	Dissolved substances from FeCrAl-ODS	Existing substances derived from spent fuel et al.*
Fe	0.023	1.3
Cr	0.003	0.3
Al	0.002	3.1
FP		9.8

* Spent fuel, corrosion product of equipment materials, material of glass

1 - 31   Study on Hydrogen Generation from Cement Solidified Samples Loading Low-level Radioactive Liquid Wastes at Tokai Reprocessing Plant

F. Sato, R. Matsushima and Y. Ito

Tokai Reprocessing Technology Development Center, NCL, JAEA

Cement solidification of Low-level radioactive Liquid Wastes (LLWs) generated from Tokai reprocessing plant is planned in Low-level radioactive Waste Treatment Facility (LWTF). There are two kinds of LLWs, concentrated liquid waste and phosphate liquid waste. In LWTF, the concentrated liquid waste is categorized into "sodium carbonate effluent" with low radioactivity and "slurry" with comparatively high radioactivity by radionuclide separation process and nitric acid ion decomposition process [1]. The sodium carbonate effluent is planned to solidify with BC cement, which is a mixture of 70 wt% Blast Furnace Slag and 30 wt% Ordinary Portland Cement. And the phosphate liquid waste is also planned to solidify with 'Super Cement', which is a commercial product of JGC Co. and is an alkali activated slag cement with various minor additives.

It is known that $G(H_2)$ value of a cement solidified product containing radionuclides varies with cement and effluent composition. In this study, as in last year, we investigated hydrogen generation from cement solidified samples containing these effluents [2].

Figure 1 shows an example of the irradiation samples. The samples were prepared by mixing simulated liquid waste and these cement using the composition planned in LWTF [3], then filled into a container (ϕ13 mm x 50 mmH) at 20 °C for a month to 8 months. After curing, these samples were put into a vial container (50 mL) one by one and were sealed with rubber septum. These samples were irradiated by Co-60 gamma-rays at about 2.5 kGy/h for 20 hours (shown in Fig. 2). After the gamma irradiation, concentration of hydrogen gas generated in the vial was measured by gas chromatography and $G(H_2)$ was calculated using blank data measured previously.

As a result of the irradiation test, the followings were clarified:

When the sodium carbonate effluent is solidified with the BC cement, it became clear that the $G(H_2)$ value of the solidified product (water cement ratio (W/C): 0.75, salt packing ratio: 20 wt%) is about 0.03 to 0.05 n/100 eV in each curing periods. From this result, it is thought that $G(H_2)$ value of what solidified carbonate solution with BC cement becomes constant in about one month. It is reported that chemical reactions (hydration reactions) in mixture of BC cement and sodium carbonate effluent will continue for about two years after mixing in small scale test [4]. So it is considered that $G(H_2)$ is not affected by the progress of the hydration reaction inside of cement solidified sample;

Assuming the waste liquid with insufficient in the nitric acid ion decomposition, effluent of sodium carbonate (70-90%) with sodium nitrate (5-15%) and sodium nitrite (5-15%) was solidified with the BC cement and irradiated. $G(H_2)$ values of the solidified product containing nitrate and nitrite is about 0.02 to 0.04 eV in each curing periods and smaller than that of pure carbonate. It is considered that nitrate and nitrite salt have a suppression effect of H_2 gas generation from solidified products;

When the phosphate liquid waste is solidified with the Super Cement after insolubilizing of the phosphate using calcium hydroxide, it became clear that the $G(H_2)$ value of the solidified product is about 0.05 to 0.38 n/100 eV and increase as W/C ratio (0.95-2.15) and salt packing ratio (4 wt%-12 wt%) increase. It is considered that main components of this waste such as calcium phosphate have promotion effect on H_2 gas generation, and as the water contained in the solidified product increases, the amount of water decomposed into H_2 gas also increased.

Sodium Carbonate Effluent Solidified with BC Cement   Vial Container (50 mL) Sealed with Rubber Septum
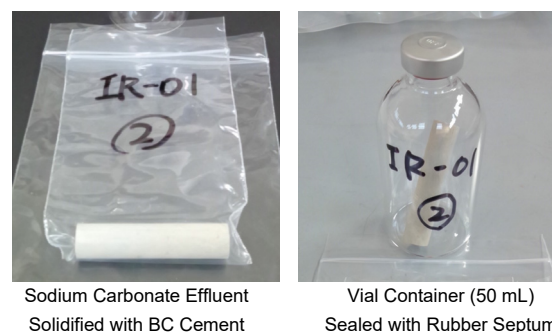
Fig. 1. Example of Irradiation Samples.
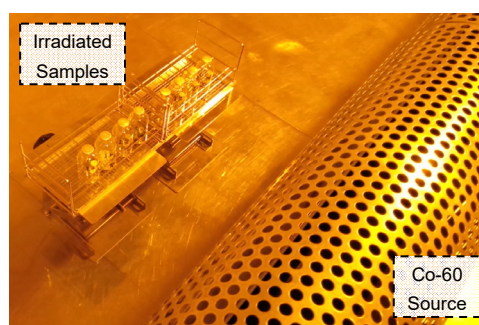
Fig. 2. Status of Sample Irradiation by Co-60.

References
[1] A. Sugaya *et al.*, WM2011 Conf. 11078 (2011).
[2] F. Sato *et al.*, Proc. of 2018 Fall Meeting of AESJ, 3J02 (2018).
[3] R. Matsushima *et al.,* Proc. of 2018 Fall Meeting of AESJ, 3J01 (2018).
[4] K. Horiguchi *et al.,* Proc. of 2015 Fall Meeting of AESJ, G53 (2015).

1 - 32　　Quantitative Analysis of Zr Adsorbed on IDA Chelating Resin Using Micro-PIXE

Y. Arai [a, b)], S. Watanabe [a)], S. Ohno [a)], K. Nomura [a)], F. Nakamura [c)], T. Arai [c)], N. Seko [d)], H. Hoshina [d)], and T. Kubota [b)]

a) Department of Reprocessing Technology Development, NCL, JAEA,
b) Ibaraki University,
c) Shibaura Institute of Technology,
d) Department of Advanced Functional Materials Research, TARRI, QST

The spent PUREX(Plutonium Uranium Redox Extraction) solvent containing U and Pu is generated from the reprocessing process of spent nuclear fuel. The nuclear material removal is important for safety storage or disposal of the spent solvent. Adsroption recovery of Zr(IV), which is used as simulant of Pu(IV), from simulated spent PUREX solvent by various type of adsorbent has been experimentally investigated in our previous study [1]. The adsorbent with imino diacetic acid (IDA) functional group was revealed to be one of the most promising materials to design the Pu(IV) recovery process. In order to evaluate applicability of the IDA type chelating rein for the spent solvent treatment and its adsorption performance, adsorption capacity and adsorption mechanism should be precisely understood. We focused on high sensitivity of Particle Induced X-ray Emission (PIXE) analysis for trace elements detection [2]. This sutdy aim to investigate ability of Micro-PIXE analysis for quantitative analysis of adsorbed Zr(IV) onto chelating resin (DIAION™ CR11).

Micro-PIXE analysis was carried out at light-ion microbeam line connected to the 3-MV single-ended accelerator in TIARA at QST, Japan. The beam spot size and irradiation area were 1×1 μm^2 and 800×800 μm^2, respectively. Energy resolution of the detector at 2.3 - 10.5 keV was 110-220 eV.

In order to prepare the calibration curve of the amount of adsorbed Zr onto the CR11, we measured the chelationg resin adsorbed with a known amount of Zr. Figure 1 shows correlation of the amount of adsorbed Zr onto chelating resin and total Zr-Kα intensity normalized with the irradiation dose. The obtained correlation is written as follows;

$$W_{Zr} = C_{Zr} / 74.26 \quad (1)$$

　W_{Zr} : Amount of adsorbed Zr [mg-Zr/g]
　C_{Zr} : Normalized Zr-Kα intensity [C^{-1}]

If Zr-Kα line is observed, amount of adsorbed Zr can be estimated from the equation. Figure 2 plotted the amount of absorbed Zr estimated by the equation (1). As the results, the estimated smallest amount of adsorbed Zr was 0.5 mg-Zr/g. Since the limit of quantification of Micro-PIXE analysis is less than the limit of quantification of X-ray fluorescence analysis ($\fallingdotseq$ 1 mg-Zr/g), Micro-PIXE analysis proved that it is an effectual method for quantitative analysis of trace adsorbed elements. Moreover, it was

estimated that the total amount of adsorbed element onto the adsorbent is quantified by Micro-PIXE analysis of a particle of adsorbent.
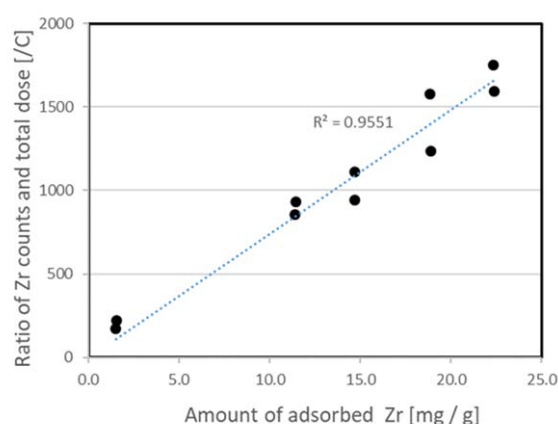
Fig. 1. The correlation of the amount of adsorbed Zr and the ratio of Zr counts and irradiation dose.
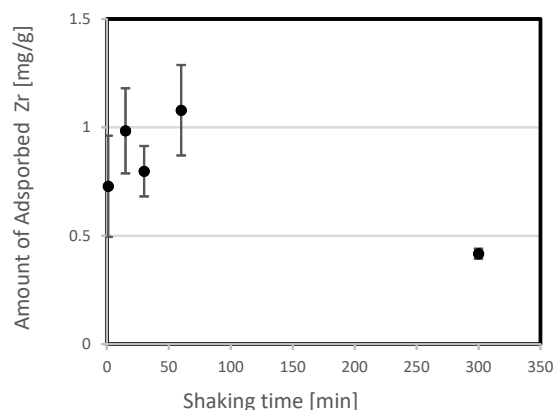
Fig. 2. Estimated the amount of adsorbed Zr recovered from the simulated spent solvent.

References
[1] F. Nakamura *et al.*, Proc. DEM 2018 **195** (2018).
[2] B. Gonsior *et al.*, Talanta, **30**, 6 (1983).

1 - 33   Evaluation of Effects of Modification on Hydrogen Storage Characteristics of Palladium by Ion Irradiation

H. Abe [a)], S. Aone [b)], R. Morimoto [b)] and H. Uchida [b)]

[a)] Department of Advanced Functional Materials Research, TARRI, QST,
[b)] Course of Applied Science, Graduate School of Engineering, Tokai Univ.

For hydrogen-metal systems, the effect of surface modification on the hydrogen absorbing behavior is also a very important study topic from both industrial and fundamental viewpoint. From the academic point of view, most research had focused interest on Pd-H system in ultrafine structured Palladium (Pd), because it is a typical face centered cubic (f. c. c.) metal and can absorb a large amount of hydrogen [6]. Surface phenomena occur in the process of Pd-H system formation during H_2 interaction with Pd samples [1]. The induction of vacancy on Pd was found to be effective for an increase in the hydrogen absorption rate [2]. Regarding the hydrogen storage in materials, it was reported that the absorption concentration of hydrogen atoms and the hydrogen absorption rate depend strongly on the surface state of metals. For the surface modification of materials, ion implantation is known to be a quite useful method. These facts give the possibility that the hydrogen absorptivity in Pd is improved by surface modification using ion irradiation.

The samples used in this study were Pd sheets (99.99 % purity, 7.5 x 7.5 x 0.1 mm^3). Prior to ion irradiation, all Pd samples were annealed in nitrogen atmosphere for an hour at 1173 K. N^+ irradiation onto the Pd samples was made at room temperature using the 400 kV ion implanter and the 3 MV tandem accelerator of TIARA in QST. The hydrogen absorption rate of the irradiated Pd was investigated using an electrochemical method. Pd surface was prepared by electrolysis using a cathode, the opposite electrode of Pt sheet as an anode. An Hg/HgO was used as the reference electrode in an open cell. Details of the electrochemical measurements have been reported elsewhere [3].

Figure 1 shows the representative initial hydrogen absorption curves of Pd samples after 350keV-N^+ irradiation, doses of 1 x 10^{16} cm^{-2}, initial hydrogen absorption/desorption cycles from 1 to 10 charges. Increasing a hydriding charge, the initial hydrogen absorption rate was increased. The 10 charges hydriding Pd has four times higher initial hydrogen absorption rate than that of the 1 charge hydriding Pd. Since vacancy type defects are introduced by irradiation and such vacancies might act as hydrogen trapping sites, the enhancement of the initial hydrogen absorption rate obtained in this study can be interpreted in terms of an increase of hydrogen trapping sites near the surface region due to irradiation of N^+ into Pd.

Regarding the relationship between the work function of Pd ($\Delta\phi$ [ev]) and the initial hydrogen absorption rate before and after N ion irradiation at energies from keV to MeV, the value of $\Delta\phi$ is depicted as a shift from un-irradiated sample (Fig. 2). The $\Delta\phi$ is estimated from $\Delta\phi = V_E / (\Delta V - 1)$, where V_E is the contact potential difference with a reference electrode and the Pd, and ΔV represents the voltage difference between the probe tip and Pd sample. As for the hydrogen absorption rate, the value increased with increasing irradiation energy of N ions. The Pd surface became revitalized and the defects were formed to the surface phase by N^+ irradiation. The work function value shifted to a negative side compared with un-irradiated Pd. Therefore, surface potential of Pd became low and easy to exchange the electron. As a result, the initial hydrogen absorption rate of 5 MeV 1e14 irradiated Pd was five times higher than un-irradiated one. These results imply that the value of $\Delta\phi$ decreases and the hydrogen absorption rate increase with increasing vacancy concentration.
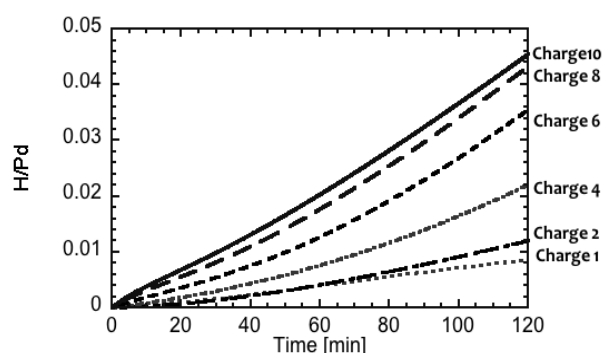
Fig. 1. Hydrogen absorption, from 1 to 10 charges, curves of Pd irradiated by 350 keV N^+.
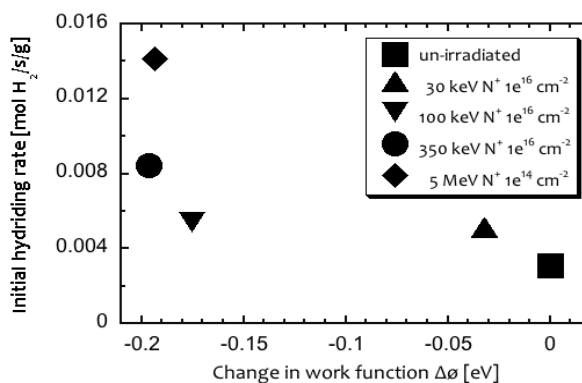
Fig. 2. Relationship between the work function of Pd and the initial hydrogen absorption rate before/after N^+ irradiation.

References
[1] H. Uchida *et. al.*, J. Alloys Comp., **253-254**, 547-549 (1997).
[2] H. Abe *et. al.*, Nucl. Instrum. Meth. Phys. Res. B, **206**, 224-226 (2003).
[3] H. Uchida *et. al.*, J. Alloys Comp., **253-254**, 525-528 (1997).

Part Ⅱ

2. Life Science

2 - 01   Establishment of a Method for Heavy-ion Microbeam Irradiation Using Specially-Designed Cell Irradiation Dish

T. Funayama and M. Suzuki

Department of Radiation-Applied Biology Research, TARRI, QST

The applications of heavy ions, such as heavy-ion cancer therapy and ion-beam breeding, depend on its characteristic biological effects. This characteristic biological effect of heavy-ion is considered to be derived from a non-uniform distribution of microdosimetrical energy deposition of heavy-ion radiation, which result to cells in a cell population irradiated by heavy ion to be not hit with same number of heavy-ions. On the other hand, heavy-ion radiation has a high elementary dose brought from its high-LET property enough to induce biological effect even with single hit. Such combination of the non-uniform dose distribution and the high elementary dose induces mixture of hit and non-hit cells within a cell population irradiated with low fluence of heavy-ion particles.

Bystander effect is a radiation-induced phenomenon that are induced in unhit neighboring cells by intracellular signaling from cells hit by radiation. In such non-uniform dose distribution in a cell population irradiated with heavy-ion radiation, the contribution of bystander effect in their radiation response become increased. Therefore, radiation induced bystander effect is considered to play an important role in low-fluence high-LET radiation effect.

Heavy-ion microbeam is a useful tool for analyzing heavy-ion-induced bystander effect. To explore the mechanism underlying the bystander effect, we have developed heavy-ion microbeam systems in QST-Takasaki, and carried out experiments for analyzing the mechanisms of the bystander effect [1]. However, there were issues that cannot be solved in a general-purpose microbeam irradiation dish. One of these issues is an analysis of the distance limit of intercellular communication in bystander effect induction. Therefore, we established a method to develop a specially-designed cell dish for microbeam irradiation, which is designed and manufactured to adapt specific experiments that cannot be carried out with a general-purpose microbeam irradiation dish.

A largest microbeam irradiation dish which can be placed on the sample stage of the microbeam cell targeting system has a shape of the cell culture dish of 60 mm in diameter, limiting analysis of the bystander signal transduction between more than 60 mm distance. Therefore, we made a specially-designed cell irradiation dish that can analyze the signal transduction at more than 60 mm distance.

A specially-designed dish was manufactured by adhering a bottom material to which cells attach to a wall surface component manufactured by cutting a polycarbonate material. Using three-dimensional CAD software, a maze-shaped wall component was designed (Fig 1, left). It was designed to be stored within a 60 mm diameter petri dish, and has a distance of 259 mm between the farthest cells by arranging grooves in a maze shape. As the bottom material, a cover glass treated with vacuum plasma was used. A maze-shaped wall component and a cover glass were adhered, washed, and sterilized by 70% ethanol treatment (Fig. 1, right).

HeLa cells were inoculated to confirm cell attachment and growth in a manufactured dish. The cells exhibited cell attach and growth performance equivalent to commercially available cell culture dishes. Thereafter, we placed the dish on the sample stage of a collimating heavy ion microbeam system of TIARA, and irradiated with a carbon ion microbeam of 250 μm in diameter. The cells in the maze end of the dish was clearly observed with a microscope of the cell targeting system, indicating that we are able to target specific cells in the manufactured maze dish. The irradiated ions were detected by an ion detector placed immediately beneath the sample, indicating a controlled number of ions are able to be irradiated to the targeted cells. These results indicated that the method we established enables to carry out the analysis of the heavy ion irradiation effect that was difficult to work out with the conventional general-purpose microbeam irradiation dishes.
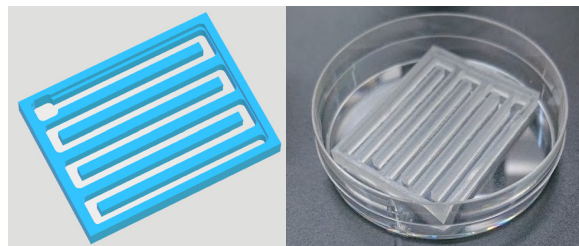
Fig. 1. A wall surface component of the tailor-made dish, which has a maze shaped grooves, were designed using 3D CAD software (left). The wall surface components were manufactured by cutting polycarbonate with a desktop cutting machine and adhered to a cover glass to form dish shape (right).

Reference

[1] T. Funayama *et al.*, J. Radiat. Res., **49**, 71 (2008).

2 - 02   Bystander Effects in Non-irradiated Normal Cells via Secreted Factor(s) from Carbon-ion Irradiated Tumor Cells

M. Suzuki [a)], T. Funayama [b)], M. Suzuki [b)], Y. Yokota [b)] and Y. Kobayashi [b)]

[a)] Department of Basic Medical Sciences for Radiation Damages, NIRS, QST,
[b)] Department of Radiation-Applied Biology Research, TARRI, QST

We have been studying the cellular bystander effects, such as cell killing and gene mutation, in normal human fibroblasts using the C-, Ne- and Ar-ion microbeams. In the field of radiological sciences, communication between irradiated tumor and non-irradiated normal cells is one of the important concerns for radiotherapy. It should be important for developing radiotherapy to understand the communication between irradiated tumor and non-irradiated normal cells. This year, we examined biological effects in non-irradiated normal cells, focusing on the bystander effect via secreted factor(s) to culture medium from the carbon-ion irradiated tumor cells.

Human glioblastoma cell line (T98G) was irradiated with carbon-ion microbeams generated with the TIARA at the HZ1 port. Irradiations were carried out by the 256-cross-stripe method [1]. Briefly, the beam size of each irradiation point of the microbeam was 20 µm in diameter and the irradiations in each point were performed to deliver 8 ions. At 24 h after the irradiations, the medium from the irradiated T98G cells was transferred to the flask inoculated on the normal human skin fibroblasts (NB1RGB) and incubated for 24 h in a CO_2 incubator at 37 °C. Then the normal cells were assayed for cell-killing effect, which was measured by a colony-forming assay and gene mutation at the *HPRT* (Hypoxanthine-guanine phosphoribosyltransferase) locus, which was detected by the incidence of 6-thioguanine resistant clones.

In order to investigate what kinds of secreted factor(s) it is affected, we used either dimethyl sulfoxide (DMSO: 1.3 mM) as a scavenger of reactive oxygen species or ascorbic acid (AsA: 5 mM) as a specific scavenger of long-lived radicals. These chemicals were treated in the medium of the irradiated T98G cells during the 24 h of post-irradiation incubation.

The results were shown in figures 1 (cell-killing effect) and 2 (gene mutation). The medium transfer from the carbon-ion irradiated T98G cells to the non-irradiated NB1RGB cells resulted in increasing cell-killing effect and gene mutation in the NB1RGB cells. It suggests that bystander effects occur via secreted factor(s). Furthermore, increased biological effects were returned to the control level by treating with ascorbic acid, but not dimethyl sulfoxide.

There is clear evidence that the medium from the irradiated tumor cells enable to induce damage in the neighboring non-irradiated normal cells via bystander effects mediated by the secreted factor(s), which were scavenged by the ascorbic acid.
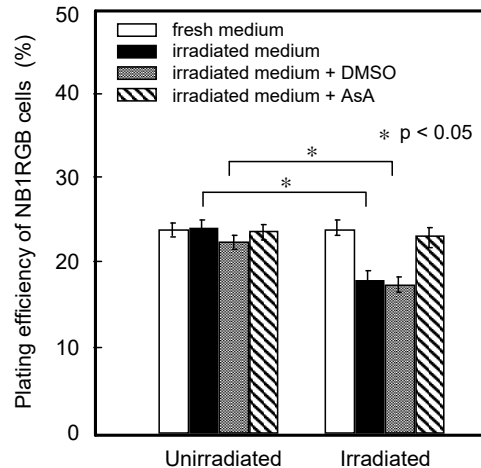
Fig. 1. Cell-killing effect induced in NB1RGB cells, which were transferred the medium from carbon-ion irradiated T98 cells. Also, effects of ascorbic acid and dimethyl sulfoxide to bystander effects via secreted factor(s). The results were the means and standard errors from 3 independent experiments. (∗ *p* <0.05).
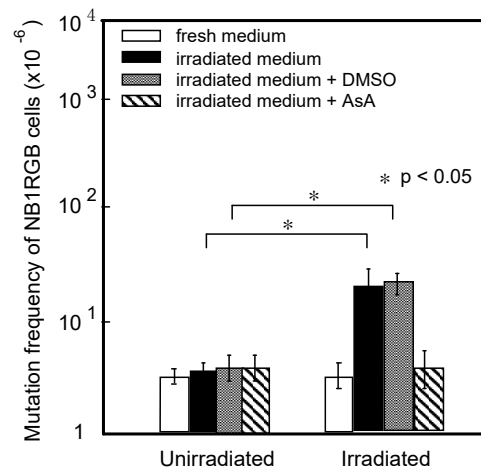
Fig. 2. Gene mutation induced in NB1RGB cells, which were transferred the medium from carbon-ion irradiated T98 cells. Also, effects of ascorbic acid and dimethyl sulfoxide to bystander effects via secreted factor(s). The results were the means and standard errors from 3 independent experiments. (∗ *p* <0.05).

Reference

[1] M. Suzuki *et al.*, JAEA Takasaki Ann. Rep. 2006, JAEA-Review **2007-060**,107 (2008).

2 - 03 Imaging of the Area of Oxidative DNA Damage Generated in Carbon Beam Track with Different LET Using DNA Thin Sheet

A. Ito [a), K. Kano [a), K. Urano [a), R. Uchiyama [a), S. Yoshida [a), R. Hirayama [b),
Y. Furusawa [c), Y. Yokota [d) and T. Funayama [d)

[a) School of Engineering, Tokai University,
[b) Department of Charged Particle Therapy Research, NIRS, QST,
[c) Department of Basic Medical Sciences for Radiation Damages, NIRS, QST,
[d) Department of Radiation-Applied Biology Research, TARRI, QST

Generally accepted track structure model for heavy ions consists of dual areas, core region with high ionization density and penumbra region where secondary electrons mainly contribute to energy deposition, with relatively low LET nature. To evaluate the contribution of low LET region to biological effects of heavy ions, we have been interested in the visualization of the low LET penumbra area in the high-LET ion beam. By considering that OH radicals are responsible for the low LET region in water environment, we visualized the area of OH radical induced DNA damage 8-hydroxydeoxyguanosine (8-OHdG) in DNA thin sheet, by using an immunostaining method for the fluorescent antibody against the damage product. In our preceding study, we detected significant production of 8-OHdG along a heavy ion track by irradiating the DNA sheet set in parallel with incident beam [1]. We also observed fluorescence dots probably originated from 8-OHdG generation under the irradiation condition where DNA sheet was set perpendicular to a beam track. In the present study, we compared the size of fluorescence dots due to the perpendicular irradiation of carbon beams with different energy and LET using TIARA and HIMAC at the National Institute of Radiological Science (NIRS).

Carbon beam irradiation was carried out as follows: 190 MeV carbon beam at TIARA with an LET of 117 keV/μm was irradiated to a DNA sheet made on a coverglass set perpendicular to ion beams. The DNA sheet was pretreated with Bouin fixative. During irradiation, the DNA sheet on which water was dropped was covered with mylar film to maintain water environment around the DNA sheet. The similar irradiation setup was applied to HIMAC beams of 290 MeV carbon with an LET of 13 keV/μm, although beam direction was horizontal instead of vertical at TIARA. The irradiated DNA sheet was processed according to a fluorescence immunostaining protocol. The obtained fluorescence images were analyzed using Image J, an image processing software.

Figure 1 shows the image of fluorescence dots on DNA sheet with perpendicular irradiation with a dose of 1 Gy. To display the fluorescence dots more easily, black and white colors of the image were inverted. Using Image J software, image thresholding was conducted, and the areas of the dots were measured. Table 1 summarized the area of two kinds of carbon ions with different LET. Several hundred dots were measured and the average and standard error

were calculated. The area was found to increase with increasing LET. The results are also consistent with the theoretical study by Chatterjee and Schaefer [2]. In the QST Takasaki annual report of last year [1], we reported the width of 8-OHdG area along a carbon beam track under parallel irradiation at HIMAC. That value, 1.02 μm is approximately the same as the diameter of the present dots, 1.2 μm under the assumption that the dots are circle. Further extension to other ion species and LETs is in progress.
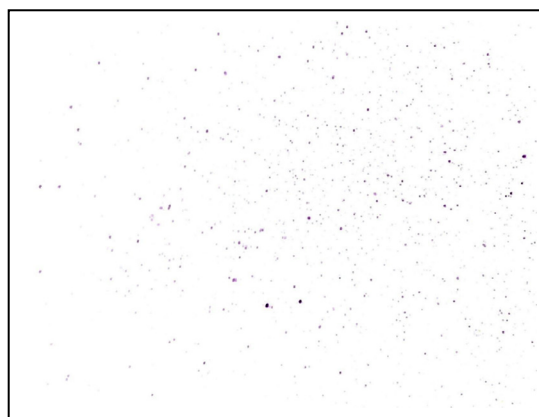
Fig. 1. Fluorescence dots observed on DNA sheet upon carbon beam irradiation. Black and white colors were inverted for easy observation of fluorescence dots.

Table 1
Area of fluorescence dots produced upon carbon beam irradiation.

Energy (MeV)	190	290
LET (keV/μm)	117	13
Area (μm^2)	2.58 ± 0.71	1.11 ± 0.14

References
[1] A. Ito *et al.*, QST Takasaki Annu. Rep. 2017, **QST-M-16**, 81 (2019).
[2] A. Chatterjee and H. J. Schaefer, Radiat. Environ. Biophys., **13**, 215-227 (1976).

2 - 04   Heavy Ion Irradiation Induced G2/M Arrest on Silkworm Eggs at Cleavage Stage

R. Isoyama [a)], M. Yahagi [a)], Y. Souma [a)], T. Funayama [b)], M. Suzuki [b)],
Y. Kobayashi [b)] and K. Shirai [a)]

[a)] Faculty of Textile Science and Technology, Shinshu University,
[b)] Department of Radiation-Applied Biology Research, TARRI, QST

Generally, in the animals eggs, there is no or incomplete checkpoint mechanism to perform the rapid cell cycle at early developmental stage. However, many unknown points are left at the checkpoint mechanisms in early developmental eggs.

We have studied the radiation response in the early developmental egg of *Bombyx mori*. We have already confirmed that when silkworm eggs are irradiated with heavy ions at the cleavage stage, the development is delayed according to the irradiation dose. This developmental delay is thought to be caused by the checkpoint mechanism, but the details remain unknown. The estimation of the stage of the cell cycle arrest is usually performed by measuring the amount of DNA in cells using a cell sorter or the like. However, this method cannot use the analysis, because the silkworm eggs in the cleavage stage are multinucleated cells and the number of nuclei is small.

Cyclin B is important protein for driving M phase. The fluctuation of the amount of cyclin B reflects the cell cycle, and its amount is maximized immediately before M phase. Therefore, we considered that the fluctuation of the amount of cyclin B reflects the cell cycle, and the stage of cell cycle arrest can be estimated by measuring the amount of cyclin B.

The silkworm used in the studies was pigmented, non-diapause (*pnd p*[S]) strain, and reared by artificial diets in the laboratory. The eggs were irradiated with 20 Gy of 190 MeV carbon ions beams accelerated by an AVF cyclotron at TIARA, TARRI, QST at 6 hours after oviposition. The irradiated eggs were incubated at 25 °C, then fixed with Carnoy's solution for analysis of the developmental arrest stage. At the same time, some eggs were treated with SDS-PAGE sample solution for analysis of cyclin B in the eggs. The amount of cyclin B in eggs was investigated using an anti-cyclin B antiserum.

At first, the cell cycle arrest of heavy ion irradiated silkworm eggs was investigated. The number of nuclei in the egg was counted, and determined the developmental stage (division cycles) of the egg. The number of nuclei in the non-irradiated eggs up to 8 hours after oviposition was examined. The number of nuclei at 6 hours after oviposition (just after irradiation) was 8 or 16. That is, it is presumed that the developmental stage of the eggs at the time of irradiation was mostly cycle 4 (a part is cycle 5). After that, the nuclei continued to divide, and the number of nuclei at 8 hours after oviposition (2 hours after irradiation) was 30-60 (cycle 6 or cycle 7). Therefore, the division cycle of silkworm eggs in this study is estimated to be 35 minutes to 50 minutes / times.

At immediately after irradiation, the developmental stage of the irradiated egg was cycle 4 or 5, similarly to the stage of the non-irradiated egg. However, the irradiated eggs were remained at stage 4 or 5, even 2 hours after irradiation (8 hours after oviposition). In other words, silkworm eggs stopped their development immediately after irradiation. In addition, it was confirmed that the developmental arrest was not caused by the spindle checkpoint. Because there were the nuclear in the developmental arrest eggs.

Next, the fluctuation of cyclin B in the eggs after irradiation was examined using a specific antiserum. As a result, cyclin B (and it's derivative) in the egg was always maintained at a high level even though the development was stopped (Fig. 1). That is, it is considered that the developmental arrest occurs at the G2 / M checkpoint.

Cell cycle arrest in response to radiation also occurs in G2 / M checkpoint in cultured silkworm cells (BmN4) [1]. This study suggests that the G2 / M checkpoint mechanism also exists in early developmental eggs of *Bombyx* whose cell cycles are controlled by maternal factors. In the silkworm cells or egg, the reason why cell cycle arrest induced by irradiation are observed only at the G2 / M checkpoint needs to be further investigated.
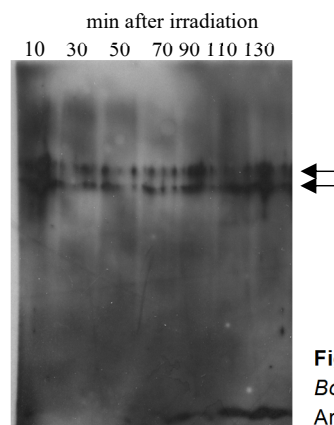
Fig. 1. Changes in Cyclin B in *Bombyx* eggs after irradiation Arrows indicate cyclin B.

Reference
[1] M. Takahashi *et al.*, J. Insect. Biotechnol. Sericol., **75**, 23-30 (2006)

2 - 05   Induction of Testis-Ova by Proton Beams Irradiation in p53 Deficient Medaka Testis

S. Oda [a)], K. Nagata [a)], T. Yasuda [a)], T. Kajihara [a)], A.C.G. Peh [a)], M. Suzuki [b)],
T. Funayama [b)], Y. Kobayashi [b)] and H. Mitani [a)]

[a)] Department of Integrated Biosciences, The University of Tokyo,
[b)] Department of Radiation-Applied Biology Research, TARRI, QST

Japanese medaka, *Oryzias latipes*, is a small teleost fish, which has been used as an excellent model organism to investigate the biological effects of irradiation in vertebrates. In 2016, we established a protocol for the targeted irradiation of low-energy carbon-ion ($^{12}C^{6+}$, 26.7 MeV/u) microbeam to adult medaka testis using broad- and microbeam facilities of TIARA [1] and revealed that direct irradiation of testis induces ovum-like cells in testis (testis-ova) of p53 deficient males. Previously, we have reported the induction of testis-ova in the p53 deficient medaka males after irradiation with 1 - 5 Gy of gamma-rays [2] and recently one of the authors reported that even 2 Gy of carbon-ion ($^{12}C^{6+}$, 26.7 MeV/u) beam can efficiently induce testis-ova in the p53 deficient testis as gamma-rays do [3].

In this study, we conducted broad- and micro-beam irradiation of proton (H$^+$, 15 MeV/u) onto the p53 deficient male medaka to investigate the testis-ova induction by proton irradiation.

In the broad-beam irradiation, we found that 2 Gy of proton beam irradiation can induce miss-differentiation of spermatogonia into testis-ova 7 days after the irradiation (Fig. 1A, B). The histological appearances of the testis irradiated with the 2 Gy of carbon-ion beam and the 2 Gy of proton beam were almost equal. Immuno-histochemical study revealed that proton beam irradiation induced a large number of apoptotic type B spermatogonia which were positive to anti-cleaved caspase 3 antibody staining in wild-type testis (Fig. 1C). Since most of the type A spermatogonia did not conduct apoptotic cell death, these findings strongly suggest that irradiation might disturb normal differentiation of spermatogonia and let spermatogonia miss-differentiate into ovum-like. In wild-type testis, miss-differentiated testis-ova would be removed via p53 dependent apoptotic cell death, whereas the miss-differentiated testis-ova might survive and grow in the absence of p53 functions.

In the microbeam experiment, we used a ø250 μm microaperture and conducted targeted proton irradiation (2 Gy) in the restricted areas of the testis of the p53 deficient male. Seven days after the irradiation, we prepared histological sections of the testis and found that testis-ova were induced in the cysts of spermatogonia in the confined area of the irradiated testis (Fig. 2), confirming the previous finding that direct irradiation of p53 deficient testis is enough for the miss-differentiation of spermatogonia into testis-ova.

In this study, we revealed that the testis-ova were induced after proton beams induction in testis of the p53 deficient medaka 7 days after the irradiation in the same manner as when the testis was irradiated with gamma-rays and carbon-ion. Our data suggest that the lack of p53-dependent apoptosis might be a cause of the testis-ova induction by irradiation in the p53 deficient medaka and that the testis-ova induction in the p53 deficient medaka can be more highly sensitive than we had thought.

References
[1] K. Nagata *et al.*, Sci. Rep., **6**, 28691 (2016).
[2] Yasuda *et al.*, Cell Death Disease, **10**, 718 (2012).
[3] K. Nagata Doctoral Thesis, The Univ. of Tokyo (2019).
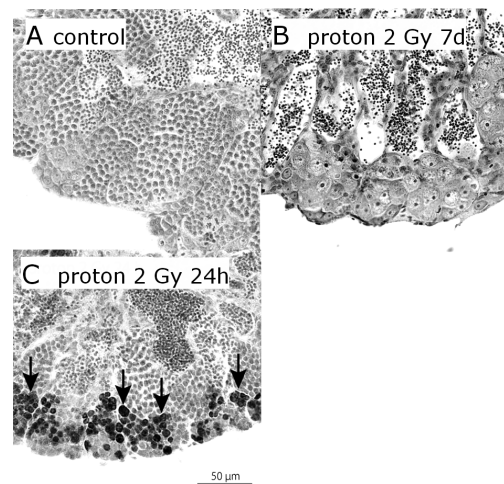
Fig. 1. Histological sections of the testis of p53 deficient medaka irradiated with 2 Gy of proton broad-beam. (A) Testis not irradiated. (B) A large number of ovum-like cells (testis-ova) were induced in cysts with spermatogonia. (C) Apoptotic cell death of spermatogonia were induced 24 hours after the irradiation (arrows) which were positive in immunohistochemistry with anti-cleaved caspase 3 antibody.
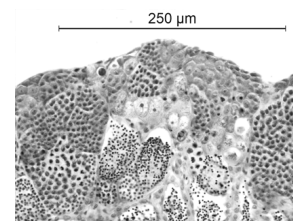
Fig. 2. Confined induction of testis-ova in the testis of p53 deficient medaka 7 days after the irradiation with 2 Gy proton microbeam 250 um in diameter. Testis-ova were induced in cysts of spermatogonia which were located peripherally in medaka testis.

2 - 06   Targeted Irradiation to the Central Nervous System Elicited Dose-dependent Effects on Motility in *C. elegans*

M. Suzuki and T. Funayama

Department of Radiation-Applied Biology Research, TARRI, QST

Previous experiments showed that motility (locomotion) in the nematode *Caenorhabditis elegans* was significantly reduced by whole-body irradiation with either gamma rays or carbon ions, in a dose-dependent manner, but not by targeted irradiation of any individual region, including the central nervous system (CNS) [1]. This suggests that radiation inhibits motility by a whole-body mechanism, potentially involving motoneurons and/or body-wall muscle cells, rather than affecting motor control via the CNS or a stimulation response. In these experiments, we targeted a limited area with a diameter of 20 μm and irradiated with a single dose (500 Gy) that induced a reduction of motility after whole-body irradiation. Thus, it remains unknown whether irradiated area-dependent and dose-dependent effects on motility by targeted irradiation both exist.

Targeted irradiation was delivered using a collimating microbeam irradiation system at HZ1 port of TIARA. To target the whole nerve ring equivalent to the CNS of *C. elegans*, we newly fabricated a micro-aperture cylinder (beam exit) with 60-μm diameter, which is same size of the CNS. In addition, to count ions exactly and maintain animals in good condition during irradiation, we employed an ion-penetrable ultra-thin microfluidic chip (Worm Sheet) [2] and permitted careful control of the number of ions (dose) applied [2-4]. In previous targeted-irradiation experiments [1], carbon ions could not pass through the microfluidic chip enclosing animals and, therefore, did not reach the ion counter located under the sample stage, as the thickness of the chip was thicker than the range of carbon ions (~1 mm). In contrast, as the sample thickness (including Worm Sheet-enclosed animals and cover films) was only 500 μm, 190 MeV of carbon ions whose range in water is only 930 μm are able to pass through. By employing Worm Sheets, we conducted targeted CNS irradiation with an exact number of carbon ion particles, and examined dose responses by controlling the number of irradiated ions (corresponding to dose of irradiation). For comparison, we also examined the dose response after whole-body irradiation with carbon ions using the broad beam irradiation equipment at HY1 port of TIARA.

As shown in Fig. 1(a), the motility of irradiated animals was reduced in a dose-dependent manner. In the case of CNS-targeted irradiation, whereas irradiation with 500 Gy did not induce any effect on the motility even if the irradiated area was extended from 20 μm to 60 μm in diameter, an effect was observed in animals irradiated with 1,000 Gy (Fig. 1(b)). From these results, it can be stated that a dose-dependent effect of CNS-targeted irradiation on motility exists, whereas irradiated area (beam size)-dependent effects do not exist, at least within a
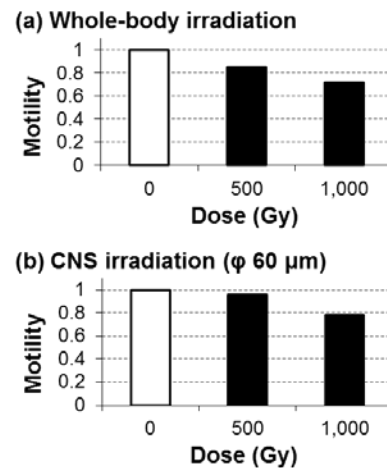
Fig. 1. Motility of *C. elegans* immediately after carbon-ion irradiation with a dose of 500 Gy or 1,000 Gy. (a) Normalized numbers of body bends (20 s) in whole-body irradiated animals. (b) Normalized numbers of body bends in CNS-irradiated animals. Numbers of body bends (20 s) were averaged from three animals. The value for each irradiation group was normalized by the mean number of body bends in non-irradiated control animals tested at the same time. Finally, data for three independent irradiation experiments were averaged for each group.

60-μm diameter. Although a dose of 500 Gy is enough to reduce motility using whole-body irradiation, it required 1,000 Gy to induce the same effects with CNS irradiation. Thus, the CNS may be a key tissue, but it is not the main effector of radiation-induced changes in motor control.

The results provide the first evidence for involvement of the CNS in radiation-induced reduction of motility in adult hermaphrodite *C. elegans* irradiated area and dose dependency. These results have important implications for research into the individual effects of radiation.

References
[1] M. Suzuki *et al.*, J. Radiat. Res. **58**, 881 (2017).
[2] M. Suzuki *et al.*, QST Takasaki Annu. Rep. 2017, **QST-M-16**, 84 (2019).
[3] M. Suzuki *et al.*, J. Neurosci. Methods. **306**, 32 (2018).
[4] M. Suzuki *et al.*, J. Vis. Exp. **145**, e59008 (2019).

2 - 07 Analysis of the Effects of EGFR Signaling on Radiation Effects

T. Hara [a], T. Aoki [a], H. Sato [b], T. Funayama [c], Y. Nakagami [d], A. Okazaki [e], Y. Suzuki [f] and T. Nakano [b]

[a] Department of Radiological Technology, Gunma Prefectural College of Health Sciences,
[b] Department of Radiation Oncology, Gunma University Graduate School of Medicine,
[c] Department of Radiation-Applied Biology Research, TARRI, QST,
[d] Department of Radiology, Dokkyo Medical University,
[e] Department of Radiation Oncology, Tsuboi Cancer Center Hospital,
[f] Department of Radiation Oncology, Fukushima Medical University School of Medicine

In order to clarify the role of the intercellular communication pathway in the cell effect of radiation, we have investigated the role of the epidermal growth factor receptor (EGFR) pathway in the induction of the irradiation effect in colon cancer cells. We investigated whether there were differences in X-rays and carbon ions in the effects of EGFR on radiosensitivity.

Exponentially growing cells were prepared by plating 3×10^4 cells in 35-mm culture dishes 48 h before experimentation. When we irradiated X-rays, all irradiation was carried out with an X-ray generator (MBR-1520R-3, Hitachi Medico, Tokyo, Japan) operated at 150 kV and 20 mA with a 1 mm aluminum equivalent filter, at a source to surface distance of 40 cm and a dose rate of 4 Gy/min at room temperature. Prior to heavy-ion irradiation, conditioned medium from cell monolayers was collected, and the dishes were covered with 8-μm-thick Kapton polyimide film to keep the cells hydrated. Soon after carbon ions (18.3 MeV/nucleon, 108 keV/lm), the conditioned medium was transferred back to the dishes. After irradiation, cells were incubated at 37 °C for 24 h in the presence or absence of cetuximab, an inhibitor of EGFR. When cells were treated with a combination of cetuximab and irradiation, the drug was added immediately before irradiation.

The growth inhibitory effects of cetuximab or irradiation, or both, were also assessed with clonogenic assays. After 24 h treatment with cetuximab or radiation, cells were trypsinized, counted, and replated in 60-mm culture dishes with 150-20,000 cells/dish based upon the dose of radiation and the concentration of the cetuximab at which 100 colonies/dish were obtained. Cells were incubated for 10-14 days to allow colony formation, and then were stained with 0.5% crystal violet.

The results are shown in Fig. 1 and Fig. 2. As shown in Fig. 1, treatment with 0.1 μM of cetuximab enhances the radiation-induced death of HT29 cells. However, as shown in Fig. 2, in contrast to the effect on X-ray irradiation, even this concentration of cetuximab does not greatly increase the cytotoxic effect of carbon irradiation in HT29 cells.

In summary, regarding photon irradiation, it has been reported that EGFR translocates to the nucleus after irradiation, and that translocation of EGFR to the nucleus is inhibited by cetuximab [1]. Therefore, the radiosensitization effect shown when X-rays and cetuximab are used in combination is considered to be due to the inhibition of EGFR nuclear translocation. However, no sensitizing effect was observed with carbon ion radiation, and it is considered that EGFR did not translocate nucleous.
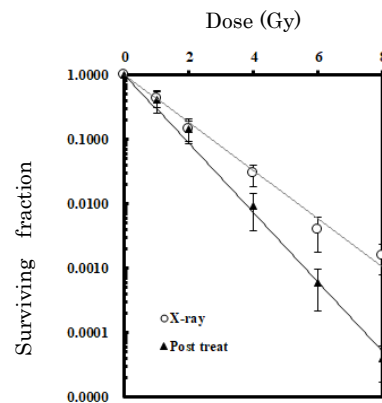
Fig. 1. Effect of Cetuximab on X-ray irradiation in HT29 cells. Cetuximab increased the cytotoxic effects of radiation.
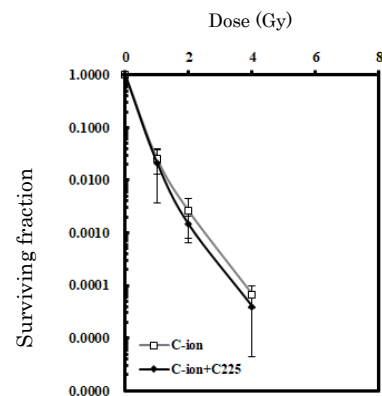
Fig. 2. Effect of Cetuximab on carbon ion irradiation in HT29 cells. Cetuximab did not increased the cytotoxic effects of radiation.

Reference
[1] DJ. Chen *et al.*, Clin. Cancer Res., **13 (22)**, 6555-6560 (2007).

2 - 08 Foci Formation of Phosphorylated H2AX After Mixed High-LET Radiation Exposure

R. Tetsuka [a)], T. Funayama [b)] and A. J. Nakamura [a)]

[a)] College of Science, Ibaraki University,
[b)] Department of Radiation-Applied Biology Research, TARRI, QST

It is well known that organisms are exposed to various types of stresses in space. Especially, space radiation exposure is considered severe stress that affects organism health as the exposure dose is larger than the earth. These space radiations including high energy particles induce complex DNA damage. Furthermore, radiation exposure would occur under microgravity environment in space that might induce different response for radiation exposure from that on the ground. Since failure of DNA damage repair may induce genomic instability and increase the risk of developing cancer, it is important to understand the difference of DNA damage response after space radiation exposure. Therefore, in this study, we evaluate the DNA damage responses after radiation exposure by immunostaining for phosphorylated H2AX (γ-H2AX) to assess the biological impact of those stresses in space.

Histone H2AX, which is as key protein in DNA repair, is rapidly phosphorylated at the site of DNA double-strand breaks (DSBs) following DNA damage induction [1-3]. Upon DNA DSB induction by ionizing radiation (IR), the accumulation of hundreds of molecules of various DNA repair proteins including γ-H2AX can be visualized as a large focus at the DNA DSB site which is known as Ionizing Radiation Induced Foci (IRIF) [4]. The γ-H2AX foci serve as sites of accumulation of DNA repair proteins and may also induce chromatin remodeling possibly to aid access of repair proteins to the DSB sites. Therefore, the formation of γ-H2AX foci is critical for efficient DNA repair and for the maintenance of genome stability.

In this study, we analyzed kinetics of γ-H2AX foci formation and cell survival rate by colony formation assay after exposure of proton beam (20 MeV), helium ion beam (63 MeV) and carbon ion beam (190 MeV) that are considered as a component of cosmic rays. Moreover, we investigated the foci formation after the combination of helium ion beam and carbon ion beam exposure.

TIG-3 (normal human diploid skin fibroblast) were plated on chamber slides and exposed to radiation. Cells were fixed by 2% paraformaldehyde and immunostained for γ-H2AX. As shown in figure 1, carbon ion beam, which causes more complex DNA damage than the helium ion, induced larger γ-H2AX foci size than helium ion beam at one hour after exposure. Interestingly, both large and small size of foci formation was observed in carbon and helium ion mixed beam irradiated cells. These results indicate that the radiation-induced γ-H2AX foci size is depend on energy of the radiation and large γ-H2AX foci might be resulted by clustered DNA lesion. Our finding that show this
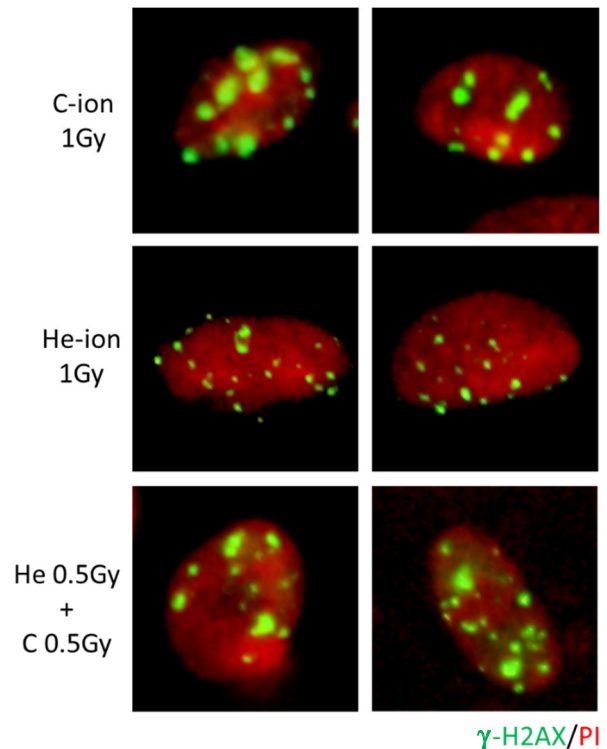
Fig. 1. Representative Images for γ-H2AX foci formation after radiation exposure. TIG-3 cells were exposure to either C-ion (1 Gy), He-ion (1 Gy), or both C-ion (0.5 Gy) and He-ion (0.5 Gy), and then fixed at 1 h post irradiation.

heterogeneity of γ-H2AX foci size which may affect DNA damage repair response, is quite unique and novel.

This study might provide new insights into DNA damage repair responses in space.

References

[1] W. M. Bonner *et al.*, Nat Rev Cancer. **12,** 957 (2008).
[2] E. Rogakou *et al.*, J Cell Biol. **146**, 905 (1999).
[3] E. Rogakou *et al.*, J Biol Chem. **273**, 5858 (1998).
[4] T. T. Paull *et al.*, Curr Biol. **10,** 886 (2000).

2 - 09　　DSB Production in DNA Irradiated with $^4He^{2+}$ and $^{12}C^{6+}$ in a Cell-Mimetic Aqueous Solution

K. Akamatsu and N. Shikazono

Department of Quantum Beam Life Science, KPSI, QST

Introduction

Ionizing radiation-induced DNA damage can cause mutation and carcinogenesis. In particular, "clustered damage", that is a DNA region with two or more lesions within a few helical turns, is believed to be hardly repaired. This damage is considered to be induced around high-LET ionizing radiation tracks. However, detail of the damage is unknown. So far we have studied non-DSB type clustered damage using FRET (Förster resonance energy transfer) method [1]. We are now developing another method for studying structural feature of DNA DSB end and affinity between the DSB end and a repair protein. We have tried to irradiate ^{60}Co γ-rays, helium-, and carbon- ion beam with LET of ~0.3, ~19, and ~150 keV/μm, respectively, to pUC19 in a cell-mimetic buffered solution. We found that the high LET carbon ions tend to produce direct DSB (except for a DSB produced by opposed close SSBs) compared with ^{60}Co γ-rays.

Experiments and Results

Super-coiled pUC19 was used for DNA samples to be irradiated. The DNA was dissolved in 0.2 M Tris-HCl buffer (pH 7.5), which is a cell-mimetic condition, to be ~10 g/L. The DNA solution was transferred to a glass plate (thickness of the solution: 0.1 mm), and was irradiated with $^4He^{2+}$ (50 MeV, LET: ~19 keV/μm, HY) and $^{12}C^{6+}$ (190 MeV, LET: ~150 keV/μm, HY). In addition, ^{60}Co γ-rays were also used as a standard radiation source. The irradiated DNA was purified by ethanol precipitation, followed by being dried in vacuum. The dry DNA pellet was kept at -20 °C until use.

The irradiated DNA was dissolved in TE (2 g/L). The DNA samples were analyzed by agarose gel electrophoresis (1% gel, 70 V, 4 °C, 5 h). The separated DNA fractions (form I, II, III) dyed with ethidium bromide were quantified using a gel image analyzer.

Figure 1 shows relationships between fractions of three forms of pUC19 and absorbed dose of the radiation tested. The ratios of DSB to SSB yield for the γ-rays, helium and carbon beam were approximately 0.08, 0.08, and 0.26, respectively. It is clearly found that high LET carbon beam tends to produce a direct DSB (except for a DSB by sequentially-produced opposed close SSBs) compared with the other lower LET radiation sources.

We now study how a repair protein recognize and process a DSB end using form III fraction obtained by the irradiation experiments.
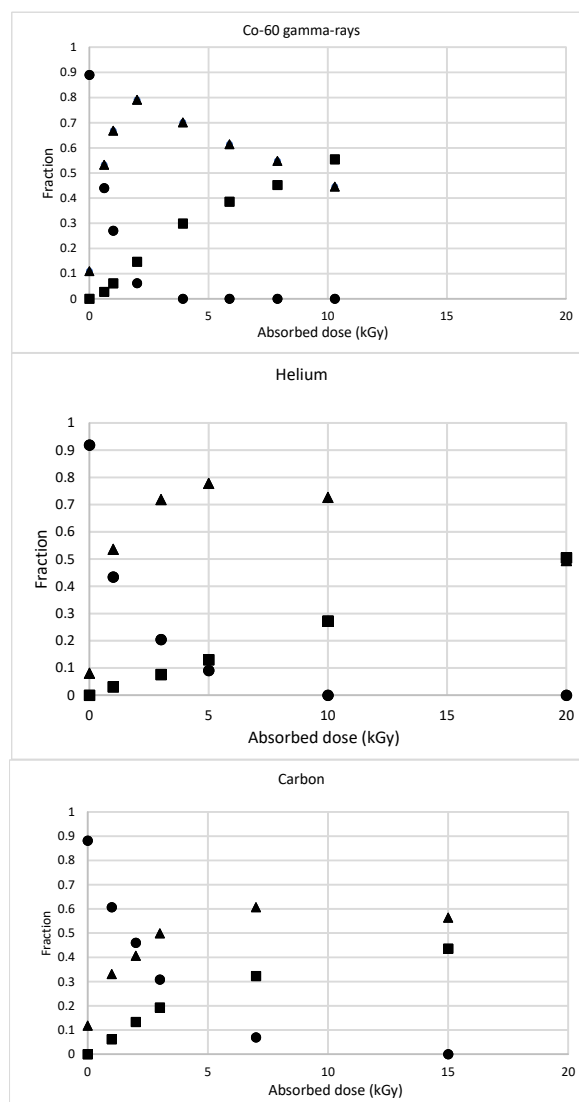
Fig. 1. Fractions of super coiled (●: form I), open circular (▲: form II), and linear (■: form III) DNA for ^{60}Co γ-rays (upper panel, LET: ~0.3 keV/μm), helium (center, LET: ~19), and carbon ion beam (lower, LET: ~150) as a function of absorbed dose.

Acknowledgments

Reference

[1] K.Akamatsu *et al.,* Anal. Biochem., **536** ,78-89 (2017).

2 - 10   Identification of Candidate Genes for Mutated Phenotype by Genome Analysis of Ion-beam-induced Rice Mutants

Y. Oono [a), H. Ichida [b), R. Morita [b), S. Nozawa [c), K. Satoh [a), A. Shimizu [d), H. Kato [d), T. Abe [b) and Y. Hase [a)

[a) Department of Radiation-Applied Biology Research, TARRI, QST,
[b) Beam Mutagenesis Group, RIKEN Nishina Center,
[c) Department of Research Planning and Promotion, QuBS, QST,
[d) Radiation Breeding Division, Institute of Crop Science, NARO

Ion beams are useful mutagens for plant and microbe breeding. They are thought to cause mutations by distinct mechanism from chemical mutagens or gamma rays. To understand the property of induced mutations at a genomic level, we have conducted exome analysis of genomic DNA of rice mutants isolated from a carbon ion-beam-mutagenized population [1-3].

Five independent rice (cultivar Nipponbare) mutant lines (2 dwarfs (lines A and B) and 3 early-heading-date mutants (lines C to E)), of which phenotype was confirmed in the M3 generation, were isolated from seed-irradiated popullation (40 Gy of 320-MeV $^{12}C^{6+}$ ions) [1,2]. The exome analysis identified a total of 56 mutations. The average number of mutations per line was 11.2 ± 3.3 [3]. Among 56 mutations, 6 (1.2 mutations per line on average) were classified as high-impact mutations that cause a frame shift or loss of exons and putativelly generate defective proteins. The identification of a small number of high-impact mutation suggests that it could be easy to detect a causal gene responsible for the mutant phenotype. Indeed, we have found candidate genes likely causing the mutant phenotype in the 4 out of the 5 mutants.

In one of the dwarf lines, line A, the only high-impact mutation was a 128-bp deletion spanning the 3rd intron and 4th exon of the guanine nucleotide-binding protein alpha-1 subunit (*GPA1*, also called *RGA1* or *D1*) gene (Fig. 1(a)). The functional disruption of this gene is known to cause the Daikoku Dwarf phenotype.

Three high-impact mutations were found in the line C, an early-heading-date mutant line. Among them, the *PHYTOCHROME B* (*PHYB*) gene with 5-bp deletion was likely a causual gene because similar phenotypes were also reported in a rice *phyB* mutant (Fig. 1(b)).

The only high impact mutation identified in another early-heading-date mutant line D was a 33.6-kb large deletion with 5 genes (Fig. 1(c)). The *HEDAING DATE 16* (*HD16*) gene was the most likely candidate for the early-heading phenotype. The *HD16* gene encodes a casein kinase I protein and is known to act as an inhibitor of rice flowering.

The line E is also an early-heading-date mutant and has one high-impact mutation, which was a 543-kb inversion on chromosome 6 (Fig. 1(d)). The *HEADING DATE 1* (*HD1*) gene was desrupted by this inversion. *HD1* gene encodes a transcription factor regulating the expression of HEADING DATE 3, a mobile flowering signal.
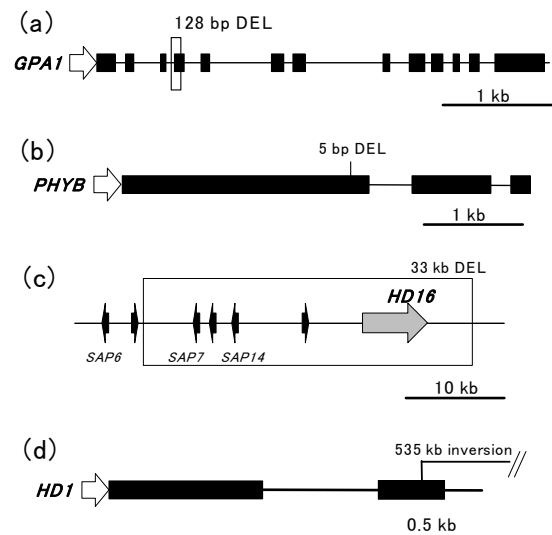
Fig. 1. Structure of candidate genes and position of mutations. Black boxes indicate exons, and a white arrow represents the 5' untranslated region. Introns and 3' untranslated regions are indicated by black lines.
(a) The mutation in the *GPA1* gene of the line A is indicated by a blank box.
(b) The 5-bp deletion in the *PHYTOCHROM B* gene of the line C.
(c) Relative position of the genes (solid arrows) in and near the 33-kb deletion in the line D. The *HD16* gene is indicated with a gray arrow.
(d) One of the break points of the 535-kb inversion in the line E is located in the second exon of the *HD1* gene.

References
[1] Y. Oono *et al.*, QST Takasaki Ann. Rep. 2015, **QST-M-2**, 127 (2017).
[2] Y. Oono *et al.*, QST Takasaki Ann. Rep. 2016, **QST-M-8**, 93 (2018).
[3] Y. Oono *et al.*, QST Takasaki Ann. Rep. 2017, **QST-M-16**, 87 (2019).

2 - 11　Construction of Mutant Lines of the Parasitic Plant *Cuscuta campestris* Yuncker by Carbon Ion Irradiation

R. Yokoyama [a)], K. Satoh [b)] and Y. Oono [b)]

[a)] Graduate School of Life Sciences, Tohoku University,
[b)] Department of Radiation-Applied Biology Research, TARRI, QST

Parasitic plants have a remarkably broad host range, and cause vast damage in agriculture. *Cuscuta* species is one of the most widespread group of parasitic plants that subsists on various plant species, including economically important crops (Fig.1) [1]. Understanding the molecular basis of the parasitic processes of *Cuscuta* species is of critical importance to crop production [2]. At present, however, several tools for molecular genetics and genomics in *Cuscuta* species have not been developed including mutant collections and whole genome sequencing.

Fig. 1. *Cuscuta campestris* infecting the host plant *Arabidopsis thaliana*.

We chose *Cuscuta campestris* as a model system for molecular genetics and genomics in *Cuscuta* species because of its relatively small genome size (550 Mb). We established homozygous lines of *C. campestris* for identical genotype by self-pollination, and sequenced the the genomes of the homozygous lines. Following the sequencing of *C. campestris* genome, we planned to produce ion-beam irradiated *C. campestris* populations on a large scale for finding the various mutants in the same genetic background.

We first investigated the dose-response relationship of the rates of germination, seedling growth and parasitism to determine the irradiation dose suitable for producing a large scale of population harboring mutants. We irradiated *C. campestris* seeds with 30 to 3000 Gy of 190-MeV carbon ions. The seeds were germinated and grown on wet paper in petri-dishes. After 2 weeks in culture, the effects of different irradiation doses on seed germination and seedling growth were evaluated. There was little relationship of irradiation to the rate of seed germination, whereas subsequent seedling growth was affected by higher doses of irradiation. The ratio of the number of seedlings growing to >3 cm in height decreased when the seeds were irradiated at 300 Gy and 3000 Gy (Fig.2).

We next examined the effects of irradiation on parasitism. The *C. campestris* seedlings were attached to the basal stem region of *Arabidopsis thaliana* (the host plant), and irradiated with blue light, which is known to promote parasitism in *Cuscuta* species. After 2 days of blue light irradiation, the seedlings were grown with the host plants in continuous white light at 22 °C. Successful parasitism was clearly inhibited when the seeds were irradiated at a dose higher than 100 Gy. The ratio of the number of parasitism in the irradiated seedlings decreased as the irradiation dose to the seeds increased, with 51%, 21% and 8% of the number of parasitism in non-irradiated seedlings when irradiated at 100 Gy, 300 Gy and 3000 Gy, respectively (Fig.3). These results indicated that the survival rate of the seedlings irradiated at a dose higher than 100 Gy was less than about 50% since *C. campestris* completely depends on its host for resources. We further plan to evaluate parasitism of seedlings irradiated at doses ranging from 30 to 100 Gy to determine the irradiation condition suitable for producing a large scale of population harboring mutants.
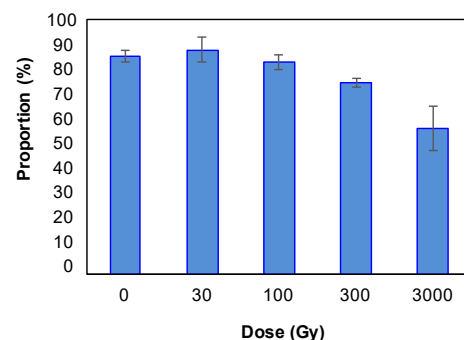
Fig. 2. Effect of irradiation of seedling growth. The proportion of the seedlings growing to >3 cm in height was examined after 2 weeks in culture. Error bars represent SE (n=3).
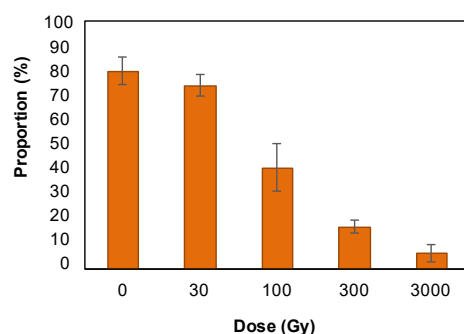
Fig. 3. Effect of irradiation of parasitism. The proportion of the seedlings parasitizing the host plants. Error bars represent SE (n=3).

References
[1] Y. Kaga *et al.,* Seibutsu-Kagaku-Iden, **70**, 284 (2016).
[2] A. Hozumi *et al.,* Plant Cell Physiol., **58**, 1868 (2017).

2 - 12 Analysis of Mutation Frequencies on Flavonoid Biosynthetic Genes in Irradiated Arabidopsis Plants

S. Kitamura [a), S. Hirata [a,b), K. Satoh [a), I. Narumi [b) and Y. Oono [a)

[a) Department of Radiation-Applied Biology Research, TARRI, QST,
[b) Graduate School of Life Sciences, Toyo University

As ionizing radiations such as gamma-rays and ion beams can induce mutations effectively, they are widely used for modifying agronomically important characteristics in plants and microbes. In general, mutations are thought to occur in random. However, it has been reported that there might be a kind of rules in occurrence of mutations spontaneously [1] and those induced by ionizing radiations [2, 3]. We previously reported an experimental system that can easily detect mutated tissues by visual inspection using two genes required to synthesize flavonoid pigments in Arabidopsis [4]. Here, using this system, we expanded the number of plants analyzed and found a statistical difference in frequency of two mutated tissues.

In Arabidopsis, flavonoid pigments are synthesized by an enzymatic pathway in which a single copy gene is involved in each enzymatic step. Inactivation of one of those genes results in colorless seed coat, called transparent testa (tt). Using the pathway, we constructed a mutation detection system based on loss of heterozygosity. We generated a double heterozygous plant *TT4/tt4 TT8/tt8*. This plant shows brown in seed coat, although *tt4* and *tt8* homozygous mutants show pale yellow and pale brown in seed coat, respectively. Therefore, if wild-type *TT4* or *TT8* allele is inactivated by mutations in the heterozygous plant, the resulting *tt4-* or *tt8*-homozygous cells could contribute to the production of paler colored seeds that are easily discriminated from wild type brown seeds.

The double heterozygous seeds were sown on nutrient media. The germinated 1-day-old seedlings were irradiated with carbon ion beams with similar LETs (220 MeV $^{12}C^{5+}$ carbon ions, LET = 121.5 keV/μm; 190 MeV $^{12}C^{6+}$ carbon ions, LET = 148.7 keV/μm) at TIARA, TARRI, QST. The irradiated seedlings were grown under normal conditions, and color of the seeds from those plants was investigated.

Using total RNA from 1-day-old seedlings of the double heterozygous plants, reverse transcription polymerase chain reaction (RT-PCR) was performed. As shown in Fig. 1, transcripts of *TT4* were easily detected but those of *TT8* were hardly detected. Semi-quantitative RT-PCR indicated that the transcripts of *TT4* were approximately two orders of magnitude abundant than those of *TT8*. This implies that, when irradiated, *TT4* rather than *TT8* is highly expressed in the double heterozygous seedlings. Until now, more than 8,000 irradiated plants were investigated for their seed colors. As shown in Table 1, forty-one plants that produced colorless seeds were found in carbon ion irradiated plants. Among them, 3 plants produced pale yellow (*tt4*-type) and 38 plants produced pale brown
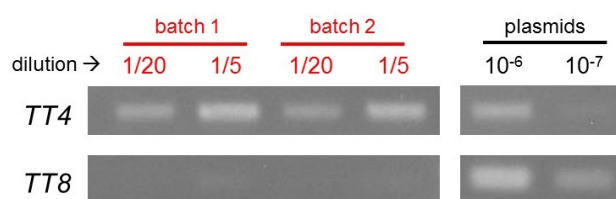
Fig. 1. RT-PCR of *TT4* and *TT8* with RNA from 1-day-old seedlings. Two batches of seedlings gave similar results. Control PCR with cloned plasmids was also shown.

(*tt8*-type) seeds. Chi-squared test indicated that the plants producing *tt8*-type seeds appeared more frequently than those producing *tt4*-type seeds with the statistical difference ($p < 0.01$). The lower frequency of *tt4*-type seeds might be involved in higher expression of *TT4* during mutagenesis. If this is the case, the results observed here is related to mechanisms like a transcription coupled DNA repair [5, 6]. Alternatively, the lower frequency of *tt4*-type seeds might reflect the result of cell competition after mutagenesis; because *TT4* encodes the first committed enzymatic step in flavonoid synthesis, *tt4*-homozygous cells that completely lack flavonoids might be slower in their growth than surrounding normal cells. Further analysis will be necessary to address the mutagenesis mechanisms in plant cells.

Table 1

Screening of *tt* mutations in double heterozygous plants.

mutagen	No. of plants	No. of plants with colorless seeds		
		total	*tt4*-type	*tt8*-type
none	3,278	1	0	1
carbon ions	8,186	41	3	38 *

Asterisk indicates significantly higher than a fraction of *tt4* (Chi-squared test, $p < 0.01$).

References

[1] I. Martincorena *et al.*, Nature, **485**, 95 (2012).
[2] Y. Hase *et al.*, Plant Biotechnol., **27**, 99 (2010).
[3] M. Okamura *et al.*, Euphytica, **202**, 333 (2015).
[4] S. Hirata *et al.*, QST Takasaki Annu. Rep. 2016, **QST-M-8**, 94 (2018).
[5] V. Kamarthapu and E. Nudler, Curr. Opin. Microbiol., **24**, 15 (2015).
[6] T. Yasuhara *et al.*, Cell, **175**, 558 (2018).

2 - 13   Lethal Effect of Carbon Cluster Ion Beams from TIARA 3 MV Tandem Accelerator in Bacterial Spores

Y. Hase [a), K. Satoh [a), A. Chiba [b), Y. Hirano [b), Y. Saito [b) and K. Narumi [b)

[a) Department of Radiation-Applied Biology Research, TARRI, QST,
[b) Department of Advanced Radiation Technology, TARRI, QST

It has been known that the cluster ion beams have specific irradiation effects, such as nonlinear increase of secondary particle emission, due to their unique features in energy deposition [1]. However, the biological effects of cluster ion beams are yet to be determined. The currently available cluster ion beams are in keV to MeV energy range of electrostatic accelerators. In order to consider the biological effects of cluster ion beams, we employed the spores of *Bacillus subtilis*, because they are thin enough (< 1 µm) compared to the calculated range of the cluster ion beams (> 3µm) and also tolerant to vacuum environment for irradiation. In our previous studies, we established the preparation method for monolayered spore samples [2], and also confirmed the accuracy of particle fluence for monomer and cluster carbon ion beams using a solid-state track detector [3]. Here, we report the results on the lethal effects of monomer and cluster carbon ion beams from TIARA 3MV tandem accelerator in the spores.

Figure 1 shows the lethal effects of 2 MeV C, 4 MeV C_2 and 6 MeV C_3. The data are the mean ± SD of three independent experiments. Contrary to our expectations, as shown in Fig. 1(a), there was no significant difference between the cluster and monomer ion beams per particle. This indicates that the 4 MeV C_2 and 6 MeV C_3 are two times and three times less effective per atom, compared with 2 MeV C, respectively (Fig. 1(b)).

These results could be due to the very high LET of 2 MeV C (1141 keV/µm). To gain insights on this point, the LET - RBE (relative biological effectiveness) relationship was examined. The spores were irradiated with five kinds of ion beams from TIARA AVF cyclotron and ^{60}Co gamma rays. The RBE was determined based on the dose required to reduce the surviving fraction to 0.1. As shown in Fig. 2, the RBE peaked at 156 keV/µm, and dropped below 1.0 for 2 MeV C and 310 MeV Ar (2214 keV/µm). These results suggest that the single atoms of 2 MeV C deposit energy more than enough to kill the spores, and therefore, there was no significant difference between the cluster and monomer ion beams under this experimental condition. We will further examine the biological effect of cluster ion beams in the LET range less than 150 keV/µm using proton ions.

Acknowledgment

References

[1] A. Chiba *et al.*, Nucl. Instr. Meth. Phys. Res. B, **315**, 81-84 (2013).
[2] Y. Hase *et al.*, QST Takasaki Annu. Rep., 2016, **QST-M-8**, 103 (2018).
[3] Y. Hase *et al.*, QST Takasaki Annu. Rep., 2017, **QST-M-16**, 93 (2019).
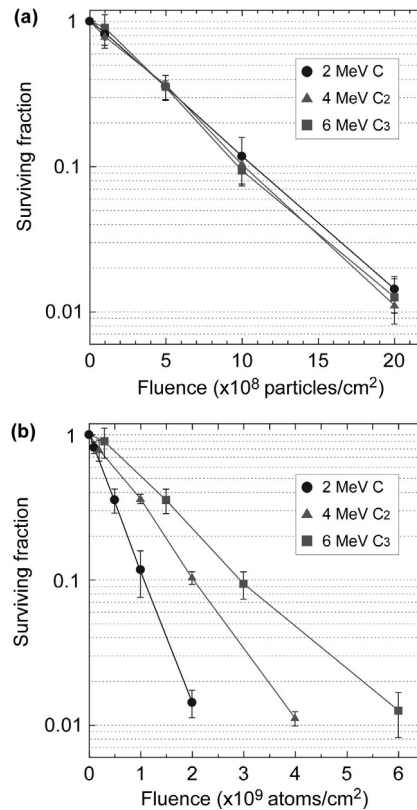
Fig. 1. Surviving fraction of *B. subtilis* spores irradiated with 2 MeV C[+], 4 MeV C_2[+] and 6 MeV C_3[+]. Surviving fraction is shown as a function of particles/cm² (a) and atoms/cm² (b).
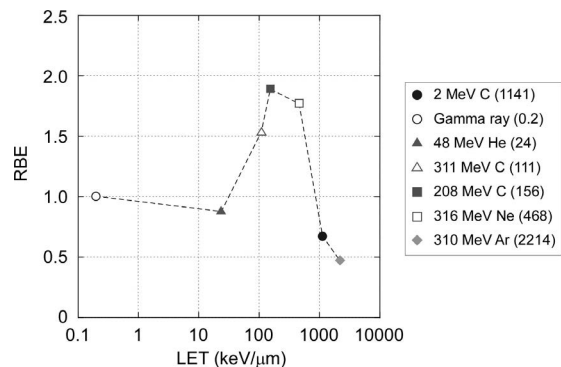
Fig. 2. Relationship between LET and RBE based on the dose required to reduce the surviving fraction to 0.1. Values in parenthesis represent the LET (keV/µm) for each ion species.

2 - 14   Generation and Screening of *Azospirillum* Mutants with Improved Plant Growth-Promoting Effects Using Ion-Beam

M. Yasuda [a)], K. Satoh [b)], Y. Oono [b)], T. Yokoyama [a)] and S. Okazaki [a)]

[a)] Tokyo University of Agricultural and Technology,
[b)] Department of Radiation-Applied Biology Research, TARRI, QST

Higher plants are continually exposed to a huge variety of microbes. Some rhizosphere bacteria are well-known as plant growth-promoting rhizobacteria (PGPR), and the PGPR can enhance plant growth by a wide variety of mechanisms including phytohormone production, biofilm production, biological nitrogen fixation and rhizosphere engineering etc. *Azospirillum*, one of the well-studied PGPR, are widespread in soil and their inoculation on cereals and forage crops results in yield increases in many field experiments, not only due to nitrogen fixation, but also through the production of plant growth-promoting substances, such as the phytohormones.

Azospirillum sp. B510 (B510) is a diazotrophic endophyte that has been isolated from the stems of a rice plant (*Oryza sativa* cv. Nipponbare) [1]. Increased seed production by B510-colonized rice plants was demonstrated under greenhouse, paddy field, and laboratory conditions [2,3]. Moreover, rice plants inoculated with this bacterium induced resistance against rice blast disease and rice blight disease [4]. The complete genome sequence of B510 has been determined [5]. A comparative metabolomic analysis revealed that rice plants inoculated with B510 induced a modified metabolic response in shoots and roots, suggesting that this bacterium triggers a systemic response against pathogens [6]. Recently, we reported that the colonization of B510 of rice plants is affected by nitrogen fertilizers [7]. In this study, we conducted mutagenesis using ion beam irradiation and screened B510 mutants with improved beneficial phenotypes for PGBR such as motility.

The B510 was grown in nutrient broth (NB) at 28 °C for 30 h. Aliquots (0.1 mL) of bacterial suspension (5×10^7 cfu/mL) were dropped onto sterilized membranes in petri dish (30 mm diameter) and these dishes were covered with sterilized polyimide film. Cells were irradiated at different doses (0, 10, 50, 100, 200, 500, 750 and 1000 Gy) with carbon ion beams ($^{12}C^{6+}$, 190 MeV) accelerated by an AVF cyclotron at TIARA, QST. Survival rates were determined by comparing the number of colonies per dish and the most appropriate doses to produce mutants were selected.

As expected, survival rates were decreased by radiation dose (Fig. 1). We then decided to use irradiation dose 50 and 100 Gy to generate mutants as it resulted in the survival rate of approximately 1%. It was known that motility is important for many PGPR to move and colonize on the surface of host plants. We therefore screened mutants with improved motility ability using the B510 cells exposed to the irradiation. We inoculated mutants on a semi-solid agar plate (NB containing 0.6% agar) and incubate at 28 °C for 24 h in dark condition. Until now, we analyzed over 400 colonies and got 6 mutants that showed enhanced motility (Fig. 2).

In conclusion, we set up the condition of Ion-beam mutagenesis for a PGPR *Azospirillum* sp. B510. In a first screening, we successfully isolated 510 mutants with enhanced motility, suggesting that the Ion-beam mutagenesis is a useful tool to generate mutants with ideal characteristics.
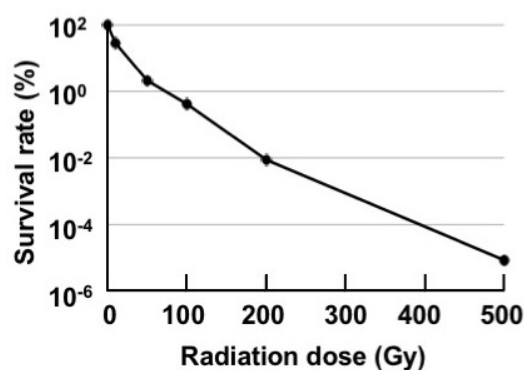
Fig. 1. Survival of *Azospirillum* sp. B510 to carbon ion beams.
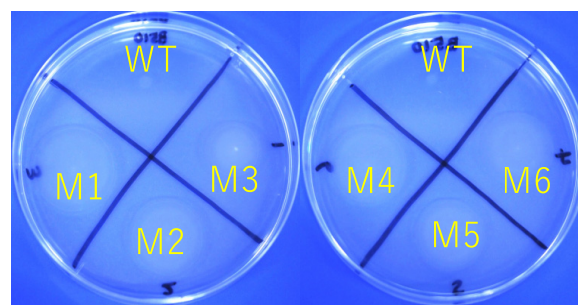
Fig. 2. Comparison of motility ability between *Azospirillum* sp. B510 (WT) and mutants (M1 to 6). Enhanced motility means the bacteria can move faster to colonize host plants.

References
[1] A. Elbeltagy *et al.*, Appl. Environ. Microbiol., **67**, 5285 (2001).
[2] T. Isawa *et al.*, Microbes Envion., **25**, 58 (2010).
[3] K. Sasaki *et al.*, Soil. Sci. Plant Nutr., **56**, 636 (2010).
[4] M. Yasuda *et al.*, Biosci. Biotech. Biochem., **73**, 2595 (2009).
[5] T. Kaneko *et al.*, DNA Res., **17**, 37 (2010).
[6] A. Chamam *et al.*, Phytochemistry, **87,** 65 (2013).
[7] K. Naher *et al.*, Microbes Environ., **33**, 301 (2018).

2 - 15　Functional Analysis of DNA Double-Strand Break Repair Genes Using Knockout Strains of *Physcomitrella patens*

Y. Yokota and A. N. Sakamoto

Department of Radiation-Applied Biology Research, TARRI, QST

Introduction

Many plants are known to be radiation resistant, but the mechanism has not been fully elucidated. *Physcomitrella patens* is a model moss plant that has a genome size of 511 Mb and 17 chromosomes and spends most of its life cycle as haploid. We have shown that cells of *P. patens* are 200-times more radioresistant than mammalian cells [1]. This study analyzes the function of the DNA double-strand break (DSB) repair genes in *P. patens*.

Methods

Dr. Nogué (INRA, France) provide us the *P. patens* knockout strains of *LIG4*, *RAD51B* and *POLQ*, which are genes involved in non-homologous end joining (NHEJ), homologous recombination (HR) and alternative end joining (alt-EJ) pathway of DSB repair, respectively. The plant tissues were irradiated with ^{60}Co gamma rays or 220-MeV carbon ions (LET = 108 keV/µm). To estimate the radiosensitivity, irradiated plant tissues were grown for 6 days and dry weight was measured.

Results and Discussion

When *lig4*, *rad51b* and *polq* strains in which *LIG4*, *RAD51B* and *POLQ* were knocked out, respectively, were irradiated with gamma rays, the *rad51b* strain was the most radiosensitive among them (Fig. 1). Next, the relationships between dose and growth suppression were investigated by measuring dry weight as an indicator (Fig. 2). The *lig4* strain was slightly more radiosensitive than the wild type, meaning that the wild type repaired a part of DSBs by the NHEJ pathway. The *rad51b* strain was significantly more radiosensitive than the wild type, indicating that the wild type repaired most DSBs by the HR pathway. The *polq* strain was slightly more radioresistant than the wild type in the low dose range and slightly more radiosensitive in the high dose range. In human tumors, POLQ gene product has been reported to negatively regulate error-free HR [2]. Thus, in the *polq* strains of *P. patens*, it is thought in the low dose range that DSB repair is error-free and radioresistance is increased because the HR pathway processes excess DSBs that are normally repaired by the error-prone alt-EJ pathway. In contrast, it is thought in the high dose range that DSB repair is delayed and radiosensitivity is increased because DSB yield exceeds the capacity of the HR pathway. The doses of gamma rays and carbon ions that reduced the dry weight of plant tissue by half are 430 Gy and 100 Gy for the wild type, 300 Gy and 100 Gy for the *lig4* strain, 10 Gy and 3.5 Gy for the *rad51b* strain, and 380 Gy and 70 Gy for the *polq* strain, respectively. In *P. patens*, the effect of carbon ions on growth suppression was three to five times greater than that of gamma rays at the same dose.

References

[1] Y. Yokota *et al.*, Genes **9**, 76 (2018).
[2] R. Ceccaldi *et al.*, Nature **518**, 258 (2015).
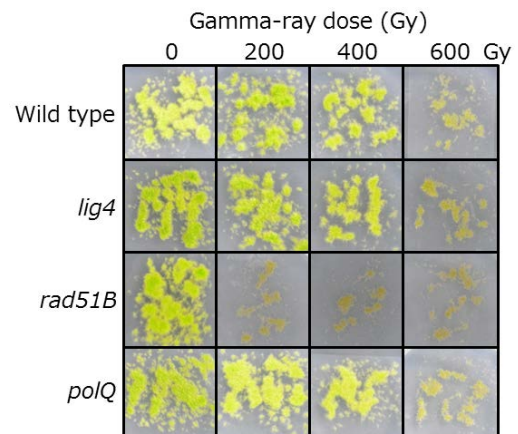
Fig. 1. Representative photos of *P. patens* 6 days after gamma-ray irradiation.
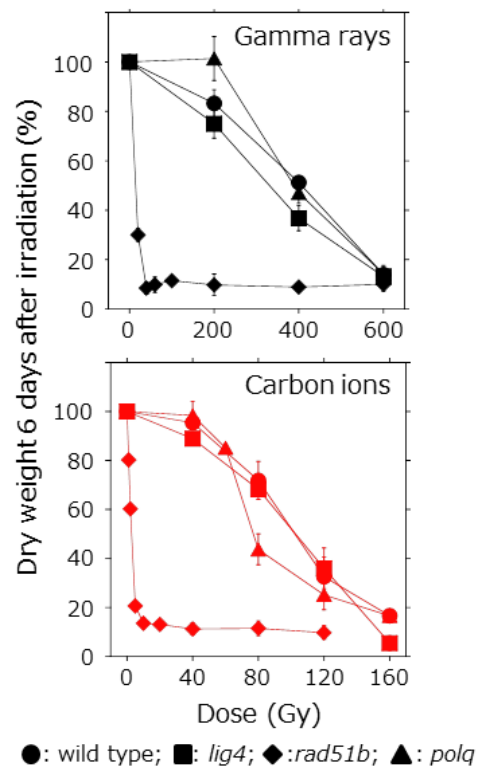
Fig. 2. Growth inhibition of *P. patens* 6 days after gamma-ray or carbon-ion irradiation. Data represent the mean value ± standard error of three or more independent experiments.

2 - 16　　Mutagenesis of the Oil-producing Algae by Heavy Ion Beam Irradiation

H. Araie [a], Y. Hase [b], Y. Iwata [c], Y. Oono [b] and I. Suzuki [d]

[a] Department of Biosciences, Kanto Gakuin University College of Science and Engineering,
[b] Department of Radiation-Applied Biology Research, TARRI, QST,
[c] Electronics and Photonics Research Institute, AIST,
[d] Faculty of Life and Environmental Sciences, University of Tsukuba

For biofuel production by microalgae, it is necessary to improve the algae to high biomass or oil contents strain. In this study, we focused on very-long-alkyl ketones so-called alkenone (Fig. 1) that are thought to be good candidates for biofuels [1]. We selected one of the alkenone-producing haptophytes, *Tisochrysis lutea* (Strain T-Iso)*,* to mutate by heavy ion beam irradiation that is known as a good method to obtain useful mutants [2, 3]. In addition, the mutants obtained by this method can be applicable in the open system as non-GMO.
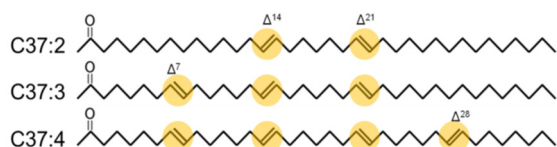
Fig. 1. Alkenone structures. The carbon number of these alkenones is 37 and they have two to four *trans*-type double bonds and a keto group at a C2 position.

So far, we have selected high oil-producing strains by monitoring fluorescence intensity of lipids stained with Nile red regent by using microplate reader. It is considered that these high oil-producing strains will have features such as high photosynthetic activity, high growth rate, and high ratio to lipid in intracellular carbon or the suppression of lipid degradation. Here, we focused on suppression of alkenone degradation.

Alkenone is known to degrade as an energy source like polysaccharides under dark condition [4]. Therefore, we stained intracellular neutral lipids with Nile red regent (final conc. 1 µg / mL) and monitored fluorescence intensity of stained lipids under dark condition by using microplate reader (SYNERGY HTX, BioTek). The excitation and emission wavelengths were 485 and 575 nm for detecting neutral lipids, and 440 and 575 nm to determine the chlorophyll content, respectively.
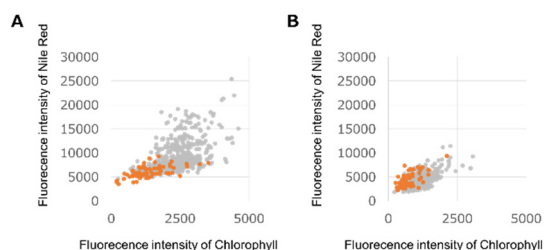
First, we cultured selected high oil-producing strains with 96-well plate for 2 weeks and then put them in dark condition for 1 week. When we compared the fluorescence intensity of lipids before and after 1-week dark condition, we observed a little decrease in fluorescence intensity from 72 strains (Fig. 2). For second screening, we cultured obtained 72 strains with 96-well plate for 2 weeks and then put them in dark condition for 1 week again. As the results, we obtained 9 strains that remained the highest fluorescence intensity in both Nile Red and Chlorophyll as first candidates and following 22 strains as second candidates (Fig. 3).
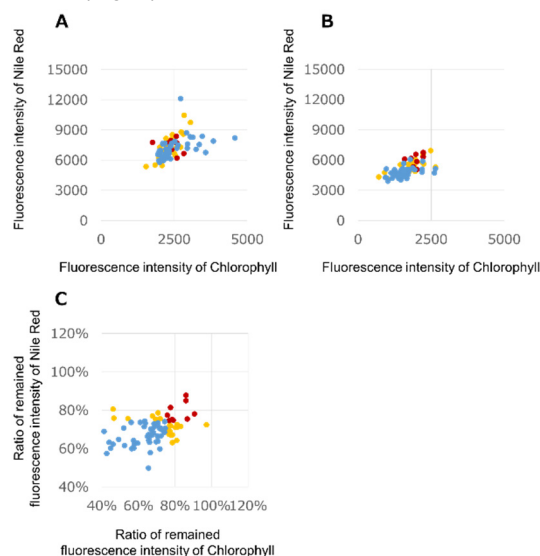
Fig. 3. The second screening of mutants that suppressed lipid degradation. Fluorescence intensity of Nile Red and Chlorophyll before (A) and 1 week after dark condition (B) were measured from 72 strains obtained from first screening. The ratio of remained fluorescence intensity of Nile Red and Chlorophyll after 1 week dark condition (C). Red circle: 9 strains that remained highest fluorescence intensity in both Nile Red and Chlorophyll, Orange circle: 22 strains that remained higher fluorescence intensity in both Nile Red and Chlorophyll, Blue circle: the other strains.

Fig. 2. The first screening of mutants that suppressed lipid degradation. Fluorescence intensity of Nile Red and Chlorophyll before (A) and 1 week after dark condition (B) were measured from 607 strains that were screened as high oil-producing strains. Orange circle: 72 strains that remained high fluorescence intensity in both Nile Red and Chlorophyll, Grey circle: the others.

References
[1] O'Neil *et al.*, Energy Fuels **29**, 922-930 (2015).
[2] Ota *et al.*, Biotechnology for Biofuels **9**, 13 (2016).
[3] Yamada *et al.*, Scientific Reports **6**, 26327 (2016).
[4] Tsuji *et al.*, Marine Biotechnology **17**, 428-440 (2015).

2 - 17 Development of New Strains with Sporeless Mutation in Mushrooms Using Ion Beam Irradiation

M. Kasai [a], M. Ishikawa [a], Y. Hase [b], S. Nozawa [c] and K. Ouchi [a]

[a] Mushroom Research Laboratory, Hokuto Corporation,
[b] Department of Radiation-Applied Biology Research, TARRI, QST,
[c] Department of Research Planning and Promotion, QuBS, QST

To develop novel strains of sporeless mutants, chlamydospores derived from a commercial strain of *Grifola frondosa* were irradiated with 50 MeV helium ion beam. As a result, two sporeless mutants were obtained with the dose of 50 Gy and 100 Gy. Frequency of sporeless mutation and other mutations including unfavorable traits suggested that under 50 Gy were thought to be adequate for developing sporeless mutants with sufficient quality for commercial use.

きのこの胞子飛散は、商品の品質低下や栽培従事者の呼吸器疾患等の問題を起こす可能性がある。これらの問題を解決するため、イオンビーム照射により無胞子性品種を開発し、実用化を目指した。本研究では、マイタケ品種「Grifon120」を供試体とし、無胞子性変異のスクリーニングおよび照射線量の検討を行った。

「Grifon120」菌糸体から厚壁胞子（一部の細胞が厚膜化して形成される無性生殖細胞）を取得し、1.0×10³個/mL に調製した。寒天培地に塗布し、カプトンフィルムで密封した後、高崎量子応用研究所の AVF サイクロトロンにより発生させたイオンビーム（⁴He²⁺, 50 MeV）を 25 Gy-200 Gy の範囲で照射を行った。イオンビーム無照射培地における再生コロニー数に対する照射培地のコロニー数から生存率を算出した。再生コロニーを分離して子実体を発生させ、傘を黒紙上に置いて 20℃ で一晩静置した後、胞子落下の有無を目視で確認した。「Grifon120」よりも胞子落下量が明らかに少ない菌株については栽培試験を反復して再現性を確認した上で、無胞子性変異体とした。また、菌糸生長不良や子実体生育不良といった不良変異を含め、「Grifon120」と明らかに性質が異なる場合、その他の変異体として変異率を算出した。本稿では、計 5 回の照射実験および栽培試験から得られた結果を報告する。

厚壁胞子生存率は、線量の増加に伴って低下した（Fig. 1）。各線量区から再生したコロニーを合計 8134 株分離し、現在までに 4044 株の栽培試験が終了している。その中で、2 株の無胞子性変異体を取得した（Fig. 2A）。これらの菌株は、「Grifon120」と比べて胞子落下量が顕著に少ない性質の再現性が確認でき、イオンビーム照射によりマイタケの無胞子性変異体を作出可能であることが明らかになった。しかしながら、No.97 は栽培性や収量性に問題なく明らかな不良変異を伴わないものの、栽培環境によっては管孔（傘裏に形成される胞子形成器官）の形状が「Grifon120」と異なること（Fig. 2B）、No.1985 は高温での菌糸伸長が悪いことから、商品の見た目や大型栽培に問題が生じる可能性を考慮し、実用化を目指した品種育成には至らなかった。

栽培試験が終了した試験区について、生存率と、無胞子性変異体が得られた確率およびその他の変異率との関係を示した（Table 1）。無胞子性変異体は生存率 70%以上でも得られた。一方、その他の変異率はほとんどが栽培過程での不良変異であり、不良変異を伴わない変異体を得るためには、生存率 70%以上になるような線量すなわち 50 Gy 以下で照射するのが良いと考え

られた。今後は、栽培試験を継続して新たな無胞子性変異体の取得を目指すとともに、交配による改良も検討し、無胞子性変異体の実用化を目指したい。
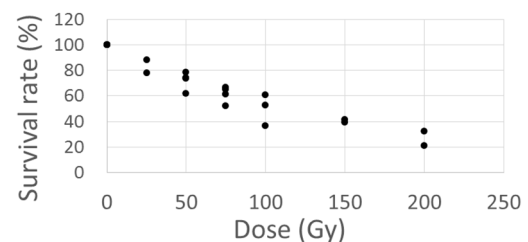
Fig. 1. Effects of ion beam irradiation on survival rate of chlamydospores.
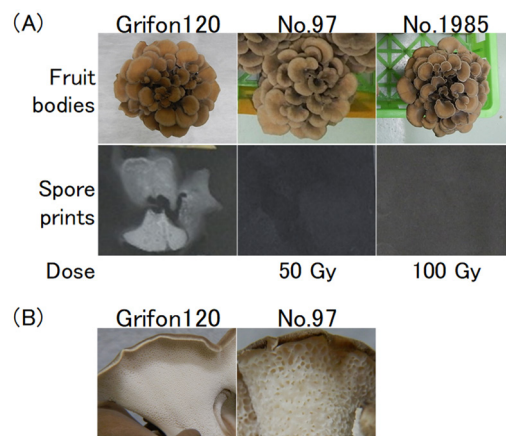
Fig. 2. (A) Fruit bodies and spore prints on black paper of Grifon120 and sporeless mutants obtained by ion beam irradiation with the dose of 50 Gy and 100 Gy.
(B) Morphological difference of tube between Grifon120 and sporeless mutant No.97.

Table 1
Relationship between survival rate and mutant frequency.

Survival rate (%)	Number of regenerated colonies	Number of mutants (Mutant frequency)	
		Sporeless	Other
0–10			
11–20			
21–30	168		168 (100%)
31–40	0		
41–50	377		366 (97.1%)
51–60	0		
61–70	2177	1 (0.05%)	1448 (66.5%)
71–80	1267	1 (0.08%)	449 (35.4%)
81–90	0		
91–100	55		

2 - 18　Pilot-Scale Sake Brewing Tests Using Non-Urea Producing Gunma KAZE Yeasts Which Are Suitable for Export

T. Watanabe [a], K. Satoh [b], Y. Oono [b], H. Hayashi [c] and T. Masubuchi [a]

[a] Gunma Industrial Technology Center,
[b] Department of Radiation-Applied Biology Research, TARRI, QST,
[c] Maebashi Institute of Technology

Urea is a main precursor in Japanese sake of ethyl carbamate which is classified the group 2A "probably the cause of cancer" by International Agency for Research on Cancer. Therefore, it is considered that the countries regulating volume of ethyl carbamate in Japanese sake would be increased. The purpose of this study was to reduce the volume of ethyl carbamate in Japanese sake, we attempted to breed Gunma KAZE yeasts that do not produce urea. However, it was difficult to obtain canavanine resistant mutants, candidates of non-urea producing strains from KAZE2 by natural mutation [1]. Therefore, we demonstrated ion-beam irradiation ($^{12}C^{5+}$, 220 MeV) and obtained two candidates named 100Gy-5 and 100Gy-7. Fermentation profiles of these strains were virtually same as that of parent strain KAZE2 with laboratory-scale sake brewing test using 200 g of total rice [1]. KAZE2 produced 4.9 mg/L of urea in sake brewing whereas no urea was detected in sake brewing using these candidates [1]. For the practical use of these strains, further experiments such as pilot-scale and practical scale sake brewing test are needed. In this year, we demonstrated pilot-scale sake brewing tests using 60 kg of total rice.

By the preliminary experiments, 100Gy-7 was selected as the non-urea producing candidate of KAZE2 (data not shown). Pilot-scale sake brewing tests were performed using 60 kg of total rice (40% polishing of *Yamadanishiki*). *Koji* making was performed using a seed *koji*, High-G (Higuchi Matsunosuke Shoten). KAZE2 and 100Gy-7 were pre-incubated in 25 mL of Koji-extracts at 23 °C for 4 d. *Sokujyo* seed mash was maked using 1 kg of koji, 2 kg of steamed rice, 24 mL of lactic acid, 25 mL of pre-culture, and 4 L of distillery water. Three-step preparation (*soe*, *naka*, and *tome*) for fermentation mash was performed. Each fermentation profile of KAZE2 and 100Gy-7 was almost same (Table 1). Sensory evaluation by 20 sake brewery workers revealed that there were no difference between two sake samples. On the other hand, KAZE2 produced 9.0 mg/L of urea in sake brewing, while 100Gy-7 did not. Therefore, we will examine the fermentation profile of 100Gy-7 with practical scale sake brewing tests.

Reference

[1] T. Watanabe *et al.*, QST Takasaki Annu. Rep. 2017, **QST-M-16**, 97 (2019).

Table 1

Fermentation profile of KAZE2 and 100Gy-7 with pilot-scale sake fermentation test.

KAZE2	Sokujyo seed mash				Fermentation mash															
	2d	4d	5d	BU*	0dori	4d	6d	8d	11d	13d	15d	18d	20d	22d	25d	27d	29d	32d	33d	35d
Ethanol (%)	0.0	6.6	9.7	10.0	3.3	4.6	7.0	9.2	12.5	13.6	14.9	16.1	14.9	15.5	16.4	16.9	16.8	17.6	–	–
Glucose (%)	13.1	11.3	7.9	7.9	15.3	12.7	11.5	9.6	6.9	5.6	4.9	4.2	4.6	4.2	3.9	3.5	3.4	2.9	–	–
Maltose (%)	4.4	3.8	3.3	3.0	3.4	2.1	2.2	2.1	1.8	1.6	1.5	1.3	0.5	0.4	0.8	0.6	0.6	0.4	–	–
Yeast cell number (10^8 cells/mL)	–	1.9	1.8	1.6	1.4	–	1.9	1.8	1.5	1.4	1.6	1.3	0.9	1.1	0.8	0.9	–	–	–	–
Viable cell rate (%)	–	94.7	97.1	96.8	100.0	–	100.0	91.9	94.7	88.5	89.3	92.9	91.7	88.9	76.5	82.4	70.0	65.0	–	–
Isoamyl alcohol (ppm)	–	–	–	–	–	55.4	80.0	98.4	128.3	134.7	143.0	141.7	136.2	143.3	147.7	153.8	137.8	144.3	–	–
Isoamyl acetate (ppm)	–	–	–	–	–	0.5	1.3	2.2	3.4	3.6	3.9	3.7	2.4	3.2	2.1	2.7	1.0	1.5	–	–
Ethyl caproate (ppm)	–	–	–	–	–	0.6	2.4	3.7	5.8	6.5	7.3	7.1	4.3	5.6	4.2	5.0	2.4	3.6	–	–
Ethyl acetate (ppm)	–	–	–	–	–	9.3	20.0	29.6	46.8	54.4	56.7	55.7	39.4	54.5	40.0	51.8	20.5	31.9	–	–
Isobutyl alcohol (ppm)	–	–	–	–	–	21.7	31.4	38.6	47.3	47.0	47.6	46.0	44.6	44.9	45.5	47.7	41.2	45.3	–	–
E/A ratio (–)**	–	–	–	–	–	0.9	1.7	2.2	2.6	2.7	2.7	2.6	1.7	2.2	1.4	1.8	0.7	1.0	–	–

100Gy-7	Sokujyo seed mash				Fermentation mash															
	2d	4d	5d	BU*	0dori	4d	6d	8d	11d	13d	15d	18d	20d	22d	25d	27d	29d	32d	33d	35d
Ethanol (%)	0.0	6.5	9.3	10.5	3.1	4.5	6.8	9.0	11.8	13.3	14.7	15.4	14.3	15.0	16.2	16.6	16.4	17.0	–	17.2
Glucose (%)	12.7	10.7	8.9	7.9	15.1	12.1	12.2	10.6	7.9	6.4	5.6	4.7	5.2	4.7	4.4	3.9	3.8	3.6	–	3.8
Maltose (%)	5.2	4.0	3.1	2.9	3.9	1.6	2.2	2.2	1.9	1.7	1.5	1.4	0.6	0.6	0.9	0.6	0.6	0.5	–	0.6
Yeast cell number (10^8 cells/mL)	–	2.4	2.5	1.5	1.2	–	1.4	1.3	1.4	1.3	1.1	1.2	1.0	1.0	0.8	0.8	0.7	0.7	–	–
Viable cell rate (%)	–	97.9	95.9	96.6	100.0	–	100.0	96.2	93.1	91.7	90.9	90.9	90.5	88.9	85.7	80.0	84.6	73.3	–	–
Isoamyl alcohol (ppm)	–	–	–	–	–	83.6	98.2	118.4	147.3	152.0	161.4	166.7	158.1	151.3	160.3	162.0	144.6	151.4	–	164.0
Isoamyl acetate (ppm)	–	–	–	–	–	0.7	1.9	3.2	4.6	4.8	5.0	5.0	3.3	4.0	2.5	3.4	1.1	1.7	–	3.3
Ethyl caproate (ppm)	–	–	–	–	–	0.9	2.7	4.1	5.6	7.0	7.8	8.0	5.1	6.2	4.0	5.3	2.4	3.5	–	6.7
Ethyl acetate (ppm)	–	–	–	–	–	10.5	19.3	32.2	56.5	51.9	56.9	60.1	42.7	55.1	36.7	49.7	19.0	21.8	–	54.2
Isobutyl alcohol (ppm)	–	–	–	–	–	28.3	35.7	44.7	55.5	49.3	53.2	53.5	47.9	47.2	49.3	49.7	42.7	43.8	–	50.2
E/A ratio (–)**	–	–	–	–	–	0.8	1.9	2.7	3.1	3.1	3.1	3.0	2.1	2.7	1.6	2.1	0.8	1.1	–	2.0

2 - 19 Overcoming Decreased Lipid Accumulation Under Light/Dark Conditions by Selective Breeding of Oil-Rich *Chlamydomonas* Mutants

Y. Kato [a)], C. Ogino [a, b)], T. Hasunuma [a, c)], K. Satoh [d)], Y. Oono [d)] and A. Kondo [a, b, c)]

a) Engineering Biology Research Center, Kobe University,
b) Graduate School of Engineering, Kobe University,
c) Graduate School of Science, Technology and Innovation, Kobe University,
d) Department of Radiation-Applied Biology Research, TARRI, QST

Microalgae are promising biofuel producers due to their high ability to produce oil photosynthetically. The oleaginous green alga *Chlamydomonas* sp. JSC4 is a hopeful candidate that shows high growth potential together with high oil content through activation of the starch-to-lipid biosynthesis switching mechanism [1]. However, oil accumulation of JSC4 is significantly decreased under light/dark conditions, which is inevitable in large-scale outdoor cultivation [2]. To overcome this critical obstacle, this study aimed to obtain a mutant strain with high oil content under light/dark conditions.

Selective breeding of oil-rich *Chlamydomonas* mutant was performed by combining heavy ion beam mutagenesis and fluorescence-activated cell sorting (FACS). JSC4 cells seeded on agar plates were exposed to 50 Gy of the carbon ion beams ($^{12}C^{5+}$, 220 MeV) accelerated by an AVF cyclotron at TIARA, QST. Mutant cells were cultured under light/dark conditions, followed by FACS-based screening for oil-rich cells using BODIPY fluorescence and chlorophyll fluorescence as the indicators of oil and cell size, respectively (Fig. 1). Consequently, an oil-rich mutant strain KOR1 was obtained.

KOR1 was characterized by time-course profiling during laboratory scale cultivation under light/dark conditions. Biomass production of KOR1 was initially comparable with that of JSC4, while it was decreased after nitrate depletion (Fig. 2a and 2b). Carbohydrate content were also decreased in KOR1 (Fig. 2c), suggesting that KOR1 is a mutant related to starch synthesis/degradation. Oil content of KOR1 was significantly higher than that of JSC4 (Fig. 2d). The maximum oil content of JSC4 and KOR1 during 14 days' cultivation were 27.0% and 41.9%, respectively.

Transmission electron microscopy (TEM) analysis revealed that JSC4 cells accumulated both oil droplets and starch granules, while KOR1 cells accumulated more oil droplets compared with JSC4 and no large starch granule (Fig. 3).

Thus, the present study has provided an oil-rich strain suitable for biofuel production in outdoor cultivation.

Acknowledgment
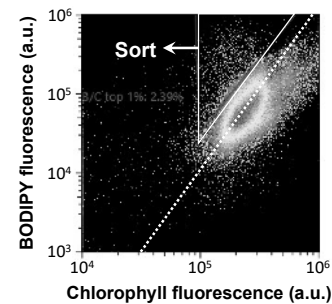
Fig. 1. Fluorescence-activated cell sorting (FACS) for oil-rich *Chlamydomonas* mutant cells.
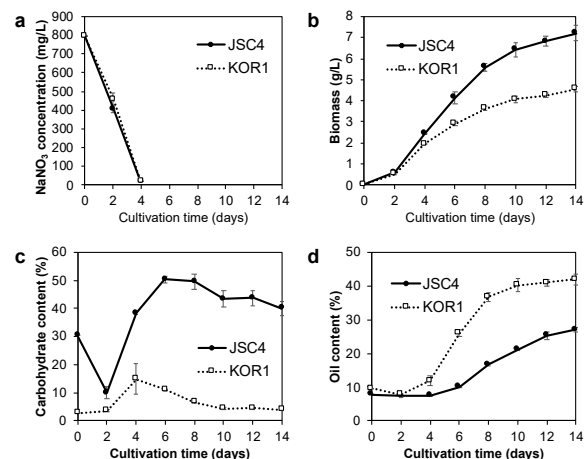
Fig. 2. Time-course profiles of JSC4 and KOR1. (a) nitrate concentration, (b) biomass, (c) carbohydrate content, (d) oil content.
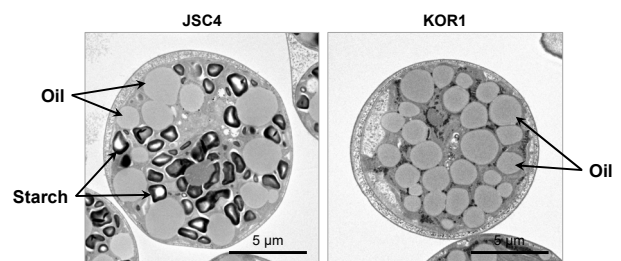
Fig. 3. Transmission electron microscopy (TEM) images of JSC4 and KOR1 at Day 10.5.

References

[1] S. H. Ho *et al.*, Sci. Rep., **7**, 45471 (2017).
[2] Y. Kato *et al.*, Biotechnol. Biofuels., **12**, 39 (2019).

2 - 20　Functional Analysis of PprI in the DNA Damage Response Mechanism of *Deinococcus radiodurans*

K. Satoh [a)], T. Sanzen [a, b)], Y. Oono [a)] and I. Narumi [b)]

[a)] Department of Radiation-Applied Biology Research, TARRI, QST,
[b)] Faculty of Life Sciences, Toyo University

Deinococcus radiodurans is a representative strain of radioresistant bacteria and has extremely high resistance to various DNA damage caused by gamma rays, ultraviolet rays, desiccation, oxidation, and DNA cross-linkers. The previous studies revealed that the expression of a unique DNA repair-related protein PprA was up-regulated by a DNA damage response regulator PprI following DNA damage in *D. radiodurans* [1]. Analysis of the genome sequences of *Deinococcus* spp. discovered the radiation/desiccation response (RDR) motif, existing upstream of the radiation-inducible genes (RDR regulons) such as *pprA* and *recA* genes. The RDR motif serves as an operator sequence in the unique DNA repair response system [2]. Another regulatory protein DdrO binds RDR motif. Following DNA damage, the metalloprotease activity of PprI cleaves DdrO, resulting in induction of the RDR regulon [3]. However, the detailed functional site of PprI protein in the DNA damage response mechanism is poorly understood. In an effort to gain an insight into the role of the PprI in DNA damage response mechanism in *D. radiodurans*, firstly, we generated a *pprI*-deleted mutant strain and *pprI* expression plasmid.

A *pprI*-deleted strain designated as SXPI was generated by replacement with an *Escherichia coli* hygromycin resistance gene that is controlled by the *D. radiodurans* catalase promoter. Expression plasmid for complementation was constructed as follows. A 1.0-kb *pprI*-coding sequence was amplified by PCR and ligated into pRAD1 plasmid carrying chloramphenicol (Cm) resistance gene. A 0.2-kb *pprI* promoter sequence was amplified by PCR and ligated at upstream of *pprI*-coding sequence in the plasmid. The resulting plasmid was designated as pEXpprI. The complementation plasmid pEXpprI was transformed into the strain SXPI. As controls, empty pRAD1 vector was transformed into strains R$_1$ (wild-type) and SXPI. *D. radiodurans* cells carrying the plasmids were incubated at 30 °C for 24 h in TGY broth containing 3 µg/mL Cm. Cells were harvested, washed, and resuspended in 10 mM sodium phosphate buffer (pH 7.0, PB). Aliquots (0.1 mL) of the cell suspension were dispensed into test tubes and irradiated at room temperature with ^{60}Co gamma rays at Food Irradiation Facility, TARRI, QST. The irradiation dose ranged from 0.2 to 8 kGy. After the treatments, cells were diluted appropriately with PB, drop onto TGY agar, and incubated at 30 °C for 1 or 2 days prior to the enumeration of colonies. The surviving fraction was determined by calculating the number of colonies (treatment) divided by the total number of viable cells (mock treatment).

We successfully generated complete deletion strains for the *D. radiodurans pprI* genes. This deletion strain SXPI carrying pRAD1 exhibited extreme sensitivity to gamma-rays compare to the wild type strain carrying pRAD1. In the strain SXPI carrying pEXpprI, the survival rate following treatment with gamma rays was restored to the similar level of that in the wild type (Fig. 1). This result suggests that *D. radiodurans* PprI is a key protein for the repair of damage induced by gamma rays as shown in the previous study [1]. We confirmed the resistance phenotype to DNA damage was restored by functional complementation with expression of the *pprI* gene on the plasmid. Although the constructions of mutated pprI-expression plasmids are still in progress, complementation tests to DNA damage agents with pprI mutation library will help to delineate the functional site of PprI in regard to the DNA damage response mechanism in *D. radiodurans*.
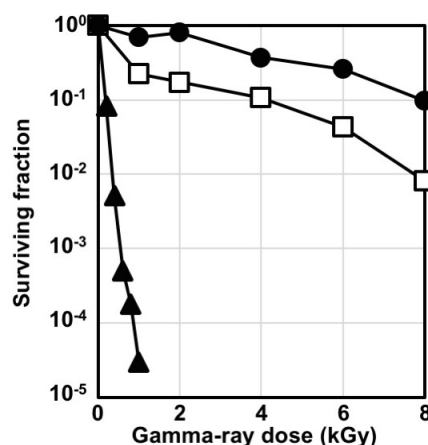
Fig. 1. Complementation tests of *D. radiodurans pprI*-deleted mutant to gamma rays. Symbols: closed circulars, wild-type R$_1$ carrying plasmid pRAD1; closed triangles, *pprI*-deleted mutant SXPI carrying plasmid pRAD1; open squares, *pprI*-deleted mutant SXPI carrying *pprI* expression plasmid pEXpprI.

References

[1] Y. Hua *et al.*, Biochem. Biophys. Res. Commun., **306**, 354 (2003).
[2] M. Ludanyi *et al.*, Mol. Microbiol., **94**, 434 (2014).
[3] H. Lu *et al.*, DNA Repair, **11**, 139 (2012).

2 - 21   Effect of Ion Beams and Gamma Rays Irradiation on Mutation Induction in *Bacillus subtilis* Spores

N. H. P. Uyen [a)], T. Sakai [a)], H. Den [a)], M. Furuta [a)], K. Satoh [b)] and Y. Oono [b)]

a) Quantum Radiation Engineering, Graduate School of Osaka Prefecture University,
b) Department of Radiation-Applied Biology Research, TARRI, QST

Bacillus subtilis is known as Gram-positive, rod-shaped, aerobic, a spore-forming bacterium that is naturally found in soil. The spore is resistant to environmental factors such as heat, desiccation, chemical, and radiation [1]. Besides, ionizing radiation induces DNA damages including single-strand breaks and double-strand break and generates reactive oxygen species which also induces DNA strand breaks. Ion beams have a high linear energy transfer (LET, keV/μm) and give DNA damage containing double-strand break locally (clustered damage) than gamma rays do [2]. Recently, ion beams have been used for mutation breeding in biological objects including rice, flowers and bacteria [3]. Mutations in the RNA polymerase β subunit of the *B. subtilis*, encoded by *rpoB* gene, related to rifampicin resistance and can be generated by irradiation method.

In this work, we utilized ion beams to check mutation induction for rifampicin to characterize the mutation by high LET ion beam irradiation to *B. subtilis* spores.

The spores of *B. subtilis* 168 (*trpC*2) were prepared by inoculating the vegetative cells onto the Schaeffer's sporulation medium [4] at 37 ºC for 4 days, harvested and treated sequentially with 1 mg/mL lysozyme and 1% SDS. Aliquots (1 mL) of the spore suspensions at 10^9 CFU/mL were dropped onto the sterilized cellulose membrane and dried then irradiated four kinds of ion beams (^{4}He^{2+} [50 MeV; 19.4 keV/μm], ^{12}C^{5+} [220 MeV; 121.8 keV/μm], ^{12}C^{6+} [190 MeV; 148.7 keV/μm]; ^{20}Ne^{8+} [350 MeV; 440.8 keV/μm] and ^{40}Ar^{13+} [460 MeV; 1649.6 keV/μm]) accelerated by an AVF cyclotron at TIARA, TARRI, QST or with ^{60}Co gamma rays (0.2 keV/μm) at Osaka Prefecture University. The irradiation doses ranged from 0.6 to 6 kGy.

Irradiated spores were recovered from membranes, and cultivated in 96-well microplate containing LB broth (0.2 mL) with shaking by Multiskan GO Microplate Spectrophotometer. During the cultivation, OD$_{600}$ of the culture was automatically measured. The spores also spread onto either LB agar supplemented with rifampicin (Rif, 50 μg/mL) or the Spizizen agar [5] supplemented with 5-Fluorouracil (5-FU, 1 μM), and incubated at 37 ºC for 3 days to screen mutants. The numbers of Rif- or 5-FU-resistant (Rif^R or FU^R) colonies were counted. All the obtained Rif^R colonies were picked up by toothpicks, spotted onto the new Rif-LB agar, and incubated for 3 days to confirm the Rif resistance.

The lethal effect of spore was estimated to be in the order ^{12}C^{5+} > ^{12}C^{6+} > ^{20}Ne^{8+} > ^{4}He^{2+} > ^{60}Co > ^{40}Ar^{13+}. The relative biological effectiveness value of ^{12}C^{5+} ion beams was 3.03, suggesting that ^{12}C^{5+} ion beams had the most lethal effects for *B. subtilis* spores as shown in our previous results [6].

The initial spore germination process seemed not to be affected by ion–beam irradiation. Outgrowth phase after the germination became longer with the irradiation dose as well as ^{60}Co gamma-rays (Fig. 1). These results suggest that damaged sites in spores are similar between gamma- and ion-beam irradiations.

By the screening of Rif^R and FU^R mutants, a certain number of Rif^R mutants was obtained for ^{4}He^{2+}, ^{60}Co, ^{40}Ar^{13+} irradiation within lower doses showing relatively lower lethality, however, no FU^R mutants has been obtained so far.
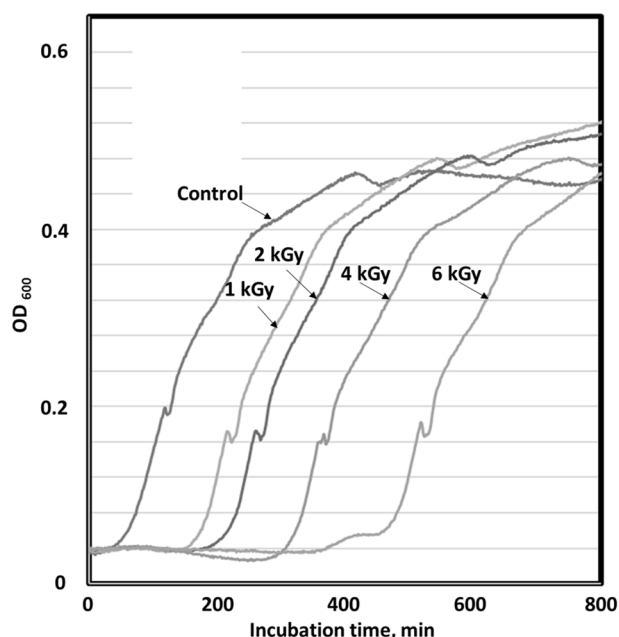
Fig. 1. Growth curve of ^{4}He^{2+}-irradiated *Bacillus subtilis* spores.

References
[1] F. Kunst, *et al.,* Nature, **390**, 249 (1997).
[2] C. F. Dunne, Br. J. Hosp Med., **74**, 166 (1999).
[3] S. Mahadtanapuk, Nucl. Instrum. Methods Phys. Res., **326**, 209 (2014).
[4] P. Schaeffer *et al.*, Proc. Natl. Acad. Sci. USA, **54**, 704 (1965).
[5] J. Spizizen, Proc. Natl. Acad. Sci. USA, **44**, 1072 (1958).
[6] N.H.P. Uyen *et al.*, QST Takasaki Annu. Rep. 2016, **QST-M-8**, 104 (2018).

2 - 22   Molecular Analysis of High-LET Carbon Ion Beams Induced Cells Effects in Budding Yeast *S. cerevisiae*

Y. Matuo [a)], A. N. Sakamoto [b)], Y. Hase [b)] and K. Shimizu [c)]

[a)] Department of Nuclear Power and Energy Safety Engineering, University of Fukui,
[b)] Department of Radiation-Applied Biology Research, TARRI, QST,
[c)] Radioisotope Research Center, Osaka University

Mutations caused by ion beams have been well-studied in plants, including ornamental flowers, rice, and algae. It has been shown that ion beams have several significantly interesting features, such as high biological effect and unique mutation spectrum, which is in contrast to low linear energy transfer (LET) radiation such as gamma rays. To elucidate the mechanism of the biological effect, we investigated the cell lethal effect of high-LET carbon ion beams in DNA Repair-Deficient Strains of Saccharomyces cerevisiae.

Wild-type and repair-deficient haploid strains of S. cerevisiae were used to investigate the repair pathway of DNA damage induced by the carbon ion beam. The relevant genotype was as follows: S288c (*MATα SUC2 gal2 mal2 mel flo1 flo8-1 hap1 ho bio1 bio6*), G160/2b (*MATα, rad52*), ogg1 (*MATα, ogg1*), and msh2 (*MATα, msh2*). *G160/2b* (*MATα, rad52*) was obtained from Yeast Genetic Stock Center (UC Berkeley). The ogg1 and msh2 strains were generated using one-step gene disruption by homologous recombination in this study. Yeast extract-Peptone-Dextrose (YPD) medium was used to grow yeast cultures at 30 °C.

The carbon ion ($^{12}C^{5+}$, 18.3 MeV/u) beam used in this study was generated by the cyclotron at the TARRI, QST, Japan. The LET of the carbon ion beam was 107 keV/μm.

The cells were collected by filtering with a 0.45 μm nitrocellulose membrane filters (EMD Millipore, Billerica, MA, USA). The membrane filters, containing $2 \times 10^{2-3}$ cells for determining survival rate. The cells were put on ϕ 60-mm plastic petri dishes and covered with a 5-μm thick sterilized Kapton film. To measure cell survival, the irradiated membrane filters were incubated on YPD plates at 30 °C for 2 days. Survival rate was determined by counting the numbers of colonies on YPD plates.

Figure 1 shows the survival rate of the *rad52, ogg1*, and *msh2* cells irradiated with a carbon ion beam. The rad52 cells were extremely sensitive to carbon ion irradiation; approximately 26 times more sensitive than wild-type cells at 100 Gy. The *rad52* strain was hypersensitive to the high-LET carbon ion beam. In our previous study, the *rad52* strain also showed hypersensitivity to a carbon ion beam with a relatively low LET (13 keV/μm) [1]. It has been shown that DSBs are mainly repaired by HR or the non-homologous end joining (NHEJ) pathway. NHEJ functions in the G1/S/G2 phases, whereas HR becomes active only in the S/G2 phase after DNA replication [2]. The widely accepted role of RAD52 is to repair DSBs by HR. The high sensitivity of the *rad52* strain indicated that HR is essential for the repair of DSBs induced by ion beams with the wide range of LET in yeast. In contrast, no significant difference was observed in radiation sensitivity between *ogg1, msh2*, and *wild*-type. This observation suggested that the incorporation of the oxidative damage into the genome only slightly affected the cell survival after ion beam irradiation in yeast.
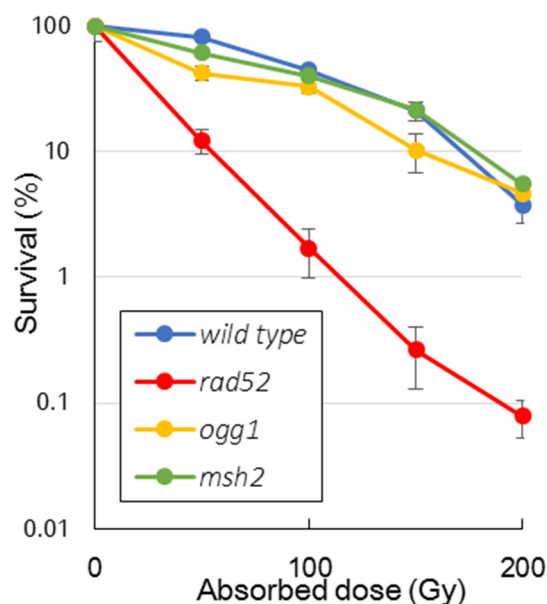
Fig. 1. Survival rates for yeast strains S288c (*wild*-type), *rad52, ogg1*, and *msh2* after irradiation by carbon ion beams. Data are the means of five replicates. Data for yeast strain S288c (wild-type) were taken from. Bars indicate SD.

References
[1] Y. Matuo, *et al.*, Mutat. Res., **810**, 45 (2018).
[2] F. Delacote, *et al.*, Cell Cycle, **7**, 33 (2008).

2 - 23   Inactivation of *Escherichia coli* O157 in Raw Beef liver by Gamma Irradiation

S. Kawasaki [a)], H. Seito [b)] and S. Todoriki [a)]

[a)] Food Research Institute, National Agriculture and Food Research Organization (NARO),
[b)] Department of Advanced Radiation Technology, TARRI, QST

Since July 2012, serving raw beef liver in restaurants has been prohibited in Japan, due to high rates of contamination with coliform bacteria, including enterohemorrhagic *Escherichia coli* (EHEC) [1]. Several studies have reported the effectiveness of irradiation treatment at reducing the risk of EHEC in meat and ready-to-eat foods. The present study compared variations in the irradiation sensitivity of *E. coli* O157 in ground beef and beef liver at frozen temperatures (-80 °C), under aerobic and anaerobic conditions.

Enterohemorrhagic non-verotoxin-producing *E. coli* O157 strain, DT66—isolated from bovine feces—was grown overnight at 37 °C in 30 mL of trypticase soy broth. The cells were collected by centrifugation and resuspended in 8 mL of phosphate-buffered saline. Inoculum (100 μL; 20 μL × 5 positions -10^9 CFU/mL) was injected into raw beef liver and raw ground beef (25 g each) using a medical syringe. The bacterial concentration of each sample was -7 log CFU/g. Inoculated samples were immediately air-packaged or vacuum-packaged in gas-impenetrable laminate film bags and stored at -80 °C for more than 2 h before irradiation.

To determine the D_{10} value, inoculated samples were irradiated at 0–3.0 kGy with dry ice, in a Gamma Cell-220 (Nordion International Inc., Kanata, Ontario, Canada) at Food Research Institute, NARO, Japan. All experiments were performed in triplicates, and D_{10} values were calculated as the inverse of the slope derived from the liner regression inactivation curves. Predicted confidence intervals (95–99%) were determined from each inactivation curve.

Liver samples (25 g) inoculated with high amounts of *E. coli* O157 DT66 (10^4 - 10^7 CFU/g) were vacuum-packed and gamma-irradiated at a gamma room in QST, Takasaki (No. 7 cell). After irradiation, *E. coli* O157 survival or death was determined in beef liver samples. Samples (25 g; n = 5) were enriched with 225 mL of Buffered Peptone Water at 35 °C for 24 h. Enriched samples were streaked on VRBG agar plate.

Table 1 shows the D_{10} values of *E. coli* O157 in ground beef and beef liver under various atmospheric conditions (air and vacuum) at -80 °C. The D_{10} values in beef liver were higher than those in ground beef samples. Moreover, a significant difference in the D_{10} value of *E. coli* O157 DT66 was observed in beef livers that were packaged using air and using (0.85 vs. 0.95 kGy).

To verify the effectiveness of bacterial inactivation by irradiation in the background of high levels of bacterial contamination (10^4 - 10^7 CFU/g), the survival/death interfaces of *E. coli* O157 DT66 in beef liver under vacuum-packaged and frozen conditions were evaluated (Fig. 1). All inoculated samples exposed to radiation at >95% of the predicted confidence estimates—according to irradiation inactivation curves for *E. coli* O157 DT66—were negative. These results suggested that an applied dose range of 5.3 kGy to 5.5 kGy was sufficient to kill 10^5 CFU/g of *E. coli* O157 at 95–99% predicted confidence intervals.

Table 1
D_{10} values (kGy) for *E. coli* O157 DT66 in ground beef and beef liver under frozen conditions.

Material	Air			Vacuum		
Ground beef	0.69±0.01	R^2 = 0.95	Aa*	0.78±0.07	R^2 = 0.97	Aa
Beef liver	0.85±0.11	R^2 = 0.96	Aa	0.95±0.08	R^2 = 0.98	Bb

Values are mean ± standard deviation. Within each row and column, means with different uppercase and lowercase letters, respectively, are significantly different (p < 0.05).
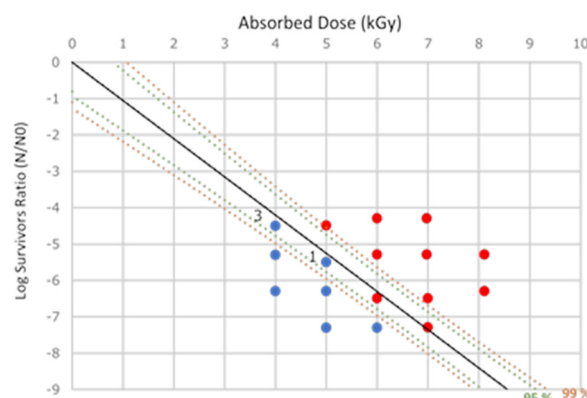
Fig. 1. Survival/death interface for *E. coli* O157 DT66-inoculated, vacuum-packaged beef liver after gamma irradiation at frozen temperature (under dry ice condition). The solid line represents linear regression and dotted green and orange lines indicate 95% and 99% predicted confidence intervals calculated from survival plots of *E. coli* DT66 under same conditions, respectively. Blue or red circle show survival or death after enrichment, and the numbers describe bacterial positivity in five samples.

Reference
[1] K. Shinagawa, Food Sanitation Research **62**, 7 (2012).

2 - 24　　Breeding of New Potted Flower Varieties Using Ion Beam

M. Tsukagoshi [a], S. Nozawa [b] and Y. Hase [c]

[a] Study Group for farmer Advanced technology informatization research of Takasaki,
[b] Department of Research Planning and Promotion, QuBS, QST,
[c] Department of Radiation-Applied Biology Research, TARRI, QST,

To establish ion-beam breeding technology for potted flowers, marguerite, and rhodansemums, cuttings of these plants were irradiated by He (63 MeV) ions and effects of the irradiation were examined. Under this irradiation condition, no mutation to flower color could be confirmed.

高崎市は鉢花類の生産が盛んであり、オリジナル品種の育成は、有利販売や地域の活性化に非常に有用である。鉢花類の育種は、一般に系統間の交雑または枝変わり等の選抜が利用されるが、従来の育種は、長い年月を必要とすること、望まれる形質や性質を得ることが困難な場合も多いこと、種子を獲得することが難しい品目では育種が進まないなど課題も多い。本研究では、花き類で利用されているイオンビーム育種を中心とした突然変異育種技術を活用するため、高崎量子応用研究所のイオン照射研究施設においてイオンビーム照射を実施してきた。

前年はイオン種 He-63 MeV を用い効果発現が期待できる線量を検討したところ、30 Gy 付近が有望であるとの結果が得られたため、今年度はこの付近の線量を中心にイオンビームを照射し、生育調査と変異形質の確認試験を行った。

今回の研究には、昨年度供試したローダンセマム(Rhodanthemum (Vogt) B. H. Wilcox *et al.*)と新たにマーガレット(Argyranthemum frutescens (L.) Sch. Bip.)を材料とし高崎量子応用研究所イオン照射研究施設の AVF サイクロトロンを利用してイオンビーム照射を行った。具体的な実施方法は、脇芽の分裂組織にイオンビームが到達するよう、茎および葉を調整した挿穂をシャーレ内に配置後、カプトン膜で覆い、深度制御種子照射装置の運転台を用いてヘリウムイオンを連続的に照射した。照射量は、マーガレットが 20, 30, 40 Gy の 3 段階、ローダンセマムは 0, 10, 20, 30, 40 Gy の 5 段階で行った。照射後は、重イオン準備室内の培養器内で保管した。

Fig. 1. Plants after irradiation. (Left : Marguerite, Right : Rhodanthemum)

（照射方法）
１回あたりの総所要時間＝１時間
（照射日：平成 30 年 5 月 15 日）
（サンプル搬入）→（照射〜１分×40 回＋搬送時間）
　→（片付け、照射装置内で冷却）

その後、生産者のほ場で開花まで管理し、照射後の生存株数及び開花時の花色の変異について調査を行った(Fig. 1)。

照射後の穂を挿芽し、生存株数を確認したところ、両品目ともに 40 Gy 区では生存株数が半数以下と低くなった(Table 1)。ローダンセマムでは無処理でも 4 割程度枯死株が発生したが、夏場の高温に弱い品目でありその影響を受けたと考えられる。

Table 1
Number of surviving plants.

Gy	Marguerite	Rhodanthemum
0	–	8/14
10	–	22/30
20	22/35	15/21
30	25/42	16/21
40	10/21	10/21

Note. Denominator: Irradiation number
Numerator: Survival number
Investigation date:8/3(Marguerite),
　　　　　　　　　6/27(Rhodanthemum)

生存した株はそのまま開花まで管理し、葉や花色の変異について各処理区で比較を行った。高温期の初期生育は、照射線量よりも個体による差が大きい傾向であったが、秋以降は順調に生育した。葉については、生育初期は個体による葉の大きさの差が見られたものの後半は差が見られなくなった。葉の形状について大きな違いは見られなかった(Fig. 2)。花色については、開花期（マーガレット：12 月、ローダンセマム：3 月）に調査を行った。調査対象は、各株から発生する側枝の頂花を中心に変異の確認を行った（株あたりの花数は、マーガレットでは約 20 花、ローダンセマムでは約 30 花程度）が、花色や形状の変異は、確認できなかった。

Fig. 2. Shape of leaf after irradiation. (Left : 20 Gy, Center : 30 Gy, Right : 40 Gy)

以上の結果から、今回の試験では、葉の形質や花色に対する変異は確認できなかった。今後は、摘心等により開花側枝を増やし、調査個数を増やすなどの技術的対策や照射品種の変更、実生への照射なども検討する必要がある。

2 - 25   Identification of Genes Responsible for the Contact-dependent RED Response in *Streptomyces coelicolor*

S. Asamizu [a,b)], T. Ishizuka [a)], M. Yanagisawa [a)], K. Satoh [c)], Y. Ohno [c)] and H. Onaka [a,b)]

[a)] Graduate School of Agricultural and Life Sciences, The University of Tokyo,
[b)] Collaborative Research Institute for Innovative Microbiology, The University of Tokyo
[c)] Department of Radiation-Applied Biology Research, TARRI, QST

Actinomycetes, filamentous Gram-positive bacteria, are a major source of bioactive natural products which can be drug candidates. Genome sequences of actinomycetes revealed the variety of previously unrecognized secondary metabolite biosynthetic gene clusters, which indicates the huge potential of actinomycetes to produce more diverse secondary metabolites. We are studying about the bacterial-bacterial interaction induced secondary metabolism by filamentous actinomycetes e.g. *Streptomyces* species. Mycolic acid-containing bacteria, e.g. *Tsukamurella pulmonis* TP-B0596 (here after Tp) possess ability to induce production of secondary metabolites in a range of filamentous actinomycetes, which are not produced in their single culture. Until now, 7 classes, total 29 new compounds had been discovered from the combined-culture with various filamentous actinomycetes and Tp [1]. Object of this study is to elucidate the gene(s) which are involved in the response for activation of secondary metabolism within filamentous actinomycetes. Elucidation of the mechanism may lead for development of versatile genetic tools to discover novel bioactive natural products.

Streptomyces lividans TK23 and *Streptomyces coelicolor* JCM4020 were observed to produce red pigment compound (undecylprodigiosin, here after RED) in response to direct cell-cell contact interaction of Tp [2,3]. We investigated the gene(s) responsible for the activation of RED which was induced by Tp using *S. coelicolor* JCM4020 as a model to explore the molecular basis of the response mechanism. We employed carbon ion beams ($^{12}C^{5+}$, 220 MeV), accelerated by the AVF cyclotron at TIARA, to induce mutagenesis on spores to generate mutant library of *S. coelicolor*. We screened the RED production deficient mutants of *S. coelicolor* by mixing them with Tp on agar plates. Using red / white color phenotype of the colonies as indication, we obtained 118 RED production deficient mutants from totally around 152,000 tested spores. We further tested the phenotype of 118 mutants by growth on minimum medium and formation of aerial mycelia. Finally we obtained 59 mutants which were deficient in induced RED production by Tp, but were normal in their apparent growth and morphological developments [4,6]. We re-sequenced the genome of 16 mutants using MiSeq and identified mutational points existed in CDS [5,6].

We performed gene complementation experiments for the genes which were identified to contain mutation(s) in CDSs of the mutant genomes. For now, phenotype of four RED production deficient mutants were successfully recovered by respective gene complementation experiments. Glutamate synthase gene (*gltB*), primary metabolism gene responsible for glutamate biosynthesis and nitrogen metabolism contained a mutation. RED response phenotype of the mutant was rescued by *gltB* gene complementation *in trans* [6]. Restriction of precursor supply was suggested to be responsible for RED production deficient phenotype in the mutant (Fig.1A). Elongation factor G gene (*fusA*), essential factor in ribosomal translation, contained a mutation. RED response phenotype of the mutant was rescued by *fusA* gene complementation *in trans* [6]. Rate limitation in ribosomal peptide synthesis stage was suggested to be the cause of RED production deficient phenotype in the mutant (Fig.1B). Putative membrane protein (*sarA*) which deletion of the gene was known to cause the deficiency in biosynthesis of RED contained mutations [6]. RED response phenotype of the mutant was rescued by *sarA* gene complementation *in trans* [6]. However, reasons of the RED production deficiency in this mutant are still obscure.
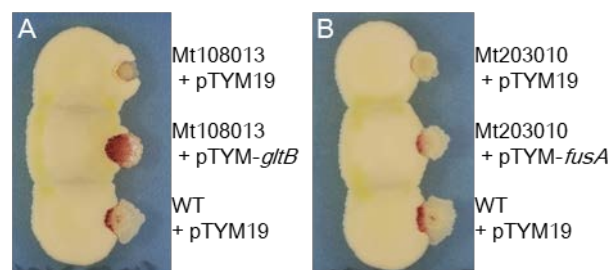
Fig. 1. Phenotype (RED production) of the mutants were rescued by gene complementation. A: Mt108013 contained mutation in *gltB* gene. B: Mt203010 contained mutation in *fusA* gene. pTYM19 is a genome integration vector plasmid used for the experiment.

References
[1] S. Hoshino *et al.*, J Ind Microbiol Biotechnol., **46**, 363 (2019).
[2] H. Onaka *et al.*, Appl. Environ. Microbiol., **77**, 400 (2011).
[3] S. Asamizu *et al.*, PLOS One, **10**, e0142372 (2015).
[4] M. Yanagisawa *et al.*, QST Takasaki Annu. Rep. 2016, **QST-M-8**, 97 (2018).
[5] S. Asamizu *et al.*, QST Takasaki Annu. Rep. 2017, **QST-M-16**, 106 (2019).
[6] S. Asamizu *et al.*, IFO Res. Commun., **32**, 95 (2018).

2 - 26   Expression of the *Deinococcus grandis imuB* and *dnaE2* Genes in *Escherichia coli*

T. Sanzen [a, b)], K. Satoh [b)], Y. Oono [b)] and I. Narumi [a)]

[a)] Faculty of Life Sciences, Toyo University,
[b)] Department of Radiation-Applied Biology Research, TARRI, QST

Although the radioresistance of organisms varies greatly among species, there is a group of bacteria that shows extraordinary resistance to ionizing radiation. Members of the genus *Deinococcus* are the best known as radioresistant bacteria. Radioresistance of *Deinococcus* species is attributed to their highly proficient DNA repair capacity, in which a set of proteins involved in DNA repair is induced following exposure to ionizing radiation [1,2]. *Deinococcus grandis*, formerly *Deinobacter grandis*, is a Gram-negative, red-pigmented, radioresistant, rod-shaped bacterium isolated from freshwater fish in Japan [3]. Recently, we determined the draft genome sequence of *D. grandis* type strain ATCC 43672 [4]. The genome analysis revealed that *D. grandis* possesses two *lexA-imuB-dnaE2* cassettes which are gene clusters related to error-prone DNA repair [5]. LexA, the gene product of *lexA*, binds to palindromic operator sites of regulated genes and represses their expression. ImuB, the gene product of *imuB*, is an apparently inactive paralog of the DNA polymerase V catalytic subunit UmuC. DnaE2, the gene product of *dnaE2*, is an alternative and catalytically active paralog of DNA polymerase III α-subunit [6]. In the *D. grandis* genome, one *lexA-imuB-dnaE2* cassette was located in chromosome II, and another *lexA-imuB-dnaE2* cassette was located in chromosome III. In previous study, we showed that a *dnaE2*-overexpressed *D. grandis* strain exhibited increased resistance to ultraviolet-C rays, and that the mutation rate of the *dnaE2*-overexpressed *D. grandis* strain was increased compared to wild type irrespective of ultraviolet-C irradiation [7]. In this study, we examined the effect of expression of the *D. grandis imuB* and *dnaE2* genes in *Escherichia coli*.

The *imuB* and *dnaE2* genes were cloned in p15A-based vector and pET-based vector, respectively, and introduced in *E. coli* BL21(DE3) cells. Mutant frequency was measured by colony formation assay based on rifampicin resistance. As a result, when both the *imuB* and *dnaE2* genes were expressed in *E. coli* under IPTG induction, the mutant frequency was increased (Fig. 1), confirming that the functionality of *imuB* and *dnaE2* as mutagenesis genes. However, when either *imuB* or *dnaE2* gene was separately expressed in *E. coli*, no increase in mutant frequency was observed. These results suggest that co-expression of both gene products is necessary to activate mutagenesis. Unlike the *dnaE2*-over expressed *D. grandis*, the recombinant *E. coli* strains constructed in the present study did not show resistance to ultraviolet-C. Instead, slight sensitivities to ultraviolet-C were observed for the recombinant *E. coli* strains (Fig. 2), suggesting that the expression of ImuB and

DnaE2 inhibits the repair process of ultraviolet-specific DNA damage by intrinsic DNA repair proteins. On the other hand, all *E. coli* strains examined showed comparable sensitivities to gamma rays, suggesting that these proteins do not involved in repair pathway of gamma-ray specific DNA damage.

References

[1] I. Narumi, Trends Microbiol., **11**, 422 (2003).
[2] Y. Ishino *et al.*, Curr. Opin. Microbiol., **25**, 103 (2015).
[3] H. Oyaizu *et al.*, Int. J. Syst. Bacteriol., **37**, 62 (1987).
[4] K. Satoh *et al.*, Genome Announc., **4**, e01631-15 (2016).
[5] I. Erill *et al.*, Nucleic Acids Res., **34**, 66 (2006).
[6] L. Aravind *et al.*, Biology Direct, **8**, article 20 (2013).
[7] K. Omoso *et al.*, QST Takasaki Annu. Rep. 2016, **QST-M-8**, 106 (2018).
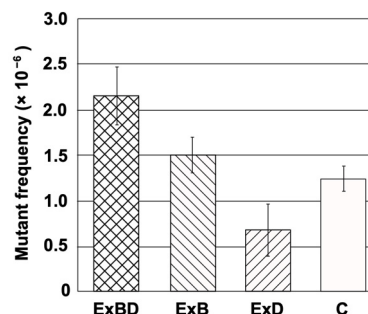
Fig. 1. Mutant frequency of *E. coli* strains expressing *imuB* and *dnaE2* (ExBD), *imuB* (ExB), and *dnaE2* (ExD). C indicates vector control.
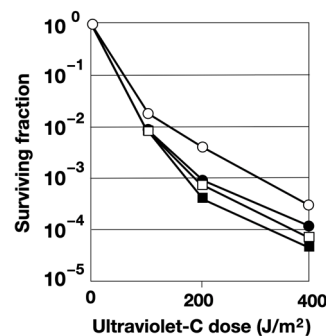
Fig. 2. Sensitivity of the *E. coli* strains expressing *imuB* and *dnaE2* (closed squares), *imuB* (closed circles), and *dnaE2* (open squares) to ultraviolet-C. Open circles indicate vector control.

2 - 27　　Real-time Analysis of Photosynthate Translocation into Strawberry Fruits by Using Positron-emitting Tracer Imaging System

K. Hidaka [a)], Y. Miyoshi [b, c)], S. Ishii [b)], Y.-G. Yin [b)], N. Suzui [b)], K. Kurita [d)] and N. Kawachi [b)]

[a)] Kyushu Okinawa Agricultural Research Center, NARO,
[b)] Department of Radiation-Applied Biology Research, TARRI, QST,
[c)] JSPS Postdoctoral Research Fellow,
[d)] Materials Sciences Research Center, JAEA

In protected cultivation of strawberry, environmental control based on photosynthate translocation is essential for optimizing fruit quality and yield, because the process of photosynthate translocation directly affects dry matter partitioning into fruits. Several studies have examined the influences of inflorescence development and environmental conditions on photosynthate translocation in strawberry plants by using ^{14}C and ^{13}C tracer methods [1]. However, translocation mechanism of strawberry has not yet been adequately clarified, and aforementioned measurement techniques require the destruction of plant tissues. Positron-emitting tracer imaging system (PETIS) can non-invasively visualize the dynamics of photosynthate translocation [2]. In this study, real-time translocation of photosynthates into intact strawberry fruits was examined by using PETIS [3].

Strawberry plant (*Fragaria × ananassa* Duch. cv. Fukuoka S6) was placed between two opposing PETIS detectors. The fruits were located in the field of view of the PETIS as shown in Fig. 1 (A). An individual leaf developing immediately below the inflorescence was inserted into the exposure cell. The exposure cell was then connected to $^{11}CO_2$ gas circulation system consisting of pumps, mass flow controllers, electric valves, and a CO_2 trap containing freshly prepared soda lime. At the start of imaging, room air was fed into the exposure cell. Then $^{11}CO_2$ mixed with room air was introduced from the CO_2 trap into the exposure cell. The $^{11}CO_2$ was then flushed off, and substituted with non-radioactive room air. PETIS images were acquired every 10 s for 180 min. The image data were automatically calibrated for the ^{11}C decay assuming a half-life of 20.39 min and recorded on a personal computer. The environmental conditions around the PETIS was controlled at photosynthetically active radiation of 500 µmol photons m^{-2} s^{-1}, air temperature of 20 °C, relative humidity of 60% and CO_2 concentration of 380 µmol mol^{-1}.

Figure 1 (B) shows serial images of ^{11}C photosynthate translocation into fruits. About 1 h after $^{11}CO_2$ feeding, ^{11}C photosynthate reached to fruit 1. Thereafter, photosynthate accumulation into the other two fruits (fruit 2 and fruit 3) also gradually increased over time. About 3 h after, ^{11}C photosynthate translocation into the fruit 1, fruit 2 and fruit 3 were clearly confirmed.

Figure 2 shows time courses of ^{11}C radioactivity in fruit 1, fruit 2 and fruit 3. The ^{11}C radioactivity level in fruit 1 began to increase about 50 min after $^{11}CO_2$ feeding, and those in fruit 2 and 3 began to increase about 100 min after $^{11}CO_2$ feeding. The rate of increase in radioactivity was highest for fruit 1, and the terminal ^{11}C radioactivity level in fruit 1 was 7 times and 28 times higher than those in fruit 2 and fruit 3.

In summary, real-time analysis of ^{11}C photosynthate translocation with PETIS successfully visualized the dynamics of photosynthate translocation from a source leaf to sink fruits in intact strawberry plant. Furthermore, the quantities of translocated photosynthates differed among the fruits of various positions on the same inflorescence.
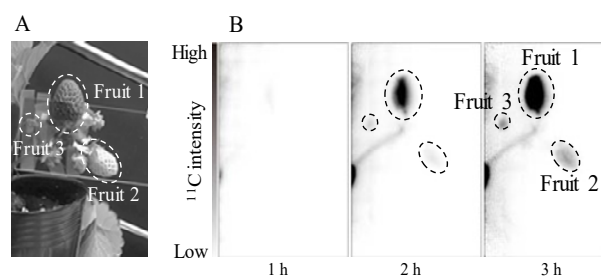
Fig. 1. (A) Photograph of fruits in the PETIS field of view. (B) Serial images of ^{11}C-photosynthate translocation into fruits.
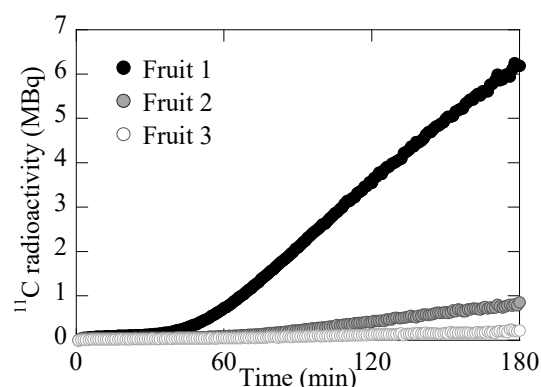
Fig. 2. Time courses of ^{11}C radioactivity in fruits 1, 2 and 3.

References
[1] K. Hidaka *et al.*, Environ. Control Biol., **52**, 63-71 (2014).
[2] K. Kikuchi *et a*l., J. Jpn. Soc. Hortic. Sci., **77**, 199-205 (2008).
[3] K. Hidaka *et al.*, Front. Plant Sci., **9**, (2019).

2 - 28 Effects of Organic Acids on Cadmium Behaviors in Oilseed Rape Plants

S. Nakamura [a)], N. Suzui [b)], Y.-G. Yin [b)], S. Ishii [b)], S. Fujimaki [b)] and N. Kawachi [b)]

[a)] Faculty of Life sciences, Tokyo University of Agriculture,
[b)] Department of Radiation-Applied Biology Research, TARRI, QST

Cadmium (Cd) is one of harmful elements. Cd, accumulating in crops, can impair our health. Therefore, it is expected to establish a novel method to cultivate safe crops with low level of Cd. Organic acids are good metal chelators. Effects of them on Cd mobilization and plant Cd availability are reported [1]. In addition, it was speculated that organic acids are functioning for controlling Cd behaviors in plant bodies. So, we investigated effects of organic acids, applied to roots site-specifically, on Cd behaviors in oilseed rape plants (*Brassica napus* L.). Our results indicated oxalate had inhibitory effects on Cd translocation from roots to shoots (Fig. 1A). On the other hand, citrate had no inhibitory effects (Fig. 1B). To investigate effects of oxalate on Cd behaviors in oilseed rape plants in more detail, we tried to analyze the experimental data which is obtained from positron imaging experiments.

^{107}Cd (half-life 6.5 h) was used as a positron emitter in our PETIS experiments. ^{107}Cd was produced and purified as previously described [2], [3]. 18-day-old seedlings, grown hydroponically in a growth chamber which can control plant growth condition completely, were used. Images of the ^{107}Cd distribution in plants (control plant and oxalated treated plant) were obtained every 4 minutes for 24 h. Time-activity curves, temporal changes of ^{107}Cd signals in specific regions of interest (leaves, node and so on), were generated from these PETIS data, following the methods of *Nakamura et al.*, 2013.

We succeeded in visualizing Cd behaviors in 18-day-old oilseed rape plans (Fig. 2). The node where the petiole occurred was the site with the strongest ^{107}Cd signal in these plans (Fig. 2). We also could see strong ^{107}Cd signal in node of shoot base (Fig. 2). These results demonstrated that each node is playing important roles in distributing Cd in oilseed rape plants. The node is reported to be an important site for mineral distribution in plants [5]. There were different patterns in ^{107}Cd accumulation in the node where the petiole occurred in control plant and oxalated treated plant (Fig.3). These results suggested oxalate is also working in upper parts of plants in addition to the root zone.
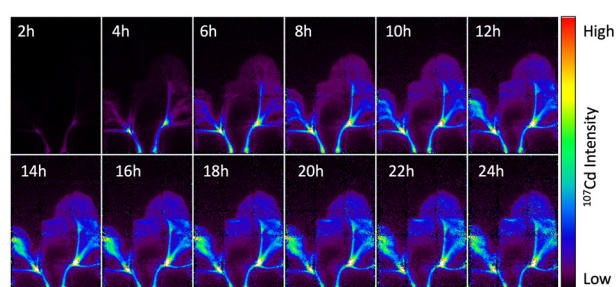
Fig. 2. Time series of PETIS images showing the ^{107}Cd signal (0–24 h) after decay correction. 18-day-old oilseed rape plants are exposed to ^{107}Cd in the root medium with or without oxalate. Right; oxalate treated plant, Left; control plant.
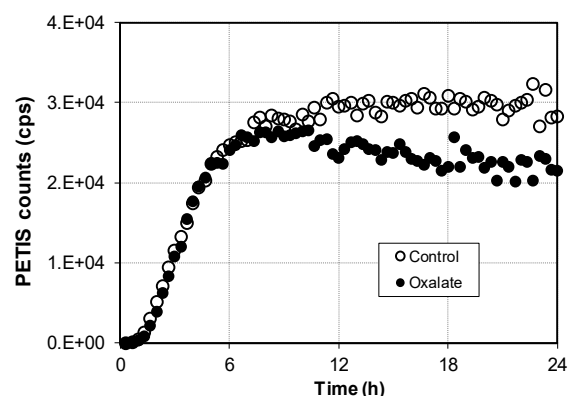
Fig. 3. Accumulation of ^{107}Cd signals in the node where petiole occurred. This image is integration of obtained images, corresponding to 24 hours (From 0 hour to 24 hours after the start of experiments). ○; control plant, ●; oxalate treated plant.
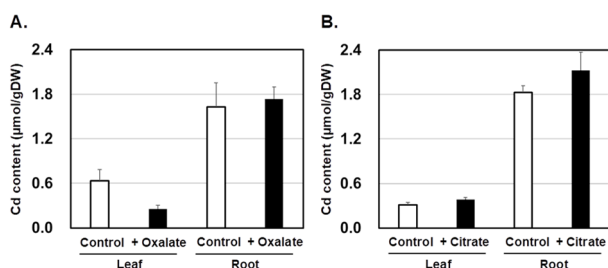
Fig. 1. Cd content in shoots and roots of control plant and (A) oxalated and (B) citrate treated plant. From the results of the ICP-OES analysis and their dry weights, Cd content were calculated. Data are means ± standard error (SE) (n > 3).

References
[1] R. Nigam *et al.*, Plant and Soil, **230**, 107-113 (2001).
[2] N.S. Ishioka *et al.*, JAEA Takasaki Ann. Rep. 2005 162 (2006).
[3] S. Fujimaki *et al.*, Plant Physiol., **152**, 1796-1806 (2010).
[4] S. Nakamura *et al.*, J. Exp. Bot., **64**, 1073-1081 (2013).
[5] N. Yamaji and J.F. Ma, Trends in Plant Science. **19**, 556 (2014).

2 - 29　　　A New Method to Generate High-Purity and High-Yield [^{13}N]N$_2$ Gas

Y.-G. Yin [a], S. Ishii [a], N. Suzui [a], M. Igura [b], K. Kurita [c], Y. Miyoshi [a], N. Nagasawa [a], M. Taguchi [a] and N. Kawachi [a]

[a] Department of Radiation-Applied Biology Research, TARRI, QST,
[b] Institute for Agro-Environmental Science, NARO,
[c] Materials Sciences Research Center, JAEA

Nodulated leguminous plants provides an enormous amount of nitrogen (N) to agricultural systems by N fixation, which plays an important role for increasing the yield of crops. Therefore, improving the N fixation and translocation in the nodulated leguminous plants are an effective way to increase crop yields and to decrease the input of chemical fertilizer into soil. In previous study, a purification method was developed to generate ^{13}N-labeled N ([^{13}N]N$_2$) tracer gas for determination of the N fixation and translocation in soybean plant by using a positron-emitting tracer imaging system (PETIS). The purification method allowed the visualization of N fixation in nodules of living soybean plant non-invasively [1]. However, the purification method had the disadvantages in terms of purity and yield. In this study, we aimed to develop a simple and rapid purification method to produce high-purity and high-yield [^{13}N]N$_2$ for visualization of N fixation in nodules of soybean plant using PETIS [2].

A new purification system was developed as shown in Fig. 1. The ^{13}N was produced via the ^{16}O(p, α)^{13}N reaction by irradiation of pure CO$_2$ gas using an azimuthally varying field cyclotron located at the Takasaki Ion Accelerators for Advanced Radiation Application (TIARA), TARRI, QST (Gunma, Japan). The irradiated gas contained large amount of CO$_2$ and the main product of the [^{13}N]N$_2$ and a slight amount of ^{13}NO$_2$, ^{13}NO and [^{13}N]N$_2$O. First, the irradiated gas was collected in a bag which contained 15 mL of N$_2$ Gas. Then the mixture gas of the bag was sucked up by a syringe to purify [^{13}N]N$_2$ through soda-lime and 600 °C copper. The CO$_2$ was absorbed by soda-lime and the [^{13}N]NO$_x$ was deoxidized by reduced copper. Approximately 214 MBq of the [^{13}N]N$_2$ radioactivity was finally obtained. The purification efficiency of the system was approximately 81.6% and it took only approximately 3.2 min from the end of the beam time to the end of the purification (Table 1). In the 50 mL of final tracer gas composition, the conversion of the specific activity was approximately 0.8-1.8 × 10^{11} Bq mol^{-1} N$_2$.

The 50 mL of [^{13}N]N$_2$ tracer gas was fed to a clump of nodules near the root base area using a syringe pump and the PETIS was immediately started to obtain images (Fig. 2). Clear ^{13}N signals were observed in the nodules (a white triangular arrow). It suggests that our purification method is suitable for analysis of N fixation because the method can obtain a large amount of [^{13}N]N$_2$ and its high specific activity.

We developed a rapid purification method to produce a high-purity and high-yield [^{13}N]N$_2$ gas tracer. It can be used to analyzing and optimizing the responses of the N utilization of nodules under changes to environmental conditions.
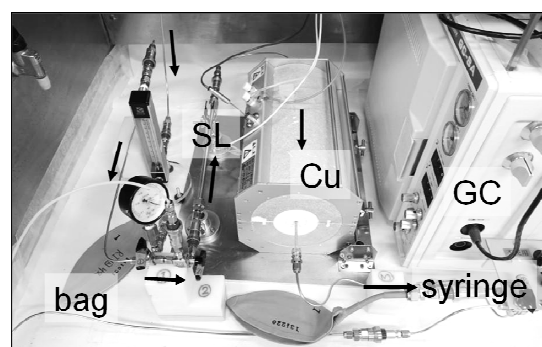
Fig. 1. A photograph of the [^{13}N]N$_2$ purification system. The irradiated gas was purified by soda-lime and reduced copper and collected by a syringe. SL: soda-lime, Cu: copper, GC: gas chromatograph.

Table 1
Efficiency of [^{13}N]N$_2$ purification.

Yield (MBq)	Efficiency (%)	Required time (min)
214 ±61	81.6 ±5.9	3.2 ±0.3

Mean ±SD, n=5
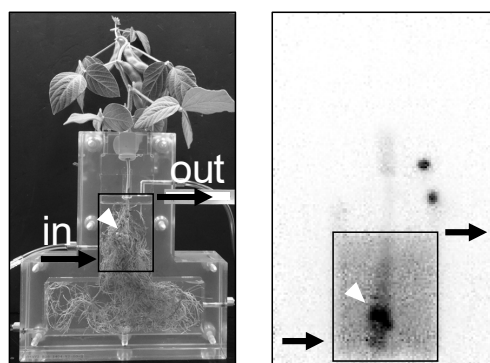
Fig. 2. Photograph of set up of the test plant (left) and PETIS image data (right). A white triangular arrow indicates the ^{13}N distributions in the nodules (right).

References
[1] S. Ishii *et al.*, Soil Sci. Plant Nutr., **55**, 660-666 (2009).
[2] Y.-G. Yin *et al.*, Appl. Radiat. Isot., **151**, 7-12 (2019).

2 - 30   A Convenient Synthesis of Astatinated Phenylalanine Derivatives via the Electrophilic Desilylation

S. Watanabe [a)], M. A.-U. Azim [b)], I. Nishinaka [c)], I. Sasaki [a, d)], Y. Ohshima [a)],
K. Yamada [d)] and N. S. Ishioka [a)]

[a)] Department of Radiation-Applied Biology Research, TARRI, QST,
[b)] National Institutes of Nuclear Medicine & Allied Science, Bangladesh
Atomic Energy Commission, Bangladesh,
[c)] Tokai Quantum Beam Science Center, TARRI, QST,
[d)] Gunma University Graduate School of Science and Technology

Since amino acid transport is generally increased in malignant cancer cells compared to normal cells, amino acid transporters are attractive targets for molecular imaging and targeted radiotherapy of various cancers. Targeted alpha therapy (TAT), radionuclide therapy using an α-emitting radionuclide, is one of the promising and trustworthy approaches for oncology treatment. Astatine-211 ([211]At) has been considered as potentially suitable because of the following reasons; [211]At emits high–energy α-particles with 100% of its decays, has no long-lived α-emitting daughters, and has a half-life ($t_{1/2}$ = 7.21 h) compatible with a variety of molecule carriers [1,2]. These backgrounds led us to develop [211]At labeled amino acid derivatives, 4-[[211]At]astato-L-phenylalanine **1**, to the applications in cancer therapy. Since [211]At has similar chemical properties to iodine, classical iodination approach, electrophilic destannlyation have been employed for the synthesis of the astatinated compound. However, the low acid-resistance of stannyl group necessitates the use of an N- and/or C- terminus-protected phenylalanine precursor, which results in a low overall radiochemical yield (RCY) due to the multiple synthetic steps. It is known that electrophilic desilylation reactions are also available for the preparation of radiohalogenated compounds. The use of electrophilic desilylation is therefore an alternative for labeling phenylalanine with [211]At. This paper describes the synthesis of 4-[[211]At]astato-L-phenylalanine **1**, from the corresponding 4-triethylsilyl-L-phenylalanine **2** and N-Boc-4-(tributylstannyl)-L-phenylalanine methyl ester **3** (Scheme 1).
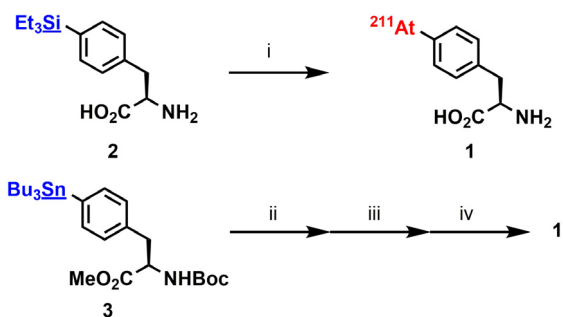
Prior to the synthesis studies, [211]At was produced via the [209]Bi(α,2n)[211]At and it was then isolated from the irradiated target by the dry distillation approach. [211]At was recovered by using chloroform ($CHCl_3$) and N-chlorosuccinimide-methanol solution (NCS-MeOH). Each solution was evaporated to dryness. The reaction was performed in the presence of **2** (200 µg, 0.72 µmol), NCS (400 µg, 3.0 µmol), and 10 mL of trifluoroacetic acid (TFA) at 70 °C for 10 min. After removing TFA, the desired compound was fractionated by the preparative high-performance liquid chromatography (HPLC). As a result, RCYs of **1** were 75% ($CHCl_3$) and 64% (NCS-MeOH) respectively. These results showed that the electrophilic desilylation was found to be very effective for the synthesis of the [211]At labeled phenylalanine. The astatinated compound **1** was also synthesized from the stannylated precursor **3** (Scheme 1). Three steps were required to obtain the desired compound. Consequently, the overall RCYs was (10-17%) and the processing time was about 3 hours including reaction and work up, which was lower and longer than those of the electrophilic desilylation (1 h) as summarized in Table 1.

Table 1

Summary of syntheses of astatinated phenylalanine **1**.

Precursor	Steps	Processing time	RCYs
2	1	1 h	**64-75%**
3	3	3 h	**10-17%**

These results strongly indicated that electrophilic desilylation is a more promising and reproducible method for the synthesis of astatinated aromatic amino acids. This approach can certainly be applied to the syntheses of other promising phenylalanine derivatives such as α-methyl phenylalanine and astatinated peptides containing aromatic residue via silylated precursors [3].

Scheme 1. Synthesis of 4-[[211]At]astato-L-phenylalanine **1** from the silyl precursor **2** and stannyl precursor **3**. (I) NCS, TFA, 70 °C; (ii) NCS, 0.1%AcOH-EtOH, r.t.; (iii) TFA, r.t.; (iv) 2M NaOHaq., reflux.

References
[1] D.S. Wilbur, Nature Chem., **5**, 246 (2013).
[2] F. Guerard et al., Cancer Biother. Radiopharm., **28**, 1 (2013).
[3] S. Watanabe et al., Org. Biomol. Chem., **17**, 165 (2019).

2 - 31   Identification of Multi-element Accumulation Mechanism in Legume

J. Furukawa [a], M. Ouchi [a], N. Suzui [b], Y.-G. Yin [b], K. Kurita [b], N. Kawachi [b] and T. Satoh [c]

[a] Life and Environmental Sciences, University of Tsukuba,
[b] Department of Radiation-Applied Biology Research, TARRI, QST,
[c] Department of Advanced Radiation Technology, TARRI, QST

Plants need various elements for its growth. Not only major elements, such as nitrogen, phosphorous and potassium, but many essential trace elements are needed for plant development. The analysis of trace element content and localization in the focused organ or tissue is important to identify its functions. Especially, under some stress conditions, information about the localization of trace elements in the tissue level is highly valuable for investigating where the deficiency or toxicity of elements is perceived and how to control the mechanisms for keeping homeostasis of plant body. Micro-PIXE (Particle Induced X-ray Emission) method can detect multi-element distributions in the same sample and visualize those localizatons with high-resolution images [1, 2]. As for the element behavior induced by its deficiency or excess, the regulations of the activities in root mineral uptake and/or root to above ground part, shoot, translocation are well observed. Therefore, we combined the PETIS (Positron Emitting Tracer Imaging System) technique, which has a huge advantages in measureing element translocation in plants [3], with Micro-PIXE. In this study, iron (Fe) localization in the roots and zinc (Zn) translocation activity of *Lotus japonicus* were focused. *L. japonicus* is a model legume and its two experimental lines, MG-20 and B-129, have a diversity in some metal concentrations including Fe and Zn in seed [4].

ICP-AES measurement revealed manganese, nickel, copper, Zn concentrations are higher in B-129 both in shoot and root. And Fe concentration in shoot was higher in MG-20, but its concentration in root was obviously higher in B-129. These Fe allocation pattern suggests the Fe translocation activity from root to shoot is low in B-129. To identify what kind of steps are involved in the suppression of Fe translocation to shoot, the comparison of Fe localization between two cultivars using Micro-PIXE was carried out. As for the preparation of PIXE imaging, root samples were embedded in the compound for a freeze sectioning and sliced to 20 μm sections by freezing microtome and then pasted on the polycarbonate film for 3 MeV H$^+$ beam exposure. The spectrum of Fe was well observed in B-129 samples around the root surface and root center, suggesting low activities in Fe uptake and Fe loading into xylem vessels (data not shown).

In *Arabidopsis*, it is known that the mutant lacking one gene involved in long distance Fe translocation induces shoot Fe deficiency and root Fe accumulation [5]. In addition, multi-mineral accumulation was observed in shoot and root in that mutant [6]. To identify the similar mechanisms are working in *L. japonicus* or not, we examined Zn behavior using PETIS with plants subjected to different Fe nutrition treatments. After 4-week-cultivation of MG-20 and B-129 with hydroponics using 1/10 Hoagland's solution, plants were transplanted to Fe deficient (1/10 Fe) and Fe excess (10× Fe) solutions for 4 days. PETIS experiments were started by adding ^{65}Zn containing Hoagland's solution and the images were obtained every minute for 48 hours.
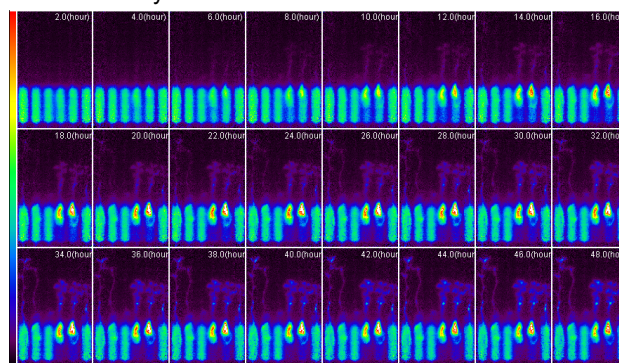
Fig. 1. Real-time Zn localization images obtained by PETIS. Six sets of plant and treatment solution are observed in each frame and the samples are MG-20s (Control, 1/10 Fe, 10×Fe) to B-129s (Control, 1/10 Fe, 10×Fe) from left to right.

The image obtained shows the Fe nutrient condition affects Zn uptake in *L. japonicus*. Fe deficient plant showed higher Zn uptake and Fe excess one showed suppressed Zn uptake, comparing to control condition (Fig. 1). These responses were observed both in MG-20 and B-129, however, it was more obvious in B-129. And it was also indicated Zn translocation of root to shoot was not affected by Fe conditions.

These results suggest the low activity in root to shoot Fe translocation activity induces multi-mineral accumulation in *L. japonicus* similar to *Arabidopsis*. And the mechanisms for perceiving Fe deficiency and excess in shoot should be one of the key components for this mineral accumulation.

References
[1] T. Yamamoto *et al.*, JAEA Takasaki Annu. Rep. 2014, 88 (2016).
[2] Y. Noda *et al.*, QST Takasaki Annu. Rep. 2015, **QST-M-2**, 151 (2017).
[3] N. Suzui *et al.*, Plant Methods, **13**, 40 (2017).
[4] M.A. Klein and M.A. Grusak, Genome, **52**, 677-691 (2009).
[5] T.P. Durrett *et al.*, Plant Physiol., **144**, 197-205 (2007).
[6] E. Delhaize, Plant Physiol., **111**, 849-855 (1996).

2 - 32 Elucidation of Cesium Transport Behavior in Soybean Root System

M. Igura [a)] and T. Satoh [b)]

[a)] Institute for Agro-Environmental Science, National Agriculture and Food Research Organization,
[b)] Department of Advanced Radiation Technology, TARRI, QST

Soybean shows higher nutrient uptake compared to other crops, and it has been suggested that symbiotic bacteria such as rhizobia are involved in element uptake. Elucidation of cesium and coexistence element uptake mechanism in the soybean root system is indispensable for development of cesium reduction technology of soybean.

The purpose of this study is to clarify the distribution of elements in roots and root nodules in the root system of soybean and to elucidate the accumulation site in the root system and the transport route to the above-ground parts.

The Japanese soybean cultivar Enrei infected with the rhizobia (*Bradyrhizobium japonicum*) was cultivated for about one month by hydroponic culture, and 100 μM of the stable cesium (Cs-133) was absorbed from the soybean root system. Distribution of stable cesium and potassium in roots and root nodules was analyzed by PIXE analysis.

Soybean was allowed to uptake Cs-133 for 24 hours in hydroponic solution, after which soybean roots and root nodules were harvested. Frozen blocks of the collected samples were prepared, and frozen sections (50 μm thick) of roots and root nodules were prepared using a cryostat (CM3050-Cryostat, LEICA Co.,). Elemental distribution analysis in soybean root and root nodule tissues was conducted by PIXE analysis of frozen sections. In addition, the Cs-133 concentration was quantified by ICP-MS.

The stable cesium and potassium distributions of root and root nodule tissues are shown in Fig. 1. While potassium was evenly distributed in the root tissue, cesium was slightly localized near the central vascular bundle (Fig. 1 a)). On the other hand, potassium tended to be distributed in the epidermis in root nodules, but cesium was evenly distributed to the inside, and this distribution was different from that in the roots (Fig. 1 b)). A clear distribution of cesium was confirmed in the root nodule tissue compared with the roots, and it was considered that the cesium was accumulated in the root nodules.

The relationship between the stable cesium concentration in the water culture medium and the stable cesium concentration in the root system tissue was shown in Fig. 2. The stable cesium concentration in roots and root nodules increased depending on the stable cesium concentration in the water culture medium, and the cesium concentration in root nodules was about 1.5 to 2 times that of roots.

Cesium accumulation in soybean root nodules was confirmed by in this study. In the future, we will clarify the behavior of cesium accumulated in root nodules and evaluate the effect of root nodules on uptake of cesium into the above-ground parts of soybean.
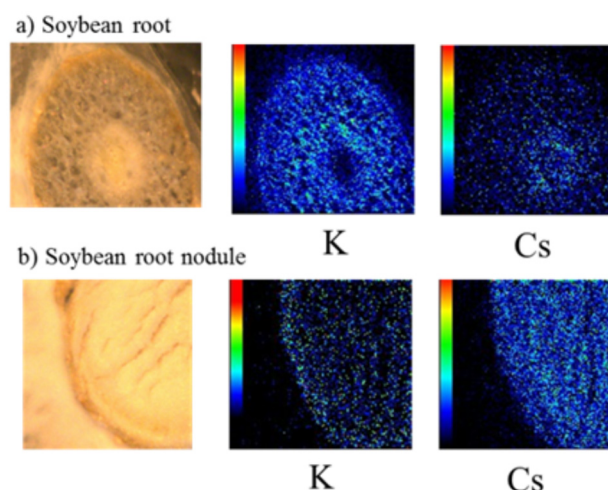
Fig. 1. Stable potassium and cesium distribution for soybean root and root nodule.
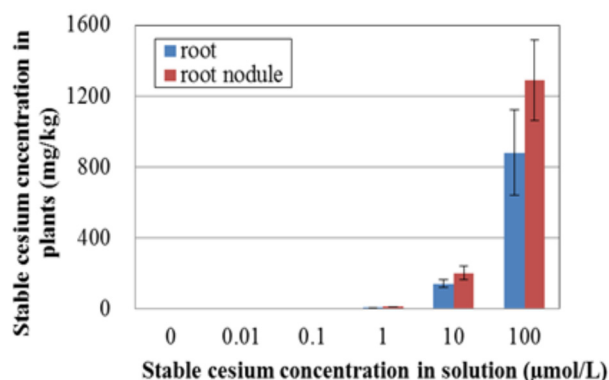
Fig. 2. Stable cesium accumulation in soybean root and root nodule.

2 - 33   Visualization of Sodium Localization in Salt-tolerant Species of the Genus *Vigna*

K. Naito [a), Y. Noda [a), J. Furukawa [b), N. Suzui [c), Y.-G. Yin [c) and N. Kawachi [c)

[a) Genetic Resources Center, National Agriculture and Food Research Organization,
[b) Life and Environmental Sciences, University of Tsukuba,
[c) Department of Radiation-Applied Biology Research, TARRI, QST

Elucidating mechanisms of salt tolerance in plants is an important issue to solve problems of salt stress in agriculture. Now almost 30% of irrigated field is salt-damaged, and 20% will be salt-damaged in the near future. In addition, resource of fresh water is running out and there is a growing demand for salt-tolerant crop that can be cultivated with brackish or sea water.

Across the plant taxa, genus *Vigna*, a reservoir of diversity, is outstanding because multiple species are adapted to coastal environment. In addition, our previous studies revealed that at least six species have independently acquired salt tolerance in relatively short evolutionary time, suggesting evolution of salt tolerance is genetically simple than previously considered [1].

However, the detail of salt tolerance mechanisms in these species are not known at all. Thus, to elucidate the mechanisms of their salt tolerance, we visualized sodium localization in the plant body with ^{22}Na and BAS-imaging on the salt tolerant species; *V. nakashimae, V. riukiuensis, V. trilobata, V. luteola* and *V. marina*. As a result, we found the amount of absorbed Na$^+$ in the plants and Na$^+$ localization were totally different from each other (Fig. 1). Especially, the most tolerant species *V. marina* kept the plant body almost free from Na$^+$.

This result indicated that these species have acquired different mechanisms of salt tolerance during evolution. We first assumed that Na$^+$ is isolated to vacuoles in the leaves of *V. riukiuensis*, but our SEM-EDX analysis revealed that Na$^+$ was specifically accumulated in chloroplasts (data not shown). On the other hand, *V. luteola* accumulated Na$^+$ specifically on the youngest fully-expanded leaf (Fig. 1). This kind of phenomenon has never been observed before and thus further investigation is needed to elucidate the physiological mechanisms.

To further investigate how *V. marina* deal with Na$^+$ around the root, we used PETIS [2] to perform real-time imaging analysis. As a result, the gamma-counts/sec (of ^{22}Na) in the culture media increased over time (Fig. 2). This result indicated that Na$^+$ is excreted from the root of *V. marina*. In addition, we found a diurnal oscillation in Na$^+$ excretion (Fig. 3). That is, Na$^+$ was excreted only at daytime while it was stopped at night. Furthermore, we performed another BAS-imaging on seedlings of *V. marina* and found that the Na$^+$ excretion occurred at the basal section of the root.

Together with genomic and genetic studies we have done, the results will facilitate identification of salt tolerance genes.
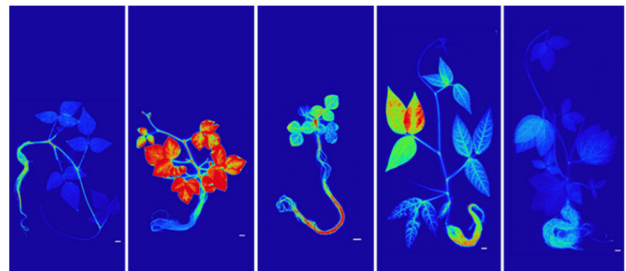
Fig. 1. Na$^+$ localization in the salt tolerant species of the genus *Vigna*. From left: *V. nakashimae, V. riukiuensis, V. trilobata, V. luteola,* and *V. marina*.
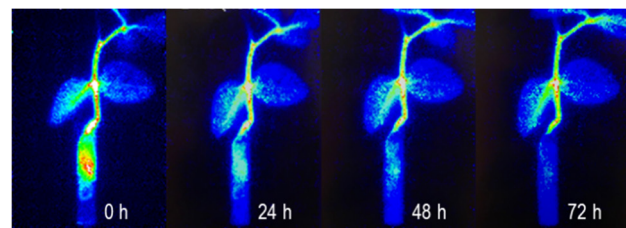
Fig. 2. Real-time imaging by PETIS on Na$^+$ extrusion from the root of *V. marina.*
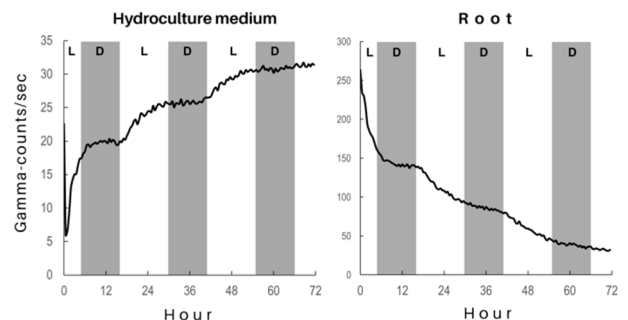
Fig. 3. Gamma-counts/sec in hydroponic culture media and the root of *V. marina* during the PETIS real-time imaging.

References
[1] K. Iseki *et al.*, PLoS One, **11**, e0164711 (2016).
[2] S. Fujimaki *et al.*, Plant Cell Physiol., **56**, 943-950 (2015).

2 - 34   Protamine-Hyaluronic Acid Particles as a Drug Delivery System and Their Application to Radiotherapy

S. Harada [a)] and T. Satoh [b)]

[a)] Iwate Medical University, School of Medicine, Department of Radiology,
[b)] Department of Advanced Radiation Technology, TARRI, QST

We have been developing targeted cancer chemotherapy, using particles that release anticancer drugs in response to irradiation. The released anticancer drugs attack tumors synergistically with the radiation, which will lead to increased anticancer effects. Localized release of the anticancer drug reduces the potential for adverse effects. Previously, we have developed encapsulated Protamine-Hyaluronic acid particles, which releases carboplatin with response to radiation. As hyaluronic acid decomposes into acetyl glucosamine when irradiated [1], it is postulated that the hyaluronic acid-protamine particles can decompose following irradiation. When protamine-hyaluronic acid particles were to contain carboplatin, the particles release carboplatin in response to radiation-induced decomposition. In this study, protamine-hyaluronic acid particles containing carboplatin (a platinum-containing anticancer drug) were generated, and their ability to increases antitumor effect were tested IN VIVO in C3He/N mice.

Protamine (2 mg), 1.6 mg hyaluronic acid, and 2 mg Paraplatin (a branded preparation of carboplatin) were mixed with 10 mL of 0.1 mmol/L Tris buffer, and incubated for 30 minutes at room temperature. The generated particles were filtered through a 0.8-μm cellulose filter. The particles that were trapped in the cellulose filter were re-suspended in 0.1 mmol/L Tris buffer. Finally, that solution of particles were injected into an ample of Lipid capsules (Coatsome EL-010, Nichiyu) and used in experiments. 1×10^{10} Particles were injected into MM48 tumor, which was inoculated into left hind legs of C3He/N mice. Then, irradiations were performed only to tumors with 140-KeV soft X-ray at a dose rate of 0.301 Gy/min by using Softex M150 WE. The irradiated tumors were excised and processed to be analyzed using a micro PIXE camera [1]. Each PIXE sample was irradiated with a 3 MeV proton beam, and the X-rays induced were recorded using a silicon-lithium detector. All micro PIXE analyses were carried out at the Takasaki Advanced Radiation Research Institute, QST. The antitumor effect was tested by measuring tumor diameter every day.

The particles were imaged using the micro PIXE camera, based on the distribution of Pt. The mean diameter of the generated particles was 5.2 ± 0.5 μm (Fig. 1-A). Before irradiation, particles were round in shape with clear margins (Fig. 1-A). After irradiation, particles were fragmented, which was considered to indicate rupturing of particles (Fig. 1-B). The percentages of ruptured particles are shown in
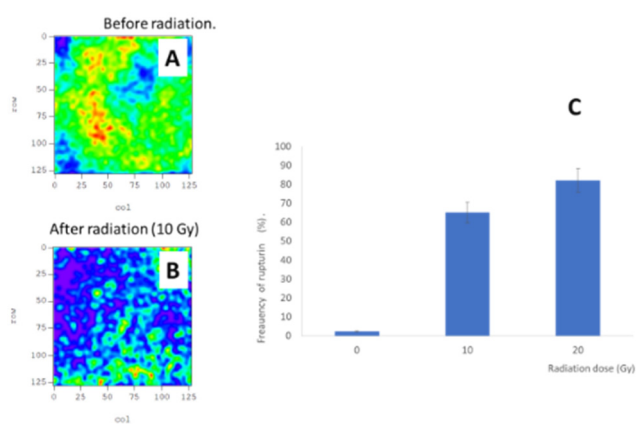
Fig. 1. Particles in the tumor tissue.   A: Before radiation.   B: After 10 Gy radiation.   C: Frequency of ruptured.
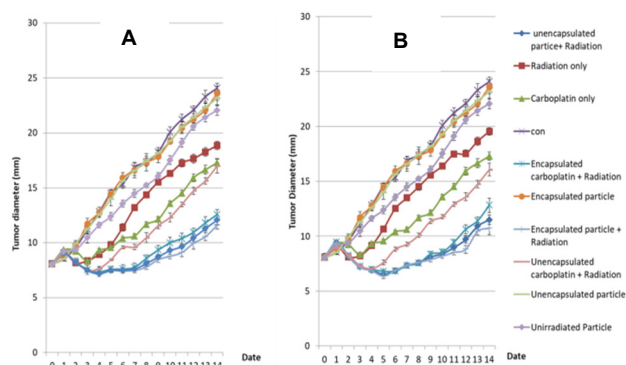
Fig. 2. Antitumor effect.   A: 10 Gy, B: 20 Gy.

Fig. 1-C. Particles released carboplatin dependently on radiation doses. The released carboplatin attacked carboplatin with radiation, which resulted in increased antitumor effect. However, there were no significant increases of antitumor effect among unencapsulated carboplatin, carboplatin encapsulated into Protamine-Hyaluronic Acid particles, carboplatin encapsulated into Protamine-Hyaluronic Acid particles and carboplatin encapsulated into Protamine-Hyaluronic Acid particles coated with lipid, under 10 Gy (Fig. 2-A) and 20 Gy (Fig. 2-B) radiation.

References
[1] S. Harada, S. Ehara et al., Biomed. Phamacother., **70**, 196 (2015).
[2] S. Harada, S. Ehara et al., Int. J. PIXE, **24**, 137 (2014).

2 - 35   Analysis of Trace Elements in Acute Myelogenous Leukemia Cell Line Using In-Air Micro-PIXE

T. Kasamatsu, Y. Kanai and H. Murakami

Gunma University Graduate School of Health Sciences

Acute Myelogenous leukemia (AML) is a cancer of the myeloid line of blood cells, characterized by the rapid growth of abnormal cells that build up in the bone marrow and interfere with normal blood cells. Symptoms include feeling tired, easy bleeding, and increased risk of infections. As an acute leukemia, AML progresses rapidly and is typically fatal within weeks or months if left untreated. To elucidate the pathophysiology of AML, we analyzed the trace elemental changes in AML cell using in-air micro-PIXE method.

Two AML cell line, HL-60 and KG-1, were used in this study. For comparison, a multiple myeloma cell line KMS-11 was also used. These cell lines were grown in RPMI with 10% heat-inactivated fetal bovine serum, and antibiotics. AML cells were treated with doxorubicine (DXR), an anthracycline antibiotic with antineoplastic activity, for 24 h (HL-60; 0 nM and 850 nM, KG-1; 0 μM and 100 μM). The cells were centrifuged by cytocentifuge for 500 rpm, 15 minutes on a 0.5 μm polycarbonate film after washing and resuspension in TRIS-HNO$_3$ (pH 7.4). The film was sunk into isopentane chilled with liquid nitrogen down to its melting point (-160 °C), then lyophilized by vacuum evaporation at 1.0 × 10^{-2} Torr. Three point zero MeV proton beams, 1 μm diameter, were generated by the TARRI single-ended accelerator at the National Institutes for Quantum and Radiological Science and Technology, Takasaki.

In X-ray spectrum derived from HL-60 and KG-1, potassium yield was higher than KMS-11 (Fig. 1). Other elemental yields were almost similar among these cell lines. Subsequently, we compared the spectrum between 0 nM and 850 nM DXR treatment HL-60 cells. Potassium yield of 850 nM DXR treatment cells was lower than 0 nM DXR treatment cells (Fig. 1). However, potassium yield of 100 μM DXR treatment KG-1 cells was the same extent as 0 μM. There were no differences in other elemental yields.

Almost all cells possess an Na$^+$-K$^+$-ATPase, which pumps Na$^+$ out of the cell and K$^+$ into the cell and leads to a K$^+$ gradient across the cell membrane (K$^+$in>K$^+$out). Cell proliferation and apoptosis are two counterparts that share the responsibility for maintaining normal tissue homeostasis. Evidence has been accumulating from fundamental studies indicating that tumour cells possess various types of potassium channels, and that these potassium channels play important roles in regulating tumour cell proliferation and apoptosis, i.e. facilitating unlimited growth and promoting apoptotic death of tumour cells [1]. Doxorubicin intercalates between base pairs in the DNA helix, thereby preventing DNA replication and ultimately inhibiting protein synthesis. Additionally, doxorubicin inhibits topoisomerase II, which results in increased and stabilized cleavable enzyme-DNA linked complexes during DNA replication and subsequently prevents the ligation of the nucleotide strand after double-strand breakage. In this study, DXR treatment caused the decrease of intracellular potassium levels in HL-60. Our result suggested that DXR may affect the cell death via potassium homeostasis directly or indirectly and that its mechanism depends on the cell types.

Reference

[1] Z.Wang *et al.*, Pflugers Arch., **448**, 274-286(2004).
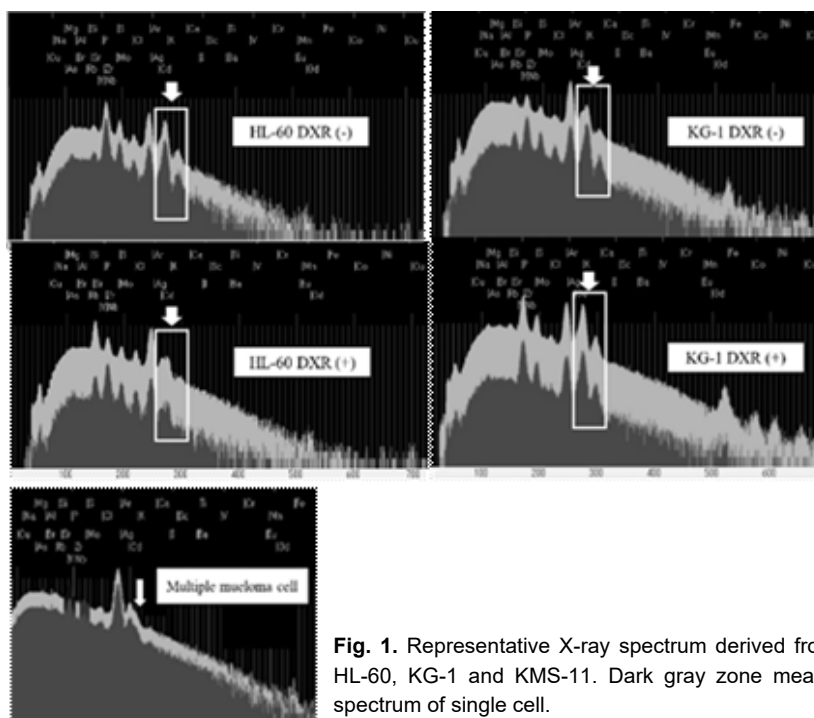
Fig. 1. Representative X-ray spectrum derived from HL-60, KG-1 and KMS-11. Dark gray zone means spectrum of single cell.

2 - 36 Accumulated Silica in the Lungs in Patients with Idiopathic Pulmonary Fibrosis

Y. Koga [a)], T. Satoh [b)], K. Kaira [c)], M. Koka [b)], T. Hisada [d)] and K. Dobashi [e)]

[a)] Department Allergy & Respiratory Med, Gunma University Graduate School of Medicine,
[b)] Department of Advanced Radiation Technology, TARRI, QST,
[c)] Saitama Medical University International Medical Center, Department Respiratory Med,
[d)] Gunma University Graduate School of Health Sciences,
[e)] Jobu Respiratory Hospital

It has been well known that inhalation of asbestos can be a risk factor of interstitial pneumonia. The relationship between inhalation of elements and interstitial pneumonias still remains unknown. In this study, we focused on idiopathic pulmonary fibrosis (IPF) revealed by the histology obtained from video-assisted thoracic lung surgery and examined the inhaled elements in the lungs by in-air micro particle-induced X-ray emission analysis (in-air micro PIXE). The relationship between contents of elements in the lungs and the progression of IPF were analyzed. In-air micro PIXE detected elements such as magnesium, iron, silica, aluminum, sulphur, phosphorus, and zinc in the lungs. Accumulation of inhaled silica/silicates were correlated with annual declined forced vital capacity, while other elements detected by in-air micro PIXE did not show any correlation with the progression of IPF. Furthermore, high levels of inhaled silica/silicates in the lungs decreased mortality of IPF, indicating that accumulated silica/silicates in the lungs are possible predictive marker of IPF prognosis. This study showed that small amounts of inhaled elements in the lungs detected by in-air micro PIXE is useful for the analysis of progression in IPF patients.

はじめに

微量な肺組織を用いた元素分布の測定が可能な大気マイクロ PIXE (Particle Induced X-ray Emission)により我々は肺と縦隔リンパ節における元素濃度の検討を行ってきた[1]。同様の手法を用いて特発性肺線維症を対象とした肺組織中の元素解析を行い、肺組織中の元素濃度と特発性肺線維症の進行度及び予後との関連性を検討した。

方法

胸腔鏡下肺生検で得られた肺組織検体のパラフィン切片にイオンマイクロビームを照射し、パラフィン切片内の元素分布を測定した。対象検体は病理学的に usual interstitial pneumonia pattern と診断された特発性肺線維症症例のみとした。

結果

大気マイクロ PIXE 分析により検出された、肺組織中の元素、Al, Mg, Si, S, P, Ca, Fe, Zn の中で、唯一シリカと特発性肺線維症の肺機能の変化との間に有意な相関関係を認めた (Fig.1A)。さらにシリカ濃度(Si/S)が 0.11 以上の症例ではそれ以下の症例より有意に予後が悪かった(Fig. 1B)。

考察

大気マイクロ PIXE によって検出された肺組織中シリカ濃度が、特発性肺線維症の進行度や予後を予測出来る可能性が示唆された。

Reference

[1] Y. Koga *et al*., Environ Health Prev. Med., **21**(6), 492-500 (2016).
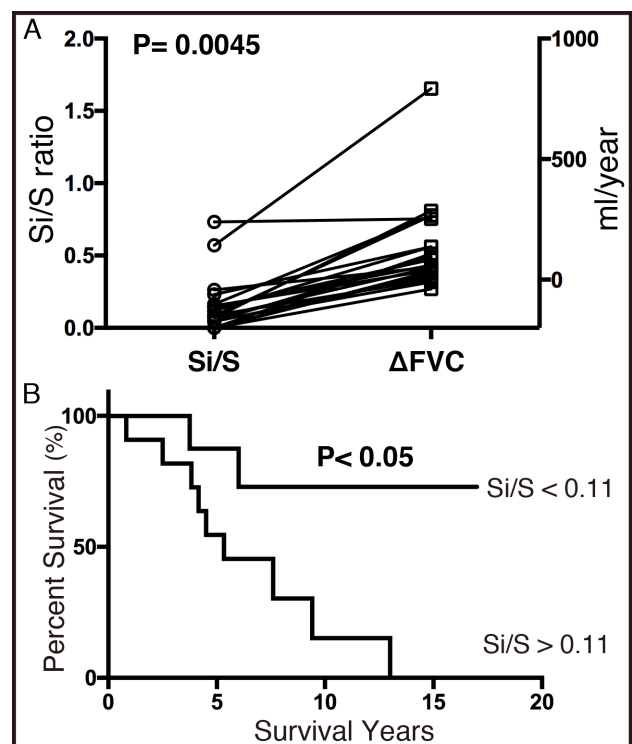
Fig. 1. Accumulated silica/silicates in the lungs decreased annual forced vital capacity:FVC (A) and increased mortality (B) in IPF cases.
Accumulation of silica/silicates (Si/S) in the lungs significantly correlated with annual declined forced vital capacity (A). Accumulated silica/silicates (Si/S) more than 0.11 significantly decreased mortality compared with less than 0.11 of Si/S in IPF patients.

2 - 37 Elements Distribution into Tooth Structure by Titanium Fluoride Treatment -Effects of Various pH of Solution-

K. Okuyama [a)], Y. Matsuda [b)], H. Yamamoto [c)], K. Naito [c)], T. Saito [b)], M. Hayashi [c)],
Y. Yoshida [d)], Y. Tamaki [a)], T. Satoh [e)] and N. Yamada [e)]

[a)] Asahi University School of Dentistry,
[b)] School of Dentistry, Health Sciences University of Hokkaido,
[c)] Graduate School of Dentistry, Osaka University,
[d)] Faculty of Dental Medicine, Hokkaido University,
[e)] Department of Advanced Radiation Technology, TARRI, QST

Introduction

Titanium fluoride (TiF_4) is expected to one of the solutions for topical fluoride treatment. This solution is used in foreign countries, however it is not allowed to use for patients in Japan because of low pH of the solution. The purpose of this study is to evaluate distribution of fluorine and titanium at various pH values of TiF_4 solution.

Materials and methods

Extracted human teeth were sliced (500 µm thickness) longitudinally, coated with wax except for buccal dentin surface. Specimens were performed on pH cycling (pH 4.5 and 7.0, 6 cycles/day; simulate oral condition) for 8 weeks to prepare artificial carious dentin. During this cycle, specimens were soaked into 1% TiF_4 solution adjusted to pH 4, 5, 6 or unadjusted solution (pH 1) for 5 min once every two weeks. After pH cycling, calcium, fluorine and titanium distribution was analyzed by an in-air micro-PIXE/PIGE system with a 1.7-MeV $^1H^+$ microbeam at TIARA [1]. The outermost surface of the dentin was defined as the position containing 5% of the calcium concentration in intact dentin. For comparison of fluorine or titanium uptake, cumulative concentration of fluorine or cumulative contents of titanium in each specimen was calculated as an area of 100 µm from the defined surface. Quantitative results of fluorine and calcium were obtained by calibrating the PIXE/PIGE yield using hydroxyapatite with various reference materials [$Ca_{10}(PO_4)_6(OH)_{2-2x}F_{2x}$, where x = 0, 0.25, 0.5, 0.75, or 1]. The titanium contents were measured by the ratio of titanium counts/ copper counts owing to luck of titanium reference materials. The obtained data were analysed by Kruskal-Wallis test and Mann-Whitney U test (α=0.05).

Results

Figure 1 shows representative elemental PIXE/PIGE mapping images of specimen treated with pH 1 or 6 TiF_4 solution. Fluorine was distributed to the deep area of both pH groups. Titanium was distributed to underneath demineralized dentin area at pH 1 group, however, titanium was detected on a superficial dentin area at pH 6 group. Higher fluorine distribution at pH 1 and 6 solution were indicated than that at pH 4 and 5 (Table 1). The highest titanium distribution at pH 1 was showed among all used pH values (Table 1).

Discussion

On fluorine and titanium distribution, there was different allocated depth or deposited site on specimen between both two elements. These differences might be due to that fluorine was bonded with hydroxyapatite on dentin or calcium fluoride (CaF_2) was deposited on the site. Because titanium has larger atomic weight than fluorine, titanium could not infiltration to the deep area. In pH 1 group, large area of dentin was demineralized and might be created deposit area for both elements. On pH 6 group, there was higher fluorine distribution and not significantly different titanium distribution than that at pH 4 and 5. It is suggested that pH 6 TiF_4 solution may be expected to caries inhibition.
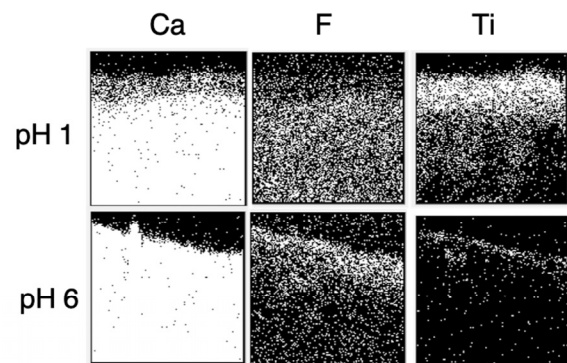
Fig. 1. Representative elemental PIXE/PIGE mapping images of specimen processed by pH 1 or 6 TiF_4 solution. Left images show calcium (Ca) by PIXE. Middle images show fluorine (F) by PIGE. Right images show titanium (Ti) by PIXE. White dots in the map represent each element. Superficial surface is at the upper side of each image.

Table 1

Cumulative penetrated fluorine (F) and titanium (Ti) into dentin at 100 µm depth area from superficial surface.

	F ($\times 10^6$ ppm $\times$ µm)	Ti ((Counts/Cu counts) $\times$ µm)
pH1	1.96 (0.65-3.66) [a]	2.94 (0.80 -12.4)
pH4	1.06 (0.30-1.98) [b]	0.43 (0.22-3.99) [A]
pH5	1.03 (0.30-1.82) [b]	0.70 (0.23-1.66) [A]
pH6	1.84 (0.35-2.56) [a]	0.24 (0.15-0.68) [A]

Median (minimum-maximum)
Same letters no indicate significant differences (p>0.05).

Reference

[1] Y. Matsuda *et al.*, Nucl. Instrum. Meth. Phys. Res. B **348**, 156-159 (2015).

Part Ⅱ

3. Advanced Quantum-Beam Technology

3 - 01   Demonstration of Hollow Profile Shaping of a High-Energy Ion Beam Using Multipole Magnets

Y. Yuri, T. Yuyama and T. Ishizaka

Department of Advanced Radiation Technology, TARRI, QST

It is essential to properly manipulate the transverse intensity distribution or irradiation field of a charged-particle beam extracted from an accelerator for the utilization of the beam. Various types of magnets are employed to shape a beam profile and irradiate a target sample according to user demands. For example, the transverse spatial intensity distribution can be made approximately uniform through the nonlinear focusing force using multipole (mainly, octupole) magnets in a beam transport line. This fact indicates that the proper use of multipole magnets enables the diverse beam profile shaping that cannot be achieved by common linear focusing using quadrupole magnets. We have, therefore, investigated the feasibility of the beam profile shaping by means of nonlinear focusing. Recently, we have experimentally demonstrated the formation of an ion beam with a hollow transverse profile using octupole and sextupole magnets [1]. Here, the hollow beam can be defined as a beam whose peripheral intensity is higher than that of the central part in the transverse beam cross-section.

The beam experiment was conducted at the LB line of the TIARA cyclotron where two octupole and two sextupole magnets were installed together with several quadrupole magnets. The ion species chosen for the experiment was 10-MeV proton. Different from the beam optics for the uniform-beam formation, the present beam optics for the hollow-beam formation has the horizontal–vertical coupling of the ion's betatron oscillation at the multipole magnets. The betatron coupling is crucial for the formation of a hollow beam with various cross-sectional shapes.

The spatial profiles of the beam on a target are shown in Fig. 1. When the beam was focused using two octupole magnets with proper polarities and strengths, the tail of the original beam was folded inward and the elliptical hollow beam (7~8 cm in diameter) was formed, as shown in Fig. 1(a). The steep high-intensity peak surrounding the central low-intensity part of the beam was generated in the periphery of the beam. The peripheral edge of the beam was distinct because the beam intensity was very low at the outside of the edge. The peak height was not even along the edge but was maximized near the horizontal and vertical axes. The maximum contrast between the edge peak and center was over 10 and the peak width was 1~2 mm. In Fig. 1(a), the eight "streaks" grew from the four peaks slightly inside the edge on the axes, due to a strong nonlinear kick of ions with large betatron amplitude at the octupole magnets. We have confirmed that the streaks could be removed by the beam tail collimation 2.2 m before the first octupole magnet. Following this beam collimation, the resultant cross-sectional shape of the hollow beam was nearly circular, as shown in Fig. 1(b).

Moreover, the focusing effect of sextupole magnets (instead of octupole magnets) was also investigated. It has been confirmed, by systematic experiments and numerical simulations, that the cross-sectional shape of the beam varied diversely (e.g., a rounded rectangle, rhombus, and triangle) depending on the type and strength of the applied multipole magnets.

The phase-space information is necessary to understand the behavior of the beam focused by multipole magnets in detail. In order to measure the phase-space profile of the beam, a pepper-pot mask was fabricated and installed in the target chamber of the LB line. The first beam test indicates that the configuration of the mask and beam measurement method (such as phosphor screens) must be improved for fine and precise data acquisition.

In summary, the hollow-beam formation using multipole magnets has been demonstrated experimentally. The present method, based on existing accelerator technologies, is applicable to various charged-particle beams of different parameters such as the particle species, kinetic energy, and time structure because the source of the nonlinear force is the magnetostatic field produced by multipole magnets. A further study is ongoing for the improvement of the hollow-beam characteristics and the application.

Acknowledgments

Fig. 1. Transverse spatial profiles of the beam, measured using radiochromic films [2]. The field gradient of the two octupole magnets is (-10500 m^{-4}, 3100 m^{-4}) in both cases, which corresponds to the excitation current of (100 A, 30 A). Note that the beam tail was collimated in the case of (b). The 1D distribution along the vertical axis (dashed line) is also plotted.

References

[1] Y. Yuri *et al.*, Prog. Theor. Exp. Phys. **2019**, 053G01 (2019).

[2] Y. Yuri *et al.*, Nucl. Instrum. Meth. Phys. Res. B **406**, 221 (2017).

3 - 02   Assembling Gold Nanoparticles by Dielectrophoresis with Pit Arrays on PMMA Fabricated by Proton Beam Writing

T. Shibuya [a)], S. Uchida [b)], Y. Ishii [c)] and H. Nishikawa [a)]

[a)] Dept. of Electrical Engineering, Shibaura Institute of Technology,
[b)] Dept. of Electrical Engineering, Tokyo Metropolitan University,
[c)] Department of Advanced Radiation Technology, TARRI, QST

Assembled nanoparticles of metals and oxides have attracted much attention for sensing applications such as strain gauges and gas sensors [1]. Among various techniques for the assembly of nanoparticles, dielectrophoresis (DEP) was found to be a useful technique to manipulate and collect colloidal particles under application of unequal AC electric field.

We have applied proton beam writing (PBW) to fabricate microstructures such as arrays of pillars and pits on dielectric materials, which were effective to modulate the electric field to apply DEP force on Ag nanowires and nanoparticles [2].

In this study, we studied DEP to assemble Au nanoparticles using pit arrays of PMMA on a film of indium tin oxide (ITO) on polyethylene terephthalate (PET) fabricated by PBW. We investigate dependence of the assembly of Au nanoparticles on the frequency of applied AC voltage.

We performed PBW to fabricate pit arrays (5 × 5 to 10 × 10 arrays in 200-μm area) in a PMMA layer on a conductive indium-tin-oxide (ITO)/PET film using a dedicated proton beam writer at SIT or a microbeam line with a single-ended accelerator at QST Takasaki.

Figure 1 (a) shows a photograph image of a 20-mm squared ITO-PET film, which is spin-coated with PMMA. We measured a SEM image in Fig. 1 (b) of the 5 × 5 pit arrays formed on the PMMA by scanning electron microscope (SEM, JEOL JSM-7610F).

Figure 2 shows a schematic illustration of the cross section for assembly of the Au particles into the pit arrays by DEP. The diameter of the pit is 4 μm. Colloidal gold particles of 250 nm in diameter were used for the DEP experiments to fill the pit arrays with the nanoparticles.

We investigated effects of the dimension of pit arrays and the frequencies of applied AC voltage on the fill factor of gold nanoparticles to each pit and the distribution over the whole arrays. In order to avoid degradation of electrode at the application of voltage for DEP experiment, we gradually increase the AC voltage, where it increases with a 1.0 V step combined with three levels of the offset DC voltage from 0, 10 mV, and 1.0 V.

In Fig. 3(a), assembled Au nanoparticles by DEP at the site of pit arrays were observed after the removal of PMMA pit arrays. The height of the assembled Au nanoparticles in Fig. 3 (b) is 3.4 μm in average, which is half the depth of the PMMA pit arrays.

In Fig. 3 (a), we note there are missing Au microstructures, which might be peeled off at the timing of PMMA removal. We need to improve the adhesion of these microstructures to ITO electrodes to obtain homogeneous deposition of the assembled Au nanoparticles.

References

[1] Meital Segev-Bar and Hossam Haick, ACS Nano, **7**, 8366-8378 (2013).
[2] R. Kataoka, H. Tokita, S. Uchida, R. Sano and H. Nishikawa, Journal of Physics: Conference Series **646**, 012005 (2015).
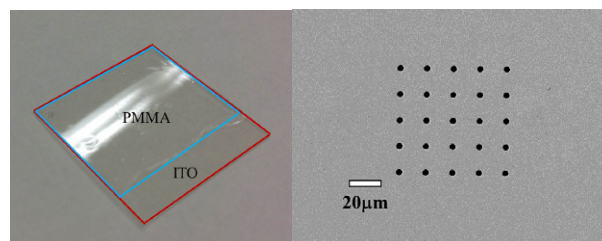
Fig. 1. (a) A photograph image of a 20-mm squared ITO-PET film, which was spin-coated with PMMA to a thickness of ~5 μm and (b) a SEM image of 20-μm spaced, 5 × 5 pit arrays formed on PMMA on ITO-PET film by PBW at 1.0 MeV.
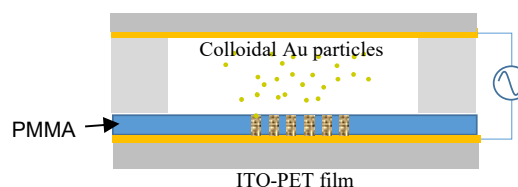
Fig. 2. Schematic illustration of the cross section for collection of Au nanoparticles into 20-μm spaced, 5 × 5 pit arrays on 7-μm thick PMMA by DEP. The ITO-PET films are separated by a 500-μm thick PDMS spacer for DEP of the colloidal Au particles.
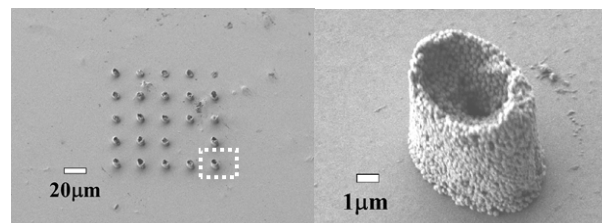
Fig. 3. (a) Overall and (b) magnified SEM images of the structures of Au nanoparticles assembled by DEP using 5 × 5 PMMA pit arrays after the removal of PMMA. Time sequence was used for AC and DC voltage applications during DEP. The colloidal Au particles of 5.0 mL with concentration of 9.84×10^8 mL^{-1} was used.

3 - 03

Electrical Property Tolerance to 2 MeV Electrons of n-GAAFETs with Different Gate Length

K. Takakura, M. Yoneoka and I. Tsunoda

National Institute of Technology, Kumamoto College

Multiple gate devices were considered as an alternative for planar complementary metal oxide semiconductor (CMOS) scaling. Gate-all-around (GAA) devices with the gate fully wrapped around the device body promising candidates for the next generation technology nodes. The scaling of CMOS technologies leads to an intrinsic hardening against certain radiation effects, like Total Ionising Dose (TID) damage, so that the implementation of commercial-of-the-shelf ULSI components and circuits for harsh environments is expected. In this study, an electric characteristic of the n-GAAFETs such as short channel effect by reduction of gate length and degradation of input and output (I/O) characteristics after irradiation of 2 MeV electrons are investigated.

Devices without applied bias voltage were irradiated with 2 MeV electrons up to 1×10^{16} e/cm^2 at room temperature at the Takasaki QST. The gate stack used in all devices was obtained by a replacement Metal Gate high-k process and it consists of an interfacial layer-SiO$_2$ and a high-k dielectric (HfO$_2$) [1]. Figure 1 shows the schematic draw of device structure of the SOI nGAAFET. Gate width (W) fixed W= 1.0 µm, and gate length (L) changed L=0.25, 0.45 and 1.0 µm. I/O characteristics of the device were measured by using Keysight Technology B1500A device parameter analyzer.

Figure 2 shows the I/O characteristics of the L=0.25 µm and 1.0 µm devices before and after the 2 MeV electron irradiation (1×10^{16} e/cm^2). For a long gate length device, there is almost no change in drain current (I$_D$) with respect to electron irradiation, however, as the gate length becomes shorter, the threshold voltage (V$_T$) seems to show negative sifts. In addition to that, in the output characteristic, the I$_D$ is not saturated at high V$_D$ in the L=0.25 µm device after irradiation. The reduction of the potential barrier at the S/D junctions can lead to an increase I$_D$ such as punch-through. Drain induced barrier lowering (DIBL) determined as eq. (1) is adopted as an indicator of potential barrier height at source and/or drain (S/D).

$$\text{DIBL} = \frac{V_{T\,V_D=0.8V} - V_{T\,V_D=0.1V}}{0.8-0.1} \quad (1),$$

here, V$_T$ estimated by extrapolation the linear region of the input characteristics. The V$_T$ shift and DIBL are shown in Fig. 3 as a function of electron fluence. The values of V$_T$ for all samples decrease with increasing electron fluence. In particular, the V$_T$ with the shortest gate length, L=0.25 µm, is greatly shifted. Similarly, DIBL increases with electron irradiation for devices with shorter gate lengths. An increase in DIBL indicates that the S/D potential barrier became lowered. It was found that the electrical properties of the n-GAAFET against electron irradiation were less tolerant when the gate length is short, but higher as the gate length became longer.

Acknowledgments

Reference

[1] F. Andrieu, *et. al.*, Proc. Int. Electron Dev. Meet., 3.2.1 (2010).
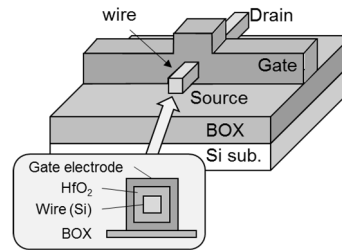
Fig. 1. Device structure of the SOI nGAAFET. Nano wire is surrounded by gate electrode.
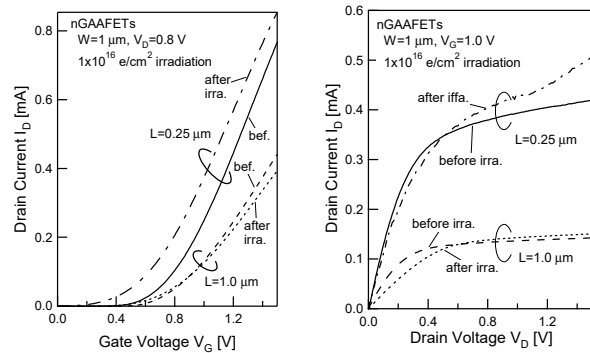
Fig. 2. I/O characteristics of the L=0.25 and 1.0 µm devices before and after electron irradiation (1×10^{16} e/cm^2).
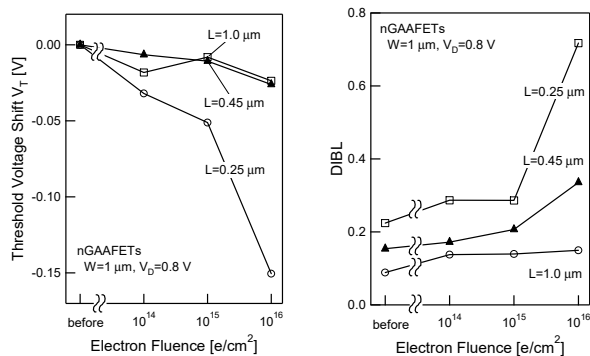
Fig. 3. The V$_T$ shift and DIBL of the devices as a function of electron fluence.

3 - 04   Vacancy-induced Magnetism in Gd-doped GaN Film Probed by Spin-polarized Positron Beam

M. Maekawa, S. Sakai, K. Wada, A. Miyashita and A. Kawasuso

Department of Advanced Functional Materials Research, TARRI, QST

Diluted magnetic semiconductors (DMSs) materials have attracted interest because the both of semiconducting and magnetic properties are emphasized at development of spintronics devices. Gadolinium-doped GaN (GaGdN) is expected as one of such the DMSs. To synthesis GaGdN, Gd ion implantation is carried out. Actually, it has been observed that Gd ion implanted GaGdN crystals exhibit room temperature ferromagnetism [1]. Although each Gd atom has a magnetic moment of 7 µB, the anomalous large magnetic moment as high as 4000 µB per one Gd atom has also been reported in low Gd concentration [2]. The reason for such the anomalous magnetic moments is still unclear. Vacancy defects has been proposed as one possible candidate. Around Gd atoms, vacancy defects are magnetized and produce a large magnetic moment [3]. In order to elucidate the magnetism of GaGdN, it is necessary to clarify the magnetism induced by vacancies.

Magnetic Doppler broadening (MDB) method, which is the Doppler broadening of annihilation radiation (DBAR) measurement using spin-polarized positrons in a magnetic field, is emerged as a powerful tool to detect local magnetic moments localized at vacancy-type defects. In this study, we investigated the relationship between magnetism and vacancy-type defects in GaGdN by the MDB method.

Samples used in this study were Gd-implanted GaN films with the thickness of 2 µm grown on sapphire substrates. These samples were implanted with Gd ions at 100 keV to doses of 1×10^{13} cm^{-2} (low dose) and 1×10^{15} cm^{-2} (high dose) at room temperature using a 400 keV ion implanter. The Doppler-broadening annihilation radiation (DBAR) spectra were obtained in the magnetic fields of ± 0.91 T at 20 K. Magnetization (M-H) curves were also obtained by a superconducting quantum interference device (SQUID) apparatus at 10 K.

Figure 1 shows the M-H curves for the GaGdN samples. After the implantation, magnetizations are observed. From this results, magnetization per Gd atom for the low and high dose samples are 300 µB/Gd and 4 µB/Gd, respectively. It is confirmed that the magnetization per Gd atom becomes anomaly large when the Gd concentration is low.

Figure 2 shows the MDB spectra, which is differential DBAR spectra in positive and negative magnetic fields, for GaGdN samples. Gray fine lines are raw experimental data and bold lines are 10-points smoothed data. MDB intensity increases with increasing implantation dose. Since positrons are known to be trapped in Ga defects, these results indicate that Ga vacancies are magnetized.

When only Ga vacancies are introduced, almost no magnetization is observed [4]. These results indicate that the implanted Gd magnetizes the Ga vacancies.

In the high dose sample, the larger MDB intensity appeared due to the higher vacancy concentration. On the other hand, the magnetization per implanted Gd atom approaches the magnetization per single Gd atom. This might be because when the Gd amount is large, the ferromagnetic component of the implanted Gd becomes dominant. When the Gd concentration is low, it is considered that the effect of the magnetization of the vacancies, which causes the anomalous magnetic moment, becomes remarkable.
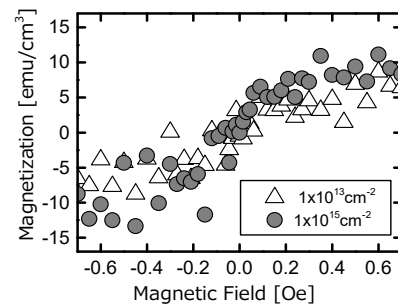
Fig. 1. Dose dependence for Gd-implanted GaN samples of M-H measurements.
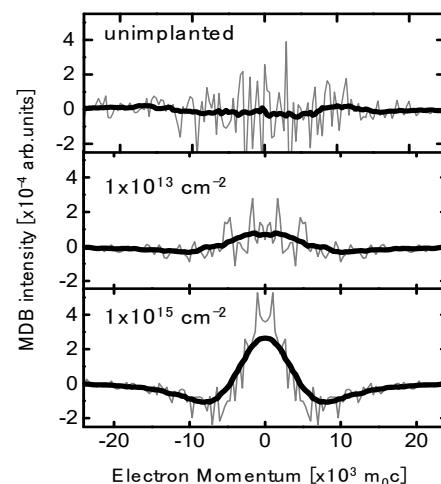
Fig. 2. Dose dependence for Gd-implanted GaN samples of MDB measurements.

References

[1] N. Teraguchi *et al.*, Solid State Comm., **122,** 651 (2002).

[2] M. A. Khaderbad *et al.*, Appl. Phys. Lett., **91**, 072514 (2007).

[3] S. Dhar *et al.*, Phys. Rev. Lett., **94,** 037205 (2005).

[4] M. Maekawa *et al.*, QST Takasaki Annu. Rep. 2017, **QST-M-16**,125 (2019).

3 - 05 Experimental Verification of Relative Angular Distribution of the n-p Elastic Scattering Reaction Using a Proton Recoil Telescope

T. Matsumoto [a)], A. Masuda [a)], H. Harano [a)] and S. Kurashima [b)]

[a)] National Metrology Institute of Technology, National Institute of Advanced, Industrial Science and Technology,
[b)] Department of Advanced Functional Materials Research, TARRI, QST

In many cases, recoil protons produced by the n-p elastic scattering reaction are used in neutron detectors and neutron dosimeters [1][2]. Especially, information on the angular distribution of n-p elastic scattering reaction is important for proton recoil telescopes (PRTs) that are used to determine the neutron fluence in neutron energy region above several MeV [2]. Energy dependent detection efficiency of a PRT is usually obtained using simulation codes with an evaluated data file such as LA150 and JENDL-HE files. However, the angular distribution of the n-p elastic scattering reaction has discrepancy between LA150 and JENDL-HE2007 in high energy regions above 20 MeV. In our previous study, a PRT composed of a Si surface barrier detector and a liquid scintillation detector was developed to measure high energy neutrons above 20 MeV. The recoil angle of 10 degrees in laboratory system was used in the PRT. In this case, the detection efficiency for 45-MeV neutrons had 5% discrepancy between LA150 and JENDL-HE2007 [2].

We have experimentally verified the relative angular distribution of the n-p elastic scattering reaction for 45-MeV and 60-MeV neutrons at TIARA. In 2017 and 2018, the relative angular distribution for 45-MeV neutrons was verified by changing the recoil angle from 10 to 30 degrees using the PRT composed of a 6.0-cm diameter and 0.5-mm thick Si detector (ΔE) and a 7.62-cm diameter and 7.62-cm thick liquid scintillation detector (E: BC501A). In general, experiments for the n-p elastic scattering reaction are perform using the neutron time-of-flight (TOF) method. However, it is not easy for the neutron TOF method to evaluate background neutrons in comparison with the recoil proton measurements in the present experiments. The neutrons were produced by the ^{7}Li(p,n) reaction in the LC0 beam line at TIARA. A high-density polyethylene plate was used as an n-p converter in the PRT. A carbon plate was also used to subtract background due to Carbon included in Polyethylene. Proton pulse height spectra of the liquid scintillation detector were successfully observed in ΔE-E coincidence measurements of the PRT. Figure 1 shows the recoil proton pulse height spectra of the PRT. The neutron fluences were derived for recoil angles from 10 to 30 degrees using detection efficiencies calculated with the MCNPX code using the LA150 and JENDL-HE files, respectively. Figure 2 shows preliminary results of normalized neutron fluence. In Fig. 2, the data were normalized at the result of 10 degrees obtained using the JENDL-HE file. Error bar in Fig. 2 shows only statistical

uncertainty. To obtain the final results, TOF data for the recoil protons in the PRT have been also analyzed. Moreover, we will also measure the n-p elastic scattering reaction at 60 MeV for recoil angles from 10 to 30 degrees in laboratory system in 2019.

References
[1] T. Shimoyama *et al.*, Radiat. Prot. Dosim., **126**, 130 (2007).
[2] T. Matsumoto *et al.*, J. Nucl. Sci. Technol., **54(5)**, 529 (2017)
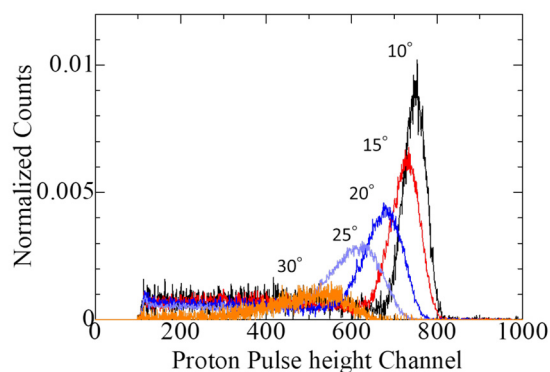
Fig. 1. Recoil proton pulse height spectra of the PRT for recoil angles from 10 to 30 degrees.
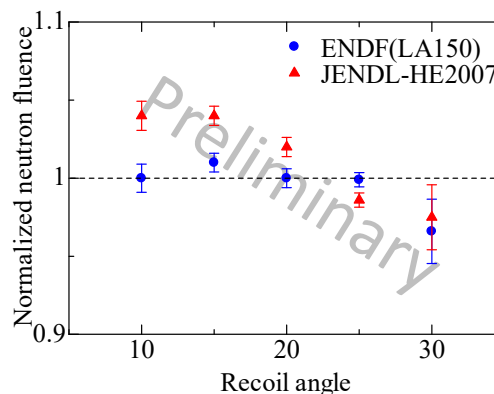
Fig. 2. Preliminary results of normalized neutron fluence obtained for the recoil angles from 10 to 30 degrees.

3 - 06   Comparison of Total Yields of Negative Secondary Ions Emitted by Sub MeV C_{60} Ion Impacts on a Poly(methyl methacrylate) Target

K. Hirata [a], K. Yamada [b], A. Chiba [b], Y. Hirano [b], K. Narumi [b] and Y. Saitoh [b]

[a] National Institute of Advanced Industrial Science and Technology (AIST),
[b] Department of Advanced Radiation Technology, TARRI, QST

When primary ions are injected into a solid target, secondary ions (SIs) are emitted from the target surface with various emission properties. The distribution of the number of SIs emitted for one primary ion is one of the important emission properties that include information on how the SIs are emitted from the target. Detailed measurement and analysis of the distribution are difficult for a monoatomic ion impact because the mean SI number per impact is too small to accurately obtain the distribution. In contrast, cluster ion impacts give higher mean numbers of emitted SIs in comparison with the impact of the corresponding monoatomic ion with the same velocity [1]. The higher mean number of emitted SIs allows us to measure their number distributions [2]. In this paper, we report impact energy dependence of total yields of negative secondary ions (N-SIs) emitted by sub MeV C_{60} ion impacts on a poly(methyl methacrylate) (PMMA) target, which were obtained from measurement and analysis of their experimental number distributions [3].

The experiments were performed using 0.12 MeV C_{60}^{+}, 0.27 MeV C_{60}^{2+}, and 0.54 MeV C_{60}^{2+} beams at QST/Takasaki. A direct C_{60} ion beam with a current of several tens of fA was pulsed by electrostatic deflection plates triggered by a pulse generator and a series of collimators to obtain single impact per pulse condition. The pulsed C_{60} ion beam was incident on a PMMA film target at an angle of 45º to the target surface. The number of N-SIs for each ion pulse p were counted by a time-of-flight (TOF) SI mass spectrometer, based on event-by-event N-SI counting measurements. It should be noted that only the event data for $p \geq 1$ are used because it is impossible for $p = 0$ to distinguish between events where no SI is emitted by the primary ion impact and where no primary ion exists for the start signal. The counted N-SI number p were analyzed using an analytical model that can derive the distributions of the number of emitted SIs n from experimental counting data obtained by a TOF SI mass spectrometer combined with pulsed primary ion beams [2,3].

The analytical model assumes that the emitted N-SI number n has a probability distribution with a mean number μ, $P_n(\mu)$. The calculated p distribution $P_{cal}(p)$ can be expressed by

$$P_{cal}(p) = \sum_{n=1}^{n_{max}} \frac{P_n(\mu)}{1 - P_0(\mu)} \frac{{}_nC_p(1-\gamma)^{n-p}\gamma^p}{1-(1-\gamma)^n}$$

where γ is the SI detection efficiency and $P_0(\mu)$ is the probability that an SI is not emitted even when the primary ion is incident on the target [2]. It should be noted that, because only the event data for $p \geq 1$ are used for analysis of the p number, ${}_nC_p(1-\gamma)^{n-p}\gamma^p$ and $P_n(\mu)$ should be respectively divided by $1-(1-\gamma)^n$ and $1-P_0(\mu)$, as shown in the equation. $P_n(\mu)$ was derived by fitting $P_{cal}(p)$ to experimental p distribution $P_{exp}(p) = N_p/N_{p\text{-}total}$, where N_p is the number of events for which the number of detected SIs for one start signal is p and $N_{p\text{-}total}$ is the total number of events for $p \geq 1$, under the assumption that $P_n(\mu)$ can be expressed by a linear combination of two Polya distributions. The fitting results show that $P_n(\mu)$ can be well approximated by a single Poisson distribution. Figure 1 shows comparison among the fitting parameter μ for a fixed γ value for 0.12 MeV C_{60}^{+}, 0.27 MeV C_{60}^{2+} and 0.54 MeV C_{60}^{2+} impacts. This gives information on the relative N-SI emission yield for one ion impact; the total N-SI emission yields for 0.27 MeV C_{60}^{2+} and 0.54 MeV C_{60}^{2+} impacts are enhanced by factors of ca. 1.5 and 2 in comparison with that for the 0.12 MeV C_{60}^{+} impact, respectively [3].
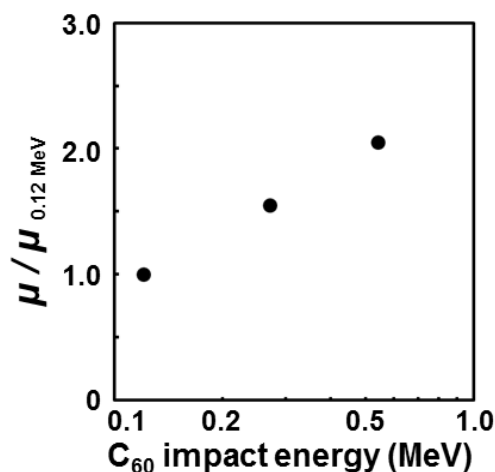
Fig. 1. Dependence of relative yields of negative secondary ions for a PMMA target on C_{60} ion impact energy.

References
[1] K. Hirata *et al.*, Appl. Phys. Lett., **81**, 3669 (2002).
[2] K. Hirata *et al.*, J. Chem. Phys., **145**, 234311 (2016).
[3] K. Hirata *et al.*, Nucl. Instr. and Meth. B, in press.

3 - 07   Shape Elongation of Embedded Metal Nanoparticles Induced by C_{60} Cluster Ion Irradiation

H. Amekura [a], K. Narumi [b], A. Chiba [b], Y. Hirano [b], K. Yamada [b],
S. Yamamoto [c] and Y. Saitoh [b]

[a] National Institute for Materials Science (NIMS),
[b] Department of Advanced Radiation Technology, TARRI, QST,
[c] Department of Advanced Functional Materials Research, TARRI, QST

Shape elongation of embedded nanoparticles (NPs) induced under swift heavy ion (SHI) irradiation has been extensively studied for this decade [1]. While the mechanism is still under debate, the majority agree with an assumption that large electronic energy deposition induced by SHIs plays an important role.

Primarily SHI is defined by its high velocity, i.e., large kinetic energy per nucleon, which is higher than ~0.1 MeV/u. An arising question is whether the shape elongation of NPs is induced under irradiation with slow ions but high electronic stopping power S_e. We have irradiated Zn NPs with 6 MeV C_{60}^+ ions, which have a slow velocity of 0.008 MeV/u. The S_e value of the C_{60} ions was estimated as the sum of independent 60 pieces of 6 MeV/60 = 0.1 MeV carbon monomer ions. The estimated value was 15.5 keV/nm in silica, which was comparable to S_e of 200 MeV Xe SHIs.

However, contrary to SHIs, the cluster ions interact with NPs in shallow depth only. A C_{60} ion injected into a solid can be no longer stable as in a vacuum, which is suffered by atomic collisions with constituent atoms in the solid. The interatomic distances increase with the depth and finally the C_{60} ion is no longer a cluster ion but 60 pieces of C monomer ions. While the ion range of 100 keV C-monomer ion is 315 nm in silica, the cluster effect can be active only in the ion range much shallower than 315 nm. We formed Zn NPs in the surface layer of silica (SiO_2) shallower than 70 nm [2] using 60 keV Zn^+ ion implantation to a fluence of 1×10^{17} ions/cm^2.

The C_{60}^+ ion irradiations were carried out at TIARA, QST, using a newly developed high-flux C_{60} negative ion source. While the samples were irradiated with four different energies, i.e., 1, 2, 4, and 6 MeV of C_{60}^+ beams, the beam current was maintained lower than ~50 (100) pA for 6 (1, 2, and 4) MeV through an aperture of 3 mm in diameter. To detect the shape elongation of NPs by the optical linear dichroism (OLD) spectroscopy [3], the samples were irradiated with an incident angle of 45°.

Figure 1 shows the fluence dependences of shape elongation of Zn NPs detected by OLD method [3] at four different ion energies. Anisotropic signal, probably due to the NP elongation, was observed at all the energies. For comparison, the dependence evaluated under 200 MeV Xe^{14+}, i.e., SHI, irradiation is also plotted. In the low fluence region between 10^{11} and 10^{12} ions/cm^2, the elongation induced by 4 MeV C_{60} ions is slightly higher than that of 200 MeV Xe ions at the same fluence. In both the cases,

the elongation increases linearly with the fluence at the low fluences. However, the deviation from the linearity was observed for 4 MeV C_{60} ions at the fluences higher than 10^{12} ions/cm^2, while 200 MeV Xe ions maintain the linearity up to 10^{13} ions/cm^2. With exceeding 10^{13} ions/cm^2, the elongation induced with 4 MeV C_{60} ions turns to decrease. Both the deviation from the linearity above 10^{12} ions/cm^2 and the decrease exceeding 10^{13} ions/cm^2 are ascribed to destruction of the elongated NPs induced by the enhanced sputtering of cluster ions. Similar behaviors were observed at different energies of C_{60} ion irradiation.
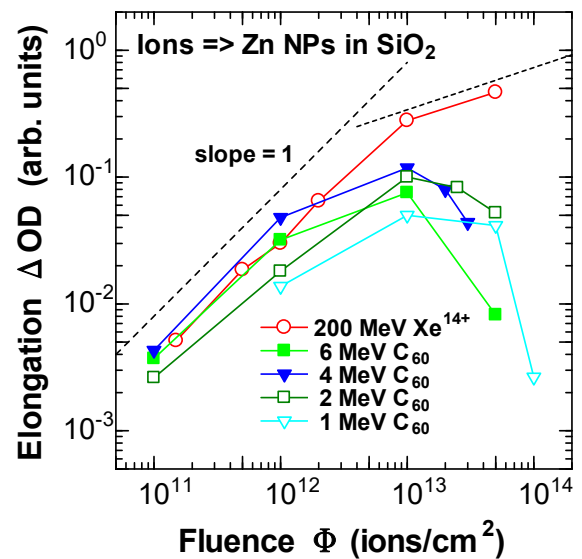
Fig. 1. Fluence dependence of shape elongation of Zn nanoparticles in SiO_2, irradiated with C_{60}^+ cluster ions of 1, 2, 4, and 6 MeV. For reference, the dependence of 200 MeV Xe^{14+} ions is also plotted [4]. The elongation degree was determined by optical linear dichroism spectroscopy.

References

[1] G. Rizza and M.C. Ridgway, in *"Ion Beam Modification of Solids"*, ed. W. Wesch and E. Wendler (Springer, New York, 2016) Chap. 11.

[2] H. Amekura and N. Kishimoto, in *"Lecture Notes in Nanoscale Science and Technology"* Vol. 5, ed. Z. Wang (Springer, New York, 2009), p. 1~75.

[3] H. Amekura *et al.*, Phys. Rev. **B 83**, 205401 (2011).

[4] H. Amekura *et al.*, Nanotechnology **25**, 435301 (2014).

3 - 08   Surface Structures on Ge and Si Irradiated with C_{60} Cluster Ion Beams

N. Nitta [a)], Y. Murao [a)], H. Tsuchida [b)], S. Tomita [c)], K. Sasa [d)], K. Hirata [e)], H. Shibata [f)],
Y. Hirano [g)], K. Yamada [g)], A. Chiba [g)], Y. Saitoh [g)], K. Narumi [g)] and Y. Hoshino [h)]

[a)] School of Environmental Science and Engineering, Kochi University of Technology,
[b)] Quantum Science and Engineering Center, Kyoto University,
[c)] Institute of Applied Physics, University of Tsukuba,
[d)] Tandem Accelerator Complex, University of Tsukuba,
[e)] National Institute of Advanced Industrial Science and Technology (AIST),
[f)] The Institute of Scientific and Industrial Research, Osaka University,
[g)] Department of Advanced Radiation Technology, TARRI, QST,
[h)] Department of Mathematics and Physics, Kanagawa University

Ion beam irradiation of semiconductor materials induces many point defects by the cascade damege. Porous structure formation has been reported due to diffusion and aggregation of point defects on Ge [1], GaSb [2], and InSb [2] surfaces. However, a porous structure has not been observed on a Si surface. Semiconductor with a porous structure has a potential for applications in electronic and photonic devices. Si is widely used in electronic devices, if it is possible to form a porous structure, the range of applications can be expanded. Cluster ion irradiation is effective for the growth of a porous structure because it enhances the point defect creation by the overlapping of cascade regions. In this study, Ge and Si surfaces were irradiated with C_{60} cluster beams with two different energies of 540-keV and 6-MeV. In addition, we confirmed the structure formed by oblique incidence irradiation with cluster ion beams.

The experiments were performed using two types of ion accelerators (an ion implanter and a tandem Pelletron accelerator) at TIARA, QST. A well-collimated C_{60} projectile with incident energy of 540-keV or 6-MeV was incident at 0°, 30°, and 60° to the surface normal of samples. The samples were mirror-polished Ge and Si single crystal wafers with (001) orientation. The fluence of the C_{60} beams was set to 1×10^{14}–1×10^{15} ions cm^{-2}. The irradiation temperature was room temperature. The evaluation of the as-irradiated surface was performed with scanning electron microscopy (SEM) and transmission electron microscopy (TEM) at Kochi University of Technology.

Figure 1 shows surface SEM images of Ge irradiated with 6-MeV C_{60}^+ beam. The fluence of the C_{60} beam was 1×10^{14} ions cm^{-2}. A porous structure was observed on Ge surfaces. The size of porous structure was no change with increasing the tilt angle.

Figure 2 shows surface SEM images of Si irradiated with 6-MeV C_{60}^+ beam. The fluence of the C_{60} beam was 1×10^{14} ions cm^{-2}. The porous structure was also observed on Si surfaces. The size of porous structure and feature changed with increasing the tilt angle. It was thought that the angle dependence was influenced by the atomic sputtering. However, the porous structure was formed on the surface at 0° irradiation. The effect of the sputtering at low angle irradiation is small. The elucidation of formation mechanism of this structure is a future task.

References

[1] I. H. Wilson, J. Appl, Phys. **53**, 1698-1705 (1982).
[2] D. Kleitman and H. J. Yearian, Phys. Rev. **108**, 901 (1957).
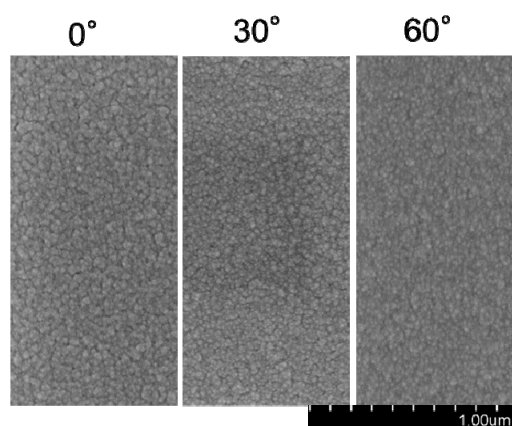
Fig. 1. Surface SEM images of Ge irradiated with 6-MeV C_{60}^+ beams. Observation angle was parallel to the surface normal of the samples.

Fig. 2. Surface SEM images of Si irradiated with 6-MeV C_{60}^+ beams. Observation angle was parallel to the surface normal of the samples.

3 - 09   Structural Analysis of Eu-HONTA Complex Formed in Adsorbent
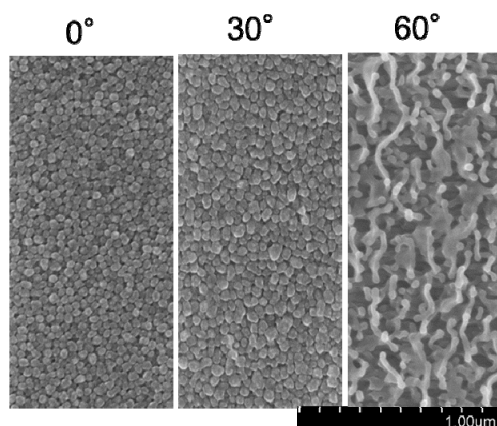
S. Watanabe [a), M. Okada [b), H. Matsuura [b), W. Kada [c), M. Koka [d), R. Yamagata [d),
N. Yamada [d), Y. Yuri [d), T. Satoh [d) and Y. Ishii [d)

a) Nuclear Fuel Cycle Engineering Laboratories, JAEA,
b) Atomic Energy Research Laboratory, Tokyo City University,
c) Faculty of Engineering, Gunma University,
d) Department of Advanced Radiation Technology, TARRI, QST

Partitioning and transmutation of trivalent minor actinides (MA(III)) are an important and challenging task for reduction in volume and radiotoxicity of nuclear waste. The extraction chromatography technology is effective for efficient MA(III) recovery from nitric acid medium [1]. Hexaoctyl-nitrilotriacetamide (HONTA) is one of the most promising extractants for the separation of MA(III) from trivalent lanthanides (Ln(III)) which have chemically similar properties with MA(III) [2], and the systematic investigation on its applicability for the extraction chromatography is currently underway.

The extraction behavior of Ln(III) onto HONTA in solvent and adsorbent showed different dependence on acidity of the nitric acid. The difference in the extraction mechanism between these two systems is one of our interests to establish efficient MA(III) recovery process. In this study, the structural information of Eu-HONTA complexes formed in the adsorbent and in the solvent system was investigated by Particle Induced X-ray Emission (PIXE) combined with Ion Beam Induced Luminescence (IBIL). For further chemical composition analysis, Extended X-ray Absorption Fine Structure (EXAFS) analysis was also carried out.

Eu-L_{III} edge (keV) EXAFS measurements were carried out at the BL5S1 beamline of Aichi Synchrotron Radiation Facility, Japan. The adsorbent was put in a SUS flat washer with 1 mm thickness and 10 mm inner diameter, and then sealed by two Kapton films.

The IBIL measurements were performed using Ion Luminescence Microscopic Imaging and Spectroscopy (ILUMIS) system equipped in the light-ion microbeam line connected to a 3-MV single-ended accelerator in TIARA. A few particles of the adsorbent or 10 μL of the solvent were put on a Kapton film attached to a sample holder, and sealed by a Kapton film. The samples were irradiated by 3 MeV proton beam with a beam current of about 100 pA.
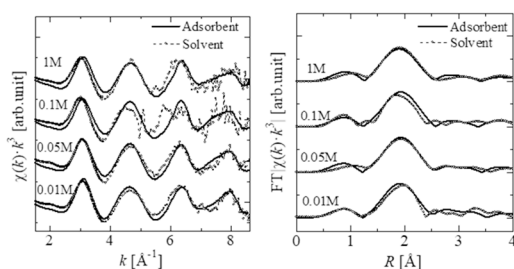
The IBIL Spectra were observed by an UV-vis spectrometer (Solid Lambda CCD, Spectra CO., Ltd.).

The EAXFS oscillations and radial structure functions obtained for Eu loaded HONTA/SiO_2-P and HONTA/nDD are shown in Fig. 1. A slight difference in the phase of the oscillations could be confirmed between the two systems. A predominant peak observed at R = 1.9 Å in the radial structure function could be assigned to be Eu-O correlation. A little difference in Eu-O distance between the two systems was confirmed and the distance scarcely depended on the acidity. Local structural parameters obtained by fitting analysis showed that local structure in the adsorbent and the solvent system are similar to each other and that the same structural model can be proposed for both systems.

The IBIL spectra obtained for the adsorbent and the solvent systems are shown in Fig. 2. Characteristic peaks could be attributed to the transition of 4f electrons in Eu^{3+} ion. A distinct difference in the two systems was the shape of spectrum at λ = 680 - 710 nm which corresponds to $^0D_6 \rightarrow ^7F_4$ transition. The profile seems to have two peaks at 686 and 697 nm for the adsorbent system, while the peak at λ = 697 nm was not clearly found for the solvent. This feature was confirmed at any acidity conditions and considered to suggest a difference in the structure of the complex. The one-dimensional structural parameters obtained by the EXAFS analysis did not show a distinct difference in the structure of the two systems. Therefore, the difference in the IBIL might suggest a different symmetricity in the arrangement of ligands around Eu. Simulation on IBIL profile with varying symmetricity of ligands would be effective for further discussion.

References

[1] S. Watanabe *et al.*, J. Radioanal. Nucl. Chem., **316**, 1113 (2018).
[2] Y. Sasaki *et al.*, Chem. Lett., **42**, 91 (2013).

Fig. 1. EXAFS oscillations and radial structure functions obtained by Eu-L_{III} edge EAXFS.
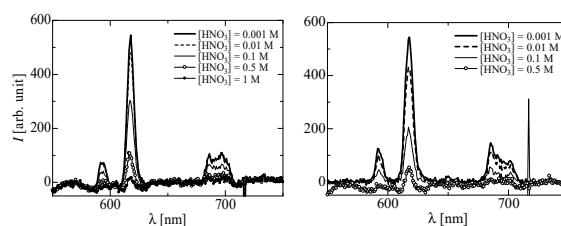
Fig. 2. IBIL spectra of the adsorbent (left) and the solvent (right).

3 - 10　　Dating of the Yamada Fault Distributed on Tango Peninsula Using Radiation Defect Radical Centers Part 2

T. Fukuchi

Graduate Faculty of Interdisciplinary Research, University of Yamanashi

It is an urgent issue to evaluate the activity of unrecognized active faults in the region with unclear tectonic landform or without Quaternary overlying sediments because at any time such faults may cause earthquake disaster such as the 2018 Hokkaido Eastern Iburi earthquake (M6.7). To cope with this problem, at this stage we have no choice but to estimate the age of the latest fault movement from the formation age of fault gouge or from the age of the resetting attained by seismic frictional heating using absolute dating techniques such as the ESR (electron spin resonance) dating technique.

In ESR dating of fault movement, we assume that ESR signals in fault gouge have been once reset by frictional heating [1]. Then, the ESR age (T) is calculated by dividing the total radiation dose (TD) to which the fault rocks have been subjected since the resetting of the ESR signals by the annual radiation dose (D); T=TD/D. The TD is obtained by extrapolating the growth curve calculated from the ESR intensities before and after artificial γ-irradiation. However, if the ESR signals are incompletely reset, the TDs obtained are overestimated, and then the ESR ages obtained are older than the actual age (T_a) of the latest fault movement. Thus, the ESR ages (T_{esr}) theoretically give the upper limit of the actual age ($T_a \leq T_{esr}$).

Here, I apply the ESR dating technique to the fault gouge collected from the Yamada fault located at the Mushiu district in Toyooka city on Tango Peninsula. Although the Yamada fault may have moved in the 1927 Kita Tango earthquake, its actual activity is still unclear. The artificial γ-irradiation for determining the TDs was carried out with a ^{60}Co source at 2 cell irradiation facility in the food irradiation building, Takasaki Advanced Radiation Research Institute, QST. The irradiation dose rate is 390.2 Gy/h.

As a result of ESR measurements, the surface E' center, Al and Ti centers in quartz [1] were detected from the Yamada fault gouge just on the fault plane, which was formed by the latest fault movement. Moreover, the γ-irradiation shows that they regularly increase with increasing radiation dose, implying that these radical centers probably give more precise TD values (Fig.1).

The youngest ESR age of 0.26 ± 0.06 Ma is obtained from the fault gouge using the Al center, an impurity defect center derived from a hole trapped at an Al atom site in quartz. This means that the age (T_a) of the latest fault movement along the Yamada fault in the Mushiu district is estimated as Ta ≤ 0.26 ± 0.06 Ma on the basis of the principle of ESR dating of fault movement, and thus this supports that the Yamada fault is indeed an active fault that has moved since the Middle Pleistocene. I conclude that
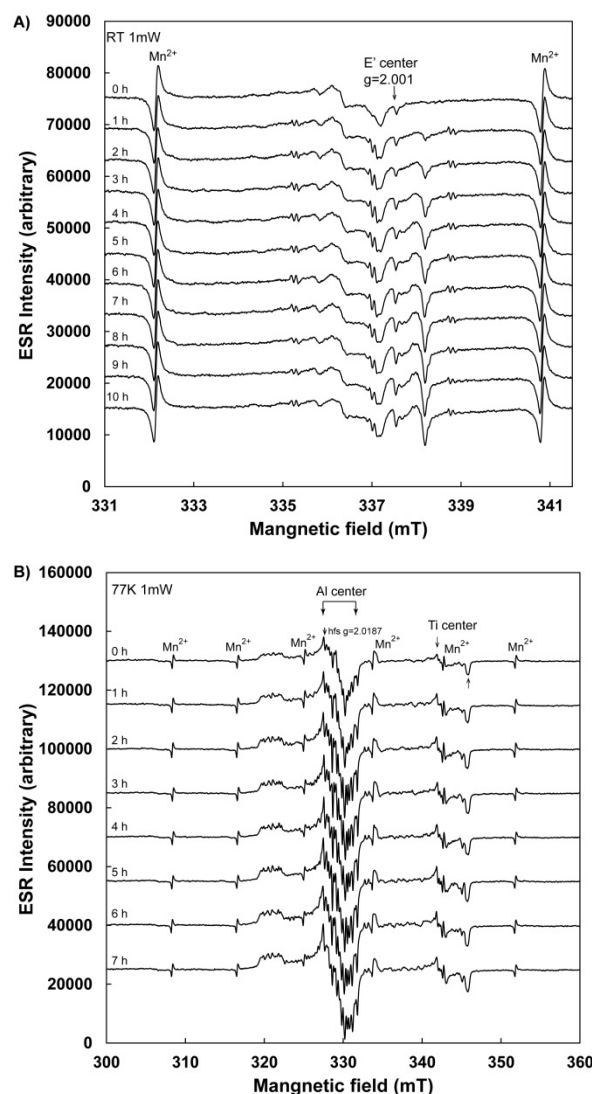
Fig. 1. A) γ-irradiation effect on the surface E' center in quartz in the Yamada fault gouge just on the fault plane. B) γ-irradiation effect on the Al and Ti centers in quartz in the Yamada fault gouge just on the fault plane. The irradiation dose rate is 390.2 Gy/h and the irradiation time is 0-10 hours.

the ESR dating technique is available for the assessment of fault activity of unrecognized active faults that have moved since the Middle Pleistocene.

Reference

[1] T. Fukuchi, ESR dating of fault movement- Its principle and practice. Fukadaken Library 63, 45pp (2004).

3 - 11   Electron Excitation Processes in Collisions of Swift MeV/atom Carbon Cluster Ions with Gases and Solids

T. Kaneko [a)], Y. Saitoh [b)], A. Chiba [b)] and K. Narumi [b)]

[a)] Department of Applied Physics, Okayama University of Science,
[b)] Department of Advanced Radiation Technology, TARRI, QST

In case of MeV/atom swift cluster ion beams penetrating solid, the so-called cluster effect has been reported in several fields, e.g., reduction of average charge after dissociation [1, 2], non-linear dependence of energy deposition [1, 3, 4], strong suppression of secondary electron yield [5-7] and strong enhancement of convoy electron yield [6] per projectile atom, compared with those under single ion incidence at equivalent speed. Recently, application of swift clusters like carbon 60 to energy deposition processes has been in progress [8]. These phenomena are related to space-time correlation in electron excitation due to multiple ion penetration. This academic year we performed the research on the positive cluster ion yield as a function of charge-changing gas pressure where the cluster effect in scattering cross sections will appear, and on the non-linearity of convoy electron yield under swift cluster impact.

First, we describe elementary processes regarding charge changing and destruction. The basic equation is the rate equation, which describes the charge state fraction $\varphi_i(x)$ of a cluster in charge state i at penetrating depth x in the charge-changing region:

$$\frac{d\phi_i(x)}{Ndx} = \sum_{j(\neq i)} \sigma_{ji}\phi_j(x) - (\sum_{j(\neq i)} \sigma_{ij} + \sigma_{id})\phi_i(x)$$

Here σ_{ij} is the cross section for changing charge from i to j of a cluster, σ_{id} denotes the destruction cross section for a cluster in charge state i in collision with a target gas, and N is the number density of a target gas. As a first step, we considered charge state $i = -1,0,1$. Solving the above equation under the initial condition, we had the analytical expressions of $\varphi_j(x)$ $(j = -1\sim1)$. Here we took into account charge state difference in destruct cross sections.

We estimated the cross sections of σ_{ij} and σ_{id} in a quantum-mechanical treatment. According to the time-dependent perturbation theory, the destruction and charge-changing processes are regarded as electron stripping from a cluster in collision with a neutral (target gas) atom. In the collision of a C_n (n = 1~4) in a linear chain structure with a rare-gas atom, the transition amplitude of an electron from the initial (i) state to a final (j) state is formulated in the framework of impact parameter method, where the target atom is assumed to move on a straight-line trajectory at constant speed. In case of a carbon cluster atom, the initial states of electrons are described by Hartree-Fock (HF) wave-functions. Here we use only the radial distribution function because the angular distribution is assumed to be averaged. The final ionized state is expressed by a distorted plane wave. On the basis of the single electron ionization probabilities as a function of impact parameter in two-body collision, together with the independent-electron model, we estimate the one- and multi-electron stripping cross sections for charge changing process. Destruction cross sections are estimated as those which yield more than doubly positive charge states of a cluster. From the present calculation, it was shown that the destruction cross section for MeV/atom carbon ions in collision with rare gas (He, Ne) showed the sub-linear dependence on atom number. In addition, we calculated the production yield of 2.5 MeV/atom C_3^+ in linear-chain and ring structures. Compared with He and Ne gases, the structure dependence of the C_3^+ fraction on gas pressure will appear more clearly for He gas. On the other hand, a significant difference was not found for Ne gas.

As for larger cluster ions like carbon 60, the doubly positive ions were created in TIARA. Then, we extended the rate equation in the previous treatment by including charge state +2, and obtained analytical expressions for each charge fraction. This formula will be used in future.

Another result is on the convoy electron yield from a carbon foil under MeV/atom cluster impact, which was greatly enhanced contrary to strong suppression of the low-energy (up to about 50 eV) secondary electron yield. By using the time-dependent perturbation in the second order, we obtained an enhanced feature.

References
[1] T. Kaneko, Phys. Rev. A**66**, 052901 (2002).
[2] A. Chiba *et al.*, Phys. Rev. A**76**, 063201 (2007).
[3] S. Tomita *et al.*, Phys.Rev. A **82**, 044901 (2010).
[4] T. Kaneko, Phys. Rev. A **86**, 012901 (2012).
[5] H. Kudo *et al.*, Jpn. J. Appl. Phys. **45**, L565 (2006).
[6] S. Tomita *et al.*, Phys. Rev. A **73**, 060910(R)(2006).
[7] T. Kaneko *et al.*, J.Phys.Soc.Jpn.**75**,034717 (2006).
[8] T. Kaneko, Bull. Okayama Univ. Sci., **53**A, 1 (2017).
[9] Y. Saitoh *et al.*, private communication.

3 - 12   Development of a Penning Ionization Gauge Type Ion Source with a Permeant Magnet for a MeV Compact Ion Microbeam System

Y. Ishii [a)], T. Ohkubo [a)] and Y. Miyake [b)]

[a)] Department of Advanced Radiation Technology, TARRI, QST,
[b)] Beam Seiko Inc. Ltd.

A compact ion microbeam system with a size of less than $2 \times 2 \times 2$ m^3 that produces an ion beam of 1 μm in diameter at energy 1 MeV ("MeV compact μ-beam system") is under development. The μ-beam system is expected to be widely used in universities and industry laboratories by the installation in a general experimental room of size of $6 \times 8 \times 3$ m^3. As a first step of the development, a 120 keV compact ion μ-beam system was made as a prototype of the MeV compact μ-beam system. The 120 keV compact ion μ-beam system consists of the three-stage compact electrostatic focusing lens (three-stage acceleration lens) and the duoplasmtron-type ion source. The three-stage acceleration lens that has high demagnification and the scalability up to 1 MeV is used to investigate the effectiveness of the formation of ion microbeam. The duoplasmatron-type ion source is used in the 120 keV compact μ-beam system to generate ion beams that the three-stage acceleration lens requires, namely a low energy ion beam with high brightness and small energy spread. A 1.8-μm-diameter hydrogen beam has, so far, been formed by 120 keV μ-beam system [2]. The energy upgrading from 120 keV to 1 MeV is now attempted by applying the voltage of 1 MV to the lens. In the upgrading, a small-size ion source with small electric power consumption is newly developed to be installed in the MeV compact ion μ-beam system. The reason is because the duoplasmatron-type ion source spends large electric power over 500 W and the supply of large electric power is difficult due to being placed in a high voltage area. In addition, a low-energy ion beam with high brightness is of importance for the ion source to obtain large beam current and a small diameter at a focusing spot. The penning ionization gauge type ion source with two electromagnets (EM-PIG) was developed [3] and was successful from a viewpoint of high brightness. However, the electric power consumption for the electromagnets was large for the upgrading.

To reduce the electric power consumption, a penning ionization gauge type ion source with a permanent magnet (PM-PIG ion source) was designed and assembled as follows. As obtained in the development of EM-PIG, the plasma confined by strong magnetic field in a small volume is effective for the high brightness. This knowledge was applied in the design of the PM-PIG ion source. Therefore, several kinds of magnetic field strength of various magnetic circuits were calculated by a simulation code, SUPERFISH [4], to obtain a strong magnetic field in a small volume. Two-dimensional half structures were

calculated for rotationally symmetric structures. Consequently, a simple magnetic circuit with one permanent magnet was found in this design.
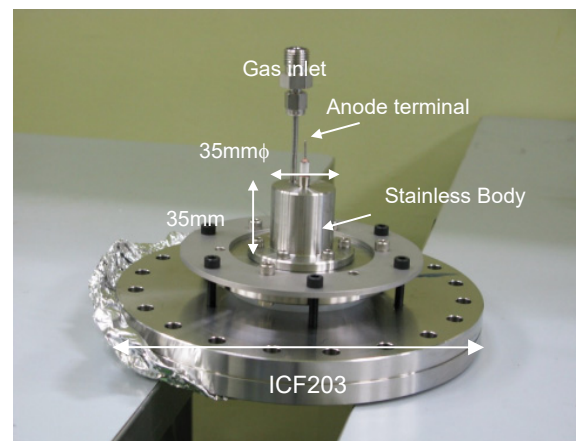
Fig. 1. Photograph of the PM-PIG ion source. The PM-PIG ion source connected to a vacuum flange of ICF203.

The PM-PIG ion source was made on the basis of the above magnetic circuit. One samarium-cobalt permanent magnet with high thermal tolerance was used for the ion source to be heated by plasma. The ion source of 35 mm in diameter and 35 mm high is shown in Fig. 1. The ion source body was made from stainless steel. The size was sufficiently small for the installation of the MeV compact μ-beam system. It was connected with a vacuum flange of ICF203. Gas is supplied from the gas inlet and anode voltage is applied to the anode terminal to generate plasma.

The measurements of beam current and brightness of the ion source will be performed in the next fiscal year.

References
[1] Y. Ishii *et al.*, Nucl. Instrum. Meth. Phys. Res. B, **332** 156-159 (2014).
[2] T. Ohkubo *et al.,* Physics Procedia **90,** 79-84 (2017).
[3] Y. Ishii *et al.*, AIP Conference Proceedings 2011, 080015 (2018).
[4] Billen, J.H.Young, L.M. Proceedings of International Conference on Particle Accelerators, 213-222 (1976).

3 - 13　　Technical Developments of the TIARA AVF Cyclotron of Fiscal 2018

N. Miyawaki, H. Kashiwagi and S. Kurashima

Department of Advanced Radiation Technology, TARRI, QST

Evaluation of the influence of space charge effect on phase bunching

Phase bunching in the central region of a cyclotron, which reduces the beam phase width, has been studied to improve beam intensity and quality. The phase bunching in the TIARA AVF cyclotron has been confirmed by low-intensity heavy ion beams with negligible space charge effect. The space charge effect spreads the beam by the Coulomb repulsive force of the beam itself. In high-intensity light ion beams, the phase bunching is weakened by the space charge effect. In this study, we have investigated the effectiveness of the phase bunching for the beam intensity and beam phase width of a high-intensity light ion beam.

In the TIARA AVF cyclotron, phase bunching is generated under the condition of accelerating harmonic mode 2 (h=2) and is not generated for the condition of h=1. To confirm the presence or absence of phase bunching under the space charge effect, beam conditions of 20 MeV H$^+$ (h=2) and 30 MeV H$^+$ (h=1) with equal parameters from ion source to cyclotron were used. The phase bunching was evaluated by beam phase widths obtained from the rate of decrease in beam intensity with changes in acceleration frequency. As a result, the beam current of 20 MeV H$^+$ was larger than 30 MeV H$^+$, and the beam phase width of 20 MeV H$^+$ was narrower. Measurements of the presence or absence of phase bunching under little space charge effect were also carried out by 260 MeV ^{20}Ne^{7+} (h=2) and 107 MeV ^{4}He^{2+} (h=1). The beam phase width of 260 MeV ^{20}Ne^{7+} was more than one third of that of 107 MeV ^{4}He^{2+}. From the results of 20 MeV H$^+$ and 260 MeV ^{20}Ne^{7+}, the space charge effect caused by the high intensity light ion beam reduced the reduction effect of the beam phase width by the phase bunching. Therefore, although the effect of phase bunching is weakened by the space charge effect in the high intensity light ion beam, the effectiveness of phase bunching for increasing the beam intensity and narrowing the beam phase width was confirmed.

Table 1

Measured beam phase width and beam current.

Condition	H$^+$ 20MeV	H$^+$ 30MeV	^{20}Ne^{7+} 260MeV	^{4}He^{2+} 107MeV
h	2	1	2	1
Phase width (RF deg)	14.78	20.68	5.89	22.69
Current (μA)	18.4	13.72	2.64	7.86

Four-dimensional emittance measurement by slit harp device

The TIARA AVF cyclotron offers a variety of light-heavy ion beams from 10-MeV H$^+$ to 490-MeV ^{192}Os^{30+}. At the beam switching, it is necessary to tune the beam injection parameters from the ion source to the cyclotron to accelerate with minimizing the beam loss. In order to perform the tuning efficiently, we are developing a method for determining the parameters by beam optics calculation using measured beam emittance. Since the beam focusing process by a solenoid magnet used in the low energy beam transport line involves the rotational movement of the beam, four-dimensional emittance data is required to calculate the optics.

We have developed a method to obtain four-dimensional emittance data by combining the horizontal and vertical slit-harp devices, which is generally used for two-dimensional emittance evaluation. In the method, an arbitrary position range is cut out from a beam using a horizontal (x) slit and a vertical (y) slit, and two kinds of three-dimensional emittance measurement are carried out to obtain the (x, y, x') distribution and (x, y, y') distribution of a beam by measuring the angular distribution in the x direction and the y direction respectively using multiwire (harp) beam detectors. Then, the beam divergence angle (x', y') at each position (x, y) is obtained from these data.

As a result of measurement tests using a 50.2-keV ^{16}O^{6+} beam, four-dimensional data (x, y, x', y') are built from the measured three-dimensional emittance data, and the distributions of the beams on the x-x', x-y', y-x', y-y', x'-y', and x-y planes are produced from the data (Fig. 1). Thus, it was confirmed that the method can construct four-dimensional emittance data from the two three-dimensional measurement data.
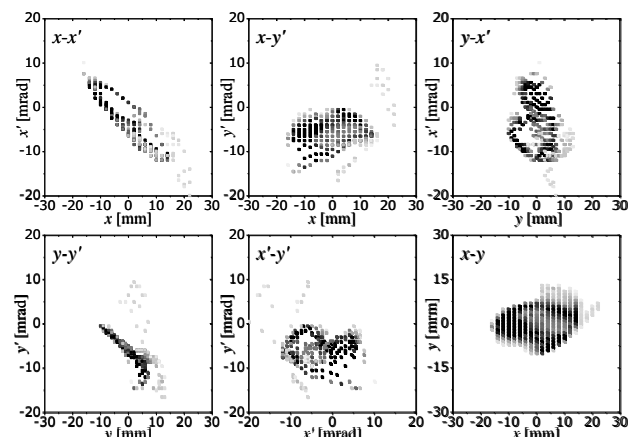
Fig. 1. Beam distribution in x-x', x-y', y-x', y-y', x'-y' and x-y planes from four-dimensional data.

3 - 14   Status Report on Technical Developments of Electrostatic Accelerators

Y. Hirano, A. Chiba, K. Yamada, A. Yokoyama, Y. Ishii, T. Nara and S. Kurashima

Department of Advanced Radiation Technology, TARRI, QST

Development of the MeV C_{60} ion micro beam

The characteristic irradiation effects of swift cluster ions such as C_{60} are expected to be applied in various fields. In order to establish high-sensitivity and high-resolution surface analysis using C_{60} ion beam, we made start of the development of the C_{60} ion micro beam formation system equipped with an electrostatic quadrupole lens. The micro beam of several μm-diameter is formed by focusing a highly directional beam in which the divergence of the beam is eliminated as much as possible by passing through the slits of several tens μm in gap distance. Therefore, when the C_{60} ion micro beam of several pA is formed, it is necessary to produce the beam with intensity of at least 1 μA or more in the ion source. In the tandem accelerator at TIARA, the novel ionization technique has been developed to enhance the C_{60} ion beam [1]. This C_{60} negative ionization technique has succeeded in increasing the beam intensity to 100,000 times compared to the conventional technique and obtaining the beam intensity (1.3 μA) necessary for the micro beam formation.

Measurement of the trace-elements distribution shifts in micro-PIXE analysis

About 2 μm shift of the trace-element images in a sample was observed within a few hours in the acquisition experiments of the trace-element distribution by the micro-PIXE analysis. In the experiments, the proton beam accelerated by the Single-end accelerator was focused to a 1 μm-diameter spot on a target and scanned on a sample. The shift causes distortion of the trace-element image. Our purpose in this study is to investigate the cause of the shift and to obtain accurate the trace-element distribution images in the micro-PIXE analysis. One of the causes of the image shifts was considered to be thermal deformation of a Kapton film that has two functions of a sample folder and a seal of vacuum in the chamber used in the micro-PIXE analysis. In 2018 fiscal year, the Kapton films with the different thicknesses of 7.5 μm and 50 μm were used to investigate the dependence of the film thickness for the shifts. A 1000 lines/inch Cu mesh image of 50 μm × 50 μm area was obtained from accumulating, on PC, the data both of the micro beam positions and the relative yields of secondary electrons emitted from the Cu mesh on the basis of scanning the micro beam. In the 7.5 μm-thick Kapton film, a barycentric coordinate of the selected region (ROI) in the Cu-mesh image shifted within 0.1 μm in horizontal and 6.9 μm in vertical. On the other hand, in the 50-μm-thick film, a barycentric coordinate of the ROI shifted within 0.3 μm in horizontal and 3.4 μm in vertical. The shift of the barycentric coordinate of the ROI was decreased according

to the usage of the thick film. The investigation of the relationship between the film thickness and the image shift will be continued in the next fiscal year.

Production of adenine ions by the Freeman ion source

The 400 kV Ion Implanter at TIARA provides ion beams of various species from hydrogen to bismuth for material science experiments. 48 ion species have been already generated using the Freeman type ion source, and we continuingly develop to generate more kinds of ion species using the ion source responding on the requirement of users. In 2018 fiscal year, adenine ($C_5N_5H_5$) ions were generated for quantum sensor development. For a generation of plasma in the ion source, the source material has to vaporize by oven if the material is solid in room temperature. The adenine has a low sublimation point of 220 °C. However, the oven temperature could not be controlled below 300 °C in usual, because a filament in an arc chamber was electrically heated for production of thermal electrons, and the heat was conducted to the oven which is connected to the arc chamber. Therefore, the filament current was attentively controlled so that the oven temperature was below 190 °C. We confirmed the adenine plasma could be generated by adjustment of the ion source parameters such as source magnetic field even though the low filament current. Figure 1 shows the mass-to-charge ratio of the extracted ion beam from adenine plasma. The characteristic fragment ions were observed in addition to the adenine ion. In the result, the adenine ion beam current was obtained few tens nA.
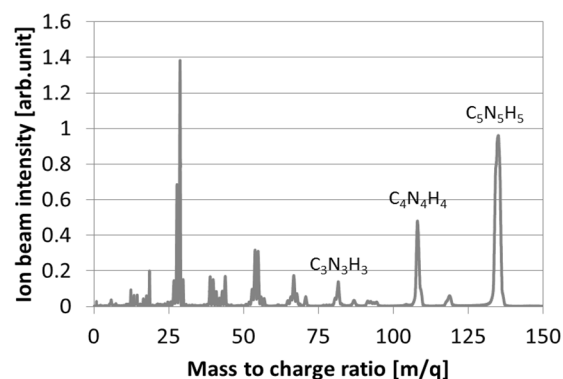
Fig. 1.   Mass-to-charge ratio of the adenine ion beam.

Reference

[1] Y. Hirano *et al.*, QST Takasaki Annu. Rep. 2016, **QST-M-8**, 134 (2018).

3 - 15　Lithium Distribution Analysis of All-solid-state Lithium Batteries Using Micro-PIXE and Micro-PIGE Techniques

K. Mima [a)], K. Suzuki [b)], T. Satoh [c)], Y. Yamada [c)], M. Finsterbusch [d)], K. Fujita [a)], T. Kamiya [e)], A. Yamazaki [f)] and Y. Kato [a)]

[a)] The Graduate School for the Creation of New Photonics,
[b)] Department of Chemical Science and Engineering, Tokyo Institute of Technology,
[c)] Department of Advanced Radiation Technology, TARRI, QST,
[d)] Institute of Energy and Climate Research, Forschungszentrum Jülich GmbH,
[e)] Graduate School of Science and Technology, Gunma University,
[f)] Faculty of Pure and Applied Sciences, University of Tsukuba

Introduction

For investigating the performance of the all-solid-state lithium battery made of a sulfide ($Li_{10}GeP_2S_{12}$, LGPS)-based solid electrolyte and a oxide ($Li_7La_3Zr_2O_{12}$, LLZ)-based solid electrolyte, the cross section of a pellet type battery was analyzed by micro-PIXE and micro-PIGE. Namely, we carried out the elemental mapping of the cross section of the battery by scanning the micro-proton beam of the 3 MeV electrostatic accelerator to obtain spatial Li distributions by the gamma ray from the $^7Li(p,p'\gamma)^7Li$. By the measurements, we observed the temporal evolution of the Li distribution for the sulfide based Li-battery and checked the feasibility of micro-PIXE and micro-PIGE analysis for the *in-situ* diagnostics of the battery made of LLZ:Ta. Further *in-situ* analysis of the cathode/anode composite electrodes of two types of the all solid state Li battery will be continued for designing a composite for high-performance all-solid-state lithium batteries.

Experiment

By the ion beam analysis with the 3 MeV micro-proton beam at TIARA, we have explored the methodology of diagnosing the Li motion in the working all solid state Li-ion battery. In 2018, we investigated two kinds of samples which are the three-layered pellet-type battery made of a cathode ($LiNbO_3$-coated $LiCoO_2$ + LGPS, a solid electrolyte (LGPS) and an anode (TiS_2+LGPS) and the two layered battery made of a cathode (LLZ:Ta) + a solid electrolyte (LLZ) and a lithium metal anode, which were fabricated by the TIT group and the Julich group.

Results

Figure 1 shows the Li distribution near the cathode and electrolyte layer of the LLZ based Li-ion battery. The difference of the Li distribution between non-charge and charge states is clearly observed. The Li density near the cathode-electrolyte interface surface is higher than in the bulk of the cathode. This may due to the non-uniformity of the electro-chemical reaction.

Figure 2 shows the elemental distributions of a sulfide ($Li_{10}GeP_2S_{12}$)-based all solid state battery near the anode and electrolyte interface. By comparing the non-discharge case (top of Fig.2) and the charge case (bottom of Fig.2), it is found that Li content was increased after charging.

The in-situ experiments as the extension of the above experiments are undergoing. The summary of the previous results of the ion beam analysis of the Li-ion battery was published as the text book [3].
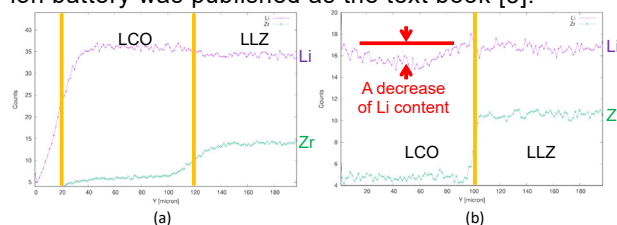
Fig. 1. Li (PIGE) and Zr (PIXE) distributions around the cathode ($LiCoO_2$) and electrolyte (LLZ) in (a) the non-charge state, (b) the charge state. The horizontal full scale is 200 μm.
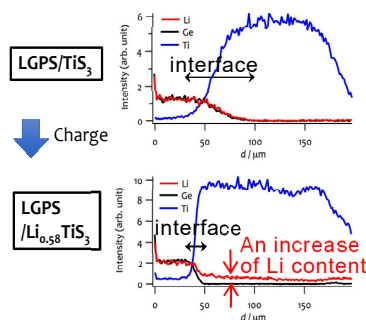
Fig. 2. Li, Ti and Ge elemental distribution at the cross section of the sulfide-base. (Top) for the non-charge Li battery, (Bottom) for the charged battery [1,2].

Acknowledgment

References

[1] K.Yoshino *et al.*, IJPIXE **27**, 11-20 (2017).
[2] M.Finshterbusch, K.Suzuki, T.Sato and K.Mima, 5th NEDO-BMBF Japan-Germany collaboration workshop
[3] T. Satoh, K. Mima, A..Yamazaki, and Y. Kato, "Lithium-ion batteries" edited by Y. Kato, Z. Ogumi, *et al.*, Pan Sanford Publishing, (2019) Chap.5 and Chap. 7.

3 - 16   Development of Micro Processing Technology by C_{60} Ion Beams

T. Kunibe [a)], H. Takeuchi [a)], H. Arai [a)], H. Hashimoto [a)], K. Yamada [b)], A. Chiba [b)],
Y. Hirano [b)], K. Narumi [b)] and Y. Saitoh [b)]

[a)] Metal technology Co., Ltd.,
[b)] Department of Advanced Radiation Technology, TARRI, QST

The surface of diamond synthesized by a plasma CVD (Chemical Vapor Deposition) method usually has unevenness of about several μm. The co-abrasive polishing method using a cast-product rotating disc embedded with diamond abrasives (Skiffe polishing method) is generally used to polish diamond samples such as cutting tools. However, the applications to heatsinks, optical windows, and semiconductor substrates require a relatively large smoothing area and are not easy due to abrasion of the polishing disk and scratching of the substrate sample. Therefore, it is not widespread except for cutting tools.

There is a research that has shown the manufacture example of the diamond knife and the micro Vickers indenter using an Ar ion beam or an O ion beam extracted from an ECR (Electron Cyclotron Resonance) ion source [2]. In that research, the beam irradiation angle dependency of surface roughness [1] and removal amount per unit time were investigated for polycrystalline diamond films or single crystal diamond substrates. These results have indicated that the polishing method using these ion beams is difficult to replace with the Skiffe polishing method because the abration rate is slow.

On the other hand, it has been shown that the Si sputtering rate by C_{60} ions accelerated to several tens of keV reaches 700 times that by atomic C ions [3]. Since the high-speed processing with C_{60} ion beams can be expected also for diamond from the result, we tried to measure the diamond sputtering rate by C_{60} ion.

In the irradiation test, a single crystal diamond substrate (3 mm × 3 mm × thickness 1 mm) and a single crystal silicon substrate (4 mm × 6 mm × thickness 0.5 mm) were irradiated with 60-keV (1 keV/atom) C_{60}^+ ions accelerated by a 400-kV ion implanter of Takasaki Ion Accelerators for Advanced Radiation Application (TIARA) at QST Takasaki.

The measurement of the etching depth of the irradiated sample was performed with the non-contact surface shaper (New View 600s, Zygo corporation) using interference of white light. With this apparatus, it is possible to measure the three-dimensional shape of the surface in an area of several mm^2, and even if the distribution of the beam is somewhat nonuniform, it is also possible to determine the sputtering rate from the etching volume.

One example of a bird's-eye view of an etched shape is shown in Fig.1. It can be seen that the sample surface is sputtered in the area of the mask opening φ2 mm by beam irradiation. The level difference between the irradiated part and the non-irradiated part was almost the same across the entire area, and was about 150 nm. The volume of the etched area was about 4.2×10^{-4} mm^3, and the sputtering rate was evaluated from this to obtain about 100 atoms/C_{60} ions (1.67 atoms/C). From the literature [2], it was found that the sputtering rate when irradiated with Ar ions of 1 keV is 0.38 atoms/Ar ion, and a large sputtering rate can be obtained by C_{60} ion irradiation.

References
[1] H. Hirata *et al.*, Precision Engineering Journal **58**, 2 (1992) 289 (in Japanese).
[2] I. Miyamoto *et al.*, Journal of the Japan Society of Grinding Engineers **46**,1 (2002-01)25 (in Japanese).
[3] K. Narumi *et al.*, "3.5 10-60 keV C_{60} ion bombardment effect on the Si surface", JAEA-Review **2009-066**, p55 (in Japanese).
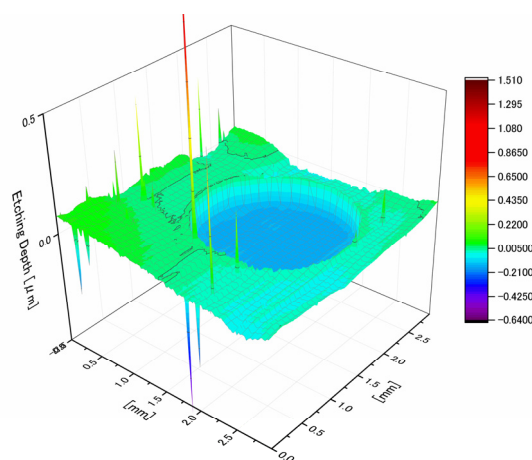
Fig. 1. Etching distribution measured with a white light interferometer after a diamond substrate was irradiated with C_{60} ions through a hole slit of φ2 mm as a mask.

3 - 17 Rapid-prototyping of Mach-Zehnder Waveguide Embedded Near-surface Region of PMMA Film by PBW

W. Kada [a), S. Yokosawa [a), K. Kasuya [a), Y. Wang [a), S. Miura [a), R. Takahashi [a),
R. Kurihara [a), R. Saruya [a), A. Kubota [a), K. Miura [a), T. Satoh [b), N. Yamada [b), Y. Ishii [b),
T. Kamiya [a) and O. Hanaizumi [a)

[a) Faculty of Science and Technology, Gunma University,
[b) Department of Advanced Radiation Technology, TARRI, QST

A Particle Beam Writing (PBW) process is an excellent rapid-prototyping tool for micrometer-scaled material modification. The formation of micrometer scaled embedded Mach-Zehnder (MZ) optical waveguide is successfully demonstrated with the flexible thin film of polydimethylsiloxane (PDMS) with a beneath of high intensity energy deposition around the Bragg peak of MeV protons [1, 2]. The proof of concept of optical switches based on these MZ waveguides were demonstrated by inducing the thermo-optical effect by thermal heaters attached on the film in post process of PBW. The fundamental function was evaluated but switching functions in thin organic film seemed to be improved if the waveguide core would be created much closer to the heater than the present waveguide. The thermal dependencies of refractive index is a factor of thermo-optical effect. Thus, the distance between heater and waveguide core would be a key factor. These changes in refractive index can be also induced by other physical parameters such as pressure, therefore such optical waveguide structures could be also considered to be utilized as passive sensors. Because the sensitivity is strongly affected by the distance between the heater and waveguide structure, the waveguide core should be formed as close as possible to the surface region. For these reasons, we have demonstrated the PBW process with tunable energy to form the waveguide core at the near-surface region of poly methyl methacrylate (PMMA) thin film. PMMA has strong chemical stability and better biological compatibility than PDMS and is able to be utilized for various applications.

Figure 1 illustrates the PBW procedure. The PBW process was performed with a microbeam line of 3 MV single-end accelerator at TARRI/QST. The thin film of PMMA with thickness from 30 -70 µm were employed for irradiation. Comparably high energy proton of up to 1.7 MeV was utilized and whole film was almost penetrated by proton and optical core was created at the very end of the target thin film. Figure 2 shows a schematic illustration and partially expanded optical microscope images of the MZ waveguide drawn in the film. MZ waveguide structure with dimension of 40 mm x 20 mm was formed by combining the two types of movement of beam scanning and sample stage.
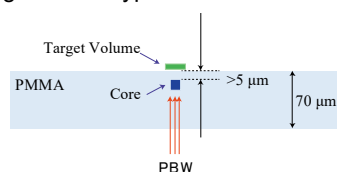
The fabricated MZ waveguide was successfully visualized in optical microscope observation as shown in Fig. 2. The width of waveguide core was evaluated as 7.5, 6.3, and 9.7 µm, for the samples irradiated with 1.7 MeV protons with beam fluence of 40, 60, 100, and 120 nC/mm^2, respectively. The film had a crack on the microbeam path when beam fluence exceeded 240 nC/mm^2.

The infrared light transportation through the sample was observed as near-field pattern (NFP) by an IR vidicon camera (Hamamatsu Photonics Ltd., C2741-03) with an input of fiber laser (SANTEC, ECL-210) with center wavelength of 1.55 µm. The comparison of output pattern of NFP from MZ waveguide on near-surface of PMMA thin film was illustrated in Fig.3. From the result it was suggested that the single-mode light propagation was formed at beam fluence from 40-60 nC/mm^2. Above those fluence, multi-mode like light propagations were observed. There are not typical leakages of light below the core where the proton had penetration path. Before the optical leakage starts, the film itself has been mechanically destroyed. The distance between core and surface was reduced at least several micrometers from previous irradiation conditions. Further investigation is necessary with these configurations with shorten distance from core to the controller/sensing volume.
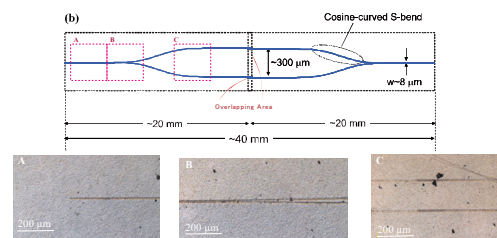
Fig. 2. Schematic illustration of MZ waveguide and optical images of particular part of waveguide fabricated on near-surface region of PMMA thin film.
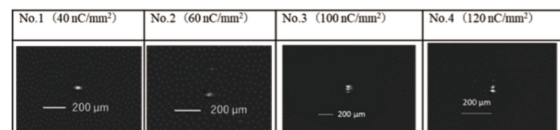
Fig. 3. Comparison of NFP observations of MZ waveguide on near-surface region of PMMA thin film.

References
[1] W. Kada *et al.*, Nucl. Instr. Meth. Sec. B. **348**, 218 (2015).
[2] R. K. Parajuli *et al.*, Jan. J. Appl. Phys. **55, 6S1,** 06GD01 (2016).

Fig. 1. Schematic illustration of PBW process for the formation of MZ waveguide embedded near-surface of PMMA thin film.

3 - 18   Effect of Linear Energy Transfer on the Scintillation Properties of Ce-doped $Ca_3B_2O_6$ Crystals

M. Koshimizu [a)], A. Kimura [b)], S. Kurashima [c)], M. Taguchi [b)], T. Yanagida [d)], Y. Fujimoto [a)] and K. Asai [a)]

[a)] Graduate School of Engineering, Tohoku University,
[b)] Department of Advanced Functional Materials Research, TARRI, QST,
[c)] Department of Advanced Radiation Technology, TARRI, QST,
[d)] Division of Materials Science, Nara Institute of Science and Technology

Heavy charged particles deposit their energy with a high density in condensed matter. The energy deposition density by a heavy charged particle is often given per unit length of the particle's trajectory, which is termed linear energy transfer (LET). LET of heavy charged particles is significantly larger than those of high-energy photons and electrons, which results in a distinct irradiation of heavy charged particles. From the viewpoint of radiation detection, the response of radiation detectors usually depends on LET. As for scintillation detectors, it has long been known that the scintillation light yield strongly depends on LET. To elucidate the dynamics of the excited states responsible for the LET dependence of scintillation properties, the LET dependence of the scintillation temporal profiles should be analyzed.

In this study, we analyzed the LET dependence of the scintillation properties of Ce-doped $Ca_3B_2O_6$. Recently, Fujimoto et al. developed scintillators based on rare-earth-doped $Ca_3B_2O_6$ [1–3]. These devices can be used for detecting thermal neutrons via the nuclear reaction of $^{10}B(n,\alpha)^{7}Li$. Here, we report the scintillation properties of Ce-doped $Ca_3B_2O_6$, emphasizing the LET effects on the energy transfer process from the host to the luminescence centers, i.e., Ce^{3+} ions.

A single crystal of Ce-doped $Ca_3B_2O_6$ was used for the measurements. The concentration of Ce was 3 mol%. The thickness of the crystal was ~1 mm. The measurements were performed at TIARA, QST, Japan. We used pulsed beams of 20 MeV H^+, 50 MeV He^{2+}, and 220 MeV C^{5+} from an azimuthally varying field cyclotron at TIARA. Heavier ions deposit energy onto samples with higher LET. The studied sample was irradiated with pulsed ion beams in air. The sample's scintillation was detected using a photomultiplier tube, and the detected signals were recorded using a digital oscilloscope. The signals were averaged over 1000 pulses to obtain the scintillation temporal profiles. The time resolution of the measurement system was ~2 ns at half width at half maximum. The measurement system is described in detail in our previous paper [4].

Figures 1(a) and (b) show, respectively, the rise and the decay parts of the scintillation temporal profiles of Ce-doped $Ca_3B_2O_6$, for irradiations of 20 MeV H^+, 50 MeV He^{2+}, and 220 MeV C^{5+}. The temporal profiles peak at ~80 ns following the pulsed beam irradiation, which is significantly longer than the time resolution of the measurement system.

A small shoulder was observed during the rise. The rise was significantly faster for the scintillation temporal profile of 20 MeV H^+ than for the other ions. The observations of the scintillation temporal profiles at different wavelengths revealed that the contribution of the fast component attributed to the localized centers (such as defects) is LET-dependent. The LET effects were explained in terms of the competition between the energy transfer from the host to Ce^{3+} ions or the localized centers, and in terms of the quenching owing to the excited states interaction in the host.
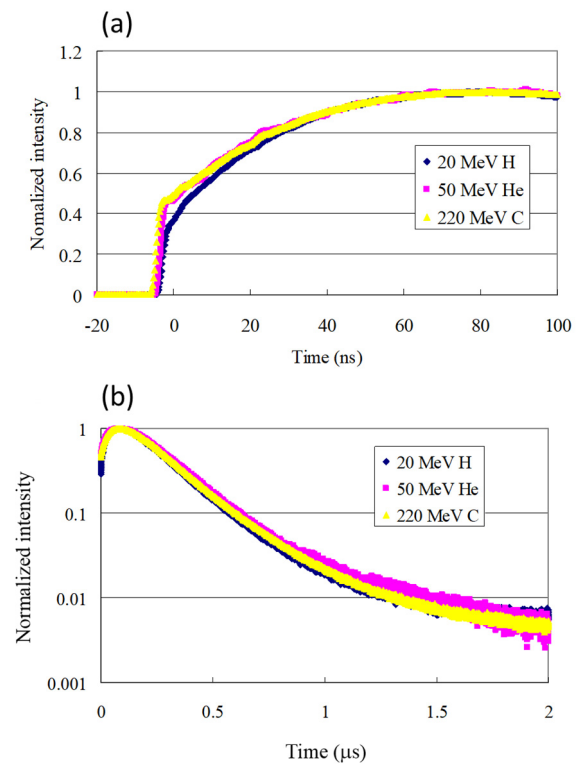
Fig. 1. (a) Rise and (b) decay parts of the scintillation temporal profiles of Ce-doped $Ca_3B_2O_6$, under irradiations of 20 MeV H^+, 50 MeV He^{2+}, and 220 MeV C^{5+}.

References
[1] Y. Fujimoto et al., Key Eng. Mater., **508**, 235 (2012).
[2] Y. Fujimoto et al., J. Cryst. Growth **318**, 784 (2011).
[3] Y. Fujimoto et al., Phys. Status Solidi b **248**, 444 (2011).
[4] M. Koshimizu et al., Rev. Sci. Instrum., **86**, 013101 (2015).

Part Ⅱ

4. Status of Quantum-Beam Facilities

4 - 01   Utilization Status at TIARA Facility

H. Hanaya [a], I. Ishibori [a], H. Takizawa [a], S. Watanabe [a],
H. Kaneko [b], S. Kaneya [b], M. Kawabata [b], K. Saga [b] and Y. Nakamura [b]

[a] Department of Advanced Radiation Technology, TARRI, QST,
[b] Takasaki Establishment, Radiation Application Development Association

Research & Industrial Use

Four kinds of accelerators, a cyclotron and three electrostatic accelerators (tandem accelerator, single-ended accelerator and an ion implanter), are used at the TIARA facility to meet various researchers' needs. The activities of research fields that the cyclotron was used for the past 5 fiscal years are shown in Fig. 1. Total utilization time amounted to about 2200 hours per year until FY 2015. However, after FY 2016, the total utilization time reduced due to the remodeling of a cooling system of the cyclotron facility and repair of the main coil of the cyclotron. The trend of each research field also changed after FY 2016. The utilization time of "Basic Technology of Quantum Beam" extremely decreased, as compared with the other three research fields.

On the other hand for the three electrostatic accelerators, as shown in Fig. 2, the utilization time of "Material Science" and "Basic Technology of Quantum Beam" accounted for more than about 60% of the total time. The utilization time of "Facility use program" increased since FY 2016, because JAEA users were categorized into "Facility use program", changing from "Internal use".

The trend of the number of users in the past 5 years is shown in Fig. 3. The total number of users decreased from FY 2014. The trend of the number of project category (Internal use, Joint research, Cooperation priority research, Funded research and Facility use program) for the past 5 years is shown in Fig. 4. The number of projects was in the range of 120 to 140 per year until FY 2015. However, the number had decreased since FY 2016, because projects of "Cooperation priority research", "Joint research" and "Internal use" were unified.
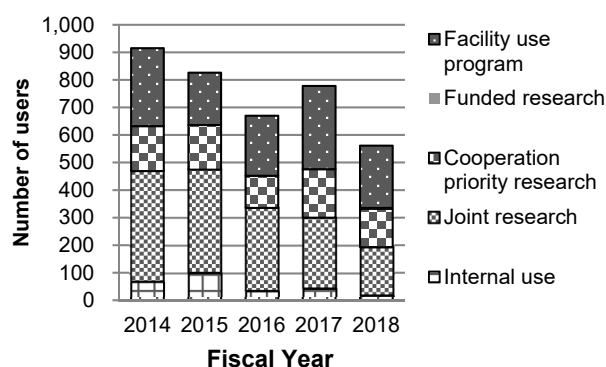
Fig. 3. The number of users for the past 5 years.
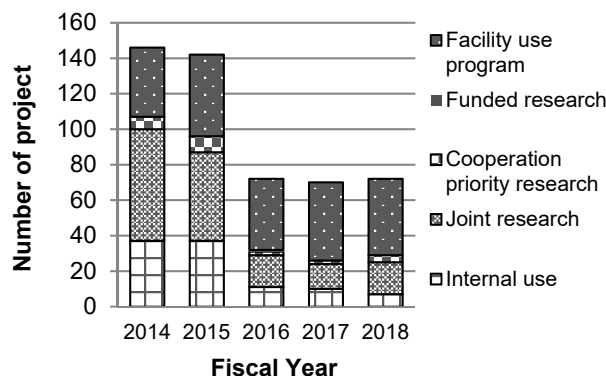
Fig. 4. The number of projects for the past 5 years.

Fig. 1. Research activities for the cyclotron for the past 5 years.

Fig. 2. Research activities for the three electrostatic accelerators for the past 5 years.

Others

QST Takasaki science festa 2018 was held successfully in December 11 and 12, 2018 at Takasaki city gallery. The numbers of oral presentations and the poster sessions were 23 and 93, respectively. The number of participants were 590, 51 more than the last meeting.

The QST Takasaki annual report 2017 including 17 research projects and 113 individual research papers was published. About 660 books were mainly distributed to domestic related departments. In addition, 43 English letters to notify the URL for the download of an electric version of the annual report were sent to overseas related departments.

4 - 02 Operation of the AVF Cyclotron

S. Kurashima [a), K. Yoshida a), T. Yuyama a), T. Ishizaka a), S. Hosoya a), I. Ishibori a),
N. Miyawaki a), H. Kashiwagi a), Y. Yuri a), S. Okumura a), T. Nara a), To. Yoshida b),
S. Ishiro b), Tu. Yoshida b), S. Kanou b), K. Takano b), H. Saitoh b) and T. Atobe b)

a) Department of Advanced Radiation Technology, TARRI, QST,
b) Beam Operation Co., Ltd.

Operation

An electrical short between two pancakes of the upper main coil of the cyclotron was found in December, 2016 and the temporary measure to bypass four of ten pancakes of the main coil was done in April and May, 2017 [1]. The maximum beam energy of the cyclotron was restricted to about 60% for one year. Replacement of the upper and lower main coils was carried out spending ten months from June, 2018. The beams were served to the experiments for only two months as shown in Fig. 1.

Table 1 shows the statistics of the cyclotron operation in fiscal 2018, with the data in fiscal 2017 for comparison. The total operation time amounted to 786 h. The percentages of operation time of the year used for regular experiments, Facility Use Program, beam tuning, and beam development are 42.7%, 17.4%, 37.1%, and 2.8%, respectively. There was no cancellation of the experiments due to machine troubles. The accumulative operation time was 83122 h and the total number of experiments was 12050 from the first beam extraction in 1991 to March, 2019.
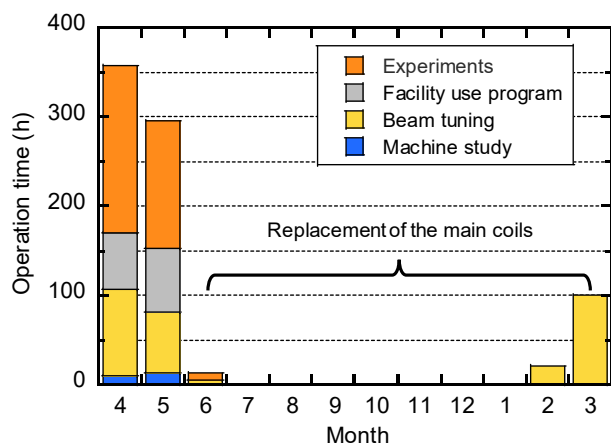
Fig. 1. Monthly operation times in fiscal 2018.

Table 1

Statistics for cyclotron operation.

Fiscal year	2017	2018
Beam service time (h)	1340	473
Beam tuning (h)	783	291
Machine study (h)	96	22
Total operation time (h)	2219	786
Change of particle and/or energy	181 times	76 times
Change of beam course	214 times	74 times
Change of harmonic number	68 times	23 times
The number of experiments	252	105
Cancellation due to machine trouble	0	0

Replacement of the main coil

To replace the main coil, most components of the cyclotron were removed from the magnet yoke for the first time since its installation in 1990. Figure 2 shows pictures of the main coil replacement work. The big problem was that the existing shield door of the cyclotron room was rather small for the main coil with outer diameter of about 3 m to pass through. Therefore, the shield wall of 4 m in thickness of the cyclotron room was temporarily bored to carry the main coil. The replacement work of the main coil was divided into five processes: 1) removing the RF resonators, the vacuum chamber, the magnet poles, the main coils, and so on; 2) boring the shield wall; 3) replacing the main coils; 4) closing the opening of the shield wall; 5) restoring the cyclotron completely. Beam tuning after the replacement work has been carried out without any serious troubles in March, 2019.

Fig. 2. Pictures of the main coil replacement work. Removing the vacuum chamber (upper) and the upper main coil (lower) from the magnet yoke.

Reference

[1] S. Kurashima *et al.*, QST Takasaki Annu. Rep. 2017, **QST-M-16**, 149 (2019).

4 - 03　　Operation of Electrostatic Accelerators in TIARA

A. Chiba [a], K. Yamada [a], A. Yokoyama [a], Y. Hirano [a], T. Nara [a],
T. Takayama [b], S. Kanai [b], Y. Aoki [b], M. Hashizume [b],
Y. Takahashi [b] and M. Hasegawa [b]

[a] Department of Advanced Radiation Technology, TARRI, QST,
[b] Beam Operation Co., Ltd.

Operation and Status

Three electrostatic accelerators in TIARA were operated according to the original operating plan of fiscal year (FY) 2018. The transitions of annual operating time of each accelerator are shown in Fig.1. The operating rate of 100% has been achieved in the 3-MV tandem accelerator and the 400-kV ion implanter. On the other hand, one of the experiments using an ion beam accelerated by a 3 MV single-ended accelerator was discontinued due to a serious failure of its boost circuit. Although the relatively minor trouble cases, such as communication error in the control systems and malfunction of the ion sources, occurred frequently in each accelerator, the annual operating times of three accelerators kept the same level as usual.

The utilization ratio of ion species used in the tandem accelerator in FY 2018 is shown in Fig. 2. The utilization of C_{60}-ion beam has increased year by year and has extended to approximately 1/5 of all ion species. One reason for this leap of the utilization rate in recent years is due to the increase of the C_{60}-ion beam intensity by the improvement of an ion source. In FY 2018, the beam intensity exceeded 1 μA and increased more than several hundred thousand times in 5 years. Furthermore, we are planning to form the world's first MeV C_{60}-ion microbeam which is one of the purposes to improve the C_{60}-ion beam in intensity and have already development the microbeam forming system with an electrostatics quadrupole lens shown in Fig. 3.

New ion beam

Two ion beams with μA order became utilizable in the ion implanter: Ba^+ and Sr^+. The vaporized samples are ionized by Ar plasma in an arc chamber of a Freeman type ion source. These ion beams were required for the experiments on a duping technique in a semi-conductor.

In the tandem accelerator, generation of Ga^+ ion beam was successful. The Ga^{2+}-ion beam of 250 pnA was accelerated with a total energy of 9 MeV.

An experiment was attempted in which the samples were directly irradiated with the low energy beam extracted from an ion source of the tandem accelerator. The ion beam was of organic compounds of which ionization by this ion source had hardly been demonstrated in the world so far. Adenine ion containing five nitrogen atoms ($C_5N_5H_5$) was generated by a Cs sputter type negative ion source, and the mass analyzed $C_4N_4H_n$ ions were successfully implanted to the diamond samples.

Maintenance

One of the experiments in FY 2018 was discontinued due to a serious trouble in the single-ended accelerator.

The cause of this trouble was a mechanical failure of the ripple adjustment system in the boost circuit. Although it took time to investigate the cause, the trouble was resolved on the same day. The number of troubles and maintenance in FY 2017 and 2018 are shown in Table 1.
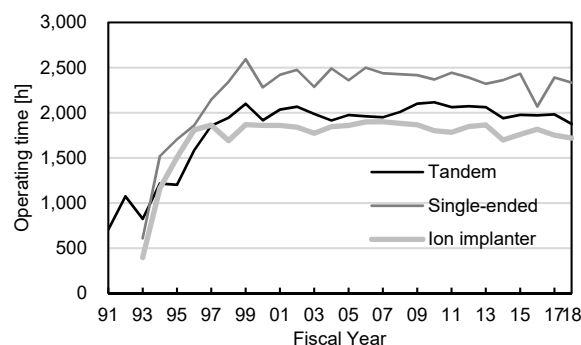
Fig. 1. Transitions of annual operating time.
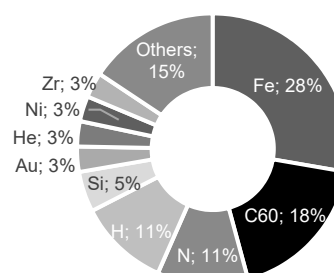
Fig. 2. Utilization rate of ions in tandem accelerator.
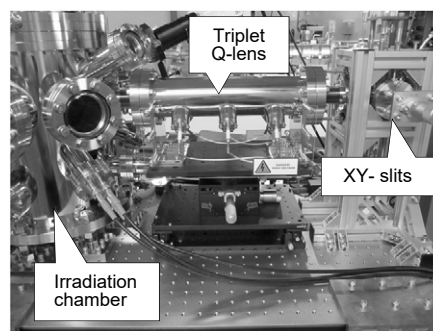
Fig. 3. Photo image of cluster-ion microbeam system.

Table 1

Number of troubles and maintenance in FY 2017 and 2018.

	Tandem		Single-ended		Ion implanter	
	'17	'18	'17	'18	'17	'18
Minor trouble	18	33	14	6	17	18
Serious trouble	6	0	4	6	5	2
Maintenance	11	16	11	13	8	10

4 - 04   Operation of the Electron Accelerator and the Gamma-ray Irradiation Facilities

T. Agematsu [a], S. Uno [a], N. Nagasawa [a], R. Yamagata [a],
H. Seito [a], Y. Nagao [a], S. Yamasaki [a], Y. Haruyama [a],
N. Yagi [b], M. Takagi [b], K. Nagai [b], T. Asai [b], K. Akaiwa [b] and K. Imai [b]

[a] Department of Advanced Radiation Technology, TARRI, QST,
[b] Takasaki Establishment, Radiation Application Development Association

Operation

The electron accelerator and the ^{60}Co gamma-ray irradiation facilities were operated approximately smoothly in Fiscal Year (FY) 2018.

The annual operation time of the electron accelerator in this FY was 1041 h, including 105 h of conditioning operation. The operation time in recent years is shown in Fig. 1. There were a lot of troubles in FY 2014 and FY 2015. Although there was trouble in the high frequency power supply unit of the accelerator for one month, the annual irradiation time in FY 2016 increased because long-time irradiation increased. The annual irradiation time in FY 2018 increased because long-time irradiation increased.

The ^{60}Co gamma-ray irradiation facilities consisting of three buildings with eight irradiation rooms cover a wide dose-rate range from 2×10^{-1} Gy/h to 9×10^{3} Gy/h as of January 2019. The annual operation times of the first and the second cobalt irradiation facilities and the food irradiation facility were 17512 h, 14715 h and 9808 h, respectively, as shown in Fig. 2.

Maintenance

・Electron accelerator

The trouble of the horizontal beam line occurred at the beginning of December 2017, and generation of the horizontal beam came to a halt. By the maintenance with opening the accelerator vessel in October 2018, we found that this trouble was due to fault at the capacitor on the power supply circuit for the electron gun, not to a filament disconnection. This repair is scheduled in FY 2019 because the parts can't be prepared soon. In addition, we performed regular maintenance on other items of the vertical beam line.

・Gamma-ray irradiation facilities

The periodical maintenance check mainly on mechanical systems for radiation source transportation is performed every year on one of the three gamma-ray irradiation facilities in turn. The maintenance check of the first irradiation facility was done in July 2018 with suspension of operation for 23 days.

The purifier system for the water pools of the three gamma-ray irradiation facilities was damaged by long-time use. The component units for removing carbonic acid were renewed in March 2019. Besides, the damaged valves and lining of the retaining wall for chemical liquid were repaired.

The total amount of ^{60}Co sources of all the facilities at the Takasaki Institute have decreased by isotope decay. New ^{60}Co sources were not installed in FY 2018. Therefore, the maximum dose rate has decreased more largely than usual years. For the protection reinforcement of the ^{60}Co sources in the gamma-ray irradiation facilities, the protection devices were installed in FY 2018.
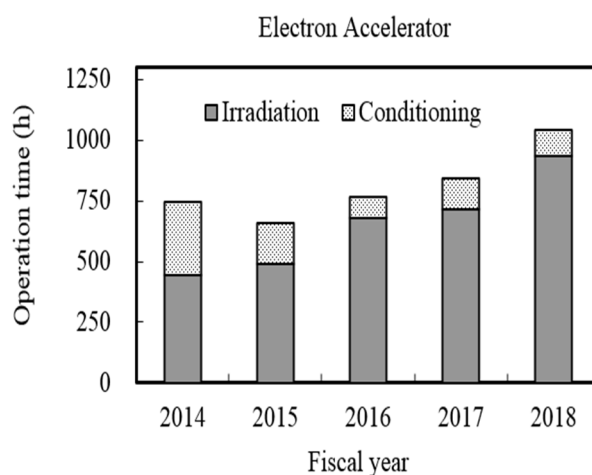
Fig. 1. Annual operation time of the electron accelerator.
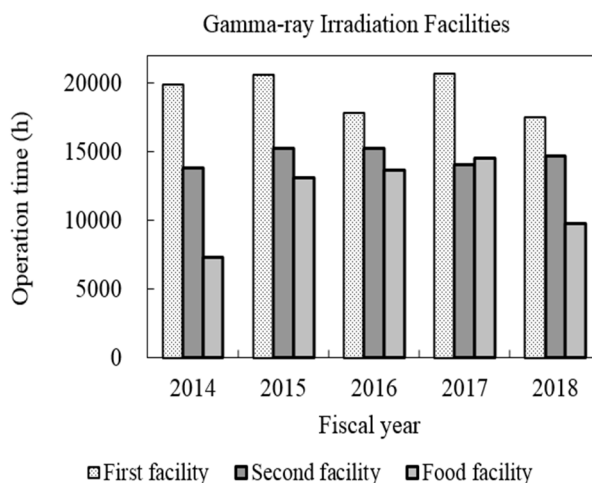
Fig. 2. Annual operation times of the ^{60}Co gamma-ray irradiation facilities.

4 - 05   Utilization Status of the Electron Accelerator and the Gamma-ray Irradiation Facilities

T. Agematsu [a], S. Uno [a], N. Nagasawa [a], R. Yamagata [a],
H. Seito [a], Y. Nagao [a], S. Yamasaki [a], Y. Haruyama [a],
N. Yagi [b], M. Takagi [b], K. Nagai [b], T. Asai [b], K. Akaiwa [b] and K. Imai [b]

[a] Department of Advanced Radiation Technology, TARRI, QST,
[b] Takasaki Establishment, Radiation Application Development Association

The electron accelerator and the three gamma-ray irradiation facilities were operated for various research subjects according to the operation plans in FY 2018. Figure 1 shows the trend of the number of irradiation experiments in each field in FY 2014-2018. The accelerator was used mainly for the experiments of graft-polymerization in new material development, radiation effect studies on semiconductors, and various experiments performed by external users. The first cobalt irradiation facility was used mainly for the experiments of long-term radiation resistance for the cables that were used in nuclear power plants and nuclear reactor facilities. The second cobalt irradiation facility was used mainly for the experiments of the development of new functional materials and the other research subjects of external users. The food irradiation facility having a lower-dose-rate field was used for the experiments of radiation resistance at wide dose rate.

The irradiation experiments in FY 2014-2015 were reclassified from old classification of JAEA into the three fields based on the research fields of QST. The classification was changed as follows. 'Materials for space', 'Nuclear facilities', 'Material processing', 'Heat-resistant materials', and 'Environment' were unified into 'Materials science'. 'Resources & Bio-technology', and 'Basic technology' were relabelled to 'Life science' and 'Quantum beam science', respectively. Figure 2 shows the time of irradiation experiments in each field in FY 2014-2018. The irradiation experiments by JAEA users were classified into 'Facility use program' since FY2016. Therefore, at the gamma-ray irradiation facilities, the time of irradiation experiments by internal users decreased, and that by 'Facility use program' increased. Furthermore, because of the decrease in long-term irradiation by JAEA, the time of irradiation experiments in FY 2016-2018 decreased as compared to that in FY 2015. Especially some irradiation experiments in 'Facility use program' were carried out for the

recovery from the accident at the Fukushima Daiichi Nuclear Power Station by external users. On the other hand, at the electron accelerator, the time of irradiation experiments in FY 2014-2015 decreased extremely because there was a lot of troubles, whereas the time of irradiation experiments in FY 2016-2017 increased due to smooth operation. Furthermore, the time of irradiation experiments in FY 2018 increased, because of the increase in long-term irradiation experiments for the research on material science, such as the production of Nitrogen-Vecancy center in diamond for the application to quantum computing.
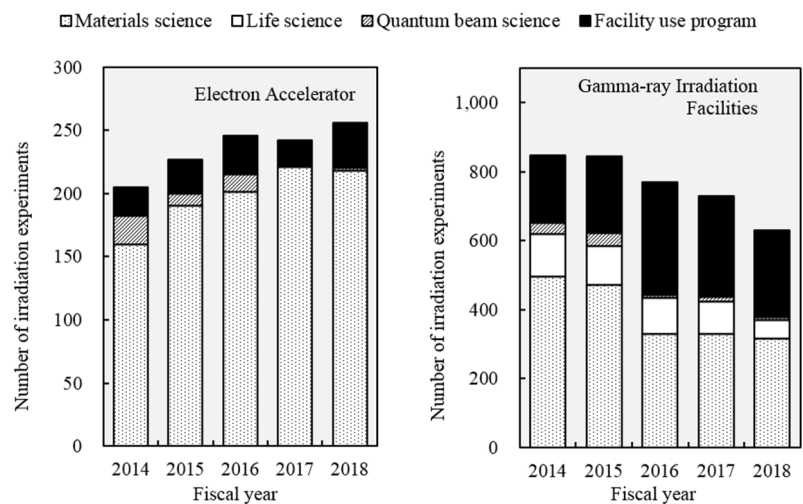
Fig. 1. The number of irradiation experiments (FY 2014-2018).
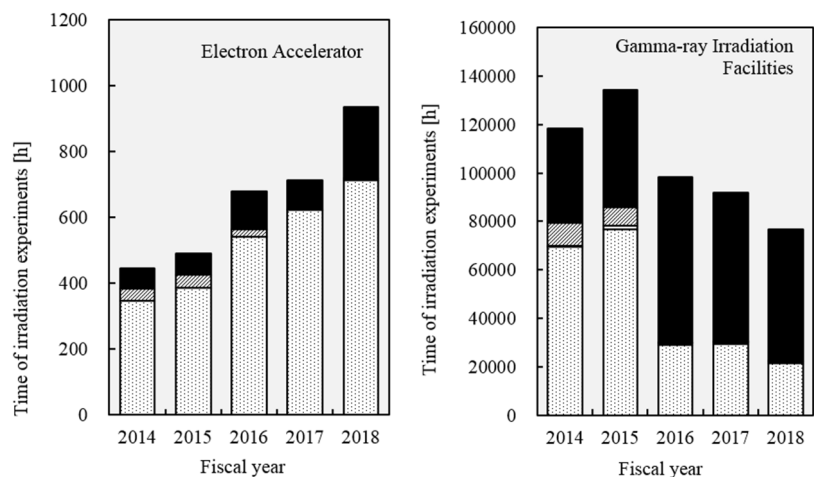
Fig. 2. The time of irradiation experiments (FY 2014-2018).

4 - 06   Radiation Monitoring in TIARA

Safety Management Section

Department of Administrative Services, TARRI, QST

Individual monitoring

(1) Individual monitoring for the radiation workers

Table 1 shows a distribution of effective dose of the radiation workers in FY 2018. The effective dose values of almost all radiation workers were below the detection limit of 0.1 mSv.

The maximum dose of the radiation workers was 0.9 mSv/y due to replacement work of the main coil of AVF cyclotron.

Table 1

Distributions of the effective dose of the radiation workers in FY 2018.

Items		Number of persons in each periods				
		1st quarter	2nd quarter	3rd quarter	4th quarter	Annual
Distribution range of effective dose HE:Effective dose [*1] (mSv)	HE < 0.1	456	429	408	433	583
	$0.1 \leqq HE \leqq 1.0$	7	2	4	7	14
	$1.0 < HE \leqq 5.0$	0	0	0	0	0
	$5.0 < HE \leqq 15.0$	0	0	0	0	0
	$15.0 < HE$	0	0	0	0	0
Total number of persons (A)		463	431	412	440	597
Exposure above 1mSv	Number of persons (B)	0	0	0	0	0
	(B)/(A)×100(%)	0	0	0	0	0
Mass effective dose (Person・mSv)		1.3	0.2	0.4	1.1	3.0
Mean dose (mSv)		0.00	0.00	0.00	0.00	0.01
Maximum dose (mSv)		0.5	0.1	0.1	0.5	0.9

*1 The dose by the internal exposure was not detected.

(2) Individual monitoring for the visitors and others

Table 2 shows the number of people who temporarily entered the radiation controlled areas. The effective doses of all people were less than 0.1 mSv.

Table 2

The number of people who temporarily entered the radiation controlled areas in FY 2018.

Periods	1st quarter	2nd quarter	3rd quarter	4th quarter	Total
Number of persons	968	1,353	1,402	1,620	5,343

Monitoring of radioactive gases and dusts

Table 3 shows the maximum radioactive concentrations and total activities for radioactive gases released from the stack of TIARA, during each quarter of FY 2018.

Small amounts of ^{41}Ar, ^{11}C, ^{18}F, ^{77}Br and ^{131}I were detected occasionally during the operation of the cyclotron or experiments, but the particulate substances (^{65}Zn, etc.) were not detected.

Table 3

Monitoring results of released radioactive gases and dust in FY 2018.

Nuclide	Periods \ Items	1st quarter	2nd quarter	3rd quarter	4th quarter	Total
^{41}Ar	Maximum concentration	$<1.4\times10^{-4}$	$<1.4\times10^{-4}$	$<1.3\times10^{-4}$	$<1.3\times10^{-4}$	
	Activity	9.2×10^{6}	0	0	0	9.2×10^{6}
^{11}C	Maximum concentration	$<1.4\times10^{-4}$	—	—	—	
	Activity	6.6×10^{7}	—	—	—	6.6×10^{7}
^{18}F	Maximum concentration	$<1.4\times10^{-4}$	—	—	—	
	Activity	1.9×10^{7}	—	—	—	1.9×10^{7}
^{77}Br	Maximum concentration	9.6×10^{-8}	—	—	—	
	Activity	1.8×10^{6}	—	—	—	1.8×10^{6}
^{131}I	Maximum concentration	1.8×10^{-9}	—	—	—	
	Activity	3.0×10^{4}	—	—	—	3.0×10^{4}
^{65}Zn	Maximum concentration	$<7.4\times10^{-10}$	$<7.4\times10^{-10}$	$<7.4\times10^{-10}$	$<6.9\times10^{-10}$	
	Activity	0	0	0	0	0

Unit : Bq/cm^3 for Maximum concentration, Bq for Activity.

Monitoring for external radiation and surface contamination

The monitoring for external radiation and surface contamination was routinely performed in/around the radiation controlled areas. Neither anomalous value of dose equivalent rate nor surface contamination was detected. Figure 1 shows a typical example of distribution of the dose equivalent rate in the radiation controlled area of the cyclotron building.
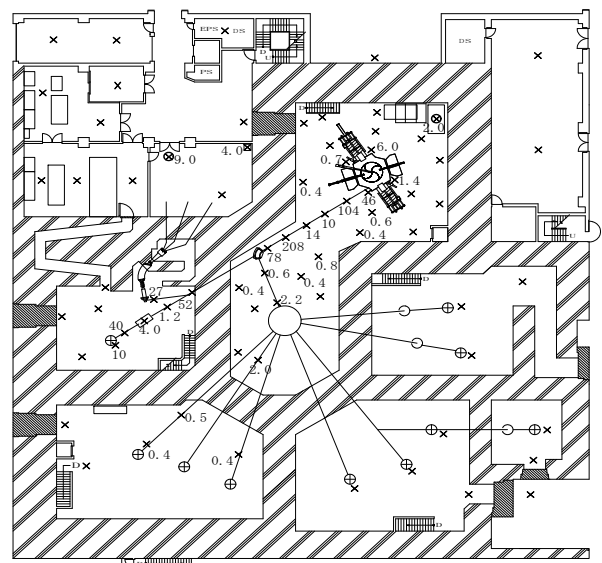
Fig. 1. Dose equivalent rate distribution in the radiation controlled area of the cyclotron building. Measurement date : 15th, 26th and 28th March 2019, Measuring position : Indicated with × (1 m above floor), Unit : μSv/h. (The values are not indicated if less than 0.2 μSv/h.).

4 - 07   Radioactive Waste Management in TIARA

N. Higuchi

Department of Administrative Services, TARRI, QST

Radioactive waste management

The radioactive waste generated in TIARA is managed by Utilities and Maintenance Section. The main radioactive waste is the solid waste generated from research experiments and the maintenance of the cyclotron. Other radioactive waste is the liquid waste such as inorganic waste fluids generated from research experiments and the air-conditioning machines in radiation controlled area. These wastes are managed according to their properties. Radioactive waste is stored in a storage facility and handed over to the Japan Radioisotope Association for disposal.

Solid radioactive waste

Table 1 shows the amounts of various types of solid waste were generated in each quarter of FY 2018. Combustible waste consists of papers and clothes, and so on. Flame-retardant waste consists of rubber gloves, plastic articles, and polyethylene articles. Incombustible waste consists of metal pieces, the glasses, and contaminated parts. Solid waste emitting α, β, and γ is classified according to the properties.

Liquid radioactive waste

Table 2 shows the amounts of liquid waste were generated in each quarter of FY 2018. Most of liquid waste was inorganic waste water generated from chemical experiments and others are condensed water going out of the air-conditioner installed in the radiation controlled area. The largest amount of waste water in summer season (2nd quarter) was the condensed water. After the treatment of evaporation of the waste water, inorganic water is reused in the radiation controlled area. Only small amounts of concentrated liquid were generated by the treatment.

Table 1
Radioactive solid waste generated in FY 2018.

Items \ Amounts	Amounts of generation in each period (m^3)					Number of package /drum
	1st quarter	2nd quarter	3rd quarter	4th quarter	Total	
Category β, γ *	0.08	0.48	2.94	0.93	4.43	88
Combustible	0.02	0	0.10	0.12	0.32	8
Flame-retardant	0.04	0.26	0.14	0.28	0.72	18
Incombustible(Compressible)	0	0	0	0.16	0.40	10
〃 (Incompressible)	0	0	3	0	2.62	52
Laboratory animal	0	0	0	0	0	0
Filters	0	0	0	0.37	0.37	0
Category α *	0	0	0	0.20	0.32	4
Combustible	0	0	0	0	0.02	0
Flame-retardant	0	0	0	0.16	0.24	4
Incombustible(Compressible)	0	0	0	0	0	0
〃 (Incompressible)	0	0	0	0	0	0
Laboratory animal	0	0	0	0.04	0.06	0
Filters	0	0	0	0	0	0

*   defined by amount in Bq (β, γ): < 2 GBq , (α) : (A) < 37 MBq (B) ≤ 37 MBq,
** 50-liter drum.

Table 2
Radioactive liquid waste generated in FY 2018.

Items \ Amounts	Amounts of generation in each period (m^3)					Number of package /drum
	1st quarter	2nd quarter	3rd quarter	4th quarter	Total	
Category β, γ *	8.97	27.14	2.27	6.21	44.59	-
1)Inorganic	8.97	27.14	2.27	6.21	44.59	-
Inorganic	8.97	27.14	2.27	6.21	44.59	treatment
Sludge, Evaporation residue	0	0	0	0	0	0 **
2)Organic	0	0	0	0	0	0
Organic	0	0	0	0	0	0
Oil	0	0	0	0	0	0
Category α *	0	0	0	0	0	0

* defined by concentrations in Bq/mL (β, γ Inorganic) : < 200 kBq, (Organic) : < 2 kBq, (α) : ≤ 1.85 kBq,
** 50-liter container.

4 - 08　Facility Use Program in Takasaki Advanced Radiation Research Institute (TARRI)

S. Nozawa, H. Hanaya and M. Seki

Department of Research Planning and Promotion, QuBS, QST

Introduction

The usage of the facilities in TARRI, QST is widely allowed for many users in universities, public institutes, R&D divisions of private companies, and so on (hereafter 'outside users') under the Facility Use Program.

Under this program, outside users can use the gamma-rays, electron beams, and ion beams that have been provided from the facilities of Co-60 gamma-ray, electron accelerator, and TIARA's four ion accelerators, and two off-line analysis instruments in TARRI. Outside users have to pay for the equipment operating costs in exchange for using facilities.

Charging system of Facility Use Program in FY2018

Charging system of Facility Use Program is classified based on the purpose of irradiation and the disclosure of experimental results, as shown in Table 1. The charging fee has been calculated from the total amount of handling fees, irradiation fees, and supplies expense (ex. additional consumables and labor costs).

For research and development (R&D) users who disclose the results of experiment by publication, partially exempted charges are applied. Research proposals of R&D users are reviewed by the expert committee members in terms of the effectiveness of the experimental design. Confirmed research proposals had been carried out under Facility Use Program with partial charge exemption. For Except R&D users, such as commercial irradiation, additional depreciation charges for irradiation facilities are claimed.

Table 1

Charging system for Facility Use Program in FY2018.

	R&D for public disclosure	Non-disclosure R&D	Except R&D
Purpose	Research and Development		Except R&D
Belonging of Results	Non-proprietary	Proprietary	
Duty for publishing	Yes	No need to public disclosure	
Charging fees*	A	B	C

*A = handling fees + expendables fee (other charges are exempted)

B = Charging fee "A" + irradiation fee + radioactive waste disposal expenses

C = Charging fee "B" + depreciation cost for irradiation facilities

Number of irradiation experiments in FY2018

The number of irradiation experiments for each facility in FY2018 is shown in Table 2.

Table 2

Number of irradiation experiments at each facility under the Facility Use Program in FY2018.

Facility		User's affiliation — University	Public Institute	Private Company	Total
TIARA	AVF cyclotron	9	4	8	21
TIARA	3 MV tandem accelerator	20	18	3	41
TIARA	3 MV single-ended accelerator	1	13	2	16
TIARA	400 kV ion implanter	13	11	3	27
Co-60 gamma-ray irradiation facilities		35	52	164	251
Electron accelerator		7	3	24	34
Total		85	101	204	390

This year, even though the operation time of AVF cyclotron was limited to only two months due to repairing of the main magnet in it, almost 400 experiments were carried out in irradiation facilities of TARRI.

The main users of the TIARA facilities were belonging to universities and public institute. On the other hand, most of users in Co-60 gamma-ray irradiation facilities and electron accelerator belonged to private companies.

Some of outside users were not experts for radiation-irradiation experiments, and they needed the more information about the irradiation facilities and related techniques. To improve the convenience of outside users, Research Planning and Promotion Office provided various kind of information, such as preparation of documents, procedure of payment, contact person of each experimental equipment, and so on.

Additional information about this program is available on the QST website as follows:

https://www.qst.go.jp/site/qubs/1954.html

Appendices

Appendix 1　Publication list

Items in gray show the works in collaboration with other projects of QST.
Bold letters and **numbers** at the last of each item mean as follows.
Letter : Accelerators or irradiation facilities used for the work.
C : Cyclotron, **T** : Tandem accelerator, **S** : Single-ended accelerator, **I** : Ion implanter,
E : Electron accelerator, **G** : Gamma-ray irradiation facilities, **N** : Not used.
Number that contains hyphen: Serial number of the related paper in Part II.

P1-1　Project "Functional Polymer"

Papers

1) Y. Zhao, K. Yoshimura, H. C. Yu, Y. Maekawa, A. Hiroki, Y. Kishiyama, H. Shishitani, S. Yamaguchi, H. Tanaka, S. Koizumi, M. Appavou, J. Houston, A. Radulescu, and D. Richter, "Small angle neutron scattering study on the morphology of imidazolium-based grafted anion-conducting fuel cell membranes", Physica B: Condensed Matter, **551**, 203-207 (2018).　　　　**G, 1-17**

2) A. Fukaya, A. Tateno, N. Iimura, Y. Ohta, K. Takahashi, T. Sodekoda, K. Suzuki, H. Takahashi, S. Hasegawa, A. Hiroki, and Y. Maekawa, "Application of graft-type poly(ether ether keton)-based polymer electrolyte membranes to electrochemical devices – Fuel cells and electrolytic enrichment of tritium", Int. J. Hydrogen Energy, **43**, 8927-8935 (2018).　　　　**G**

3) T. D. Tap, D. D. Khiem, L. L. Nguyen, N. Q. Hien, L. Q. Luan, P. B. Thang, S. Sawada, S. Hasegawa, and Y. Maekawa, "Temperature effects on mechanical properties and conductivity of graft-type polymer electrolyte membrane", Radiat. Phys. Chem., **151**, 186-191 (2018).　　　　**G**

4) T. Hamada, K. Yoshimura, A. Hiroki, and Y. Maekawa, "Synthesis and Characterization of Aniline-Containing Anion-Conducting Polymer Electrolyte Membranes by Radiation-Induced Graft Polymerization", J. Appl. Polym. Sci., **135**, 46886 (2018).　　**G**

5) Beom-Seok Ko, K. Yoshimura, S. Warapon, H. Shishitani, S. Yamaguchi, H. Tanaka, and Y. Maekawa, "Basicity-dependent properties of anion conducting membranes consisting of iminium cations for alkaline fuel cells", J. Polym. Sci. A, Polym. Chem., **57**, 503-510 (2019).　　　　**G**

6) K. Yoshimura, Y. Zhao, A. Hiroki, Y. Kishiyama, H. Shishitani, S. Yamaguchi, H. Tanaka, S. Koizumi, J. E. Houston, A. Radulescu, M. Appavou, D. Richter, and Y. Maekawa, "Reverse relationships of water uptake and alkaline durability with hydrophilicity of imidazolium-based grafted anion-exchange membranes", Soft Matter, **14**, 9118-9131 (2018).　　　　**G,1-17**

7) K. Yoshimura, A. Hiroki, H. C. Yu, Y. Zhao, H. Shishitani, S. Yamaguchi, H. Tanaka, and Y. Maekawa, "Alkaline durable 2-methylimidazolium-containing anion-conducting electrolyte membranes prepared by radiation induced grafting for direct hydrazine hydrate fuel cells", J. Membr. Sci., **573**, 403-410 (2019).　　　　**G**

8) 野村 幹弘, 小平 岳秀, 池田 歩, 名嘉 泰史, 西嶋 陽之, 今林 慎一郎, 澤田 真一, 八巻 徹也, 田中 伸幸, 久保 真治, "Development of ion-exchange membranes for the membrane Bunsen reaction in thermochemical hydrogen production by iodine-sulfur process", J. Chem. Eng. Jpn., **51**, 726 - 731 (2018).　　**C**

9) 垣谷 健太, 越川 博, 八巻 徹也, 山本 春也, 佐藤 裕真, 杉本 雅樹, 澤田 真一, "Preparation of Conductive Layer on Polyimide Ion-Track Membrane by Ar Ion Implantation", Surf.

Coating Tech., 355, (2018).　　　　**C**

10) T. Yamaki, N. Nuryanthi, A. Kitamura, H. Koshikawa, S. Sawada, K. Voss, D. Severin, C. Trautmann, "Fluoropolymer-Based Nanostructured Membranes Created by Swift-Heavy-Ion Irradiation and Their Energy and Environmental Applications", Nucl. Instrum. Meth. Phys. Res. Section B: Beam Interactions with Materials and Atoms, 435, (2018).　　　　**C**

Proceedings

1) Y. Zhao, K. Yoshimura, A. Hiroki, Y. Kishiyama, H. Shishitani, S. Yamaguchi, H. Tanaka, and Y. Maekawa, "Imidazolium-Based Grafted Anion Exchange Membranes: Interplay between the Morphology and Anion Transport Behavior", ECS Trans., **86**, 619-627 (2018).　　　　**G, 1-17**

2) Y. Zhao, K. Yoshimura, A. Hiroki, and Y. Maekawa, "SCATTERING STUDY OF STRUCTURE-PROPERTY RELATIONSHIPS OF GRAFTED ANION EXCHANGE MEMBRANES", XVII International Small Angle Scattering conference 2018, [Traverse city, USA] Abstracts, A049 (2018/10).　　　　**G, 1-17**

3) 吉村 公男, ザオ ユエ, 廣木 章博, 猪谷 秀幸, 山口 進, 前川 康成, "The Relationship between Membrane Properties and Hierarchical Structure of Radiation Grafted Anion Conducting Membranes", Advanced Energy Materials 2018, [Univ. of Surrey, UK] Abstracts, PEM04 (2018/09).　　　　**G, 1-17**

4) 廣木 章博, 吉村 公男, ザオ ユエ, 猪谷 秀幸, 山口 進, 前川 康成, "Properties of anion-conducting electrolyte membranes based on ETFE membrane and crosslinked graft polymers for fuel cells", Advanced Energy Materials 2018, [Univ. of Surrey, UK] Abstracts, PEM02 (2018/09).　　　　**G**

5) 吉村 公男, ザオ ユエ, 廣木 章博, 猪谷 秀幸, 山口 進, 前川 康成, "放射線グラフト型アニオン伝導電解質膜のアルカリ耐性と階層構造の関係", 第17回若手研究者発表討論会, [電力中央研究所, 狛江] 要旨集, 21 (2018/10).　　　　**G**

6) 吉村 公男, ザオ ユエ, 廣木 章博, 猪谷 秀幸, 山口 進, 前川 康成, "グラフト型アニオン伝導電解質膜のアルカリ耐性と階層構造の関係", 日本化学会関東支部群馬地区研究交流発表会, [群馬高専, 前橋] 要旨集, P-23 (2018/12).　　　　**G**

7) 廣木 章博, 吉村 公男, 猪谷 秀幸, 山口 進, 前川 康成, "化学的安定性を向上したグラフト型アニオン伝導高分子電解質膜", 日本化学会関東支部群馬地区研究交流発表会, [群馬高専, 前橋] 要旨集, P-49 (2018/12).　　　　**G**

8) 髙松 治文, 吉村 公男, 廣木 章博, 前川 康成, "グラフト型アニオン伝導膜の高分子構造と物性・耐久性の関係", 日本化学会関東支部群馬地区研究交流発表会, [群馬高専, 前橋] 要旨集, P-47 (2018/12).　　　　**G**

9) 吉村 公男, ザオ ユエ, 廣木 章博, 猪谷 秀幸, 山口 進, 前川 康成, "グラフト型アニオン伝導電解質膜のアルカリ耐性と

階層構造の関係", 第 28 回日本 MRS 年次大会 [北九州国際会議場, 北九州] 要旨集, B1-P19-017 (2018/12). **G**

10) 廣木 章博, 吉村 公男, 猪谷 秀幸, 山口 進, 前川 康成, "架橋構造導入により改質したアニオン伝導性高分子電解質膜の化学的安定性", 第 28 回日本 MRS 年次大会 [北九州国際会議場, 北九州] 要旨集, B1-P19-018 (2018/12). **G**

11) 澤田 真一, 安保 貴和, 匠 伸弥, 安川 政宏, 垣花 百合子, 比嘉 充, 前川 康成, "放射線グラフト陽・陰イオン交換膜を用いた逆電気透析装置の発電性能", 第 17 回放射線プロセスシンポジウム [東京大学 弥生キャンパス 弥生講堂, 東京] 要旨集, P4-5 (2018/11). **G**

12) 澤田 真一, 田中 健一, 船津 公人, 前川 康成, "機械学習による放射線グラフト電解質膜のプロトン導電率予測", Future Trend in Polymer Science 2018 [東京理科大学 神楽坂キャンパス, 東京] 要旨集, P128 (2019/03). **G**

13) 澤田 真一, 安保 貴和, 匠 伸弥, 安川 政宏, 垣花 百合子, 比嘉 充, 前川 康成, "放射線グラフト陽・陰イオン交換膜を用いた逆電気透析発電", 膜シンポジウム 2018 [神戸大学 百年記念館, 神戸] 要旨集, P113 (2018/11). **G**

14) 澤田 真一, 後藤 光暁, 越川 博, 喜多村 茜, 比嘉 充, 八巻 徹也, "Ion and water transport properties of cation exchange membranes prepared by heavy-ion-track grafting technique", 5th International Conference on Methods and Materials for Separation Processes [Hotel Verde Montana, POLAND] 要旨集, P103 (2018/08). **C**

15) 越川 博, 佐藤 裕真, 山本 春也, 杉本 雅樹, 澤田 真一, 八巻 徹也, 前川康成, "イオン穿孔膜をテンプレートとした酸化チタンナノコーンの作製", 第 17 回放射線プロセスシンポジウム [東京大学 弥生キャンパス 弥生講堂, 東京] 要旨集, P4-3 (2018/11). **C**

16) 佐藤 裕真, 越川 博, 山本 春也, 杉本 雅樹, 澤田 真一, 八巻 徹也, 前川 康成, "LET 制御による多彩な形状のイオン穿孔", 第 17 回放射線プロセスシンポジウム [東京大学 弥生キャンパス 弥生講堂, 東京] 要旨集, P4-4 (2018/11). **C**

17) 越川 博, 佐藤 裕真, 山本 春也, 杉本 雅樹, 澤田 真一, 八巻 徹也, 前川康成, "Preparation of Metal Oxide Nanocones Using Ion Track-Etched Membranes as Templates", 第 28 回日本 MRS 年次大会 [北九州国際会議場, 北九州] 要旨集, D1-P19-012 (2018/12). **C**

18) 佐藤 裕真, 越川 博, 山本 春也, 杉本 雅樹, 澤田 真一, 八巻 徹也, "Preparation of Metal Oxide Nanocones Using Ion Track-Etched Membranes as Templates", 31st International Microprocesses and Nanotechnology Conference(MNC 2018) [札幌パークホテル, 札幌] 要旨集, 15P-7-44 (2018/12). **C**

19) 喜多村 茜, 八巻 徹也, 百合 庸介, 越川 博, 澤田 真一, 湯山 貴裕, 千葉 敦也, 薄井 絢, "Control of the size of etchable ion tracks in PVDF irradiation in an oxygen atmosphere and with fullerene clusters", 10th International Symposium on Swift Heavy Ions in Matter and 28th International Conference on Atomic Collisions in Solids (SHIM-ICACS 2018) [Université de Caen Normandie, Caen] 要旨集, P2-T05-159 (2018/12). **C**

P1-2   Project "Advanced Catalyst"

Papers

1) T. T. Sasaki, Y. Takada, H, Okazaki, T. Ohkubo, T. Nakamura, T. Sato, A. Kato, Y. Kaneko, K. Hono, "Role of Ga on the high coercivity of Nd-rich Ga-doped Nd-Fe-B sintered magnet", J. Alloys Compounds, **790**, 750-759 (2019). **N**

2) D. Billington, K. Toyoki, H, Okazaki, Y. Kotani, T. Fukagawa, T. Nishiuchi, S. Hirosawa, T. Nakamura, "Unmasking the interior magnetic domain structure and evolution in Nd-Fe-B sintered magnets through high-field magnetic imaging of the fractured surface", Phys. Rev. Mater., **2**, 104413 (2019). **N**

3) M. Nomura, T. Kodaira, A. Ikeda, Y. Naka, H. Nishijima, S. Imabayashi, S. Sawada, T. Yamaki, N. Tanaka, S. Kubo, "Development of ion-exchange membranes for the membrane Bunsen reaction in thermochemical hydrogen production by iodine-sulfur process", J. Chem. Eng. Jpn, **51**, 726-731 (2018). **E, G**

4) S. Sakaguchi, T. Sakurai, J. Ma, M. Sugimoto, T. Yamaki, A. Chiba, Y. Saito, S. Seki, "Conjugated Nanowire Sensors via High-Energy Single-Particle-Induced Linear Polymerization of 9,9'-Spirobi[9H-fluorene] Derivatives", J. Phys. Chem. B, **122**, 8614-8623 (2018). **C**

5) K. Kakitani, T. Kimata, T. Yamaki, S. Yamamoto, D. Matsumura, T. Taguchi, T. Terai, "X-ray Absorption Study of Platinum Nanoparticles on an Ion-Irradiated Carbon Support", Radiat. Phys. Chem., **153**, 152-155 (2018). **I, S**

6) T. Ogawa, T. Yamaki, T. Sato, "Analysis of Scintillation Light Intensity by Microscopic Radiation Transport Calculation and Förster Quenching Model", PLoS ONE, **13**(8), e0202011(2018). **C, E**

7) K. Kakitani, H. Koshikawa, T. Yamaki, S. Yamamoto, Y. Sato, M. Sugimoto, S. Sawada, "Preparation of Conductive Layer on Polyimide Ion-Track Membrane by Ar Ion Implantation", Surf. Coat. Technol., **355**, 181-185 (2018). **C, I, S**

8) K. Kakitani, T. Kimata, T. Yamaki, S. Yamamoto, T. Taguchi, T. Kobayashi, W. Mao, T. Terai, "The interface between platinum nanoparticle catalysts and an Ar+-irradiated carbon support", Surf. Coat. Technol., **355**, 259-263 (2018). **I, S**

9) A. Rednyk, T. Mori, S. Yamamoto, A. Suzuki, Y. Yamamoto, T. Tanji, N. Isaka, P. Kúš, S. Ito, F. Ye, "Design of Active Sites on Nickel in the Anode of Intermediate-Temperature Solid Oxide Fuel Cells using Trace Amount of Platinum Oxides", ChemPlusChem, **83**, 756-768 (2018). **S**

10) T. Taguchi, S. Yamamoto, H. Ohba, "Ion irradiation-induced novel microstructural change in silicon carbide nanotubes", Acta Materialia, **154**, 90-99 (2018). **I, S**

11) T. Yamaki, N. Nuryanthi, A. Kitamura, H. Koshikawa, S. Sawada, K. O. Voss, D. Severin, C. Trautmann, "Fluoropolymer-Based Nanostructured Membranes Created by Swift-Heavy-Ion Irradiation and Their Energy and Environmental Applications", Nucl. Instr. Meth. Phys. Res. B, **435**, 162-168 (2018). **C**

12) A. Horio, T. Sakurai, K. Kayama, G.B.V.S. Lakshmi, D. K. Avasthi, M. Sugimoto, T. Yamaki, A. Chiba, Y. Saito, S. Seki, "Remarkable effect of halogenation of aromatic compounds on efficiency of nanowire formation through polymerization/crosslinking by high-energy single particle irradiation", Radiat. Phys. Chem., **142**, 100-106 (2018). **C**

13) Y. Yang, M. Yoshida, A. Idesaki, T. Ogitsu, "Influence of gamma ray irradiation on thermal conductivity of bismaleimide-triazine-based insulation tape at cryogenic temperature", Cryogenics, **89**, 107-112 (2018). **G**

14) 寺井 隆幸, 垣谷 健太, 木全 哲也, 八巻 徹也, 山本 春也, 小林 知洋, "炭素担体のイオンビーム照射欠陥による白金ナ

ノ粒子触媒の高性能化", 「炭素材料科学の進展」日本学術振興会第117委員会 七十周年記念誌, 75-78, (2018). **I, S**

15) 山本 春也, "水素検知材料の開発", NLだより, **484**, 2 (2018). **S**

Proceedings

1) 出崎 亮, "量子ビームを利用した機能性セラミック材料の合成"【招待講演】, 第 58 回東海若手セラミスト懇話会 2019 年夏期セミナー, [愛知県西尾市] 招待講演 III (2019/03). **I, S**

2) S. Yamamoto, T. Taguchi, A. Miyashita, A. Idesaki, H. Koshikawa, T. Yamaki, T. Mori, "Electron-Beam-Induced Formation of Pt Nanoparticles on Ceria Films"【Invited Talk】, 28th Annual Meeting of MRS-J 2018, [Kitakushu City] B1-I19-010 (2018/12). **E, S**

3) 八巻 徹也, "量子局在構造を利用した革新的触媒の開発"【招待講演】, 量子生命科学研究会第2回学術集会, [東京大学・東京] 一般講演 2 (2018/05). **C, I, S, T**

4) A. Idesaki, M. Sugimoto, S. Yamamoto, T. Yamaki, "Effect of ion implantation on precursor polymer for synthesis of carbon material with catalytic performance", Proceedings of the 12th Pacific Rim Conference on Ceramic and Glass Technology, 264, 33-40, (2018). **I, S**

5) 出崎 亮, 越川 博, 岡崎 宏之, 山本 春也, 前川 康成, 八巻 徹也, "イオンビーム照射炭素担体／白金触媒の性能に及ぼすイオン照射条件の効果", 電気化学会第 86 回大会, [京都] 2B01 (2019/03). **I, S**

6) 山本 春也, 越川 博, 田口 富嗣, 出崎 亮, 岡崎 宏之, 前川 康成, 八巻 徹也, "放射線還元法により作製した Pt/CeO2 及び Pt/SnO2 の酸素還元活性", 電気化学会第 86 回大会, [京都] 2B03 (2019/03). **E, G**

7) 佐藤 裕真, 越川 博, 山本 春也, 杉本 雅樹, 澤田 真一, 八巻 徹也, 前川 康成, "イオン穿孔膜をテンプレートに用いた白金ナノコーンの作製とその電極触媒応用", 電気化学会第 86 回大会, [京都] 2F07 (2019/03). **C**

8) 岡崎 宏之, 出崎 亮, 越川 博, 松村 大樹, 山本 春也, 前川 康成, 八巻 徹也, "イオンビームによる炭素担体の格子欠陥を利用した Pt ナノ微粒子触媒の炭素吸収端スペクトル", 電気化学会第 86 回大会, [京都] 2B02 (2019/03). **I, S**

9) 石飛 宏和, 山本 春也, 石井 孝文, 大場 晃介, 土岐 帆乃佳, 中川 紳好, "電子線照射したレドックスフロー電池の電極材の特性", 電気化学会第 86 回大会, [京都] 1H05 (2019/03). **E, G**

10) 森 利之, 鈴木 彰, 大久保 弘, 伊坂 紀子, 山本 春也, 伊藤 滋啓, "微量 FeOx 又は MnOx を用いた中温域 SOFC 内高性能アノード材料の設計", 日本セラミックス協会 2019 年年会, [工学院大学・東京] 2J01 (2019/03). **S**

11) 伊藤 滋啓, 佐藤 史隆, 佐藤 貴哉, 森 利之, 鈴木 彰, 大久保 弘, 伊坂 紀子, 山本 春也, "混合伝導性助触媒添加による中温域 SOFC アノード活性サイト形成とアノード性能改善効果", 日本セラミックス協会 2019 年年会, [工学院大学・東京] 2J02 (2019/03). **S**

12) 大場 晃介, 石飛 宏和, 山本 春也, 中川 紳好, "KOH 賦活処理電極を用いたレドックスフロー電池の性能評価", 化学工学会第 84 年会, [芝浦工大・東京] PA159 (2019/03). **E, G**

13) 光吉 徹, 石飛 宏和, 中川 紳好, 越川 博, 山本 春也, 八巻 徹也, "TiO2 含有カーボンナノファイバー担体への量子ビーム照射の影響", 第 21 回化学工学会学生発表会, [東京] C27 (2019/03). **C**

14) 土岐 帆乃佳, 大場 晃介, 石飛 宏和, 山本 春也, 中川 紳好, "電子線照射電極によるバナジウムレドックスフロー電池の大電流化", 第 21 回化学工学会学生発表会, [東京] C09

15) 雨宮 邦招, 清水 雄平, 越川 博, 井邊 真俊, 八巻 徹也, 蔀 洋司, "あらゆる光をとらえて逃がさない黒い材料の開発", 産総研 2018 年度計量標準総合センター成果発表会, [つくば市] (2019/02). **C**

16) S. Sawada, M. Goto, H. Koshikawa, A. Kitamura, M. Higa, T. Yamaki, "Ionic resistance and water flux of nanostructured cation exchange membranes prepared by heavy-ion-track grafting technique", 28th Annual Meeting of MRS-J 2018, [Kitakyushu City] F8-O20-010 (2018/12). **C**

17) H. Koshikawa, Y. Sato, S. Yamamoto, M. Sugimoto, S. Sawada, T. Yamaki, "Preparation of Metal Oxide Nanocones Using Ion Track-Etched Membranes as Templates", 28th Annual Meeting of MRS-J 2018, [Kitakyushu City] D1-P19-012 (2018/12). **C**

18) A. Kitamura, T. Yamaki, Y. Yuri, H. Koshikawa, S. Sawada, T. Yuyama, "Fabrication of track-etched poly(vinylidene fluoride) membranes by uniform beam irradiation in an oxygen atmosphere", 28th Annual Meeting of MRS-J 2018, [Kitakyushu City] D1-P19-011 (2018/12). **C**

19) T. Taguchi, S. Yamamoto, H. Ohba, "Ion Irradiation-Induced Novel Microstructural Change in SiC Nanotubes", 28th Annual Meeting of MRS-J 2018, [Kitakyushu City] D1-P19-003 (2018/12). **G, E**

20) H. Okazaki, A. Idesaki, H. Koshikawa, D. Matsumura, S. Yamamoto, Y. Maekawa, T. Yamaki, "Catalyst Durability of Pt Nanoparticles on the Ar+ Irradiated Glassy Carbon", 28th Annual Meeting of MRS-J 2018, [Kitakyushu City] B1-O19-011 (2018/12). **I, S**

21) A. Kitamura, N. Ishikawa, K. Kondo, Y. Okuno, S. Yamamoto, T. Yamaki, "FE-SEM observations of multiple nanohillocks on SrTiO3 irradiated with swift heavy ions", 28th Annual Meeting of MRS-J 2018, [Kitakyushu City] D1-O18-009 (2018/12). **C**

22) S. Yamamoto, H. Koshikawa, Y. Sato, T. Taguchi, A. Idesaki, T. Yamaki, "FE-SEM observations of multiple nanohillocks on SrTiO3 irradiated with swift heavy ions", 28th Annual Meeting of MRS-J 2018, [Kitakyushu City] D1-P19-009 (2018/12). **C**

23) 出崎 亮, 山本 春也, 杉本 雅樹, 八巻 徹也, "カーボン前駆体高分子のグラファイト化に及ぼす金属イオン注入の影響", 第 45 回炭素材料学会年会, [名古屋工業大学・名古屋市] P47 (2018/12). **I, S**

24) K. Amemiya, H. Koshikawa, T. Yamaki, H. Shitomi, "Design and fabrication of novel broadband near-perfect black absorber having microstructured surface", APMP TCPR 2018: Workshop on research topics to enhance TCPR activities, National Metrology Centre (NMC), [Singapore] (2018/11). **C**

25) 越川 博, 佐藤 裕真, 山本 春也, 杉本 雅樹, 澤田 真一, 八巻 徹也, "イオン穿孔膜をテンプレートとした酸化チタンナノコーンの作製", 第 17 回放射線プロセスシンポジウム, [東京大学・東京] P4-3 (2018/11). **C**

26) 佐藤 裕真, 越川 博, 山本 春也, 杉本 雅樹, 澤田 真一, 八巻 徹也, "LET 制御による多彩な形状のイオン穿孔", 第 17 回放射線プロセスシンポジウム, [東京大学・東京] P4-4 (2018/11). **C**

27) 木全 哲也, 山本 春也, 八巻 徹也, 寺井 隆幸, 中村 一隆, "イオンビーム照射炭素表面を利用した白金触媒の作製", 2018 年日本表面真空学会学術講演会, [神戸] 2P60S (2018/11). **I, S**

28) A. Idesaki, Y. Kanuma, S. Yamamoto, M. Sugimoto, T. Yamaki, "Fabrication of graphitic nanostructure with catalytic activity from precursor polymer utilizing high temperature-electron beam

irradiation", 31st International Microprocesses and Nanotechnology Conference(MNC 2018), [Sapporo city] 16P-11-32 (2018/11). **E**

29) Y. Sato, H. Koshikawa, S. Yamamoto, M. Sugimoto, S. Sawada, T. Yamaki, "Preparation of ion-track nanopores with different profile: precise control of depth-energy deposition distribution", 31st International Microprocesses and Nanotechnology Conference(MNC 2018), [Sapporo city] 15P-7-44 (2018/11). **C**

30) S. Yamamoto, T. Taguchi, A. Idesaki, H. Koshikawa, T. Yamaki, "Electron Beam Induced Formation of Pt Nanoparticles on Oxide Films", 14th International Conference on Atomically Controlled Surfaces, Interfaces and Nanostructures (ACSIN-14), [Sendai city] 23P019 (2018/10). **E, C**

31) 山本 春也, 田口 富嗣, 越川 博, 佐藤 裕真, 出崎 亮, 八巻 徹也, "電子線還元法による円柱状ナノ空間内への Pt ナノ粒子形成", 2018 年電気化学秋季大会, 1I12 (2018/09). **C, E, G**

32) 柿沼 政貴, 阿部 壮真, 石飛 宏和, 越川 博, 山本 春也, 八巻 徹也, 中川 紳好, "セリア系担体へのイオンビーム照射による高活性電極触媒開発", 化学工学会第 50 回秋季大会, [鹿児島大学・鹿児島市] PB110 (2018/09). **C**

33) 喜多村 茜, 八巻 徹也, 百合 庸介, 越川 博, 澤田 真一, 湯山 貴裕, "酸素中での大面積均一ビーム照射によるフッ素系高分子のイオン穿孔膜作製技術", 日本金属学会 2018 年秋期講演大会, [仙台市] S6.9 (2018/09). **C**

34) 木全 哲也, 山本 春也, 八巻 徹也, 松村 大樹, 寺井 隆幸, 中村 一隆, "Ar イオン照射炭素担体を利用した燃料電池用 Pt 触媒の作製:量子ビームで創る・測る", 日本原子力学会 2018 年秋の大会, [岡山大学・岡山市] (2018/09). **I, S**

35) 出崎 亮, 山本 春也, 杉本 雅樹, 八巻 徹也, "イオン注入法を利用して前駆体高分子から合成した窒素含有カーボン触媒", 日本セラミックス協会第 31 回秋季シンポジウム, [名古屋工業大学・名古屋市] 1PK02 (2018/09). **I, S**

36) 大場 晃介, 山本 春也, 石飛 宏和, 土岐 帆乃佳, 越川 博, 八巻 徹也, 中川 紳好, "電子線照射カーボンクロスを用いたレドックスフロー電池の性能評価", 化学工学会室蘭大会 2018, [室蘭市] E124 (2018/08). **E**

37) S. Sawada, M. Goto, H. Koshikawa, A. Kitamura, M. Higa, T. Yamaki, "Ion and water transport properties of cation exchange membranes prepared by heavy-ion-track grafting technique", 5th International Conference on Methods and Materials for Separation Processes, [KUDOWA ZDRÓJ, Poland] 103 (2018/08). **C**

38) A. Kitamura, N. Ishikawa, K. Kondo, Y. Okuno, T. Yamaki, "FE-SEM Observation of Chains of Nano Hillocks on Oxide Ceramics Irradiated with SHI", 10th International Symposium on Swift Heavy Ions in Matter and 28th International Conference on Atomic Collisions in Solids (SHIM-ICACS 2018), [Caen Normandie, France] P1-T03-40 (2018/07). **C**

39) A. Kitamura, T. Yamaki, Y. Yuri, H. Koshikawa, S. Sawada, T. Yuyama, A. Chiba, A. Usui, "Control of the size of etchable ion tracks in PVDF irradiation in an oxygen atmosphere and with fullerene clusters", 10th International Symposium on Swift Heavy Ions in Matter and 28th International Conference on Atomic Collisions in Solids (SHIM-ICACS 2018), [Caen Normandie,

France] P2-T05-159 (2018/07). **C**

40) 八巻 徹也, 垣谷 健太, 木全 哲也, 山本 春也, 松村 大樹, 寺井 隆幸, "XAFS によるナノ粒子触媒／イオンビーム照射担体の界面構造解析", 立命館大学 SR センター成果報告会, [立命館大学・滋賀県草津市] S17010 (2018/06). **I**

41) 越川 博, 佐藤 裕真, 山本 春也, 杉本 雅樹, 澤田 真一, 八巻 徹也, 前川 康成, "イオン穿孔膜をテンプレートとした酸化チタンナノコーンの作製", 第 17 回放射線プロセスシンポジウム [東京大学 弥生キャンパス 弥生講堂, 東京] 要旨集, P4-3 (2018/11). **C**

42) 佐藤 裕真, 越川 博, 山本 春也, 杉本 雅樹, 澤田 真一, 八巻 徹也, 前川 康成, "LET 制御による多彩な形状のイオン穿孔", 第 17 回放射線プロセスシンポジウム [東京大学 弥生キャンパス 弥生講堂, 東京]要旨集, P4-4 (2018/11). **C**

43) 越川 博, 佐藤 裕真, 山本 春也, 杉本 雅樹, 澤田 真一, 八巻 徹也, 前川 康成, "Preparation of Metal Oxide Nanocones Using Ion Track-Etched Membranes as Templates", 第 28 回日本 MRS 年次大会 [北九州国際会議場, 北九州] 要旨集, D1-P19-012 (2018/12). **C**

44) 佐藤 裕真, 越川 博, 山本 春也, 杉本 雅樹, 澤田 真一, 八巻 徹也, "Preparation of Metal Oxide Nanocones Using Ion Track-Etched Membranes as Templates", 31st International Microprocesses and Nanotechnology Conference(MNC 2018) [札幌パークホテル, 札幌] 要旨集, 15P-7-44 (2018/12). **C**

45) 喜多村 茜, 八巻 徹也, 百合 庸介, 越川 博, 澤田 真一, 湯山 貴裕, 千葉 敦也, 薄井 絢, "Control of the size of etchable ion tracks in PVDF irradiation in an oxygen atmosphere and with fullerene clusters", 10th International Symposium on Swift Heavy Ions in Matter and 28th International Conference on Atomic Collisions in Solids (SHIM-ICACS 2018) [Université de Caen Normandie, Caen] 要旨集, P2-T05-159 (2018/12). **C**

Books

1) 尾崎 公洋, 杉本 諭, 岡崎 宏之, 他, "第 3 章 微細構造解析 第 1 節 放射光 X 線回折による磁石構成相の高温挙動解析", 次世代永久磁石の開発最前線, エヌ・ティー・エス, (2019). **N**

2) 比嘉 充, 吉川 直人, 垣花 百合子, 清野 竜太郎, 佐々木 貴明, 高橋 博, 谷口 育雄, 永谷 剛, 安川 政宏, 八巻 徹也, 吉江 清敬, "イオン交換膜の工業的利用第 3 集", イオン交換膜の工業的利用第 3 集(編集), 日本海水学会, (2018). **C**

Patents

1) 山本 春也, 越川 博, 八巻 徹也, "燃料電池用酸化触媒及びその製造方法並びに燃料電池", 出願 2018-163411 (2018/08/31). **E, G**

2) 村木 勇三, 越川 博, 八巻 徹也, 前川 康成, 百合 庸介, 湯山 貴裕, 石坂 知久, 石堀 郁夫, 吉田 健一, "多孔性高分子フィルムの製造方法および多孔性高分子フィルム", 登録 6478261 (2019/02/15). **C**

Press・TV

1) 小川 達彦, 八巻 徹也, 佐藤 達彦, "シンチレーション検出器の光出力を決める仕組みを解明 －加速器、宇宙、医療現場などの陽子や重粒子線の正確な計測に向けて－", 2018/8/29, プレス発表: OplusE ウェブ版, 日刊工業新聞, 日刊工業新聞 Web 版, 科学新聞に掲載. **N**

P1-3　Project "Positron Nanoscience"

Papers

1) E. Minagawa, T. Nakanishi, M. Maekawa, A. Kawasuso and H. Tsuchida, "Effect of beam flux on radiation damage accumulation in ion-bombarded Si", Jpn. J. Appl. Phys. Conf. Proc. **7**, 011101 (2018). **N**

2) K. Wada, T. Shirasawa, I. Mochizuki, M. fujinami, T. Takahashi.

M. Maekawa, A. Kawasuso, M. Kimura and T. Hyodo, "Progress report on construction of a low-energy positron diffraction (LEPD) experiment station at KEK", Jpn. J. Appl. Phys. Conf. Proc. **7**, 011301 (2018). **N**

3) Y. Fukaya, A. Kawasuso, A. Ichimiya, and T. Hyodo, "Total-reflection high-energy positron diffraction (TRHEPD) for structure determination of the topmost and immediate sub-surface atomic layers", J. Phys. D: Applied Physics, **52**, 013002-1-19 (2019). **N**

4) K. Wada, T. Shirasawa, I. Mochizuki, M. Fujinami, T. Takahashi, M. Maekawa, A. Kawasuso, M. Kimura and T. Hyodo, "Observation of low-energy positron diffraction patterns with a linac-based slow-positron beam", e-J. Surf. Sci. Nanotech. **16**, 313-319 (2018). **N**

5) A. Kawasuso, M. Maekawa, A. Miyashita, K. Wada, T. Kaiwa and Y. Nagashima, "Positronium formation at Si surfaces", Phys. Rev. B **97**, 245303-1-8 (2018). **N**

6) K. Wada, A. Miyashita, M. Maekawa, S. Sakai and A. Kawasuso, "Spin-Polarized Positron Beams with ^{22}Na and ^{68}Ge and Their Applications to Materials Research", AIP Conf. Proc. **1970**, 040001-1-8 (2018). **N**

7) M. Maekawa, S. Sakai, A. Miyashita, A. Kawasuso, "Spin-polarized positron annihilation measurement on Ga vacancies in p-type GaN", e-J. Surf. Sci. Nanotech. **16**, 347-350 (2018). **N**

8) A. Miyashita, M. Maekawa, K. Wada, A. Kawasuso, T. Watanabe, S. Entani and S. Sakai, "Spin polarization of graphene and h-BN on Co(0001) and Ni(111) observed by spin-polarized surface positronium spectroscopy", Phys. Rev. B **97**, 195405-1-5 (2018). **N**

Proceedings

1) T. Hyodo, K. Wada, M. Masaki, I. Mochizuki, A. Kawasuso and M. Kimura, "Pulse Stretching System for Materials at KEK Slow Positron Facility", The 4th Symposium on Innovative measurement and analysis for structural materials (SIP-IMASM 2018), Tokyo, Japan (2018/11). **N**

2) S. Hagiwara and A. Kawasuso, "Theoretical study on positronium formation at metal surfaces based on two-component density functional theory", The 21st Asian Workshop on First-Principles Electronic Structure Calculations, Korea (2018/10). **N**

3) K. Wada, T. Shirasawa, I. Mochizuki, M. Fujinami, M. Maekawa, A. Kawasuso, T. Takahashi and T. Hyodo, "Observation of Low-Energy Positron Diffraction (LEPD) Patterns and LEPD I-V Characteristics", 14th International Conference on Atomically Controlled Surfaces, Interfaces and Nanostructures (ACSIN-14), Sendai, Japan (2018/11). **N**

4) M. Maekawa, S. Sakai, K. Wada, A. Miyashita, S. Hagiwara, A. Kawasuso, A. Yabuuchi and S. Hasegawa, "Magnetic Doppler Broadening Measurement on Gadolinium-doped GaN", 18th International Conference on Positron Annihilation (ICPA-18), Orland, USA (2018/08). **I, 3-04**

5) A. Kawasuso, M. Maekawa, K. Wada, A. Miyashita and S. Hagiwara, "Spin Detection with Positron and Positronium (Invited)", 18th International Conference on Positron Annihilation (ICPA-18), Orland, USA (2018/08). **N**

6) K. Wada, T. Shirasawa, I. Mochizuki, M. Fujinami, M. Maekawa, A. Kawasuso, T. Takahashi and T. Hyodo, "Observation of low-energy positron diffraction with a linac-based slow-positron beam and its applications as tool for surface structural analysis", 18th International Conference on Positron Annihilation (ICPA-18), Orland, USA (2018/08). **N**

7) 和田 健, 白澤 徹朗, 望月 出海, 藤浪 真紀, 前川 雅樹, 河裾 厚男, 高橋 敏男, 兵頭 俊夫, "加速器ベース低速陽電子ビームを用いた低速陽電子回折実験装置の開発 II", 日本物理学会 第 74 回年次大会 (2019/03). **N**

8) 萩原 聡, 河裾 厚男, "二成分密度汎関数法による金属表面におけるポジトロニウムエネルギースペクトルの理論研究", 日本物理学会 第 74 回年次大会 (2019/03). **N**

9) 河裾 厚男, 宮下 敦巳, 前川 雅樹, 和田 健, 萩原 聡, 李 松田, 圓谷 志郎, 境 誠司, "スピン偏極陽電子ビームによるグラフェン/強磁性薄膜のスピン偏極の検出", 日本物理学会 第 74 回年次大会 (2019/03). **N**

10) 前川 雅樹, 和田 健, 宮下 敦巳, 萩原 聡, 河裾 厚男, 境 誠司, "スピン偏極陽電子ビームを用いた金属酸化物・窒化物の空孔誘起磁性検出", 日本物理学会 第 74 回年次大会 (2019/03). **I, 3-04**

11) 薮内 敦, 唐津 拓弥, 木野村 淳, 前川 雅樹, 河裾 厚男, "イオンビーム合成法で作製した β-FeSi2 膜中の空孔型欠陥評価", 第 66 回応用物理学会春季学術講演会 (2019/03). **N**

12) 和田 健, "低速陽電子回折法の特徴と新規開発装置によるイニシャルデータの解析", 第 66 回応用物理学会春季学術講演会シンポジウム「陽電子回折による表面科学の新展開と高速化データ駆動科学」(2019/03). **N**

13) 兵頭 俊夫, 和田 健, 白澤 徹朗, 望月 出海, 藤浪 真紀, 前川 雅樹, 河裾 厚男, 高橋 敏男, "低速陽電子回折法による表面構造解析", 2018 年度量子ビームサイエンスフェスタ (2019/03). **N**

14) 萩原 聡, 前川 雅樹, 河裾 厚男, 飯田 進平, 長嶋 泰之, "二成分密度汎関数法によるポジトロニウムエネルギースペクトルの理論的研究", 平成 30 年度京都大学複合原子力科学研究所専門研究会「陽電子科学とその理工学への応用」(2018/12). **N**

15) 前川 雅樹, 和田 健, 宮下 敦巳, 萩原 聡, 河裾 厚男, "スピン偏極ポジトロニウム飛行時間測定装置の開発", 平成 30 年度京都大学複合原子力科学研究所専門研究会「陽電子科学とその理工学への応用」(2018/12). **N**

16) 和田 健, 白澤 徹郎, 望月 出海, 藤浪 真紀, 前川 雅樹, 河裾 厚男, 高橋 敏男, 兵頭 俊夫, "低速陽電子回折実験装置の開発 II", 平成 30 年度京都大学複合原子力科学研究所専門研究会「陽電子科学とその理工学への応用」(2018/12). **N**

17) 河裾 厚男, 和田 健, 前川 雅樹, 宮下 敦巳, 萩原 聡, 岩森 大直, 海和 俊亮, 長嶋 泰之, "単結晶 4H-SiC 表面におけるポジトロニウム生成", 平成 30 年度京都大学複合原子力科学研究所専門研究会「陽電子科学とその理工学への応用」(2018/12). **N**

18) 三木 一司, 河裾 厚男, 前川 雅樹, 田尻 寛男, 八方 直久, Ang Artoni Kevin Roquero, 林 好一, "Si 結晶中への Bi のイオン注入ドーピング", 2018 年第 79 回応用物理学会秋季学術講演会 (2018/09). **I, 1-13**

19) 前川 雅樹, 境 誠司, 和田 健, 宮下 敦巳, 萩原 聡, 河裾 厚男, 薮内 敦, 長谷川 繁彦, "スピン偏極陽電子ビームを用いたガドリニウム添加窒化ガリウム薄膜の空孔誘起磁性検出", 日本物理学会 2018 秋季大会 (2018/09). **I, 3-04**

20) 前川 雅樹, 和田 健, 宮下 敦巳, 河裾 厚男, "表面ポジトロニウム飛行時間測定装置の開発", 第 55 回アイソトープ・放射線研究発表会 (2018/07). **N**

21) 和田 健, 白澤 徹朗, 望月 出海, 藤浪 真紀, 前川 雅樹, 河裾 厚男, 高橋 敏男, 兵頭 俊夫, "Ge(001)-2x1 表面からの低速陽電子回折図形の観測", 第 55 回アイソトープ・放射

線研究発表会 (2018/07).　　　　　　　　　　　　**N**

22) 河裾 厚男, 前川 雅樹, 和田 健, 宮下 敦巳, 長嶋 泰之, 海和 俊亮, "シリコン表面におけるポジトロニウム生成", 第 55 回アイソトープ・放射線研究発表会 (2018/07).　　**N**

23) 和田 健, 白澤 徹朗, 望月 出海, 藤浪 真紀, 前川 雅樹, 河裾 厚男, 高橋 敏男, 兵頭 俊夫, "Ge(001)-2x1 表面における低速陽電子回折パターンの観測", 日本表面科学会第3回関東支部講演大会 (2018/04).　　　　　　**N**

24) 和田 健, 白澤 徹朗, 望月 出海, 藤浪 真紀, 前川 雅樹, 河裾 厚男, 高橋 敏男, 兵頭 俊夫, "低速陽電子回折(LEPD)による表面ホログラフィ実験の進捗状況", 第 2 回陽電子回折研究会 (2018/03).　　　　　　　**N**

25) 前川 雅樹, 境 誠司, 宮下 敦巳, 和田 健, 河裾 厚男, "スピン偏極陽電子ビームによる窒化ガリウム薄膜の空孔誘起磁性評価", 日本物理学会第 73 回年次大会(2018 年)

(2018/03).　　　　　　　　　　　　　**I, 3-04**

26) 河裾 厚男, 前川 雅樹, 和田 健, 宮下 敦巳, 渡邉 貴弘, 圓谷 志郎, 境 誠司, "スピン偏極陽電子ビームによるグラフェン・窒化ホウ素/強磁性薄膜のスピン偏極の検出", 日本物理学会第 73 回年次大会(2018 年) (2018/03).　　**N**

27) 薮内 敦, 木野村 淳, 前川 雅樹, 河裾 厚男, "イオンビーム合成法で作製した β-FeSi2 膜の低速陽電子ビームによる評価", 第 65 回応用物理学会 春季学術講演会 (2018/03).　**N**

28) 兵頭 俊夫, 和田 健, 白澤 徹朗, 望月 出海, 藤浪 真紀, 前川 雅樹, 河裾 厚男, 高橋 敏男, "低速陽電子回折法による表面構造解析", 平成 29 年度 KEK 量子ビームサイエンスフェスタ (2018/03).　　　　　　　　　**N**

29) 河裾 厚男, "陽電子を利用した表面・スピントロニクス材料の研究", 第 6 回先進的放射光メスバウアー分光研究会 (2018/03).　　　　　　　　　　　**N**

P1-4　Project "Spintronics in Two-dimensional Materials"

Papers

1) D. G. Kvashnin, A. G. Kvashnin, E. Kano, A. Hashimoto, M. Takeguchi, H. Naramoto, S. Sakai, P. B. Sorokin, "Two-Dimensional CuO Inside the Supportive Bilayer Graphene Matrix", J. Phys. Chem. C **123**, 17459-17465 (2019).　　**N**

2) S. Entani, M. Takizawa, S. Li, H. Naramoto, S. Sakai, "Growth of graphene on SiO2 with hexagonal boron nitride buffer layer", Appl. Surf. Sci. **475**, 6-11 (2019).　　　**N**

3) S. Li, Y. Sakuraba, T. Sasaki, S. Bosu, K. Hono, "Enhanced current-perpendicular-to-plane giant magnetoresistance by improvement of atomic order of Co2FeSi Heusler alloy film through Ag doping", AIP Adv. **8**, 075230 (2018).　　**N**

4) M. Maekawa, S. Sakai, A. Miyashita, A. Kawasuso, "Spin-polarized positron annihilation measurement on Ga vacancies in p-type GaN", e-J. Surf. Sci. Nanotech. **16**, 347-350 (2018).　　　　　　　　　　　　　　　　　　**N**

5) K. Takaoka, K. Mitsuhara, M. Takizawa, S. Entani, S. Sakai, "Chemical and electronic state analysis of oxidizing graphene", e-J. Surf. Sci. Nanotech. **16**, 320-323 (2018).　　**N**

6) A. Miyashita, M. Maekawa, K. Wada, A. Kawasuso, T. Watanabe, S. Entani, S. Sakai, "Spin polarization of graphene and h-BN on Co(0001) and Ni(111) observed by spin-polarized surface positronium spectroscopy", Phys. Rev. B **97**, 195405 (2018).　　　　　　　　　　　　　　　**N**

7) S. Sakai, S. V. Erohin, Z. I. Popov, S. Haku, T. Watanabe, Y. Yamada, S. Entani, S. Li, P. V. Avramov, H. Naramoto, K. Ando, P. B. Sorokin, Y. Yamauchi, "Dirac Cone Spin Polarization of Graphene by Magnetic Insulator Proximity Effect Probed with Outermost Surface Spin Spectroscopy", Adv. Funct. Mater. **28**, 1800462 (2018).　　**N**

Proceedings

1) K. Wada, A. Miyashita, M. Maekawa, S. Sakai and A. Kawasuso, "Spin-Polarized Positron Beams with ²²Na and ⁶⁸Ge and Their Applications to Materials Research", AIP Conf. Proc. 1970, 040001 (2018). International workshop on physics with positrons at Jefferson lab (JPos17) [Newport News, USA].　　**N**

Patents

1) 中島 悟, 長谷川 浩太, 境 誠司, 圓谷 志郎, "垂直磁気記録媒体の製造方法及び磁気記録再生装置", 登録 6485866 (2019/03/01).　　　　　　　　　　　**N**

2) 中島 悟, 長谷川 浩太, 境 誠司, 圓谷 志郎, "垂直磁気記録媒体及び磁気記録再生装置", 登録 6485867 (2019/03/01).　　　　　　　　　　　**N**

3) 中島 悟, 長谷川 浩太, 圓谷 志郎, 境 誠司, "垂直磁気記録媒体及び磁気記録再生装置 (2)", 登録 6485868 (2019/03/01).　　　　　　　　　　**N**

Press・TV

1) "磁性絶縁体を用いてグラフェンのスピンの向きを制御 ─スピントランジスタの実現に向け前進─", 2018/04/04, プレス発表:日本経済産業新聞等に掲載.　　　　**N**

P1-5　Project "Semiconductor Radiation Effects"

Papers

1) N. B. Manson, M. Hedges, M. S. J. Barson, R. Ahlefeldt, M. W. Doherty, H. Abe, T. Ohshima and M. J. Sellars, "NV⁻-NV⁺ pair centre in 1b diamond", New J. Phys., **20**, 113037 (2018).　**E**

2) E. Mizuta, S. Kuboyama, Y. Nakada, A. Takeyama, T. Ohshima, Y. Iwata and K. Suzuki, "Single-event damage observed in GaN-on-Si HEMTs for power control applications", IEEE Trans. Nucl. Sci., **65**, 1956-1963 (2018).　　　　　　　**C**

3) D. Kobayashi, K. Hirose, T. Ito, Y. Kakehashi, O. Kawasaki, T. Makino, T. Ohshima, D. Matsuura, T. Narita, M. Kato, S. Ishii, and K. Masukawa, "Heavy-ion soft error in back-biased thin-BOX SOI SRAMs: hundredfold sensitivity due to line-type multicell upsets", IEEE Trans. Nucl. Sci., **65**, 523-532 (2018).　　**C**

4) Y. Shibata, M. Imaizumi, S.-I. Sato, T. Ohshima, M. Akiyoshi and S. Okuda, "Recovery from radiation-induced degradation in InGaP solar cells by light soaking", Appl. Phys. Express, **11**, 122301-1-4 (2018).　　　　　　　　　　**E**

5) J. Barbé, H. K. H. Lee, H. Toyota, K. Hirose, S.-I. Sato, T. Ohshima, K. C. Heasman and W. C. Tsoi, "Characterization of stability of benchmark organic photovoltaic films after proton and electron bombardments", Appl. Phys. Lett., **113**, 183301-1-5 (2018).　　　　　　　　　　　　　**I, E**

6) T. Sumita, Y. Shibata, T. Nakamura, K. Shimazaki, A. Kukita, M. Imaizumi, S.-I Sato, T. Ohshima and T. Takamoto, "Flight demonstration of inverted metamorphic triple-junction solar cells in space", Jpn. J. Appl. Phys., **57**, 08RD01-1-5 (2018).　　**T, I, E**

7) S.-I Sato, T. Honda, T. Makino, Y. Hijikata, S.-Y. Lee and T. Ohshima, "Room temperature electrical control of single photon sources at 4H-SiC surface", ACS Photonics, **5**, 3159-3165 (2018). **I**

8) M. D. Haque, N. Kamata, S.-I. Sato and S. M. Hubbard, "Characterization of nonradiative recombination centers in proton-irradiated InAs/GaAs quantum dots by two-wavelength-excited photoluminescence", Jpn. J. Appl. Phys., **57**, 092302-1-6 (2018). **N**

9) I. Capan, T. Brodar, T. Ohshima, S.-I. Sato, T. Makino, Ž. Pastuović, R. Siegele, L. Snoj, V. Radulović, J. Coutinho, V. J. B. Torres and K. Demmouche, "Deep level defects in 4H-SiC epitaxial layers," Mater. Sci. Forum, **924**, 225-228 (2018). **I**

10) H. Tsunemi, T. Honda, T. Makino, S. Onoda, S.-I. Sato, Y. Hijikata and T. Ohshima, "Various single photon sources observed in SiC pin diodes", Mater. Sci. Forum, **924**, 204-207 (2018). **I**

11) Y. Abe, T. Umeda, M. Okamoto, S. Onoda, M. Haruyama, W. Kada, O. Hanaizumi, R. Kosugi, S. Harada and T. Ohshima, "Oxidation-process dependence of single photon sources embedded in 4H-SiC MOSFETs", Mater. Sci. Forum, **924**, 281-284 (2018). **N**

12) J. Kajihara, S.-I. Kuroki, S. Ishikawa, T. Maeda, H. Sezaki, T. Makino, T. Ohshima, M. Östling, C.-M. Zetterling, "4H-SiC pMOSFETs with Al-doped S/D and NbNi silicide ohmic contacts", Mater. Sci. Forum, **924**, 423-427 (2018). **N**

13) V. Ivády, J. Davidsson, N. T. Son, T. Ohshima, I. A. Abrikosov, A. Gali, "Ab initio theory of Si-vacancy quantum bits in 4H and 6H-SiC", Mater. Sci. Forum, **924**, 895-900 (2018). **N**

14) T. Kurose, S.-I. Kuroki, S. Ishikawa, T. Maeda, H. Sezaki, T. Makino, M. Östling, C.-M. Zetterling, "Low-parasitic-capacitance self-aligned 4H-SiC nMOSFETs for Harsh Environment Electronics", Mater. Sci. Forum, **924**, 971-974 (2018). **G**

15) J. Ball, Y. Yamashiro, H. Sumiya, S. Onoda, T. Ohshima, J. Isoya, D. Konstantinov, and Y. Kubo, "Loop-gap microwave resonator for hybrid quantum systems", Appl. Phys. Lett., **112**, 204102(1-5) (2018). **E**

16) G. Kucsko, S. Choi, J. Choi, P. Maurer, H. Zhou, R. Landig, H. Sumiya, S. Onoda, J. Isoya, F. Jelezko, E. Demler, N. Yao, and M. Lukin, "Critical thermalization of a disordered dipolar spin system in diamond", Phys. Rev. Lett., **121**, 023601-1-5 (2018). **E**

17) N. Oi, M. Inaba, S. Okubo, I. Tsuyuzaki, T. Kageura, S. Onoda, A. Hiraiwa, and H. Kawarada, "Vertical-type two-dimensional hole gas diamond metal oxide semiconductor field-effect transistors", Scientific Reports, **8**, 10660-1-10 (2018). **T**

18) D. Duan, V. Kavatamane, S. Arumugam, G. Rahane, Y. Tzeng, H. Chang, H. Sumiya, S. Onoda, J. Isoya, and G. Balasubramanian, "Enhancing fluorescence excitation and collection from the nitrogen-vacancy center in diamond through a micro-concave mirror", Appl. Phys. Lett., **113**, 041107-1-5 (2018). **E**

19) R. Fukuda, P. Balasubramanian, I. Higashimata, G. Koike, T. Okada, R. Kagami, T. Teraji, S. Onoda, M. Haruyama, K. Yamada, M. Inaba, H. Yamano, F. Stürner, S. Schmitt, L.McGuinness, F. Jelezko, T. Ohshima, T. Shinada, H. Kawarada, W. Kada, O. Hanaizumi, T. Tanii, and J.Isoya, "Lithographically engineered shallow nitrogen-vacancy centers in diamond for external nuclear spin sensing", New Jour. Phys. **20**, 083029-1-9 (2018). **I**

20) A. Angerer, K. Streltsov, T. Astner, S. Putz, H. Sumiya, S. Onoda, W. Munro, K. Nemoto, J. Schmiedmayer, and J. Majer, "Superradiant emission from colour centres in diamond", Nat. Phys., **14**, 1168-1172 (2018). **E**

21) K. Hayashi, Y. Matsuzaki, T. Taniguchi, T. Shimo-Oka, I. Nakamura, S. Onoda, T. Ohshima, H. Morishita, M. Fujiwara, S. Saito, and N. Mizuochi, "Optimization of temperature sensitivity using the optically detected magnetic-resonance spectrum of a nitrogen-vacancy center ensemble", Phys. Rev. Appl., **10**, 034009-1-8 (2018). **E**

22) M. Haruyama, Y. Suda, W. Kada, S. Onoda, T. Ohshima, K. Miura, and O. Hanaizumi, "Fabrication of two-dimensional arrays of fluorescent centers in single-crystalline diamond using particle beam writing", Key Eng. Mat., **790**, 48-54 (2018). **T**

23) Y. Hijikata, T. Horii, Y. Furukawa, Y. Matsushita, T. Ohshima, "Oxygen-incorporated single-photon sources observed at the surface of silicon carbide crystals", J. Phys. Commun., **2**, 111003-1-7 (2018). **N**

24) B. Magnusson, N. T. Son, A. Csóré, A. Gällström, T. Ohshima, A. Gali, I. G. Ivanov, "Excitation properties of the divacancy in 4H-SiC", Phys. Rev. B, **98**, 195202-1-15 (2018). **E**

25) T. Brodar, I. Capan, V. Radulović, L. Snoj, Ž. Pastuović, J. Coutinho, T. Ohshima, "Laplace DLTS study of deep defects created in neutron-irradiated n-type 4H-SiC", Nuclear Inst. Methods B, **437**, 27-31 (2018). **N**

26) Y. Matsushita, Y. Furukawa, Y. Hijikata, T. Ohshima, "First-principles study of oxygen-related defects on 4H-SiC surface: The effects of surface amorphous structure", Appl. Surf. Sci. **464**, 451-454 (2019). **N**

27) F. Stürner, A. Brenneis, J. Kassel, U. Wostradowski, R. Rölver, T. Fuchs, K. Nakamura, H. Sumiya, S. Onoda, J. Isoya, and F. Jelezko, "Compact integrated magnetometer based on nitrogen-vacancy centres in diamond", Diam. Rel. Mater., **93**, 59-65 (2019). **E**

28) J. Choi, H. Zhou, S. Choi, R. Landig, W. Ho, J. Isoya, F. Jelezko, S. Onoda, H. Sumiya, D. Abanin, and M. Lukin, "Probing quantum thermalization of a disordered dipolar spin ensemble with discrete time-crystalline order", Phys. Rev. Lett., **122**, 043603-1-6 (2019). **E**

29) S. Kawai, H. Yamano, T. Sonoda, K. Kato, J. Buendia, T. Kageura, R. Fukuda, T. Okada, T. Tanii, T. Higuchi, M. Haruyama, K. Yamada, S. Onoda, T. Ohshima, W. Kada, O. Hanaizumi, A. Stacey, T. Teraji, S. Kono, J. Isoya, and H. Kawarada, "Nitrogen-terminated diamond surface for nanoscale NMR by shallow nitrogen-vacancy centers", Phys. Chem. C, **123**, 3594-3604 (2019). **I**

30) D. Kobayashi, N. Hayashi, K. Hirose, Y. Kakehashi, O. Kawasaki, T. Makino, T. Ohshima, D. Matsuura, Y. Mori, M. Kusano, T. Narita, S. Ishii, and K. Masukawa, "Process variation aware analysis of SRAM SEU cross section using data retention voltage", IEEE Trans. Nucl. Sci., **66**, 155-162 (2019). **C**

31) J. Davidsson, V. Ivady, R. Armiento, T. Ohshima, N. T. Son, A. Gali, I. A. Abrikosov, "Identification of divacancy and silicon vacancy qubits in 6H-SiC", Appl. Phys. Lett., **114**, 112107-1-5 (2019). **E**

32) N. T. Son, P. Stenberg, V. Jokubavicius, T. Ohshima, J. U. Hassan, I. G Ivanov, "Ligand hyperfine interactions at silicon vacancies in 4H-SiC", J. Phys.: Condens. Matter, **31**, 195501-1-8 (2019). **E**

33) M. Capelli, A.H. Heffernan, T. Ohshima, H. Abe, J. Jeske, A. Hope, A. D. Greentree, P. Reineck, B. C. Gibson, "Increased nitrogen-vacancy centre creation yield in diamond through electron beam irradiation at high temperature", Carbon **143**, 714-719 (2019).

E, 1-01

34) Y. Masuyama, K. Mizuno, H. Ozawa, H. Ishiwata, Y. Hatano, T. Ohshima, T. Iwasaki, M. Hatano, "Extending coherence time of macro-scale diamond magnetometer by dynamical decoupling with coplanar waveguide resonator", Rev. Sci. Instrum. **89**, 125007-1-5 (2018). **E, 1-01**

35) K. Hayashi, Y. Matsuzaki, T. Taniguchi, T. Shimo-Oka, I. Nakamura, S. Onoda, T. Ohshima, H. Morishita, M. Fujiwara, S. Saito, N. Mizuochi, "Optimization of Temperature Sensitivity Using the Optically Detected Magnetic-Resonance Spectrum of a Nitrogen-Vacancy Center Ensemble", Phys. Rev. Appl. **10**, 034009-1-8 (2018). **E, 1-01**

36) Y. Yamazaki, Y. Chiba, T. Makino, S. -I. Sato, N. Yamada, T. Satoh, Y. Hijikata, K. Kojima, S.-Y. Lee, T. Ohshima, "Electrically controllable position-controlled color centers created in SiC pn junction diode by proton beam writing", J. Mater. Res. **33**, 3355-3361 (2018). [Invited Feature Paper]. **I, S, 1-01**

37) T. Ohshima, T. Satoh, H. Kraus, G. V. Astakhov, V. Dyakonov and P. G. Baranov, "Creation of Silicon Vacancy in Silicon Carbide by Proton Beam Writing toward Quantum Sensing Applications", J. Phys. D: Appl. Phys. **51**, 333002-1-14 (2018). [Topical Review], **E, I, S, 1-01**

38) S.-i. Sato, T. Honda, T. Makino, Y. Hijikata, S.-Y. Lee, T. Ohshima, "Room Temperature Electrical Control of Single Photon Sources at 4H-SiC Surface", ACS Photonics **5**, 3159-3165 (2018). **I, 1-01**

39) Y. Shibata, M. Imaizumi, S-I Sato, T. Ohshima, M. Akiyoshi and S. Okuda, "Recovery from radiation-induced degradation in InGaP solar cells by light soaking", Appl. Phys. Express, Volume **11**, Number 12. **C, T, I, E, 1-02**

40) S. Kuboyama, E. Mizuta, Y. Nakada, H. Shindo, "Physical Analysis of Damage Sites Introduced by SEGR in Silicon Vertical Power MOSFETs and Implications for Postirradiation Gate-Stress Test", IEEE Trans. Nucl. Sci., Vol. **66**, No. 7, 1710-1714 (2019). **C, 1-03**

41) K. Takeuchi, T. Sakamoto, M. Tada, A. Takeyama, T. Ohshima, S. Kuboyama and H. Shindo, "Single-Event Effects Induced on Atom Switch-based Field-Programmable Gate Array", IEEE Trans. Nucl. Sci., Vol. **66**, No. 7, 1355-1360 (2019). **C, 1-03**

Proceedings

1) M. Haruyama, Y. Suda, W. Kada, S. Onoda, T. Ohshima, K. Miura, O. Hanaizumi, "Fabrication of Two-Dimensional Arrays of Fluorescent Centers in Single-Crystalline Diamond Using Particle Beam Writing", Key Engineering Mater. 790, 48-54 (2018). **S, T, 1-01**

2) T. Nakamura, L. Zhu, M. Yoshita, M. Imaizumi, H. Akiyama and Y. Okada, "Quantitative loss analysis of voltage output characteristics on multi-junction solar cells", Proc. of 2018 IEEE 7th World Conference on Photovoltaic Energy Conversion (Waikoloa Village, HI), 0921. **T, I, 1-02**

3) Y. Shibata, M. Imaizumi, S.-I Sato, T. Ohshima, M. Akiyoshi and S. Okuda, "Recovery of Radiation Degradation in InGaP Solar Cells by Light Soaking", Proc. of 2018 IEEE 7th World Conference on Photovoltaic Energy Conversion (Waikoloa Village, HI), 1576. **E, 1-02**

4) K. Takeuchi, T. Sakamoto, M. Tada, A. Takeyama, T. Ohshima, S. Kuboyama, H. Shindo, "Single event effects induced on atom switch based field programmable gate array", Radiation Effects on Components and Systems (RADECS) 2018 Proceedings, [Goteborg, Sweden], (2018). **C, 1-03**

Patent

1) 小野田 忍, 春山 盛善, 大島 武, 千葉 敦也, 平野 貴美, 五十嵐 龍治, "ダイヤモンド単結晶およびその製造方法", 出願 特願2018-155987 (2018/08/23). **T**

Press・TV

1) "超ミクロな磁場が測れる ダイヤモンドセンサー", 2019/02/24 (再放送 2019/03/02), NHK サイエンス ZERO. **E**

P1-6　Project "Biocompatible Materials"

Papers

1) T. G. Oyama, B. J. D. Barba, Y. Hosaka and M. Taguchi, "Single-step fabrication of polydimethylsiloxane microwell arrays with long-lasting hydrophilic inner surfaces", Appl. Phys. Lett. **112**, 213704 (2018). **E**

2) Y. Hosaka, T. Kondoh, T. G. Oyama, T. Uchida, M. Taguchi, Y. Yoshida and M. Washio, "Study on Electron-beam-induced Reactions of Methyl α-Allyloxymethyl Acrylic Polymer", J. Photopolym. Sci. Tech., **31**, 85-90 (2018). **E**

3) A. Kimura, N. Matsufuji, A. Hiroki, H. Seito, M. Taguchi, "Development of High-sensitivity Intra-corporeal Catheter-type Liquid Dosimeter for Radiotherapy", Biomedical Phys. & Eng. Express, **4**, 055005 (2018). **G, 1-18**

4) H. Kudo, M. Fukunaga, K. Shotsuki, H. Takeda H. Yamamoto, and T. Kozawa, "Synthesis of hyperbranched polyacetals containing C-(4-t-butylbenz)calix[4]resorcinarene: Resist properties for extreme ultraviolet (EUV) lithography", Reactive and Functional Polym., **131**, 361 (2018). **N**

5) H. Kudo, S. Ohori, H. Ogawa, H. Yamamoto, T. Kozawa, "Synthesis and Property of Tannic Acid Derivatives and Their Application for Extreme Ultraviolet Lithography System", The Society of Photopolym. Sci. and Tech., **31**, 221-225 (2018). **N**

6) M. Koshimizu, S. Kurashima, A. Kimura, M. Taguchi, T. Yanagida, H. Yagi, T. Yanagitani, Y. Fujimoto, K. Asai, "Effect of linear energy transfer on the scintillation Properties of Ce:Gd$_3$Al$_2$Ga$_3$O$_{12}$", Nucl. Intr. Meth. B **460**, 74-79, (2019). **C**

7) A. Kimura, N. Nagasawa and M. Taguchi, "Synthesis of polysaccharide hybrid gel in ionic liquids via radiation-induced crosslinking", Polym. Degrad. Stab., **159**, 133-138 (2019). **G, 1-18**

8) H. Yamamoto, Y. Vesters, J. Jiang, D. De Simone, G. Vandenberghe, and T. Kozawa, "Role of Metal Sensitizers for Sensitivity Improvement in EUV Chemically Amplified Resist", J. Photopolym. Sci. Technol., **31**(6), 747-751 (2018). **N**

9) Y. Vesters, J. Jiang, H. Yamamoto, D. De Simone, T. Kozawa, S. De Gendt, and G. Vandenberghe, "Sensitizers in EUV chemically amplified resist: Mechanism of sensitivity improvement", J. Micro/Nanolith. MEMS MOEMS, **17**, 043506-1 043506-8 (2018). **N**

Book

1) 山本 洋揮, 「量子ビームによる金属ナノ粒子を含有した微細パターンの直接形成」, RadTech Japan NEWS LETTER, 111, 3-6 (2018). **N**

Patents

1) 大山 智子, 田口 光正, Barba Bin Jeremiah Duenas, 木下 忍, 井出 崇, "試験用基材、及び試験用基材の製造方法",

PCT/JP2018/019084 (2018/05/17). **G, E**

2) 杉本 正樹, 長澤 尚胤, 田口 光正, "耐熱耐放射線性エラストマー材料の製造方法"ノウハウ契約, 整理番号 K20018（2018/06/01）. **G, E**

3) 大山 智子, 田口 光正, 小沢 幸雄, 小谷 卓司, 山田 高史, "接合体とその接合方法及びマイクロ流体デバイスとその製造

方法", 特願 2019-056376 (2019/03/25). **G, E**

Press・TV

1) 細胞をつかまえる小さな「水たまり」を開発 ―細胞を1つ1つ捕捉・培養する先端医療用デバイスの実現へ― プレス発表 (2018/05/28). **E**

P1-7 Project "Environmental Polymer"

Papers

1) J. F. Madrid, Y. Ueki, L. V. Abad, T. Yamanobe and N. Seko, "Enhanced amination and adsorption performance of functional copolymer synthesized via RAFT-mediated radiation grafting in emulsion", J. Polym. Res., **25**, 193(1)–193(11) (2018). **E, 1-19**

2) T. Hamada, S. Yamashita, M. Omichi, K. Yoshimura, Y. Ueki, N. Seko and R. Kakuchi, "Multicomponent-Reaction-Ready Biomass-Sourced Organic Hybrids Fabricated via the Surface Immobilization of Polymers with Lignin-Based Compounds", ACS sustainable Chem. Eng., **7**(8), 7795–7803 (2019), **G, 1-21**

3) N. Hayashi, J. Chen and N. Seko, "Nitrogen-Containing Fabric Adsorbents Prepared by Radiation Grafting for Removal of Chromium from Wastewater", Polymers, **10**, 744(1)–744(14) (2018). **E, 1-21**

4) M. Zhao, N. Wada, H. Shinozaki, N. Seko, M. Mori and H. Itabashi, "Monitoring of the Palladium Concentration in River Water and Sediment at an Acidic Hot Spring Spa Area in the Gunma Prefecture", Anal. Sci., **34**, 1357–1364 (2018). **N**

Proceedings

1) 瀬古 典明, "海水ウラン捕集技術の現状"【招待講演】, 平成 30 年度「第 2 回先導原子力研コロキウム」「第 25 回つばめラウンジセミナー」, [東京工業大学科学技術創成研究院先導原子力研究所・東京] (2018/05/17). **E, G**

2) 荒井 陽一, 渡部 創, 久保田 俊夫, 新井 剛, 瀬古 典明, 野村 和則, "使用済み燃料再処理プロセスから発生する廃溶媒処理技術の開発（1）全体概要及び既存技術によるTRUEX 灰溶媒に抽出された核燃料物質の回収法の調査", 日本原子力学会 2018 秋の大会, 原子力学会, [岡山大・岡山] (2018/09/07). **E, 1-32**

3) 中村 文也, 新井 剛, 保科 宏行, 瀬古 典明, 荒井 陽一, 渡部 創, 野村 和則, "使用済み燃料再処理プロセスから発生する廃溶媒処理技術の開発（2）固体吸着材を用いた廃溶媒からの核燃料物質分離除去に関する検討", 日本原子力学会 2018 年秋の大会, 原子力学会, [岡山大・岡山] (2018/09/07). **E, 1-32**

4) 柴田 卓弥, 大場 弘則, 瀬古 典明, 若井田 育夫, "LIBS 分析と放射線グラフト重合材を融合した遠隔その場溶液分析手法の開発", Post-ASLIBS2017 International Symposium, LIBS 研究会, [東北大・仙台] (2018/09/22). **E, 1-15**

5) J. Chen, N. Hayashi, H. Hoshina and N. Seko, "Simultaneous radiation grafting of vinylbenzyl chloride onto ethylene-tetrafluoroethylene copolymer films", The 7th Asia Pacific Symposium on Radiation Chemistry (APSRC-2018), [Shanghai Institute of Applied Physics, Chinese Academy of Sciences (SINAP, CAS), China] (2018/11/06). **G, 1-21**

6) N. Hayashi, N. Seko, J. Chen, D. Matsumura, T. Tsuji and H. Saito, "In-situ XAFS Analysis on Reduction of Adsorbed Hexavalent Chromium in Radiation Grafted Adsorbent", The 7th Asia Pacific Symposium on Radiation Chemistry (APSRC-2018), [Shanghai Institute of Applied Physics, Chinese Academy of Sciences

(SINAP, CAS), China] (2018/11/06). **E, 1-21**

7) N. Seko, "Adsorption Behavior of the Rare Metals in Natural Seawater on an Amidoxime-Based Fibrous Adsorbents Synthesized by Electron Beam Graft Polymerization",【Invited talk】, The 7th Asia Pacific Symposium on Radiation Chemistry (APSRC-2018), [Shanghai Institute of Applied Physics, Chinese Academy of Sciences (SINAP, CAS), China] (2018/11/07). **E, G**

8) H. Hoshina, J. Chen, Y. Ueki and N. Seko, "Evaluation of fibrous grafted adsorbent having 2-ethylhexyl hydrogen-2-ethylhexylphosphonate as a functional group", The 12th SPSJ International Polymer Conference (IPC2018), The Society of Polymer Science, [International Conference Center Hiroshima, Hiroshima] (2018/12/06). **E, 1-21**

9) Y. Ueki and N. Seko, "Synthesis of grafted fibrous metal adsorbent", The 12th SPSJ International Polymer Conference (IPC2018), The Society of Polymer Science, [International Conference Center Hiroshima, Hiroshima] (2018/12/06). **E, 1-19**

10) J. Chen, N. Hayashi, Y. Ueki, H. Hoshina, N. Kasai and N. Seko, "GPC Analysis of Radiation-Grafted PVDF and Its Polystyrene Graft Chains", The 12th SPSJ International Polymer Conference (IPC2018), The Society of Polymer Science, [International Conference Center Hiroshima, Hiroshima] (2018/12/06). **G, 1-20**

11) N. Seko, N. Hayashi, J. Chen, D. Matsumura, T. Tsuji and H. Saito, "Adsorption performance of trivalent and hexavalent chromium in aqueous solution by electron beam grafted adsorbents", The 12th SPSJ International Polymer Conference (IPC2018), The Society of Polymer Science, [International Conference Center Hiroshima, Hiroshima] (2018/12/06). **E, 1-21**

12) N. Hayashi, M. Omichi and N. Seko, "Observation of polyethylene lamella layer on radiation grafted materials", The 12th SPSJ International Polymer Conference (IPC2018), The Society of Polymer Science, [International Conference Center Hiroshima, Hiroshima] (2018/12/07). **E, 1-20**

13) 濱田 崇, 保科 宏行, 瀬古 典明, "放射線グラフト重合によるジグリコール酸系グラフト型吸着材の合成", 第 28 回日本MRS 年次大会, 一般社団法人日本 MRS, [北九州国際会議場, 福岡] (2018/12/18). **G, 1-19**

14) 瀬古 典明, "電子線グラフト重合による材料創製研究"【招待発表】, 第 160 回ラドテック研究講演会, ラドテック研究会, [東京理科大・東京] (2019/01/29). **E, 1-19**

15) 瀬古 典明, "Emerging Applications of Radiation-induced Grafted Materials"【Invited talk】, ASEAN Next 2019, TINT, [Bangkok, Thailand] (2019/03/20). **E, G, 1-20**

16) 大道 正明, 覚知 亮平, 瀬古 典明, "多成分連結反応を活用したポリマープールの創製と機械学習による材料特性制御の試み", Future Trend in Polymer Science 2018, 高分子学会関東支部, [東京理科大・東京] (2019/03/20). **E, G, 1-20**

Patents

1) 大道 正明, 瀬古 典明, 前川 康成, "反応溶液, エマルション重合方法, エマルション重合用添加剤及びエマルション重

合用の添加剤キット", 特願2019-019705 (2019/02/06).　　**G**

2) 大道　正明, 植木　悠二, 瀬古　典明, 前川　康成, "液体中の気体を脱気する方法, 脱気容器及び化合物を反応させる方法", 特願2019-019684 (2019/02/06).　　**N**

3) 植木　悠二, 瀬古　典明, "ジチオカルバミン酸基を有する金属吸着材とその製造方法及び金属吸着方法", 特願 2018-223025 (2018/11/29).　　**E**

4) 眞壁　岳史, 押田　雅寛, 溝手　範人, 植木　悠二, 瀬古　典明,

"シリコーンゴム成形体, ブレードラバー, シリコーンゴム成形体の製造方法", 特願2018-219633 (2018/11/22).　　**E**

5) 附木　貴行, 鵜澤　潔, 大道　正明, 瀬古　典明, 杉本　雅樹, "繊維強化ポリプロピレン複合材料の製造方法及び繊維強化ポリプロピレン", 特願 2018-183161 (2018/09/28).　　**G**

6) 瀬古　典明, 保科　宏行, 笠井　昇, "グラフトセルロースパウダー及びこれを用いたろ過方法", 特願 2018-042450 (2018/03/08).　　**E, G**

P1-8　Project "Element Separation and Analysis"

Papers

1) T. Taguchi, S. Yamamoto and H. Ohba, "Synthesis of novel hybrid carbon nanomaterials inside silicon carbide nanotubes by ion irradiation", Acta materialia, **173**, 153-162 (2019).　　**N**

2) A. Matsumoto, H. Ohba, M. Toshimitsu, K. Akaoka, A. Ruas, I. Wakaida, T. Sakka, S. Yae, "Enhancement of molecular formation in fiber-optic laser ablation with a long nanosecond pulsed laser", Spectrochimica Acta Part B, **155**, 56-60 (2019).　　**G, 1-15**

3) N. Okubo, Y. Okuno, A. Kitamura, T. Taguchi, "Influence of gamma-ray irradiation on mechanical property of YSZ for oxygen sensors in ADS", Nucl. Instrum. Meth. Phys. Res. Sec. B:, **435**, 198-202 (2018).　　**N**

4) C. Shibazaki, S. Arai, R. Shimizu, M. Saeki, Y. Kinoshita, A. Ostermann, T. E. Schrader, Y. Kurosaki, T. Sunami, R. Kuroki, M. Adachi, "Hydration structures of the human protein kinase CK2α clarified by joint neutron and X-ray crystallography", J. Mol. Biol., **430**(24), 5094-5104 (2018).　　**N**

5) N. Igawa, K. Kodama, T. Taguchi, Y. Yoshida, T. Matsukawa, A. Hoshikawa, T. Ishigaki, "Local Disorder in Proton Conductor $BaSn0.5In0.5O2.75$ Analyzed by Neutron Diffraction/Atomic Pair Distribution Function", Trans. Mater. Res. Soc. Jpn., **43**(6), 329-332 (2018).　　**N**

6) M. Saeki, D. Matsumura, T. Yomogida, T. Taguchi, T. Tsuji, H. Saito, H. Ohba, "In Situ Time-Resolved XAFS Studies on Laser-Induced Particle Formation of Palladium Metal in an Aqueous/EtOH Solution", J. Phys. Chem. C, **123**(1), 817-824 (2019).　　**N**

7) Y. Sasaki, M. Saeki, K. Yoshizuka, "Extractions and spectroscopic studies of various metals with Diglycolamide-Type Tridentate Ligands", Solvent Extraction Research and Development, Japan, **26**(1), 21-34 (2019).　　**N**

8) T. Nozawa, K. Ozawa, C.H. Park, J.S. Park, A. Kohyama, A. Hasegawa, S. Nogami, T. Hinoki, S. Kondo, T. Yano, T. Shibayama, B. Tsuchiya, T. Shikama, S. Nagata, T. Tanaka, H. Iwakiri, Y. Yamamoto, S. Konishi, R. Kasada, M. Kondo, T. Kunugi, T. Yokomine, Y. Ueki, N. Okubo, T. Taguchi, H. Tanigawa, "Japanese activities of the R&D on silicon carbide composites in the broader approach period and beyond", J. Nucl. Mater., **511**, 582 -590 (2018).　　**N**

9) K. Kakitani, T. Kimata, T. Yamaki, S. Yamamoto, D. Matsumura, T. Taguchi, T. Terai, "X-ray Absorption Study of Platinum Nanoparticles on an Ion-Irradiated Carbon Support", Radiat. Phys. Chem., **153**, 152-155 (2018).　　**I, 1-14**

10) K. Kakitani, T. Kimata, T. Yamaki, S. Yamamoto, T. Taguchi, T. Kobayashi, W. Mao, T. Terai, "The interface between platinum nanoparticle catalysts and an Ar^+-irradiated carbon support", Surface and Coating Technology, **355,** 259-263 (2018).　　**I. 1-14**

11) S. Asai, M. Ohata, T. Yomogida, M. Saeki, H. Ohba, Y. Hanzawa, T. Horita, Y. Kitatsuji, "Determination of 107Pd in Pd purified by selective precipitation from spent nuclear fuel by laser ablation ICP-MS", Anal. Bioanalytical Chemistry, **411**(5), 973-983 (2018).　　**N**

12) 田村　浩司, 遠山　伸一, "厚板鋼材のレーザー切断技術－廃炉の時代の先端技術開発－", 日本原子力学会誌, **61**(5), 413 – 415 (2019).　　**N**

13) 若井田　育夫, 大場　弘則, 宮部　昌文, 赤岡　克昭, 大場　正規, 田村　浩司, 佐伯　盛久, "核燃料サイクルおよび福島第一原子力発電所廃炉への適用を念頭としたレーザー誘起ブレークダウン分光と関連分光技術", 光学（日本光学会機関誌）, **48**(1), 13-20 (2019).　　**N**

14) T. Taguchi, S. Yamamoto and H. Ohba, "Ion irradiation-induced novel microstructural change in silicon carbide nanotubes", Acta Materialia, **154**, 90-99 (2018).　　**I, 1-14**

15) A. Matsumoto, H. Ohba, M. Toshimitsu, K. Akaoka, A. Ruas, T. Sakka, "Fiber-optic laser-induced breakdown spectroscopy of zirconium metal in the air: The special feature of the plasma produced by the long-pulse laser", Spectrochimica Acta Part B: Atomic Spectroscopy, **142**, 37-49 (2018).　　**N**

16) N. Ishikawa, T. Taguchi, N. Okubo, "Hillocks created for amorphizable and non-amorphazable ceramics irradiated with swift heavy ions: TEM study", Nanotechnology, **28**(44), 445708 (2017).　　**I, 1-14**

Proceeding

1) 柴田　卓弥, 大場　弘則, 瀬古　典明, 若井田　育夫, "LIBS 分析と放射線グラフト重合材を融合した遠隔その場溶液分析手法の開発", Post-ASLIBS2017 International Symposium, LIBS 研究会, [東北大・仙台] (2018/09/22).　　**E, 1-15**

P1-9　Advanced Functional Polymer Materials Research Group

Papers

1) K. Yoshimura, Y. Zhao, A. Hiroki, Y. Kishiyama, H. Shishitani, S. Yamaguchi, H. Tanaka, S. Koizumi, J. E. Houston, A. Radulescu, M. Appavou, D. Richter, and Y. Maekawa, "Reverse relationships of water uptake and alkaline durability with hydrophilicity of imidazolium-based grafted anion-exchange membranes", Soft Matter, **14**, 9118-9131 (2018). **G**

2) K. Yoshimura, A. Hiroki, H. C. Yu, Y. Zhao, H. Shishitani, S. Yamaguchi, H. Tanaka, and Y. Maekawa, "Alkaline durable 2-methylimidazolium-containing anion-conducting electrolyte

membranes prepared by radiation induced grafting for direct hydrazine hydrate fuel cells", J. Membr. Sci., **573**, 403-410 (2019). **G**

3) Y. Zhao, K. Yoshimura, H. C. Yu, Y. Maekawa, A. Hiroki, Y. Kishiyama, H. Shishitani, S. Yamaguchi, H. Tanaka, S. Koizumi, M. Appavou, J. Houston, A. Radulescu, and D. Richter, "Small angle neutron scattering study on the morphology of imidazolium-based grafted anion-conducting fuel cell membranes", Physica B: Condensed Matter, **551**, 203-207 (2018). **G**

4) A. Fukaya, A. Tateno, N. Iimura, Y. Ohta, K. Takahashi, T. Sodekoda, K. Suzuki, H. Takahashi, S. Hasegawa, A. Hiroki, and Y. Maekawa, "Application of graft-type poly(ether ether keton)-based polymer electrolyte membranes to electrochemical devices – Fuel cells and electrolytic enrichment of tritium", Int. J. Hydrogen Energy, **43**, 8927-8935 (2018). **G**

5) T. D. Tap, D. D. Khiem, L. L. Nguyen, N. Q. Hien, L. Q. Luan, P. B. Thang, S. Sawada, S. Hasegawa, and Y. Maekawa, "Temperature effects on mechanical properties and conductivity of graft-type polymer electrolyte membrane", Radiat. Phys. Chem., **151**, 186-191 (2018). **G**

6) T. Hamada, K. Yoshimura, A. Hiroki, and Y. Maekawa, "Synthesis and Characterization of Aniline-Containing Anion-Conducting Polymer Electrolyte Membranes by Radiation-Induced Graft Polymerization", J. Appl. Polym. Sci., **135**, 46886 (2018). **G**

7) Beom-Seok Ko, K. Yoshimura, S. Warapon, H. Shishitani, S. Yamaguchi, H. Tanaka, and Y. Maekawa, "Basicity-dependent properties of anion conducting membranes consisting of iminium cations for alkaline fuel cells", J. Polym. Sci. A, Polym. Chem., **57**, 503-510 (2019). **G**

8) J. F. Madrid, Y. Ueki, L. V. Abad, T. Yamanobe and N. Seko, "Enhanced amination and adsorption performance of functional copolymer synthesized via RAFT-mediated radiation grafting in emulsion", J. Polym. Res., **25**, 193(1)–193(11) (2018). **E, 1-21**

9) N. Hayashi, J. Chen and N. Seko, "Nitrogen-Containing Fabric Adsorbents Prepared by Radiation Grafting for Removal of Chromium from Wastewater", Polymers, **10**, 744(1)–744(14) (2018). **E, 1-21**

10) M. Zhao, N. Wada, H. Shinozaki, N. Seko, M. Mori and H. Itabashi, "Monitoring of the Palladium Concentration in River Water and Sediment at an Acidic Hot Spring Spa Area in the Gunma Prefecture", Anal. Sci., **34**, 1357–1364 (2018). N**, 1-21**

11) T. Hamada, S. Yamashita, M. Omichi, K. Yoshimura, Y. Ueki, N. Seko and R. Kakuchi, "Multicomponent-Reaction-Ready Biomass-Sourced Organic Hybrids Fabricated via the Surface Immobilization of Polymers with Lignin-Based Compounds", ACS sustainable Chem. Eng., **7**(8), 7795–7803 (2019). **G, 1-19, 1-21**

Proceedings

1) Y. Zhao, K. Yoshimura, A. Hiroki, Y. Kishiyama, H. Shishitani, S. Yamaguchi, H. Tanaka, and Y. Maekawa, "Imidazolium-Based Grafted Anion Exchange Membranes: Interplay between the Morphology and Anion Transport Behavior", ECS Transactions, 86, 619-627 (2018). **G**

2) Y. Zhao, K. Yoshimura, A. Hiroki, and Y. Maekawa, "SCATTERING STUDY OF STRUCTURE-PROPERTY RELATIONSHIPS OF GRAFTED ANION EXCHANGE MEMBRANES", XVII International Small Angle Scattering conference 2018, [Traverse city, USA] Abstracts, A049 (2018/10). **G**

3) 吉村 公男, ザオ ユエ, 廣木 章博, 猪谷 秀幸, 山口 進, 前川 康成, "The Relationship between Membrane Properties and Hierarchical Structure of Radiation Grafted Anion Conducting Membranes", Advanced Energy Materials 2018, [Univ. of Surrey, UK] Abstracts, PEM04 (2018/09). **G**

4) 廣木 章博, 吉村 公男, ザオ ユエ, 猪谷 秀幸, 山口 進, 前川 康成, "Properties of anion-conducting electrolyte membranes based on ETFE membrane and crosslinked graft polymers for fuel cells", Advanced Energy Materials 2018, [Univ. of Surrey, UK] Abstracts, PEM02 (2018/09). **G**

5) 吉村 公男, ザオ ユエ, 廣木 章博, 猪谷 秀幸, 山口 進, 前川 康成, "放射線グラフト型アニオン伝導電解質膜のアルカリ耐性と階層構造の関係", 第 17 回若手研究者発表討論会, [電力中央研究所, 狛江] 要旨集, 21 (2018/10). **G**

6) 吉村 公男, ザオ ユエ, 廣木 章博, 猪谷 秀幸, 山口 進, 前川 康成, "グラフト型アニオン伝導電解質膜のアルカリ耐性と階層構造の関係", 日本化学会関東支部群馬地区研究交流発表会, [群馬高専, 前橋] 要旨集, P-23 (2018/12). **G**

7) 廣木 章博, 吉村 公男, 猪谷 秀幸, 山口 進, 前川 康成, "化学的安定性を向上したグラフト型アニオン伝導高分子電解質膜", 日本化学会関東支部群馬地区研究交流発表会, [群馬高専, 前橋] 要旨集, P-49 (2018/12). **G**

8) 髙松 治文, 吉村 公男, 廣木 章博, 前川 康成, "グラフト型アニオン伝導膜の高分子構造と物性・耐久性の関係", 日本化学会関東支部群馬地区研究交流発表会, [群馬高専, 前橋] 要旨集, P-47 (2018/12). **G**

9) 吉村 公男, ザオ ユエ, 廣木 章博, 猪谷 秀幸, 山口 進, 前川 康成, "グラフト型アニオン伝導電解質膜のアルカリ耐性と階層構造の関係", 第 28 回日本 MRS 年次大会 [北九州国際会議場, 北九州] 要旨集, B1-P19-017 (2018/12). **G**

10) 廣木 章博, 吉村 公男, 猪谷 秀幸, 山口 進, 前川 康成, "架橋構造導入により改質したアニオン伝導性高分子電解質膜の化学的安定性", 第 28 回日本 MRS 年次大会 [北九州国際会議場, 北九州] 要旨集, B1-P19-018 (2018/12). **G**

11) 澤田 真一, 安保 貴和, 匠 伸弥, 安川 政宏, 垣花 百合子, 比嘉 充, 前川 康成, "放射線グラフト陽・陰イオン交換膜を用いた逆電気透析装置の発電性能", 第 17 回放射線プロセスシンポジウム [東京大学 弥生キャンパス 弥生講堂, 東京] 要旨集, P4-5 (2018/11). **G**

12) 澤田 真一, 田中 健一, 船津 公人, 前川 康成, "機械学習による放射線グラフト電解質膜のプロトン導電率予測", Future Trend in Polymer Science 2018 [東京理科大学 神楽坂キャンパス, 東京] 要旨集, P128 (2019/03). **G**

13) 澤田 真一, 安保 貴和, 匠 伸弥, 安川 政宏, 垣花 百合子, 比嘉 充, 前川 康成, "放射線グラフト陽・陰イオン交換膜を用いた逆電気透析発電", 膜シンポジウム 2018 [神戸大学 百年記念館, 神戸] 要旨集, P113 (2018/11). **G**

14) 澤田 真一, 後藤 光暁, 越川 博, 喜多村 茜, 比嘉 充, 八巻 徹也, "Ion and water transport properties of cation exchange membranes prepared by heavy-ion-track grafting technique", 5th International Conference on Methods and Materials for Separation Processes [Hotel Verde Montana, POLAND] 要旨集, P103 (2018/08). **C**

15) 瀬古 典明, "海水ウラン捕集技術の現状"【招待講演】, 平成 30 年度「第 2 回先導原子力研コロキウム」「第 25 回つばめラウンジセミナー」, [東京工業大学科学技術創成研究院先導原子力研究所・東京] (2018/05/17). **E, G, 1-19, 1-21**

16) 荒井 陽一, 渡部 創, 久保田 俊夫, 新井 剛, 瀬古 典明, 野村 和則, "使用済み燃料再処理プロセスから発生する廃溶媒処理技術の開発 (1)全体概要及び既存技術による TRUEX 灰溶媒に抽出された核燃料物質の回収法の調査", 日本原子力学会 2018 秋の大会, 原子力学会, [岡山大・岡山] (2018/09/07). **E, 1-32**

17) 中村 文也, 新井 剛, 保科 宏行, 瀬古 典明, 荒井 陽一, 渡部 創, 野村 和則, "使用済み燃料再処理プロセスから発生する廃溶媒処理技術の開発 (2)固体吸着材を用いた廃溶媒からの核燃料物質分離除去に関する検討", 日本原子力学会 2018 年秋の大会, 原子力学会, [岡山大・岡山] (2018/09/07). **E, 1-32**

18) 柴田 卓弥, 大場 弘則, 瀬古 典明, 若井田 育夫, "LIBS 分析と放射線グラフト重合材を融合した遠隔その場溶液分析手法の開発", Post-ASLIBS2017 International Symposium, LIBS 研究会, [東北大・仙台] (2018/09/22). **E**

19) J. Chen, N. Hayashi, H. Hoshina and N. Seko, "Simultaneous raddiation grafting of vinylbenzyl chloride onto ethylene-tetrafluoroethylene copolymer films", The 7th Asia Pacific Symposium on Radiation Chemistry (APSRC-2018), [Shanghai Institute of Applied Physics, Chinese Academy of Sciences (SINAP, CAS), China] (2018/11/06). **G, 1-21**

20) N. Hayashi, N. Seko, J. Chen, D. Matsumura, T. Tsuji and H. Saito, "In-situ XAFS Analysis on Reduction of Adsorbed Hexavalent Chromium in Radiation Grafted Adsorbent", The 7th Asia Pacific Symposium on Radiation Chemistry (APSRC-2018), [Shanghai Institute of Applied Physics, Chinese Academy of Sciences (SINAP, CAS), China] (2018/11/06). **E, 1-21**

21) N. Seko, "Adsorption Behavior of the Rare Metals in Natural Seawater on an Amidoxime-Based Fibrous Adsorbents Synthesized by Electron Beam Graft Polymerization"【Invited talk】, The 7th Asia Pacific Symposium on Radiation Chemistry (APSRC-2018), [Shanghai Institute of Applied Physics, Chinese Academy of Sciences (SINAP, CAS), China] (2018/11/07). **E, G, 1-19, 1-21**

22) H. Hoshina, J. Chen, Y. Ueki and N. Seko, "Evaluation of fibrous grafted adsorbent having 2-ethylhexyl hydrogen-2-ethylhexylphosphonate as a functional group", The 12th SPSJ International Polymer Conference (IPC2018), The Society of Polymer Science, [International Conference Center Hiroshima, Hiroshima] (2018/12/06). **E, 1-21**

23) Y. Ueki and N. Seko, "Synthesis of grafted fibrous metal adsorbent", The 12th SPSJ International Polymer Conference (IPC2018), The Society of Polymer Science, [International Conference Center Hiroshima, Hiroshima] (2018/12/06). **E, 1-19**

24) J. Chen, N. Hayashi, Y. Ueki, H. Hoshina, N. Kasai and N. Seko, "GPC Analysis of Radiation-Grafted PVDF and Its Polystyrene Graft Chains", The 12th SPSJ International Polymer Conference (IPC2018), The Society of Polymer Science, [International Conference Center Hiroshima, Hiroshima] (2018/12/06). **G, 1-21**

25) N. Seko, N. Hayashi, J. Chen, D. Matsumura, T. Tsuji and H. Saito, "Adsorption performance of trivalent and hexavalent chromium in aqueous solution by electron beam grafted adsorbents", The 12th SPSJ International Polymer Conference (IPC2018), The Society of Polymer Science, [International Conference Center Hiroshima, Hiroshima] (2018/12/06). **E, 1-19**

26) N. Hayashi, M. Omichi and N. Seko, "Observation of polyethylene lamella layer on radiation grafted materials", The 12th SPSJ International Polymer Conference (IPC2018), The Society of Polymer Science, [International Conference Center Hiroshima, Hiroshima] (2018/12/07). **E, 1-20**

27) 濱田 崇, 保科 宏行, 瀬古 典明, "放射線グラフト重合によるジグリコール酸系グラフト型吸着材の合成", 第 28 回日本 MRS 年次大会, 一般社団法人日本 MRS, [北九州国際会議場, 福岡] (2018/12/18). **G, 1-21**

28) 瀬古 典明, "電子線グラフト重合による材料創製研究"【招待発表】, 第 160 回ラドテック研究講演会, ラドテック研究会, [東京理科大・東京] (2019/01/29). **E, 1-19**

29) 瀬 古 典 明, "Emerging Applications of Radiation-induced Grafted Materials"【Invited talk】, ASEAN Next 2019, TINT, [Bangkok, Thailand] (2019/03/20). **E, G, 1-19**

30) 大道 正明, 覚知 亮平, 瀬古 典明, "多成分連結反応を活用したポリマープールの創製と機械学習による材料特性制御の試み", Future Trend in Polymer Science 2018, 高分子学会関東支部, [東京理科大・東京] (2019/03/20). **E, G, 1-20**

Patents

1) 大道 正明, 瀬古 典明, 前川 康成, "反応溶液、エマルション重合方法、エマルション重合用添加剤及びエマルション重合用の添加剤キット", 特願 2019-019705 (2019/02/06). **G**

2) 大道 正明, 植木 悠二, 瀬古 典明, 前川 康成, "液体中の気体を脱気する方法、脱気容器及び化合物を反応させる方法", 特願 2019-019684 (2019/02/06). **N**

3) 植木 悠二, 瀬古 典明, "ジチオカルバミン酸基を有する金属吸着材とその製造方法及び金属吸着方法", 特願 2018-223025 (2018/11/29). **E**

4) 眞壁 岳史, 押田 雅寛, 溝手 範人, 植木 悠二, 瀬古 典明, "シリコーンゴム成形体、ブレードラバー、シリコーンゴム成形体の製造方法", 特願 2018-219633 (2018/11/22). **E**

P2-1 Project "Ion Beam Mutagenesis"

Papers

1) Y. Matuo, Y. Izumi, A. N. Sakamoto, Y. Hase, K. Satoh and K. Shimizu, "Molecular Analysis of Carbon Ion-Induced Mutations in DNA Repair-Deficient Strains of Saccharomyces cerevisiae", Quantum Beam Sci., **3**(3), 14 (2019). **C, 2-22**

2) M. Adachi, R. Shimizu, C. Shibazaki, K. Satoh, S. Fujiwara, S. Arai, I. Narumi, R. Kuroki, "Extended Structure of Pleiotropic DNA Repair-Promoting Protein PprA from *Deinococcus radiodurans*", The FASEB Journal, **33**(3), 3647–3658 (2019). **C, 2-20, G, 2-26**

3) A. N. Sakamoto, H. Kaya and M. Endo, "Deletion of TLS polymerases promotes homologous recombination in Arabidopsis", Plant Signal. Behav., **13**, e1483673 (2018). **N**

4) 阿部 知子, 森田 竜平, 大野 豊, 長谷 純宏, 高城 啓一, 畑下 昌範, "ミュータゲノミクスと変異統合データベースの構築", JATAFF ジャーナル, **7**, 19 - 23 (2019). **C**

5) 渡部 貴志, 佐藤 勝也, 林 秀謙, 増渕 隆, "輸出用に適した群馬清酒酵母の育種に関する研究(第 2 報)", 群馬県立産業技術センター研究報告(2017), 10-14 (2018). **C, 2-18**

6) 長谷 純宏, "イオンビーム育種による実用新品種の開発" NL だより, **486**, 2 (2018). **C**

Proceedings

1) 石塚 匠, 浅水 俊平, 柳澤 昌臣, 佐藤 勝也, 尾仲 宏康, "複合培養における赤色色素生産非応答性変異株の解析" 日本農芸化学会 2019 年度大会, [東京], 大会講演要旨集, 3D1p04, (2019). **C**

2) 平田 翔也, 北村 智, 佐藤 勝也, 鳴海 一成, 大野 豊, "植物色素フラボノイドに着目した変異誘発処理当代植物における突然変異検出" 日本農芸化学会 2019 年度大会, 日本農芸化学会, [東京], 大会講演要旨集, 3E8p05, (2019) **C, G, 2-12**

3) 佐藤 勝也, "イオンビームで産業微生物をつくる" 第17回放射線プロセスシンポジウム, [東京], 講演要旨・ポスター発表要旨集, 43-44, (2018). **C**

4) Natasia, K. Nakashima, Y. Hase, T. Yamada and J. Abe, "Phenotypic variation for quantitative traits in soybean mutants obtained via ion-beam irradiation", 日本育種学会第 134 回講演会, [岡山], 育種学研究第 20 巻別冊 2 号 116 (2018). **C**

5) 長谷 純宏, 佐藤 勝也, 千葉 敦也, 平野 貴美, 齋藤 勇一, 鳴海 一雅, "生物試料に対する MeV 級クラスターイオン照射効果の検討" 第 17 回放射線プロセスシンポジウム, [東京], 講演要旨・ポスター発表要旨集, 89, (2018). **T, 2-13**

6) 大野 豊, 長谷 純宏, 野澤 樹, 佐藤 勝也, 北村 智, "イオンビーム誘発変異体のゲノム解析 -どのような変異がどのくらい生じているのか全体像を探る-" 第 17 回放射線プロセスシンポジウム, 放射線プロセスシンポジウム, [東京], 講演要旨・ポスター発表要旨集, 87, (2018). **C**

7) 城下 結, 長谷 純宏, 山田 哲也, 阿部 純, 金澤 章, "イオンビーム照射により誘導した葉緑素含量に関する変異ダイズ系統におけるイソフラボン含量の多様性", 日本育種学会第 134 回講演会, [岡山], 育種学研究第 20 巻別冊 2 号 124 (2018). **C**

8) 近松 豪, 佐藤 勝也, "重イオンビーム利用による産業糸状菌の育種", 第 1 回 重・クラスターイオンビーム利用による微生物由来高生産性, エネルギー, 環境シンポジウム, [つくば], 5-6, (2019). **C**

9) 長谷 純宏, 佐藤 勝也, 千葉 敦也, 平野 貴美, 齋藤 勇一, 鳴海 一雅, "生物試料に対する MeV 級クラスターイオン照射効果の検討", 第 1 回重・クラスターイオンビーム利用による微生物由来高生産性, エネルギー, 環境シンポジウム, [つくば], 14, (2019). **T, 2-13**

10) A. N. Sakamoto, F. Nogue and Y. Yokota, "Analysis of DNA damage responses in gamma-irradiated Physcomitrella patens cells", EMBO workshop, Plant Genome Stability and Change 2018, Book of Abstracts p88, [Gatersleben, Germany] (2018/06) **C, G, 2-15**

11) 横田 裕一郎, "イオンビームを用いた生物応用研究と植物の放射線耐性研究", 【招待講演】, 2018 年東京 RBC 夏のラボ合宿, 要旨集 P12, [国立女性教育会館・埼玉県比企郡嵐山町] (2018/07). **G, 2-15**

12) 横田 裕一郎, Fabian Nogue, 坂本 綾子, "半数性モデル植物ヒメツリガネゴケの放射線抵抗性には末端結合修復ではなく相同組換え修復が寄与する", 日本放射線影響学会第 61 回大会, 要旨集 P72, [長崎ブリックホール・長崎] (2018/11). **G, 2-15**

Patents

1) 山口 絵梨香, 長谷 純宏, 野澤 樹 "はまごろも 4 号" 品種登録 27292 (2019/02/14). **C**

2) 山口 絵梨香, 長谷 純宏, 野澤 樹 "はまごろも 5 号" 品種登録 27293 (2019/02/14). **C**

P2-2　Project "Microbeam Radiation Biology"

Papers

1) M. Suzuki, T. Sakashita and T. Funayama, "Immobilization of live *Caenorhabditis elegans* individuals using an ultra-thin polydimethylsiloxane microfluidic chip with water retention" J. Vis. Exp., **145**, e59008-1~10 (2019). **C**

2) 鈴木 芳代, 平塚 哉, "微小生物を生きたまま長時間観察できる保水性マイクロチップの開発" 放射線と産業, **145**, 16-19 (2018). **C, 2-06**

3) M. Suzuki, T. Sakashita, Y. Hattori, Y. Yokota, Y. Kobayashi and T. Funayama, "Development of ultra-thin chips for immobilization of *Caenorhabditis elegans* in microfluidic channels during irradiation and selection of buffer solution to prevent dehydration", J. Neurosci. Meth., **306**, 32-37 (2018). **C, 2-06**

4) 簗瀬 澄乃, 鈴木 芳代, 秋山(張) 秋梅, 坂下 哲哉, "モデル生物線虫における放射線ホルミシスと新たな知見", 放射線生物研究, **53**, 255-264 (2018). **N**

5) Z. Soh, K. Sakamoto, M. Suzuki, Y. Iino, T. Tsuji, "A computational model of internal representations of chemical gradients in environments for chemotaxis of *Caenorhabditis elegans*", Sci. Rep., **8**, 17190 (2018). **N**

6) M. Suzuki, T. Sakashita and T. Funayama, "Immobilization of Live Caenorhabditis elegans Individuals Using an Ultra-thin Polydimethylsiloxane Microfluidic Chip with Water Retention", J. Vis. Exp., **145**, e59008-1~10 (2019). **C, 2-06**

Proceedings

1) 舟山 知夫, 鈴木 芳代, "重イオンマイクロビームを用いた生物照射技術とその利用研究", 放射線, **44**(4), 151-156 (2019). **C, 2-01**

2) 鈴木 雅雄, 宇佐美 徳子, 舟山 知夫, 横田 裕一郎, 鈴木 芳代, 小林 泰彦, "放射光マイクロビームを使った生物照射効果研究", 放射線, **44**(4), 147-149 (2019). **C, 2-02**

Patents

1) 平塚 哉, 鈴木 芳代, 坂下 哲哉, 舟山 知夫, "生物試料用マイクロチップ、カバー、生物試料封入キットおよび方法", 特願2019-045480（2019/03/13）.

2) 平塚 哉, 鈴木 芳代, 坂下 哲哉, 舟山 知夫, "生物試料用マイクロチップ", 特願2018-099452（2018/05/24）.

Press・TV

1) 量研・Biocosm株式会社, "保水性能を有する生物試料用マイクロチップを開発〜微小生物の動きを抑えて生きたまま長時間観察できる麻酔要らずの夢のチップ〜", 2018/06/14, プレス発表：化学工業日報, 科学新聞, 日経産業新聞に掲載. **C**

P2-3　Project "Medical Radioisotope Application"

Papers

1) Y. Ohshima, N. Kono, Y. Yokota, S. Watanabe, I. Sasaki, N. S. Ishioka, T. Sakashita, K. Arakawa, "Anti-tumor effects and potential therapeutic response biomarkers in α-emitting *meta*-[211]At-astato-benzylguanidine therapy for malignant pheochromocytoma explored by RNA-sequencing", Theranostics, **9**(6), 1538-1549 (2019). **C**

2) S. Watanabe, M.A. -U. Azim, I. Nishinaka, I. Sasaki, Y. Ohshima,

K. Yamada, N.S. Ishioka, "A convenient and reproducible method for the synthesis of astatinated 4-[211At]astato-L-phenylalanine *via* electrophilic desilylation", Org. Biomol. Chem., **17**, 165-171 (2019). **C, 2-30**

3) Y. Nagao, M. Yamaguchi, S. Watanabe, N.S. Ishioka, N. Kawachi, H. Watabe, "Astatine-211 imaging by a Compton camera for targeted radiotherapy", Appl. Radiat. Isot, **139**, 238-243 (2018).**C**

4) S. Watanabe, A. Shimada, S. Watanabe, H. Hanaoka, N.S. Ishioka, "Improvement and Optimization of Clinically Potent Positron Emitter 76Br Isolation Using the Dry Distillation Approach" Trans. Mat. Res. Soc. Japan, **43**, 219-222 (2018). **C**

Proceedings

1) T. Sakashita, Y. Ohshima, N. Kono, Y. Yokota, S. Watanabe, I. Sasaki, N. S. Ishioka, K. Arakawa, "RNA-seq reveals tumor radiation response and novel molecular targets on α-emitting *meta*-[At-211]-astato-benzylguanidine therapy for malignant pheochromocytoma", Abstr. 5th Theranostics world congress 2019 (TWC2019), ABSTR PP133, [Jeju, KOREA] (2019/03). **C**

2) 石岡 典子, "α線を用いたがん治療における放射性薬剤の最前線"[招待講演], 平成 30 年度放射線安全管理研修会, 放射線障害防止中央協議会, 要旨集 4, [大阪科学技術センター・大阪] (2019/03). **C**

3) 石岡 典子, "α線を用いたがん治療における放射性薬剤の最前線"[招待講演], 平成 30 年度放射線安全管理研修会, 放射線障害防止中央協議会, 要旨集 4, [文京シビックホール・東京] (2019/02). **C**

4) 山崎 直亨, 森 勝伸, 大平 慎一, 佐柄 克哉, 板橋 英之, 須郷 由美, 渡辺 茂樹, 石岡 典子, "カラム型フロー電解セルー電気透析型イオン抽出デバイスを用いた Cu(II)の分離・精製", 第 78 回分析化学討論会, 要旨集 Y1039, [山口大・宇部] (2018/05). **C**

5) 山崎 直亨, 須郷 由美, 大平 慎一, 板橋 英之, 石岡 典子, 森 勝伸, "がん診断用 Cu-64 の新規分離精製法の開発", 平成 30 年度日本化学会関東支部群馬地区研究交流発表会, 要旨集 P35, [群馬工専・前橋] (2018/12). **C**

6) 大島 康宏, "α線放出核種 211At 標識メタアスタトベンジルグアニジンの開発―褐色細胞腫モデルを用いた基礎的検討―"[招待講演], 第58回日本核医学会学術総会, 要旨集 シンポジウム 9-1, [沖縄コンベンションセンター・沖縄] (2018/11). **C**

7) 坂下 哲哉, 大島 康宏, 河野 暢明, 横田 裕一郎, 渡辺 茂樹, 佐々木 一郎, 石岡 典子, 荒川 和晴, "悪性褐色細胞腫 PC12 細胞に対する 211At 標識 MABG 投与時の RNA シーケンス解析", 第 58 回日本核医学会学術総会, 要旨集 M2B5B2, [沖縄コンベンションセンター・沖縄] (2018/11). **C**

8) 渡辺 茂樹, M. A. -U. Azim, 西中 一朗, 佐々木 一郎, 大島 康宏, 山田 圭一, 石岡 典子, "有機ケイ素前駆体を用いたアスタチン標識アミノ酸の合成", 第 58 回日本核医学会学術総会, 要旨集 M2B5B5, [沖縄コンベンションセンター・沖縄] (2018/11). **C, 2-30**

9) 西中 一朗, 橋本 和幸, 鈴木 博元, 渡辺 茂樹, M. A. -U. Azim, 石岡 典子, "Astatine chemical species in solutions prepared by a method based on dry distillation", 第 58 回日本核医学会学術総会, 要旨集 M1B1A4, [沖縄コンベンションセンター・沖縄] (2018/11). **C, 2-30**

10) Y. Nagao, M. Yamaguchi, S. Watanabe, N.S. Ishioka, N. Kawachi, H. Watabe, "Maximum-likelihood reconstruction and simulation analysis on Compton imaging of astatine-211 for targeted α-particle radiotherapy", 2018 IEEE NSS/MIC, ABSTR M-14-1411, [Sydney, Australia] (2018/11). **C**

11) 花岡 宏史, Arifudin Achmad, 山口 藍子, 対馬 義人, 須郷 由美, 石岡 典子, "抗 EGFR 抗体治療適応患者のスクリーニングにおける Cu-64 標識抗体の有用性", 第 66 回群馬県核医学研究会, 要旨集 II 4, [群大医・前橋] (2018/11). **C**

12) 佐々木 一郎, 渡辺 茂樹, 山田 圭一, 石岡 典子, "がんの診断・治療を目指した放射性ヨウ素標識ペプチドの開発：スズーハロゲン交換反応を用いた直接標識合成法の検討", 第 17 回若手研究者・技術者発表討論会（日本原子力学会関東・甲越支部）, 要旨集 20, [電中研・東京] (2018/10). **C**

13) 渡辺 茂樹, M. A. -U. Azim, 西中 一朗, 佐々木 一郎, 大島 康宏, 山田 圭一, 石岡 典子, "ケイ素―アスタチン交換反応を用いたアスタチン標識アミノ酸の合成", 第 62 回放射化学討論会, 要旨集 P51, [京大吉田キャンパス・京都] (2018/09). **C, 2-30**

14) 大島 康宏, 渡辺 茂樹, 坂下 哲哉, 佐々木 一郎, 東 達也, 石岡 典子, "MABG を用いたがん治療における Vorinostat の有効性の探索", 第 2 回日本核医学会分科会放射性薬品科学研究会/第 18 回放射性医薬品・画像診断薬研究会, 要旨集 A-5, [東京都健康長寿センター研究所・東京] (2018/09). **C**

15) 渡辺 茂樹, 山田 圭一, 佐々木 一郎, 石岡 典子, "ケイ素―ハロゲン交換反応を用いた放射性臭素標識化合物合成に関する基礎的検討", 第 2 回日本核医学会分科会放射性薬品科学研究会/第 18 回放射性医薬品・画像診断薬研究会, 要旨集 C-2, [東京都健康長寿センター研究所・東京] (2018/09). **C**

16) 石岡 典子, "がんの診断と治療に役立つ放射性同位体とその薬剤化"[招待講演], 六ヶ所・核燃料サイクルセミナー, 要旨集 I -(1), [六ケ所・青森] (2018/07). **C**

17) 大島 康宏, "α線放出 211At を利用した悪性褐色細胞腫治療薬メタアスタトベンジルグアニジン（MABG）の開発"[招待講演], 第 13 回日本分子イメージング学会総会・学術集会, 要旨集 S-09, [東大伊藤国際学術研究センター・東京] (2018/06). **C**

18) Y. Ohshima, S. Watanabe, T. Sakashita, I. Sasaki, T. Higashi, N. S. Ishioka, "Inhibition of organic cation transporter reduces non-specific uptake of MABG", 12th Congress of the World Federation of Nuclear Medicine and Biology (WFNMB2018), ABSTR P191, [Melbourne, Australia] (2018/04). **C**

19) H. Hanaoka, A. Achmad, A. Yamaguchi, H. T. Nguyen, Y. Sugo, N. S. Ishioka, Y. Tsushima, "Usefulness of Cu-64-labeled cetuximab PET screening to predict response to cetuximab treatment in non-small cell lung cancer", 12th World Congress of the World Federation of Nuclear Medicine and Biology (WFNMB2018), ABSTR 1311, [Melbourne, Australia] (2018/04). **C**

20) 石岡 典子, "α線の特性とその新規創成に関する研究"[招待講演], 第 10 回放射線ホルミシス講演会, 要旨集 特別講演 2, [学士会館・東京] (2018/01). **C**

21) H. Hanaoka, A. Yamaguchi, Y. Ohshima, T. Higuchi, N. S. Ishioka, Y. Tsushima, "Development of 18F-labeled α-methyl L-phenylalanine for tumor specific imaging", European Association of Nuclear Medicine 2017, ABSTR EP-0290, [Vienna, Austria] (2017/10). **C**

22) 吉永 恵一郎, 須藤 仁美, 須堯 綾, 辻 厚至, 永津 弘太郎, 大島 康宏, 石岡 典子, 東 達也, "褐色細胞腫マウスモデルを用いた 211At-MABG の抗腫瘍効果の病理解析による検討", 第 57 回日本核医学会学術総会, 要旨集 MM3VIC-01, [パシフィコ横浜・横浜] (2017/10). **C**

23) 花岡 宏史, 大島 康宏, 山口 藍子, 鈴木 博元, 樋口 徹也, 石岡 典子, 荒野 泰, 対馬 義人, "新規 F-18 標識αメチル-

フェニルアラニンの開発”, 第 57 回日本核医学会学術総会, 要旨集 MM2VⅢC-04, [パシフィコ横浜・横浜] (2017/10). **C**

24) 大島 康宏, 渡辺 茂樹, 佐々木 一郎, 東 達也, 石岡 典子, “MABG を用いた悪性褐色細胞腫治療における Vorinostat の有効性の探索”, 第 57 回日本核医学会学術総会, 要旨集 MP1E-02, [パシフィコ横浜・横浜] (2017/10). **C**

Books

1) 石岡 典子, 渡辺 茂樹, 大島 康宏, 坂下 哲哉, 河地 有木, “日本発 α 線放出核種を用いたがん治療薬剤の開発 - 製造からイメージングまで”, インナービジョン 2018 年 11 月号, インナービジョン, 46-48 (2018). **C**

2) 石岡 典子, 大島 康宏, “放射性同位体を使った、がんの新たな治療薬を開発中”, Newton 別冊完全図解元素と周期表新装版, ニュートンプレス, 100-101 (2018). **C**

Patents

1) 石岡 典子, 渡辺 茂樹, 近藤 浩夫, “放射性同位体の製造方法、放射性同位体製造装置”, 出願 PCT/JP2018/40359 (2018/10/30). **C**

2) 森 勝伸, 大平 慎一, 戸田 敬, 須郷 由美, 渡辺 茂樹, 石岡 典子, “分離装置、分離方法、RI分離精製システムおよびRI分離精製方法”, 出願 2018-080635 (2018/04/19). **C**

Press/TV

1) “がん治療効果の予測と向上に役立つ指標遺伝子を発見－全遺伝子の発現量変化を測定し、α線がん治療薬に特異的に応答する 4 遺伝子を特定－”, 2019/02/21, プレス発表：日経産業新聞、科学新聞、上毛新聞、山形新聞、荘内日報に掲載. **C**

P2-4 Project "Generation of Radioisotopes with Accelerator Neutrons"

Papers

1) K. Tsukada, Y. Nagai, K. Hashimoto, M. Kawabata, F. Minato, H. Saeki, S. Motoishi and M. Itoh, "^{99}Mo yield using large sample mass of MoO$_3$ for sustainable production of ^{99}Mo", J. Phys. Soc. Jpn. **87**, 043201-1~5 (2018). **N**

2) I. Nishinaka, K. Hashimoto, H. Suzuki, "Thin layer chromatography for astatine and iodine in solutions prepared by dry distillation", J. Radioanal. Nucl. Chem. **318**, 897-905 (2018). **N**

3) Y. Hatsukawa, T. Hayakawa, K. Tsukada, K. Hashimoto, T. Sato, M. Asai, A. Toyoshima, T. Tanimori, S. Sonoda, S. Kabuki, H. Kimura, A. Takada, T. Mizumoto, S. Takaki, "Electron- tracking Compton camera imaging of technetium-95m", PLoS ONE, **13**(12): e0208909 (2018). **N**

4) A. Hermanne, A. V. Ignatyuk, R. Capote, B. V. Carlson, J. W. Engle, M. A. Kellett, T. Kibédi, G. Kim, F. G. Kondev, M. Hussain, O. Lebeda, A. Luca, Y. Nagai, H. Naik, A. L. Nichols, F. M. Nortier, S. V. Suryanarayana, S.Takács, F. T. Tárkányi and M.Verpelli, "Reference cross sections for charged-particle monitor reactions", Nuclear Data Sheets, **148**, 338-382 (2018). **N**

5) 永井 泰樹, “医療用アイソトープ製造と非侵襲個別化医療”, 核データニュース, No. **121**, p.16-29 (2018). **N**

Proceedings

1) Y. Nagai, K. Hashimoto, M. Kawabata, K. Tsukada, Y. Hatsukawa, F. Minato, Y. Sugo, H. Saeki, S. Motoishi, "Diagnostic (^{99}Mo/^{99m}Tc) and Therapeutic (^{67}Cu) Radioisotopes Produced by Neutrons from C,Be(*d,n*)", Proceedings of 15th Varenna Conference on Nuclear Reaction Mechanisms (June 11-15, 2018), [Varenna, Italy] 333-340 (2019). **C**

2) Y. Nagai, K. Hashimoto, M. Kawabata, K. Tsukada, Y. Hatsukawa, Y. Sugo, Y. Nakahara, H. Saeki, S. Motoishi, "Quality control tests of ^{99m}Tc-radiopharmacuticals, biodistribution of ^{67}CuCl$_2$ in mice, and accelerator neutrons", Society of Nuclear Medicine & Molecular Imaging 2018 Annual Meeting (SNMMI 2018) [Pennsylvania, USA] J. Nucl. Med. 59, supplement 1, 1042 (2018). **C**

3) M. Kawabata, K. Hashimoto, S. Motoishi, H. Saeki, Y. Nagai, "Successful development for separating ^{99m}Tc from ^{99}Mo generated by accelerator driven neutrons", Annual Congress of the European Association of Nuclear Medicine (EANM 2018) [Düsseldorf, Germany] Abstract book EP-0881 (2018). **N**

4) 塚田 和明, 永井 泰樹, 橋本 和幸, 川端 方子, 湊 太志, 佐伯 秀也, 本石 章司, 渡辺 智, 伊藤 正俊, “加速器中性子を利用した Mo-99 の合成研究”, 2018 放射化学会年会・第 62 回放射化学討論会［京都］要旨集 3A07 (2018). **C**

5) 太田 朗生, 川端 方子, 本石 章司, 佐伯 秀也, 橋本 和幸, 塚田 和明, 初川 雄一, 永井 泰樹, “熱分離法を用いたがん治療用 ^{67}Cu 製造分離法の開発”, 2018 放射化学会年会・第 62 回放射化学討論会［京都］要旨集 P45 (2018). **N**

6) 初川 雄一, 橋本 和幸, 株木 重人, 櫛田 淳子, 塚田 和明, 浅井 雅人, 豊嶋 厚史, “テクネチウム同位体を用いたコンプトンカメラ撮像実験”, 2018 放射化学会年会・第 62 回放射化学討論会［京都］要旨集 1A10 (2018). **N**

7) 西中 一朗, 橋本 和幸, 鈴木 博元, “乾式蒸留法で調製した溶液中でのアスタチンの化学形”, 2018 放射化学会年会・第 62 回放射化学討論会［京都］要旨集 3A05 (2018). **N**

8) 瀬川 麻里子, 西中 一朗, 前田 亮, 藤 暢輔, “核医学用 ^{211}At 生成の効率化に向けたカメラ型アルファ線イメージング研究”, 2018 放射化学会年会・第 62 回放射化学討論会［京都］要旨集 3A04 (2018). **N**

9) 川﨑 康平, 新 裕喜, 青井 景都, 鷲山 幸信, 西中 一朗, 羽場 宏光, 矢納 慎也, 横山 明彦, “ラドンガス封入シリンジを利用した Rn-At ジェネレーターシステムの開発”, 2018 放射化学会年会・第 62 回放射化学討論会［京都］要旨集 P46 (2018). **N**

10) 新 裕喜, 川﨑 康平, 青井 景都, 横山 明彦, 鷲山 幸信, 西中 一朗, 矢納 慎也, 羽場 宏光, “^{211}Rn－^{211}At ジェネレーター開発のためのアスタチン溶媒抽出の研究 －^{131}I との抽出挙動の比較及び酸化剤の効果の調査－”, 2018 放射化学会年会・第 62 回放射化学討論会［京都］要旨集 P50 (2018).**N**

11) 伊藤 勇太, 秋山 和彦, 久冨木 志郎, 初川 雄一, “核反跳現象を利用した金属内包フラーレンの合成に関する研究”, 2018 放射化学会年会・第 62 回放射化学討論会［京都］要旨集 P52 (2018). **N**

Patent

1) 永井 泰樹, 橋本 和幸, 本石 章司, 佐伯 秀也, 川端 方子, 竹内 宣博, 椎名 孝行, 太田 朗生, “MoO$_3$ から ^{99m}Tc を熱分離精製する方法及びその装置”, 登録 6467574 (2019/01/25).

Press・TV

1) “医療用放射性物質 研究進む”, 読売新聞夕刊「なっとく科学」(2018/07/19)に加速器中性子製 Mo-99 の国産化研究に関する記事が掲載. **N**

P2-5　Project "Radiotracer Imaging"

Papers

1) M. Yamaguchi, Y. Nagao, N. Kawachi, "A simulation study on reduction of the background component using veto counters for imaging of therapeutic proton beams by measuring secondary electron bremsstrahlung using a parallel-hole collimator", Jpn. J. Appl. Phys., **58**, 021005-1-8 (2019).　　　　**N**

2) J. Kataoka,, A. Kishimoto, T. Taya, S. Mochizuki, L. Tagawa, A. Koide, K. Sueoka, H. Morita, T. Maruhashi, K. Fujieda, T. Kurihara, M. Arimoto, H. Okochi, N. Katsumi, S. Kinno, K. Matsunaga, H. Ikeda, E. Shimosegawa, J. Hatazawa, S. Ohsuka, T. Toshito, M. Kimura, Y. Nagao, M. Yamaguchi, K. Kurita, N. Kawachi, "Ultracompact Compton Camera for Innovative Gamma-ray Imaging", Nucl. Instrum. Meth. Phys. Res., A, **912**, 1-5 (2018).　　　　**N**

3) K. Hidaka, Y. Miyoshi, S. Ishii, N. Suzui, Y.-G. Yin, K. Kurita, K. Nagao, T. Araki, D. Yasutake, M. Kitano, N. Kawachi, "Dynamic analysis of photosynthate translocation into strawberry fruits using non-invasive ^{11}C-labeling supported with conventional destructive measurements using ^{13}C-labeling", Front. Plant Sci., **9**, 1946-1 [12 pages] (2019).　　　　**C, 2-27**

4) M. Sakai, R. K. Parajuli, M. Kikuchi, M. Yamaguchi, Y. Nagao, N. Kawachi, K. Arakawa, T. Nakano, "Effect of number of views on cross-sectional Compton imaging: A fundamental study with backprojection", Physica Medica, **56**, 1-9 (2018).　　　　**N**

5) M. Yamaguchi, M. Sakai, Y. Nagao, M. Kikuchi, K. Arakawa, N. Kawachi, "A novel estimation method of water-equivalent thicknesses of secondary particle tracks using secondary electron bremsstrahlung emitted from therapeutic ion beams for attenuation correction", Nucl. Instrum. Meth. Phys. Res., A, **954**, 161607 (2020).　　　　**N**

6) M. Sakai, M. Yamaguchi, Y. Nagao, N. Kawachi, M. Kikuchi, K. Torikai, T. Kamiya, S. Takeda, S. Watanabe, T. Takahashi, K. Arakawa, T. Nakano, "In vivo simultaneous imaging with ^{99m}Tc and ^{18}F using a Compton camera", Phys. Med. Biol., **63**, 205006 [12 pages] (2018).　　　　**N**

7) K. Kurita, M. Yamaguchi, Y. Nagao, N. Suzui, Y.-G. Yin, T. Yoshihara, N. Kawachi, "Development of an easy and simple method to measure the environmental radioactivity in trees with efficient personal dosimeters", RADIOISOTOPES, **67,** 427-434 (2018).　　　　**N**

8) S. Yamamoto, T. Akagi, T. Yamashita, J. Toivonen, M. Komori and N. Kawachi, "Source of luminescence of water lower energy than the Cerenkov-light threshold during irradiation of carbon-ion", J. Phys. Commun., **2**, 065010 [9 pages] (2019).　　　　**N**

9) Y. Nagao, M. Yamaguchi, S. Watanabe, N. S. Ishioka, N. Kawachi, H. Watabe, "Astatine-211 imaging by a Compton camera for targeted radiotherapy", Appl. Radiat. Isot., **139**, 238-243 (2018).　　　　**C, N**

10) Y. Nagao, M. Yamaguchi, N. Kawachi, H. Watabe, "Development of a cost-effective Compton camera using a positron emission tomography data acquisition system", Meth. Phys. Res., A, **912**, 20-23 (2018).　　　　**N**

11) 石岡 典子, 渡辺 茂樹, 大島 康宏, 坂下 哲哉, 河地 有木, "日本発 α 線放出核種を用いた がん治療薬剤の開発 ―製造からイメージングまで―", 月刊インナービジョン, **33**, 46-48 (2018).　　　　**C**

12) 山口 充孝, 長尾 悠人, 河地 有木, "粒子線がん治療における治療ビーム軌跡の二次電子制動輻射による画像化", Isotope News, **760**, 6-9 (2018).　　　　**N**

13) 田野井 慶太朗, 河地 有木, 古川 純, "植物科学における放射性トレーサイメージングの最前線", FBNews, **499**, 6-10 (2018).　　　　**C**

14) Y.-G. Yin, S. Ishii, N. Suzui, M. Igura, K. Kurita, Y. Miyoshi, N. Nagasawa, M. Taguchi and N. Kawachi, "On-line rapid purification of [^{13}N]N$_2$ gas for visualization of nitrogen fixation and translocation in nodulated soybean" , Appl. Radiat. Isot., **151**, 7-12 (2019).　　　　**C, 2-27, 2-29**

15) A. Wongkaew, S. Nakamura, N. Suzui, Y.-G. Yin, S. Ishii, N. Kawachi, K. Kojima, H. Sekimoto, T. Yokoyama, N. Ohkama-Ohtsu. "Elevated glutathione synthesis in leaves contributes to zinc transport from roots to shoots in Arabidopsis." Plant Sci., **283**, 416-442 (2019).　　　　**C, 2-28**

Proceedings

1) M. Yamaguchi, Y. Nagao, K. Ando, S. Yamamoto, M. Sakai, R. K. Parajuli, K. Arakawa, N. Kawachi, "Imaging of monochromatic beams by measuring secondary electron bremsstrahlung for carbon-ion therapy using a pinhole x-ray camera", 60th Annual Meeting and Exhibition American Association of Physicists in Medicine, Prgm. SU-E-202-6, [Nashville, U. S.] (2018/07).　　**N**

2) Y. Nagao, M. Yamaguchi, S. Watanabe, N.S. Ishioka, N. Kawachi, H. Watabe, "Maximum-likelihood reconstruction and simulation analysis on Compton imaging of astatine-211 for targeted α-particle radiotherapy", 2018 IEEE NSS/MIC, Prgm. M-14-411, [Sydney, Australia] (2018/11).　　　　**C**

3) M. Yamaguchi, Y. Nagao, N. Kawachi, "A simulation study on background reduction using veto counters for imaging of therapeutic proton beams by measuring secondary electron bremsstrahlung", 2018 IEEE NSS/MIC, Prgm. M-03-409, [Sydney, Australia] (2018/11).　　　　**N**

4) N. Kawachi, "Recent advances in radiation imaging techniques", Advanced Medical Imaging Physics: International Exchanges Between Egypt and Japan, Prgm. 4, [Cairo, Egypt] (2019/03).　**C**

Press・TV

1) "放射線照射により生じる水の発光現象の機序を解明、シミュレーションでも発光現象を評価可能に～新しい発光現象を利用した"高精度放射線イメージング機器"開発に期待～", 2018/06/28, プレス発表.　　　　**N**

P2-6　Project "Radiation and Biomolecular Science"

Papers

1) T. Kojima, H. Aihara, Y. Kodashima, H. Makishima, S. Nakiri, S. Takada, H. Shimada, M. Ukai, C. Ozga, X. Holzapfel, P. Schmidt, C. Küstner-Wetekam, H. Otto, D. Bloβ, A. Knie, A. Ehresmann, A. Yokoya, K. Fujii, Y. Fukuda, and Y. Saitoh, "Novel analytical study for reaction intermediates in the primary radiation interaction of DNA using a synchrotron radiation-induced luminescence spectroscopy", Radiat. Prot. Dosimetry **183**, 32-35 (2019).　　　　**N**

2) K. Nishikubo, Y. Izumi, Y. Matsumoto, K. Fujii, K. Matsuo, and A. Yokoya, "Structural analysis of DNA repair protein XRCC4 applying circular dichroism in an aqueous solution", Radiat. Prot.

Dosimetry **183**, 36-39 (2019). **N**

3) H. Nakaue, Y. Obata, K. Kaminaga, N. Akimitsu, and A. Yokoya, "Visualization of the DNA repair process in mammalian cells transfected with EGFP-expressing plasmid DNA after exposure to X-rays in vitro", Radiat. Prot. Dosimetry **183**, 79-83 (2019). **N**

4) R. Hamada, K. Kaminaga, K. Suzuki, and A. Yokoya, "Mitochondrial membrane potential, morphology and ATP production in mammalian cells exposed to X-rays", Radiat. Prot. Dosimetry **183**, 98-101 (2019). **N**

5) 渡辺 立子, 服部 佑哉, 横谷 明徳, "放射線照射による線量分布と生物影響の初期過程で生じる DNA 損傷応答のシミュレーション研究", 放射線 **44**, 131-144 (2019). **N**

6) 神長 輝一, "タイムラプスイメージングで観る X 線マクロビーム照射・非照射細胞の細胞周期変調", 放射線 **44**, 141-145 (2019). **N**

7) 横谷 明徳, "放射線生体影響解明に向けて進む放射光マイクロビーム評価技術（特集号・巻頭言）", 放射線 **44**, 125 (2019). **N**

8) K. Fujii, and A. Yokoya, "XANES spectral Changes of Hydrated Deoxyribose Induced by K-shell Ionization of Oxygen", AIP Conf. Proc. **2054**(1), 040005 (2019). **N**

9) T. Oka, A. Yokoya, K. Fujii, Y. Kino, and T. Sekine, "Substituent effect on the yield of unpaired electrons in DNA bases studied by electron paramagnetic resonance", Appl. Phys. Lett. **113**, 243701 (2018). **N**

10) T. Takayanagi, T. Nakatomi, and Y. Yonetani, "On the ion-pair dissociation mechanisms in the small $NaCl\text{-}(H_2O)_6$ cluster: A perspective from reaction path search calculations", J. Comp. Chem. **39**, 1835 (2018). **N**

11) Y. Yonetani, "Water access and ligand dissociation at the binding site of proteins", J. Chem. Phys. **149**, 175102 (2018). **N**

Proceedings

1) 横谷 明徳, "放射線 DNA 損傷と生物影響の関係"【招待講演】, 物理学会第 74 回年次大会, 要旨集 16pK404-4, ［九州大伊都キャンパス, 福岡](2019/03). **N**

2) K. Nishikubo, M. Hasegawa, Y. Izumi, K. Fujii, K. Matsuo, Y. Matsumoto, and A. Yokoya, "Structural change of DNA repair protein XRCC4 by phosphorylation at c-terminal revealed by VUV-CD", The 23rd Hiroshima International Symposium on Synchrotron Radiation, Poster Presentation, [Higashi-Hiroshima, Japan] (2019/03). **N**

3) M. Hirato, K. Fujii, A. Yokoya, S. Wada, Y. Baba, "Soft X-ray Spectroscopies for Br-incorporated DNA Nucleotide", The 23rd Hiroshima International Symposium on Synchrotron Radiation, Poster Presentation, [Higashi-Hiroshima, Japan] (2019/03). **N**

4) 西久保 開, 長谷川 真保, 藤原 悟, 松尾 龍人, 横谷 明徳, "VUV-CD を用いたリン酸化 XRCC4 の構造変化解析", 2018 年度 量子ビームサイエンスフェスタ, ポスター番号 163M, ［つくば国際会議場, 茨城](2019/03). **N**

5) 長谷川 真保, 西久保 開, 藤原 悟, 松尾 龍人, 横谷 明徳, "DNA 修復タンパク質のリン酸化構造の SAXS 解析", 2018 年度 量子ビームサイエンスフェスタ, ポスター番号 167M, ［つくば国際会議場, 茨城](2019/03). **N**

6) 平戸 未彩紀, 横谷 明徳, 馬場 祐治, 藤井 健太郎, "Br を含む DNA 関連分子の内殻電子状態の研究", 2018 年度 量子ビームサイエンスフェスタ, ポスター番号 043D, ［つくば国際会議場, 茨城](2019/03). **N**

7) 米谷 佳晃, "分子動力学シミュレーションによる DNA の水和構造解析と放射線損傷サイトの検証"【招待講演】, 分子科学研究所共同利用研究 第三回会合, ［分子科学研究所, 愛

8) 小畑 結衣, 平嵜 敬志朗, 横谷 明徳, "In vitro 照射プラスミドをトランスフェクションした細胞のライブセル観察"【招待講演】, 茨城大学理学部公開シンポジウム第 12 回 Quantum Medicine 研究会, 口頭発表, ［茨城大学, 茨城](2019/02). **N**

9) 藤井 健太郎, 横谷 明徳, M. A. Hervé du Penhoat, M. F. Politis, "XANES スペクトルによる放射線 DNA 鎖切断の観測", 第 32 回日本放射光学会年会・放射光科学合同シンポジウム, 要旨集 5B004, ［福岡国際会議場, 福岡](2019/01). **N**

10) 西久保 開, 長谷川 真保, 泉 雄大, 藤井 健太郎, 松尾 光一, 松本 義久, 横谷 明徳, "VUV-CD で見えてきた XRCC4 活性中心に対するリン酸化の分子内遠隔制御", 第 32 回日本放射光学会年会・放射光科学合同シンポジウム, ポスター番号 10P095, ［福岡国際会議場, 福岡](2019/01). **N**

11) 長谷川 真保, 西久保 開, 横谷 明徳, "DNA 修復タンパク質複合体形成過程に関する小角散乱研究の試み", 第 32 回日本放射光学会年会・放射光科学合同シンポジウム, ポスター番号 10P092, ［福岡国際会議場, 福岡](2019/01). **N**

12) 渡辺 立子, 服部 佑哉, 横谷 明徳, "DNA 損傷生成・応答に対する線量・線量率の影響モデル"【招待講演】, 日本放射線影響学会第 61 回年会, 要旨集 WS2-2, ［長崎ブリックホール, 長崎](2018/11). **N**

13) 服部 佑哉, 今岡 達彦, 横谷 明徳, 渡辺 立子, "放射線照射後の乳腺末梢芽状突起の細胞数動態推定モデル"【招待講演】, 日本放射線影響学会第 61 回年会, 要旨集 OS-1, ［長崎ブリックホール, 長崎](2018/11). **N**

14) 野口 実穂, 伊原 智一, 横谷 明徳, "正常ヒト線維芽細胞における放射線照射後の老化誘導に伴うオートファジー活性の変動", 日本放射線影響学会第 61 回年会, P2-22, ［長崎ブリックホール, 長崎](2018/11). **N**

15) 西久保 開, 長谷川 真保, 泉 雄大, 藤井 健太郎, 松尾 光一, 松本 義久, 横谷 明徳, "XRCC4 タンパク質の擬似リン酸化による構造変化の解析", 日本放射線影響学会第 61 回大会, 要旨集 P.48, ［長崎ブリックホール, 長崎](2018/11). **N**

16) 小畑 結衣, 平嵜 敬志朗, 横谷 明徳, "X 線照射した EGFP プラスミドの非照射細胞への導入と DNA 修復難易度の研究", 日本放射線影響学会第 61 回大会, 要旨集 P.72, ［長崎ブリックホール, 長崎](2018/11). **N**

17) 杉本 理峻, 浜田 涼, 服部 佑哉, 渡辺 立子, 立花 章, 横谷 明徳, "Ca2+濃度変化をパラメータとする放射線適応応答反応ネットワークのモデル化の試み", 日本放射線影響学会第 61 回大会, 要旨集 P.80, ［長崎ブリックホール, 長崎]（2018/11). **N**

18) 浜田 涼, 杉本 理峻, 木村 由佳, 神長 輝一, 鈴木 啓司, 横谷 明徳, "ヒト線維芽細胞における X 線照射によるミトコンドリアへの影響", 日本放射線影響学会第 61 回大会, 要旨集 P.91, ［長崎ブリックホール, 長崎](2018/11). **N**

19) 平戸 未彩紀, 横谷 明徳, 馬場 祐治, 藤井 健太郎, "X 線光電子分光法による Br を含む DNA 関連分子の内殻電子状態の研究", 日本放射線影響学会第 61 回大会, 要旨集 P.93, ［長崎ブリックホール, 長崎](2018/11). **N**

20) 鬼澤 美智, 芳賀 芳範, 田中 成典, 平戸 未彩紀, 横谷 明徳, "電子物性に着目したハロゲン化ピリミジンの放射線増感メカニズム解明の試み", 日本放射線影響学会第 61 回大会, 要旨集 P.97, ［長崎ブリックホール, 長崎](2018/11). **N**

21) 藤井 健太郎, 横谷 明徳, M-A. Hervé du Penhoat, M-F. Politis, "酸素 K 殻イオン化によって起こるデオキシリボースの分解過程", 第 12 回分子科学討論会, ポスター番号 4P083, [福岡国際会議場, 福岡](2018/09). **N**

22) 木村 由佳, 大内 則幸, 横谷 明徳, "薬剤及び X 線刺激に

よるヒト正常繊維芽細胞内のミトコンドリア動態の観察”，平成 30 年度 若手放射線生物学研究会 専門研究会，抄録集 14, [麻布大，神奈川](2018/09) .

23) 平戸 未彩紀，横谷 明徳，馬場 祐治，藤井 健太郎，“X 線光電子分光法による Br を含む DNA 関連分子の内殻電子状態の研究”，平成 30 年度 若手放射線生物学研究会 専門研究会，抄録集 16, [麻布大，神奈川] (2018/09) .　　　　N

24) 清野 晃平，宇佐美 徳子，鈴木 雅雄，“細胞内局所に対する X 線マイクロビーム照射の効果”，平成 30 年度 若手放射線生物学研究会 専門研究会，抄録集 17, [麻布大，神奈川] (2018/09) .　　　　N

25) 伊原 智一，野口 実穂，横谷 明徳，“放射線照射された細胞の細胞死回避メカニズムの解明”，平成 30 年度 若手放射線生物学研究会 専門研究会，抄録集 18, [麻布大，神奈川] (2018/09) .　　　　N

26) 長谷川 真保，西久保 開，松本 義久，藤原 悟，横谷 明徳，“DNA 修復応答タンパク質の活性化スイッチングとエピジェネティック構造変化の研究”，平成 30 年度 若手放射線生物学研究会 専門研究会，抄録集 19, [麻布大，神奈川] (2018/09) .　　　　N

27) 平嵜 敬志朗，小畑 結衣，横谷 明徳，“放射線照射した DNA の非照射細胞内での修復動態の観察”，平成 30 年度 若手放射線生物学研究会 専門研究会，抄録集 25, [麻布大，神奈川] (2018/09) .　　　　N

28) 小畑 結衣，平嵜 敬志朗，横谷 明徳，“非照射細胞へ導入した X 線及び制限酵素誘発鎖切断を含む EGFP プラスミド DNA の発現回復”，平成 30 年度 若手放射線生物学研究会 専門研究会，抄録集 26, [麻布大，神奈川] (2018/09) .　　　　N

29) 米谷 佳晃，中川 洋，横谷 明徳，甲斐 健師，“DNA の水和構造と放射線損傷サイトの関係：分子動力学シミュレーション解析”，日本物理学会 2018 年秋季大会，要旨集 10pA216-4, [同志社大学 京田辺キャンパス，京都](2018/09).

30) 米谷 佳晃，“蛋白質表面における水の水素結合組換え解析からリガンド解離の起源を探る”，日本物理学会 2018 年秋季大会，要旨集 9aM201-4, [同志社大学 京田辺キャンパス，京都](2018/09).　　　　N

31) 甲斐 健師，米谷 佳晃，“水の放射線分解で誘発された低エネルギー電子の動的挙動解析”，日本物理学会 2018 年秋季大会，要旨集 10pA216-3, [同志社大学 京田辺キャンパス，京都](2018/09).　　　　N

32) 横谷 明徳，“円二色性スペクトル測定による DNA 損傷応答タンパク質の二次構造変化の研究”【招待講演】，平成 30 年度 東京工業大学 科学技術創成研究院 先導原子力研究所 研究交流・発表会，[東工大・東京](2018/06).　　　　N

33) K. Fujii, A. Yokoya, ”XANES spectral changes of hydrated deoxyribose induced by K-ionization of oxygen”, International Conference on Synchrotron Radiation Instrumentation 2018, Poster Presentation, [Taipei, Taiwan] (2018/06).　　　　N

34) Y. Yonetani, “Dissociation kinetics of ion pair in water: Free-energy landscape analysis”, 第 34 回化学反応討論会，要旨集 1P28, [量子科学技術研究開発機構 関西木津，京都] (2018/06).　　　　N

35) 藤井 健太郎，横谷 明徳, M. A. Herve du Penhoat, M. F. Politis, “Proton transfers between a deoxyribose and hydrated waters after K-ionizations of constituent atoms”, 15th International Workshop on Radiation Damage to DNA, Poster Presentation, [Aussois, France] (2018/05).　　　　N

36) 西久保 開，泉 雄大，藤井 健太郎，松尾 光一，松本 義久，横谷 明徳，“VUV-CD を用いた XRCC4 タンパク質の活性化二次構造解析”，量子生命科学研究会第 2 回学術集会，要旨集 P.17, [東京大学弥生講堂一条ホール，東京](2018/05)．　　　　N

P2-7　Project "Biomolecular Function"

Papers

1) M. Adachi, R. Shimizu, C. S, Kato, T. Oikawa, "The first identification and characterization of a histidine-specific amino acid racemase, histidine racemase from a lactic acid bacterium, *Leuconostoc mesenteroides* subsp. sake NBRC 102480", Amino Acids, **51**, 331-343 (2019).　　　　N

2) M. Adachi, R. Shimizu, C. Shibazaki, K. Satoh, S. Fujiwara, S. Arai, I. Narumi, R. Kuroki, "Extended Structure of Pleiotropic DNA Repair-Promoting Protein PprA from the Extreme Radiation Resistance of *Deinococcus radiodurans*", FASEB J., **33**, 3647-3658 (2019).　　　　N

3) L. Li, M. Adachi, J. Yu, K. Kato, A. Shinoda, A. Ostermann, T.E. Schrader, T. Ose, M. Yao, "Neutron crystallographic study of heterotrimeric glutamine amidotransferase CAB", Acta Crystallogr. F Struct. Biol. Commun., **75**, 193-196 (2019).　　N

4) F.A. Laksmi, S. Arai, H. Tsurumaru, Y. Nakamura, B. Saksono, M. Tokunaga, M. Ishibashi, "Improved substrate specificity for D-galactose of L-arabinose isomerase for industrial application", Biochim. Biophys. Acta Proteins Proteom., **1866**, 1084-1091 (2018).　　　　N

5) C. Shibazaki, S. Arai, R. Shimizu, M. Saeki, T. Kinoshita, A. Ostermann, T.E. Schrader, Y. Kurosaki, T. Sunami, R. Kuroki, M. Adachi, "Hydration structures of the human protein kinase CK2α clarified by joint neutron and X-ray crystallography", J. Mol. Biol., **430**, 5094-5104 (2018).　　　　N

6) K. Hidaka, T. Kimura, R. Sankaranarayanan, J. Wang, K.F. McDaniel, D.J. Kempf, M. Kameoka, M. Adachi, R. Kuroki, J.T. Nguyen, Y. Hayashi, Y. Kiso, "Identification of Highly Potent Human Immunodeficiency Virus Type-1 Protease Inhibitors against Lopinavir and Darunavir Resistant Viruses from Allophenylnorstatine-Based Peptidomimetics with P2 Tetrahydrofuranylglycine", J. Med. Chem., **61**, 5138-5153 (2018).　　　　N

7) S. Mahatabuddin, D. Fukami, T. Arai, Y. Nishimiya, R. Shimizu, C. Shibazaki, H. Kondo, M. Adachi, S. Tsuda, "Polypentagonal ice-like water networks emerge solely in an activity-improved variant of ice-binding protein", Proc. Natl. Acad. Sci. USA., **115**, 5456-5461 (2018).

Proceedings

1) 石川 昂汰，佐藤 圭，小俣 和輝，小笠 甲人，安達 基泰，加藤 尚志，“ネッタイツメガエル赤血球産生因子エリスロポエチンの構造と種交差性”，日本動物学会関東支部 第71回大会,[東京]，要旨集 P-074 (2019).　　　　N

2) 尾瀬 農之，李 龍，安達 基泰，姚 閔，“グルタミンアミドトランスフェラーゼCAB複合体のX線・中性子線結晶構造解析”，2018 年度量子ビームサイエンスフェスタ, [つくば]，要旨集 134L (2019).　　　　N

3) 日高 興士，安達 基泰，北條 恵子，津田 裕子，“リムーバブル阻害剤の薬剤感受性試験への新規利用法”，第32回日本エイズ学会学術集会, [大阪]，要旨集 07-033 (2018).　N

4) F.A. Laksmi, S. Arai, H. Tsurumaru, M. Ishibashi, "Improved substrate specificity for D-galactose of L-arabinose isomerase for industrial application", 第 25 回日本生物工学会 九州支部鹿児島大会, [鹿児島], C-p07 (2018). **N**

5) M. Hirai, S. Ajito, S. Arai, S. Takata, H. Iwase, "DETERMINATION OF PROTEIN STRUCTURE IN MIMIC-CELL MOLECULAR CROWDING", XVII International Small Angle Scattering Conference - SAS2018, [Michigan USA], A281, PST-99 (2018). **N**

6) 日高 興士, 安達 基泰, 北條 恵子, 津田 裕子, "リムーバブル阻害剤を利用するプロテアーゼ活性の ON/OFF 繰り返し制御", 第 23 回日本病態プロテアーゼ学会学術集会, [甲府], 要旨集 演題番号 30 (2018). **N**

7) C. Shibazaki, R. Shimizu, S. Arai, M. Adachi, "Long hydrogen bonding network responsible for catalytic activity of human casein kinase II", 3rd International Symposium of Quantum Beam Science at Ibaraki University in 2018, [Mito Japan], P-2 (2018).**N**

8) M. Adachi, "Methyl Configurations Observed by Neutron Crystallography in Perdeuterated Proteins", Meeting on Deuterium Labeled Compound for Neutron Science, [Ibaraki Japan], (2018). **N**

9) M. Adachi, C. Shibazaki, R. Shimizu, S. Arai, A. Ostermann, T.E. Schrader, "First neutron structural analysis of human casein kinase II", The 31st European Crystallographic Meeting (ECM31), [Oviedo Spain], (2018). **N**

Book

1) 安達 基泰, "第3章 中性子解析に基づく不凍タンパク質の分子機能解明", 不凍タンパク質の機能と応用, シーエムシー出版, 39-46 (2018). **N**

Press・TV

1) "氷が張り付いた分子表面を発見 － 優れた凍結制御物質をデザインするヒントに －", 2018/05/08, プレス発表：科学新聞(2018/05/18)に掲載. **N**

P2-8　Project "Biomolecular Structure and Dynamics"

Papers

1) M. Ueda, Y. Hirano, H. Fukuhara, Y. Naka, M. Nakazawa, R. Sakamoto, Y. Ogata and T. Tamada, "Gene cloning, expression, and X-ray crystallographic analysis of a β-mannanase from *Eisenia fetida*", Enzyme Microb. Technol., **117**, 15-22 (2018). **N**

2) K. Kurihara, Y. Hirano, K. Oikawa, M. Harada, T. Nakamura and T. Tamada. "Instrument and shielding design of a neutron diffractometer at J-PARC for protein crystallography covering crystals with large unit-cell volume", J. Appl. Cryst., **51**, 596-605 (2018). **N**

3) K. Tashiro, K. Kusaka, T. Hosoya, T. Ohhara, M. Hansaka, Y. Yoshizawa, H. Yamamoto, N. Niimura, I. Tanaka, K. Kurihara, R. Kuroki and T. Tamada, "Structure Analysis and Derivation of Deformed Electron Density Distribution of Polydiacetylene Giant Single Crystal by the Combination of X-ray and Neutron Diffraction Data", Macromolecules, **51**, 3911-3922 (2018). **N**

4) T. Chatake, Y. Yanagisawa, R. Inoue, M. Sugiyama, T. Matsuo, S. Fujiwara, T. Ohsugi and H. Sumi, "Purification and structural characterization of water-soluble menaquinone-7 produced by *Bacillus subtilis natto*", J. Food Biochem., **42**, e12630 (2018). **N**

5) N. Okazaki, M. Blaber, R. Kuroki T. Tamada, "Crystal structure of glycosyltrehalose synthase from *Sulfolobus shibatae* DSM5389", Acta Crystallogr. F**74**, 741-746 (2018). **N**

6) M. Adachi, R. Shimizu, C. Shibazaki, K. Satoh, S. Fujiwara, S. Arai, I. Narumi and R. Kuroki, "Extended structure of pleiotropic DNA repair-promoting protein PprA from *Deinococcus radiodurans*", FASEB J., **33**, 3647-3658 (2019). **N**

7) K. Tomoyori, K. Kurihara and T. Tamada, "The design of a versatile TOF neutron diffractometer providing the complementary use of neutron and X-ray scattering from a biomacromolecular single-crystal with large unit cells", J. Phys. Conf. Proc., **22**, 011026 (2018). **N**

8) T. Matsuo, F. Kono and S. Fujiwara, "Effects of the cardiomyopathy-causing E244D mutation of troponin T on the structures of cardiac thin filaments studied by small-angle X-ray scattering", J. Struct. Biol., **205**, 196-205 (2019). **N**

9) T. Nakamura, K. Hirata, K. Fujimiya, M. Chirifu, T. Arimori, T. Tamada, S. Ikemizu and Y. Yamagata, "X-ray Structure Analysis of Human Oxidized Nucleotide Hydrolase MTH1 using Crystals Obtained under Microgravity", Int. J. Microgravity Sci. Appl., **36**, 36103 (2019). **N**

Proceedings

1) 平野 優, "量子ビーム（X 線と中性子）を相補的に利用した酸化還元タンパク質の高分解能立体構造解析", 量子生命科学研究会第 2 回学術集会, [東京] (2018). **N**

2) K. Kurihara, Y. Hirano and T Tamada, "A neutron diffractometer at J-PARC for protein crystallography covering crystals with large unit-cell volume", 3rd International Symposium of Quantum Beam Science at Ibaraki University, [Mito, Japan] (2018). **N**

3) T. Tamada, "High-resolution neutron crystal structural studies of electron transfer proteins", 3rd International Symposium of Quantum Beam Science at Ibaraki University, [Mito, Japan] (2018). **N**

4) Y. Hirano, "X-ray and neutron structure analyses of redox proteins at high-resolutions", 3rd International Symposium of Quantum Beam Science at Ibaraki University, [Mito, Japan] (2018). **N**

5) 平野 優, 栗原 和男, 日下 勝弘, 木村 成伸, 三木 邦夫, 玉田 太郎, "酸化型 NADH シトクロム b5 還元酵素の中性子構造解析", 第 18 回日本蛋白質科学会年会, [新潟], 要旨集 2WE-03 (2018). **N**

6) 平野 優, 中 裕規, 上田 光宏, 玉田 太郎, "*Eisenia fetida* 由来酵素の構造安定性と低温活性の相関", 第 18 回日本蛋白質科学会年会, [新潟], 要旨集 2P-022 (2018). **N**

7) 玉田 太郎, 平野 優, 栗原 和男, "電子伝達タンパク質の中性子構造解析", 平成 30 年度 J-PARC MLF 産業利用報告会, [東京] (2018). **N**

8) 玉田 太郎, "量子科学技術研究開発機構における研究紹介", 平成 30 年度 iBIX-JAXA-KEK-QST 合同タンパク質研究会, [東京], (2018). **N**

9) T. Tamada, "Combined Use of Neutron and X-ray crystallography for Structural Biology", 平成 30 年度化学系学協会東北大会, [秋田] (2018). **N**

10) T. Matsuo, T. Arata, T. Oda, K. Nakajima, S. Kawamura, T. Kikuchi, D. Tominaga, F. Kono and S. Fujiwara, "Analysis of the picosecond dynamics of muscle contractile proteins and their hydration water by quasielastic neutron scattering", 第 56 回日本生物物理学会年会, [岡山], 要旨集 1SDA-3 (2018). **N**

11) S. Fujiwara, T. Matsuo, F. Kono and K. Shibata, "The multiscale dynamics of proteins measured by quasielastic neutron scattering and dynamic light scattering", 第 56 回日本生物物理学会年会,

[岡山], 要旨集 1M1430 (2018).　　　　　　　**N**

12) Y. Hirano, K. Kurihara, A. Ostermann, K. Kusaka, S. Kimura, K. Miki and T. Tamada, "Neutron structure analysis of NADH cytochrome b₅ reductase", German Conference for Research with Synchrotron Radiation, Neutron and Ion Beams at Large Facilities 2018, [Munchen, Germany] (2018).　　　**N**

13) 玉田 太郎, 平野 優, 中 裕規, 上田 光宏, "*Eisenia fetida* 由来酵素の構造安定性と低温活性の相関", 平成 30 年度日本結晶学会年会, [東京], 要旨集 PC-II-23 (2018).　**N**

14) 平野 優, 栗原 和男, 日下 勝弘, A. Ostermann, 木村 成伸, 三木 邦夫, 玉田 太郎, "NADH シトクロム b5 還元酵素の高分解能構造解析", 平成 30 年度日本結晶学会年会, [東京], 要旨集 PC-II-24 (2018).　**N**

15) S. Fujiwara, "Protein deuteration for neutron scattering", Meeting on Deuteration Labeled Compound for Neutron Science, [Tokai, Japan] (2018).　　　　　　　　　　**N**

16) 玉田 太郎, "量子科学技術研究開発機構における中性子構造生物学への取り組み", iBIX 将来構想研究会, [東京] (2018).　　　　　　　　　　　　　　**N**

17) 玉田 太郎, "複数の量子ビームを相補的に用いたタンパク質の構造研究", 第 3 回次世代生物研究会, [大阪] (2018).　**N**

18) Y. Hirano, K. Kurihara, A. Ostermann, K. Kusaka, S. Kimura, K. Miki and T. Tamada, "Neutron crystal structure studies of the oxidized form of NADH cytochrome b₅ reductase", Asian Crystallographic Association Conference 2018, [Auckland, New Zealand] (2018).　　　　　　　　　**N**

19) T. Tamada, Y. Hirano, Y. Naka and M. Ueda, "Improving the low-temperature activity of β-mannanase based on its structural information", Asian Crystallographic Association Conference 2018, [Auckland, New Zealand], (2018).　**N**

20) 松尾 龍人, 菊地 龍弥, 古府 麻衣子, 河野 史明, 藤原 悟, "中性子準弾性散乱で観る心筋細いフィラメントの Ca²⁺による揺らぎ変化", 日本中性子科学会第 18 回年会, [水戸], 要旨集 P2-25 (2018).　　　**N**

21) 河野 史明, 松尾 龍人, 高田 慎一, 杉本 泰伸, 藤原 悟, "小角散乱によるヒト α-シヌクレインのアミロイド線維の構造解析", 日本中性子科学会第 18 回年会, [水戸], 要旨集 P2-28 (2018).　　　　　　　　　　**N**

22) 栗原 和男, 平野 優, 玉田 太郎, "生体高分子用中性子回折装置 BIX-3,4 の稼働再開に向けた取り組み", 日本中性子科学会第 18 回年会, [水戸], 要旨集 P2-43 (2018).　**N**

23) 松尾 龍人, "X 線散乱と中性子散乱で観る筋タンパク質水和水の構造・ダイナミクス", 「水和と ATP エネルギー」研究会, [仙台] (2019).　　　　　　　　　　　　**N**

24) 藤原 悟, "小角散乱, 中性子準弾性散乱, 中性子結晶解析による蛋白質水和水の統一的解析", 「水和と ATP エネルギー」研究会, [仙台] (2019).　　　　　　　　**N**

25) 長谷川 真保, 西久保 開, 松尾 龍人, 藤原 悟, 横谷 明徳, "DNA 修復タンパク質のリン酸化構造の SAXS 解析", 2018 年度量子ビームサイエンスフェスタ, [つくば] (2019).　**N**

P3-1　Project "LCS Gamma-ray"

Papers

1) M. Akemoto, D. Arakawa, S. Asaoka, E. Cenni, M. Egi, K. Enami, K. Endo, S. Fukuda, T. Furuya, K. Haga, R. Hajima, K. Hara, K. Harada, T. Honda, Y. Honda, T. Honma, K. Hosoyama, E. Kako, H. Katagiri, H. Kawata, Y. Kobayashi, Y. Kojima, Y. Kondou, O. Tanaka, T. Kume, M. Kuriki, H. Matsumura, H. Matsushita, S. Michizono, T. Miura, T. Miyajima, S. Nagahashi, R. Nagai, H. Nakai, H. Nakajima, N. Nakamura, K. Nakanishi, K. Nigorikawa, N. Nishimori, T. Nogami, S. Noguchi, T. Obina, F. Qiu, H. Sagehashi, H. Sakai, S. Sakanaka, S. Sasaki, K. Satoh, M. Sawamura, M. Shimada, K. Shinoe, T. Shishido, M. Tadano, T. Takahashi, R. Takai, T. Takenaka, Y. Tanimoto, T. Uchiyama, A. Ueda, K. Umemori, K. Watanabe, M. Yamamoto, "Construction and commissioning of the compact energy-recovery linac at KEK", Nucl. Instrum. Meth. Phys. Res., A. **877**, 197-219 (2018).　**N**

2) T. Hayakawa, Y. Hatsukawa, T. Tanimori, "⁹⁵ᵍTc and ⁹⁶ᵍTc as alternatives to medical radioisotope ⁹⁹ᵐTc", Heliyon, Volume **4**, Issue 1, January 2018, e00497.　　　　　　**N**

3) M. Sawamura, M. Egi, K. Enami, T. Furuya, H. Sakai and K. Umemori, "Properties of the RF transmission line of a C-shaped waveguide", Nucl. Instrum. Meth. Phys. Res. A, **882**, 30-40 (2018).　　　　　　　　　　　　　　**N**

4) N. Nishimori, R. Nagai, M. Sawamura and R. Hajima, "Development of a Multialkali Photocathode Dc Gun for a Smith-Purcell Terahertz Free-Electron Laser", Particles, **1**(1), 166-174 (2018).　　　　　　　　　　　　　　**N**

5) T. Hayakawa, H. Ko, M. -K. Cheoun, M. Kusakabe, T. Kajino, M. D. Usang, S. Chiba, K. Nakamura, A. Tolstov, K. Nomoto, M. Hashimoto, M. Ono, T. Kawano and G. J. Mathews, "Short-Lived Radioisotope ⁹⁸Tc Synthesized by the Supernova Neutrino Process", Phys. Rev. Lett. **121**, 102701 (2018).　**N**

6) H. Zen, T. Hayakawa, E. Salehi, M. Fujimoto, T. Shizuma, J.K. Koga, T. Kii, M. Katoh, H. Ohgaki, "Generation of 1-MeV quasi-monochromatic gamma-ray for precise measurement of Delbrück scattering by laser Compton scattering", J. Phys.: Conference Series **1067**, 092003 (2018).　　　　　　　**N**

7) T. Shizuma, N. Iwamoto, A. Makinaga, R. Massarczyk, R. Schwengner et al., "Dipole strength distribution in ²⁰⁶Pb for the evaluation of the neutron capture cross section of ²⁰⁵Pb", Phys. Rev. C, **98**, 064317 (2018).　　　　　　　　　　**N**

8) N. Iwamoto and T. Shizuma, "Evaluation of neutron capture cross section on ²⁰⁵Pb with photonuclear data", EPJ Web Conf, **178**, 06004 (2018).　　　　　　　　　　　　**N**

9) A.P. Tonchev, N. Tsoneva, S. Goriely, C. Bhaita, C. W. Arnold, S. L. Hammond, J. H. Kelley, E. Kwan, H. Lenske, J. Piekarewicz, R. Raut, G. Rusev, T. Shizuma, and W. Tornow, "Astrophysical relevance of the low-energy dipole strength of ²⁰⁶Pb", EPJ Web Conf, **178**, 1(2018).

10) J. W. Shin, M. -K. Cheoun, T. Kajino and T. Hayakawa, "Spectral shape analysis for electron antineutrino oscillation study by using ⁸Li generator with ²⁵²Cf source", Journal of Cosmology and Astroparticle Physics, Volume **2018**, 024 (2018).　**N**

11) Y. Hatsukawa, T. Hayakawa, K. Tsukada, K. Hashimoto, T. Sato, M. Asai, A. Toyoshima, T. Tanimori, S. Sonoda, S. Kabuki, H. Kimura, A. Takada, T. Mizumoto, S. Takaki, "Electron tracking Compton camera imaging of technetium-95m", PLoS ONE **13**(12): e0208909 (2018).　　　　　　　　　**N**

12) Y. Kikuchi, K. Ogata, T. Hayakawa, S. Chiba, "Azimuthal angle distributions of neutrons emitted from the ⁹Be(γ,n) reaction with linearly polarized γ-rays", Phys. Rev. C, **98**, 064611 (2018).　**N**

13) 朝比奈 隆志, 田中 浩基, 安部 勇輝, 森 芳孝, 余語 覚文, 長友 英夫, 花山 良平, 早川 岳人, "レーザー駆動中性子源のパルス幅評価", レーザー研究, Vol.**46**、No.10、594 (2018).　　　　　　　　　　　　　　**N**

Proceedings

1) N. Nishimori, R. Hajima, R. Nagai, M. Sawamura, "Development of a Multialkali Photocathode DC Gun for High Current Operation", Proceedings of ERL17, the 59th ICFA Advanced Beam Dynamics Workshop on Energy Recovery Linacs [Geneva, Switzerland] (2017/06).　　　　　　**N**

2) Y. Iwashita, S. Yamamoto, N. Kawamura, D. Nomura, T. Yamazaki, S. Makimura, K. Shimomura, T. Hayakawa, K. Mishima, "Diversified Application of ILC", Proceedings of 9th International Particle Accelerator Conference IPAC2018, pp.502-504 [Vancouver, BC, Canada] (2018/04)　　　**N**

3) 羽島 良一, 永井 良治, "高次高調波によるアト秒 X 線発生のための中赤外自由電子レーザの位相安定化方法の提案", 第 15 回日本加速器学会年会論文集, pp.152-156. [長岡, 新潟] (2018/08).　　　　　　　　　**N**

4) 全 炳俊, 紀井 俊輝, 大垣 英明, 羽島 良一, "京都大学中赤外自由電子レーザの引き出し効率測定",第 15 回日本加速器学会年会論文集, pp.162-166.[長岡, 新潟] (2018/08).　　**N**

5) 山本 将博, 西森 信行, 宮島 司, 本田 洋介, 羽島 良一, "compact-ERL DC 電子銃の 500 kV 長期安定運転", 第 15 回日本加速器学会年会論文集, pp.189-193. [長岡, 新潟] (2018/08).　　　　　　　　　**N**

6) 沢村 勝, 羽島 良一, 佐伯 学行, 岩下 芳久, 頓宮 拓, 中村 哲朗, 渡邉 直久, "超伝導スポーク空洞製作の現状", 第 15 回日本加速器学会年会論文集, pp.418-420 [長岡, 新潟] (2018/08).　　　　　　　　　**N**

7) 羽島 良一, 早川 岳人, 静間 俊行, 沢村 勝, 永井 良治, 宮本 修治, 松葉 俊哉, "次世代ガンマ線源のための帯域可変ガンマ線分光器の開発", 第 15 回日本加速器学会年会論

文集, pp.826-830 [長岡, 新潟] (2018/08).　　　**N**

8) 沢村 勝, 羽島 良一, 阪井 寛志, 梅森 健成, 許斐 太郎, 古屋 貴章, "C 形導波管型 HOM カップラーの開発", 第 15 回日本加速器学会年会論文集, pp.934-937 [長岡, 新潟] (2018/08).　　　　　　　　　**N**

9) 松葉 俊哉, 川瀬 啓悟, 宮本 篤, 佐々木 茂美, 藤本 將輝, 許斐 太郎, 山本 尚人, 保坂 将人, 加藤 政博, "タンデムアンジュレータによるベクトルビーム発生", 第 15 回日本加速器学会年会論文集, pp.167-170 [長岡, 新潟] (2018/08).　　**N**

10) 川瀬 啓悟, 加藤 龍好, 磯山 悟朗, "産研 FEL 光共振器の詳細評価", 第 15 回日本加速器学会年会論文集, pp.343-345[長岡, 新潟] (2018/08).　　　　　　　**N**

11) 野津 庄平, 松葉 俊哉, 川瀬 啓悟, "電子バンチ長評価を目指した放射光による 2 光子干渉計測システムの構築", 第 15 回日本加速器学会年会論文集, pp.541-543[長岡, 新潟] (2018/08).　　　　　　　　　**N**

12) 宮島 司, 布袋 貴大, 本田 洋介, 島田 美帆, 高井 良太, 帯名 崇, 加藤 龍好, 永井 良治, "cERL における空間電荷効果が支配的な電子ビームの光学関数とエミッタンス補償条件の改善", 第 15 回日本加速器学会年会論文集, pp.376-380[長岡, 新潟] (2018/08).　　　　　　　**N**

Press・TV

1) "超新星爆発ニュートリノで宇宙核時計テクネチウム 98 が生成されることを予言-ニュートリノ天体観測及び始原的隕石の分析による検証が期待される-",プレス発表：日本経済新聞朝刊他 29 件に掲載(2018/09/04).　　　　　**N**

2) "渦を巻いて飛行する「光子渦」の量子状態を調べる手法を提案", プレス発表：Nanotech Japan 他 1 件に掲載(2019/01/11).　　　　　　　　　**N**

P3-2　Beam Engineering Section

Papers

1) T. Ohshima, T. Satoh, H. Kraus, G. V. Astakhov, V. Dyakonov and P. G. Baranov, "Creation of Silicon Vacancy in Silicon Carbide by Proton Beam Writing toward Quantum Sensing Applications", J. Phys. D: Appl. Phys. 51, 333002-1-14 (2018). [Topical Review],　　　　　　　　　　　　**E, I, S, 1-01**

2) Y. Yamazaki, Y. Chiba, T. Makino, S. -I. Sato, N. Yamada, T. Satoh, Y. Hijikata, K. Kojima, S. -Y. Lee and T. Ohshima, "Electrically controllable position-controlled color centers created in SiC pn junction diode by proton beam writing", J. Mater. Res., **33**, 3355-3361 (2018).　　　　　　　　　　　　**S**

3) T. Kurobori, W. Kada, T. Shirao and T. Satoh, "Two-photon excited microscale colour centre patterns in Ag-activated phosphate glass written using a focused proton beam", Jap. J. Appl. Physics, **57**, 02CC01-1 - 02CC01-7 (2018).　　　**S**

4) Y. Ishii, T. Ohkubo, H. Kashiwagi and Y. Miyake, "Development of a prototype PIG ion source with electric magnets for a compact ion microbeam system", AIP Conference Proceedings, **2011**, 080015-1 - 080015-3 (2018/09).　　　　　　　**N**

5) H. Kashiwagi and K. yamada, "Laser-plasma-generation system with controlled interpulse delays between two laser shots: System and preliminary experiments", AIP Conference Proceedings, **2011**, 030012-1 - 030012-3 (2018).　　　　　　　**N**

6) S. Watanabe, Y. Katai, H. Matsuura, W. Kada, M. Koka, T. Satoh and T. Arai, "Ion beam induced luminescence of complexes formed in adsorbent for MA recovery process", Nucl. Inst. Meth. Phys. Res. B, **450,** 61-65 (2019).　　　　　**S, 3-09**

7) K. Hirata, K. Yamada, A. Chiba, Y. Hirano, K. Narumi, Y. Saitoh,

"0.12–0.54 MeV C_{60} ion impacts on a poly(methyl methacrylate) target: Characterization through emission properties of negative secondary ions", Nucl. Inst. Meth. Phys. Res. B **460**, 161-164 (2019).　　　　　　　　　　　**T, I, 3-06**

Proceedings

1) 長谷 純宏, 佐藤 勝也, 千葉 敦也, 平野 貴美, 齋藤 勇一, 鳴海 一雅 "生物試料に対する MeV 級クラスターイオン照射効果の検討" 第 17 回放射線プロセスシンポジウム, [東京], 講演要旨・ポスター発表要旨集, 89, (2018).　　　**T, 2-13**

2) 長谷 純宏, 佐藤 勝也, 千葉 敦也, 平野 貴美, 齋藤 勇一, 鳴海 一雅, "生物試料に対する MeV 級クラスターイオン照射効果の検討", 第 1 回重・クラスターイオンビーム利用による微生物由来高生産性, エネルギー, 環境シンポジウム, [つくば], 14, (2019).　　　　　　　　　　**T, 2-13**

3) Y. Kaneko, H. Hayashi, Y. Ishii, W. Kada, H. Nishikawa, "Refractive index change and thermo-optic effect in polydimethylsiloxane nanocomposites with oxide nanoparticles induced by proton beam writing", Paper No. O26, 16th International Conference on Nuclear Microprobe Technology and Applications (2018/07).　　　　　　　　**S, 3-02**

4) T. Shibuya, S. Uchida, Y. Ishii, H. Nishikawa, "Assembling gold nanoparticles by dielectrophoresis with pit arrays on PMMA fabricated by proton beam writing", Paper No. P15, 16th International Conference on Nuclear Microprobe Technology and Applications (2018/07).　　　　　　　　　**S, 3-02**

5) N. Miyawaki, M. Fukuda, S. Kurashima, H. Kashiwagi, " Evaluation of phase bunching for a harmonic acceleration system

in a cyclotron", Proceedings of the 15th Annual Meeting of Particle Accelerator Society of Japan, 869-872 (2018).　**C, 3-17**

6) H. Kashiwagi, N. Miyawaki, S. Kurashima, "Preliminary results of four-dimensional emittance estimation using slit-harp device", Proceedings of the 15th Annual Meeting of Particle Accelerator Society of Japan (2018) 566-568.　**C, 3-17**

7) 百合 庸介, 湯山 貴裕, 吉田 健一, 石坂 知久, "非線形集束によるビーム強度分布の変換とその利用", Proceedings of the 15th Annual Meeting of Particle Accelerator Society of Japan, pp. 678-681(2018/08).　**C, 3-01**

8) 明午 伸一郎, 武井 早憲, 松田 洋樹, 百合 庸介, 湯山 貴裕, "大強度陽子加速器のための標的上のプロファイルモニタの開発", Proceedings of the 15th Annual Meeting of Particle Accelerator Society of Japan, pp. 1035-1039(2018/08).　**C, 3-01**

9) K. Hirata, K. Yamada, A. Chiba, Y. Hirano, K. Narumi, Y. Saitoh, "Highly-sensitive time-of-flight secondary ion mass spectrometry with high energy cluster ion beams", 10th International

Symposium on Swift Heavy Ions in Matter & 28th International Conference on Atomic Collisions in Solids (SHIM-ICACS 2018)　**T, I, 3-06**

10) 平田 浩一、山田 圭介、斎藤 勇一、鳴海 一雅、千葉 敦也、平野 貴美、冨田 成夫、笹 公和、「高感度微小領域分析を目指した高速クラスターイオン照射の高度化」、日本物理学会第74回年次大会、　**T, I, 3-06**

11) T. Yuyama, S. Kurashima, A. Chiba, K. Yoshida, K. Yamada, T. Ishizaka, A. Yokoyama, Y. Hirano, S. Hosoya, N. Miyawaki, H. Kashiwagi, Y. Yuri, T. Satoh, T. Ohkubo, I. Ishibori, S. Okumura, T. Nara, "PRESENT STATUS OF TIARA AT QST", Proc. 15th Annu. Meet. Part. Accel. Soc. Jpn., 1365-1368, (2018).　**C, 4-02**

Patents

1) 福田 光宏, 百合 庸介, "荷電粒子ビーム強度分布可変装置, 荷電粒子ビーム強度分布可変方法, 二次粒子生成装置, 及び放射性同位体生成装置", 特願 2018-207270（2018/11/02 出願）.　**C, 3-01**

External Research Groups Except for Takasaki Advanced Radiation Research Institute

Papers

1) C. Ohmori and M. Paoluzzi, "Development of Radiation-Hard Solid-State Amplifiers for kilo-Gray Environments Using COTS Components", submitted to IEEE TNS on Mar. 13, 2019. **G, 1-05**

2) N. Inoue and Y. Kawamura, "Nitrogen – point defect complexes in as-grown, annealed and irradiated CZ and FZ silicon studied by infrared absorption," J. Appl. Phys., **123**, 185701 (2018); doi: 10.1063/1.5011224.　**E, 1-08**

3) K. Nakata, Y. Noguchi, M. Saito, N. Takeda, "Effects of humidity on radiation resistance of electroless Ni plating", Fusion Eng. Des., **140**, 97-101 (2019).　**G, 1-27**

Proceedings

1) J. Furuta, Y. Tsukita, K. Yamada, M. Ebara, K. Kojima and K. Kobayashi, "Impact of Combinational Logic Delay for Single Event Upset on Flip Flops in a 65 nm FDSOI Process," 2019 IEEE International Reliability Physics Symposium (IRPS), Monterey, CA, USA, 2019, pp. 1-4. doi: 10.1109/IRPS.2019.8720570, URL: http://ieeexplore.ieee.org/stamp/stamp.jsp?tp=&arnumber=8720570&isnumber=8720395,　**C, 1-04**

2) T. Okazaki et al., "Preliminary study of the portable Optically Stimulated Luminescence dosimetry system for measuring radiation doses more than 100 Gy, THP137, in Proceedings of the 15th Annual Meeting of PASJ, p.1256-1259, Nagaoka, Japan, (2018/08).　**G, 1-05**

3) 井上 直久, 川又 修一, "シリコン結晶の高感度赤外吸収と赤外欠陥動力学(13)低濃度窒素の挙動と測定", 第 78 回応用物理学会, 19p-131-13[名古屋国際会議場・名古屋](2018/09).　**E, 1-08**

4) 井上 直久, 川又 修一, "シリコン結晶中の低濃度炭素の測定 (XVI)低温における1×10¹³cm⁻³ までの赤外吸収測定," 第 78 回応用物理学会, 19p-131-14 [名古屋国際会議場・名古屋](2018/09).　**E, 1-08**

5) 井上 直久, 川又 修一, "シリコン結晶中の低濃度炭素の測定 (XVII) 1014atoms・cm⁻³ のポリシリコンの赤外吸収測定,"第 78 回応用物理学会, 19p-131-15 [名古屋国際会議場・名古屋](2018/09).　**E, 1-08**

6) N. Inoue, S. Okuda and S. Kawamata, "Measurement of Low Carbon Concentration in Polycrystalline Silicon by Second Generation Infrared Absorption Spectroscopy", ECS Transactions

Vol. 86(10), pp. 87-94 (2018/10).　**E, 1-08**

7) N. Inoue, S. Okuda and S. Kawamata, "Measurement of low concentration nitrogen in Czochralski silicon by infrared absorption spectroscopy," ECS Transactions Vol. 86(10), pp. 105-110 doi: 10.1149/08610.0087ecst. (2018/10).　**E, 1-08**

8) 井上 直久, "シリコン結晶の品質とデバイス特性(1)研究実用化の70年," 第66回応用物理学会春季講演会, 12p-M111-09 [東京工大・東京] (2019/03).　**E, 1-08**

9) 井上 直久, 川又 修一, 奥田 修一, "シリコン結晶の高感度赤外吸収と赤外欠陥動力学（14）NO 対系の赤外吸収と熱処理挙動" 第 66 回応用物理学会春季講演会, 12p-M111-10 [東京工大・東京] (2019/03).　**E, 1-08**

10) 井上 直久, 川又 修一, 奥田 修一, "シリコン結晶中の低濃度炭素の測定(XVIII) 赤外吸収と SIMS の相互較正", 第 66 回応用物理学会春季講演会, 12p-M111-11 [東京工大・東京] (2019/03).　**E, 1-08**

11) T. Okazaki et al., "Preliminary study of the portable Optically Stimulated Luminescence dosimetry system for measuring radiation doses more than 100 Gy", THP137, in Proceedings of the 15th Annual Meeting of PASJ, 1256-1259, Nagaoka, Japan (2018/08).　**G, 1-09**

12) 佐藤 史紀, 松島 怜達, 伊藤 義之, 齋藤 恭央, "東海再処理施設における低放射性廃液の処理技術開発(20)実機適用に向けたセメント固化体からの水素生成に係る検討", 日本原子力学会 2018 年秋の大会, 予稿集 3J02 (2018).　**G, 1-31**

13) Y. Kaneko, H. Hayashi, Y. Ishii, W. Kada, H. Nishikawa, "Refractive index change and thermo-optic effect in polydimethylsiloxane nanocomposites with oxide nanoparticles induced by proton beam writing", Paper No. O26, 16th International Conference on Nuclear Microprobe Technology and Applications (2018/07).　**S, 3-02**

14) T. Shibuya, S. Uchida, Y. Ishii, H. Nishikawa, "Assembling gold nanoparticles by dielectrophoresis with pit arrays on PMMA fabricated by proton beam writing", Paper No. P15, 16th International Conference on Nuclear Microprobe Technology and Applications (2018/07).　**S, 3-02**

15) H. Hayashi, W. Furukawa, H. Nishikawa, "Electronic Circuit Formation on Flexible Polymer Surface Processed by 1 MV Accelerated Hydrogen Molecular Ions", Paper No. O27, 16th

International Conference on Nuclear Microprobe Technology and Applications (2018/07). **S, 3-02**

16) 古川 航, 稲葉 公英, 内田 常幸, 落合 嘉彦, 佐藤 昇平, 森本 貴明, 林 秀臣, 西川 宏之, "溶液法による IGZO-TFT の作製とガスセンサ応用", 2018年放電学会年次大会,論文番号3-3 (2018/12). **S, 3-02**

17) 古川 航, 林 秀臣, 西川 宏之, 森本 貴明, "溶液法により作製したIGZO-TFTのオゾン暴露に対する濃度応答性", 平成31年電気学会全国大会, 講演番号2-102(2019/03). **S, 3-02**

18) 河嶋 涼介, 内田 諭, 西川 宏之, "ピット型誘電泳動デバイスにおける交流電気浸透の効果の数値解析", 平成31年電気学会全国大会, 講演番号3-189(2019/03). **S, 3-02**

19) 丸山 大貴, 内田 諭, 加藤 滉大, 西川 宏之, "ピット型電極を用いた三次元誘電泳動における直流オフセット電圧の影響", 平成31年電気学会全国大会, 講演番号3-190(2019/03) . **S, 3-02**

20) Y. Shimoda, K. Takakura, "Study on radiation hardness of three dimensional structured field effect transistor", IRID Symposium, Tokyo, Japan (2018/08). **E, 3-03**

21) T. Hamasaki, T. Sakai, K. Takakura and I. Tsunoda, "Evaluation of Au concentration for Au induced lateral crystallized Ge on insulating substrate", 37th Electron Materials Symposium, Shiga, Japan (2018/09). **E, 3-03**

22) N. Shimizu, T. Mori, K. Takakura and I. Tsunoda, "Low temperature formation of Ge (111)/Au/SiO2 by two step annealing", 37th Electron Materials Symposium, Shiga, Japan (2018/09). **E, 3-03**

23) H. Kanakogi, T. Nishijima, K. Takakura, and I. Tsunoda, "Electron irradiation effect on Sn induced lateral crystallization for amorphous Ge on insulating substrate ", 37th Electron Materials Symposium, Shiga, Japan (2018/09). **E, 3-03**

24) K. Matsuki, K. Iseri, K. Takakura, M. Yoneoka, I. Tsunoda, A. Veloso, E. Simoen and C. Claeys, "Radiation influence on transconductance of n-channel Silicon-on-Insulator Gate-All-Around FETs by 2 MeV electron irradiation", The 8th Forum on the Science and Technology of Silicon Materials 2018, Okayama, (2018/10). **E, 3-03**

25) 鹿子木 嘉城, 佐藤 亮起, 西嶋 泰樹, 小川 大輔, 高倉 健一郎, 角田 功, "非晶質 Ge/SiO2の Sn 誘起横方向低温（≦200℃）固相成長", 第79回応用物理学会秋季学術講演会・名古屋 (2019/09). **E, 3-03**

26) 濱崎 健, 坂井 拓也, 角 和章, 高倉 健一郎, 角田 功, "Au誘起横方向成長した結晶 Ge 内の Au 濃度評価", 第79回応用物理学会秋季学術講演会・名古屋(2019/09). **E, 3-03**

27) 鹿子木 嘉城, 佐藤 亮起, 西嶋 泰樹, 小川 大輔, 高倉 健一郎, 角田 功, "電子線照射 a-Ge/SiO2の Sn 誘起横方向成長", 第10回半導体材料・デバイスフォーラム・熊本 (2019/10). **E, 3-03**

28) 清水 昇, 森 貴礼, 高倉 健一郎, 角田 功, "Au 拡散抑制した Au 誘起成長法による結晶 Ge の高品質形成", 第10回半導体材料・デバイスフォーラム・熊本 (2019/10). **E, 3-03**

29) 下田 優希, 松木 賢斗, 米岡 将士, 角田 功, Eddy Simoen, Cor Claeys, 高倉 健一郎, "電子線照射 a-Ge/SiO2の Sn 誘起横方向成長", 第10回半導体材料・デバイスフォーラム・熊本 (2019/10). **E, 3-03**

30) 明午 伸一郎, 武井 早憲, 松田 洋樹, 百合 庸介, 湯山 貴裕, "大強度陽子加速器のための標的上のプロファイルモニタの開発", Proceedings of the 15th Annual Meeting of Particle Accelerator Society of Japan, pp. 1035-1039(2018/08). **C**

Appendix 2   Type of Research Collaboration and Facilities Used for Research

Paper No.	Type of Research Collaboration*1					Irradiation Facilities*2						Paper No.	Type of Research Collaboration*1					Irradiation Facilities*2					
	Joint Res.	Entr. Res.	Coop. Res.	Inter. Use	Ext. Use	C	T	S	I	E	G		Joint Res.	Entr. Res.	Coop. Res.	Inter. Use	Ext. Use	C	T	S	I	E	G
1-01				●			◎					2-08	●					◎					
1-02	●					◎	◎		◎	◎		2-09			●			◎					
1-03	●					◎						2-10	●					◎					
1-04					●	◎						2-11	●					◎					
1-05					●						◎	2-12	●					◎					
1-06					●		◎					2-13	●					◎	◎				◎
1-07					●				◎			2-14	●					◎					
1-08					●					◎		2-15	●					◎					
1-09				●					◎			2-16	●					◎					
1-10				●				◎		◎		2-17					●	◎					
1-11				●							◎	2-18	●					◎					
1-12	●								◎			2-19	●					◎					
1-13	●								◎			2-20	●										◎
1-14				●			◎		◎			2-21	●					◎					
1-15				●							◎	2-22	●					◎					
1-16	●										◎	2-23	●										◎
1-17	●										◎	2-24					●	◎					
1-18				●							◎	2-25	●					◎					
1-19				●						◎		2-26	●										◎
1-20	●									◎	◎	2-27	●					◎					
1-21				●						◎		2-28	●					◎					
1-22	●									◎		2-29	●					◎					
1-23					●			◎	◎			2-30	●					◎					
1-24					●						◎	2-31			●					◎			
1-25				●		◎	◎	◎				2-32			●					◎			
1-26				●		◎	◎	◎				2-33			●N								
1-27				●							◎	2-34			●					◎			
1-28				●							◎	2-35			●					◎			
1-29	●						◎					2-36			●					◎			
1-30					●						◎	2-37			●					◎			
1-31					●						◎												
1-32	●								◎	◎		3-01	●					◎					
1-33	●								◎			3-02	●							◎			
												3-03				●						◎	
2-01				●		◎						3-04			●							◎	
2-02	●					◎						3-05	●					◎					
2-03	●					◎						3-06			●					◎		◎	
2-04	●					◎						3-07	●							◎			
2-05	●					◎						3-08			●							◎	
2-06				●		◎						3-09	●							◎			
2-07	●					◎						3-10					●						◎

Paper No.	Joint Res.	Entr. Res.	Coop. Res.	Inter. Use	Ext. Use	C	T	S	I	E	G	Paper No.	Joint Res.	Entr. Res.	Coop. Res.	Inter. Use	Ext. Use	C	T	S	I	E	G
3-11			●N																				
3-12				●N																			
3-13				●		◎																	
3-14				●			◎	◎	◎														
3-15	●								◎														
3-16			●							◎													
3-17	●								◎														
3-18					●	◎																	
4-01						◎	◎	◎	◎														
4-02						◎																	
4-03							◎	◎	◎														
4-04										◎	◎												
4-05										◎	◎												
4-06						◎	◎	◎	◎														
4-07						◎	◎	◎	◎														
4-08						◎	◎	◎	◎	◎	◎												
Total	43	0	11	20	14	39	16	20	21	12	20												

*1 Type of Research Collaboration

Joint Res. : Joint research with external users

Entr. Res. : Research entrusted to QST

Coop. Res. : Cooperative research with plural universities through The University of Tokyo

Inter. Use : Internal use

Ext. Use : Common use based on two programs of "QST-facility-use" and "Creation of Research Platforms and Sharing of Advanced Research Infrastructure" supported from MEXT

*2 Utilization of Irradiation Facilities

C : AVF Cyclotron

T : 3 MV Tandem Electrostatic Accelerator

S : 3 MV Single-ended Electrostatic Accelerator

I : 400 kV Ion Implanter

E : 2 MV Electron Accelerator

G : Co-60 Gamma-ray Irradiation Facilities

N : Non-use of irradiation facilities at TARRI

Appendix 3　Examples of Typical Abbreviation Name for Organizations in National Institutes for Quantum and Radiological Science and Technology, and Japan Atomic Energy Agency

◆**Directorate, Institute, Center, Laboratory etc.**

【QST（量子科学技術研究開発機構）:　National Institutes for Quantum and Radiological Science and Technology】

QuBS	量子ビーム科学部門	:	Quantum Beam Science Research Directorate
TARRI	高崎量子応用研究所	:	Takasaki Advanced Radiation Research Institute
NFI	那珂核融合研究所	:	Naka Fusion Institute
RFI	六ヶ所核融合研究所	:	Rokkasho Fusion Institute
KPSI	関西光科学研究所	:	Kansai Photon Science Institute
NIRS	放射線医学総合研究所	:	National Institute of Radiological Sciences

【JAEA（日本原子力研究開発機構）:Japan Atomic Energy Agency】

NSRI	原子力科学研究所	:	Nuclear Science Research Institute
NSEC	原子力基礎工学研究センター	:	Nuclear Sciences and Engineering Center
MSRC	物質科学研究センター	:	Materials Sciences Research Center
NCL	核燃料サイクル工学研究所	:	Nuclear Fuel Cycle Engineering Laboratories
NBTC	環境技術開発センター（サイクル研）	:	Nuclear Backend Technology Center
TRTDC	東海再処理技術開発センター	:	Tokai Reprocessing Technology Development Center
CLADS	廃炉国際共同研究センター	:	Collaborative Laboratories for Advanced Decommissioning Science
J-PARC	J-PARCセンター	:	J-PARC Center

◆**Department, Division, Center etc.**
【QST】

・量子ビーム科学部門、研究企画部
　　Department of Research Planning and Promotion, QuBS, QST

・量子ビーム科学部門、高崎量子応用研究所、先端機能材料研究部
　　Department of Advanced Functional Materials Research, TARRI, QST

・量子ビーム科学部門、高崎量子応用研究所、放射線生物応用研究部
　　Department of Radiation-Applied Biology Research, TARRI, QST

・量子ビーム科学部門、高崎量子応用研究所、放射線高度利用施設部
　　Department of Advanced Radiation Technology, TARRI, QST

・量子ビーム科学部門、高崎量子応用研究所、東海量子ビーム応用研究センター
　　Tokai Quantum Beam Science Center, TARRI, QST

・量子ビーム科学部門、高崎量子応用研究所、管理部
　　Department of Administrative Services, TARRI, QST

・量子ビーム科学部門、関西光科学研究所、光量子科学研究部
　　Department of Advanced Photon Research, KPSI, QST

・量子ビーム科学部門、関西光科学研究所、放射光科学研究センター
　　Synchrotron Radiation Research Center, KPSI, QST

・核融合エネルギー部門、那珂核融合研究所、ITERプロジェクト部
　　Department of ITER Project, NFI, QST
・核融合エネルギー部門、六ヶ所核融合研究所、核融合炉材料研究開発部
　　Department of Fusion Reactor Materials Research, RFI, QST
・量子医学・医療部門、放射線医学総合研究所、放射線障害治療研究部
　　Department of Basic Medical Sciences for Radiation Damages, NIRS, QST
・量子医学・医療部門、放射線医学総合研究所、重粒子線治療研究部
　　Department of Charged Particle Therapy Research, NIRS, QST
・量子医学・医療部門、放射線医学総合研究所、物理工学部
　　Department of Accelerator and Medical Physics, NIRS, QST

【JAEA】
・原子力基礎工学研究センター
　　Nuclear Science and Engineering Center, JAEA
・原子力基礎工学研究センター、燃料・材料工学ディビジョン
　　Fuels and Materials Engineering Division, NSEC, JAEA
・物質科学研究センター
　　Materials Sciences Research Center, JAEA
・先端基礎研究センター
　　Advanced Science Research Center, JAEA
・核燃料サイクル工学研究所
　　Nuclear Fuel Cycle Engineering Laboratories, JAEA
・核燃料サイクル工学研究所、東海再処理技術開発センター
　　Tokai Reprocessing Technology Development Center, NCL, JAEA
・環境技術開発センター（核燃料サイクル工学研）、再処理技術開発試験部
　　Department of Reprocessing Technology Development, NBTC, JAEA
・J-PARCセンター、加速器ディビジョン
　　Accelerator Division, J-PARC, JAEA
・廃炉国際共同研究センター
　　Collaborative Laboratories for Advanced Decommissioning Science, JAEA

http://www.qst.go.jp